UNIVERSIDAD DE OVIEDO

Departamento de Física

Search for the Standard Model Higgs Boson associated with a W Boson using Matrix Element Technique in the CDF detector at the Tevatron

Bárbara Álvarez González

UNIVERSIDAD DE OVIEDO

Departamento de Física

Search for the Standard Model Higgs Boson associated with a W Boson using Matrix Element Technique in the CDF detector at the Tevatron

Bárbara Álvarez González

Dedicada a mi familia y amigos con mucho cariño

Contents

List of Figures

List of Tables

Chapter 1

Introduction

Understanding the mechanism that breaks electroweak symmetry and generates the mass of all known elementary particles is one of the most fundamental problems in particle physics. The Higgs model is one of the favorite candidates to explain the origin of mass. It has been extensively studied during the past decades. Prior to 1989, when the e^+e^- collider LEP at CERN came into operation, searches for the Higgs boson were sensitive only to Higgs bosons with masses below a few GeV. In the LEP1 phase, the collider operated at center of mass energies close to the mass of the Z boson. During the LEP2 phase, the energy was increased in steps, reaching 209 GeV in the year 2000 before the final shutdown. The combined data of the four LEP experiments, ALEPH, DELPHI, L3, and OPAL, was sensitive to neutral Higgs bosons with masses up to about 115 GeV and to charged Higgs bosons with masses up to about 90 GeV [1] [2].

The search for the Higgs boson continues at the Tevatron $p\bar{p}$ collider, operating at a center of mass energy of 1.96 TeV. The sensitivity of the two experiments, CDF and DØ, is improving, and has extended the Higgs boson mass coverage range beyond the LEP reach. Most existing results are expected to improve with the full Tevatron integrated luminosity.

To have a chance of finding the Higgs boson, we have to prove that we are able to find similar signals, and measure their cross sections. Figure 1.1 shows the cross section measurements of different processes like $t\bar{t}$, single top, or diboson measured by the CDF collaboration in the latest years, thanks to the great performance of the accelerator and the experiment, the increased of integrated luminosity, the good understanding of the data, and the development of new and sophisticated analysis techniques. This has lead us to observe those tiny signals, which have very similar signatures to the expected from a decay of a Higgs boson, on top of a large background.

All these aspects are essential to prove to the physics community that, if the SM Higgs boson exits, we are able to find it if enough luminosity is recorded.

The searches for the mechanism of the electroweak symetry breaking, if it is not found in the Tevatron, will continue with significantly higher sensitivities in the coming years at the LHC pp collider, and it is expected to cover masses up to about 1 TeV in the case of the SM Higgs boson [3] [4]. Once evidence for the dynamics of electroweak symmetry breaking is obtained, a more complete understanding of the mechanism will require measurements at

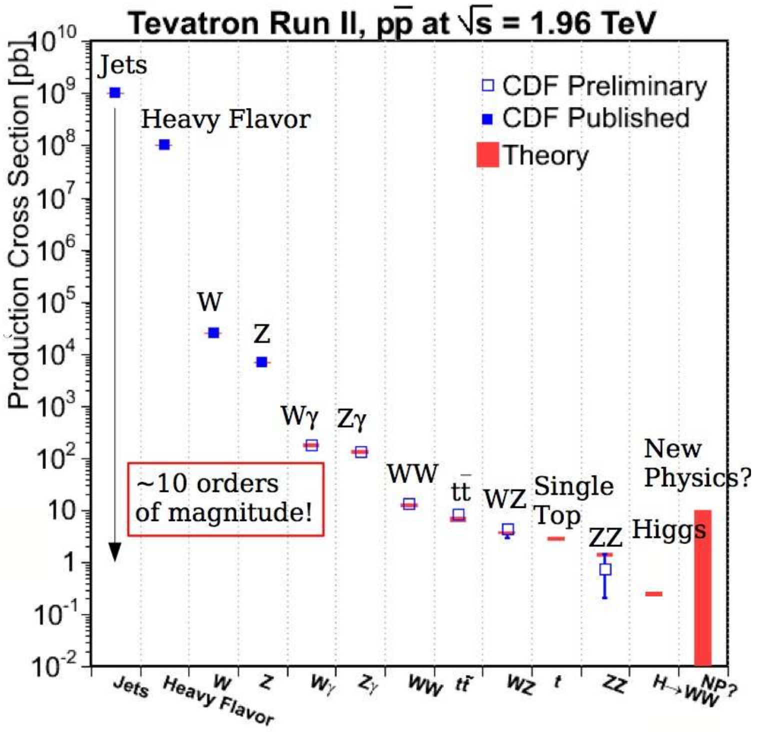

Figure 1.1: Production cross sections. The blue squares correspond to the measured cross sections by the CDF experiment. The theoretical prediction is shown in red.

future e^+e^- [5] and perhaps $\mu^+\mu^-$ colliders [6].

In this thesis a direct search for the Standard Model Higgs boson production in association with a W boson at the CDF detector in the Tevatron is presented. This search contributes predominantly in the region of low mass Higgs region, when the mass of Higgs boson is less than about 135 GeV.

The search is performed in a final state where the Higgs boson decays into two b quarks, and the W boson decays leptonically, to a charged lepton (it can be an electron or a muon) and a neutrino.

This work is organized as follows. Chapter 2 gives an overview of the Standard Model theory of particle physics and presents the SM Higgs boson search results at LEP, and the Tevatron colliders, as well as the prospects for the SM Higgs boson searches at the LHC.

The dataset used in this analysis corresponds to 4.8 fb^{-1} of integrated luminosity of $p\bar{p}$ collisions at a center of mass energy of 1.96 TeV. That is the luminosity acquired between the beggining of the CDF Run II experiment, February 2002, and May 2009. The relevant aspects, for this analysis, of the Tevatron accelerator and the CDF detector are shown in Chapter 3.

Physics processes in which a W boson is produced in association with several jets can be misidentified as WH events since they may have the same signature as the signal, these type of processes are known as the backgrounds of a given signal. One of the main aspects of the analysis is the identification and the estimation of the background and the development of strategies to reduce their contribution, allowing at the same time, to keep as many signal events as possible. Identifying long lived b hadrons in jets is essential to increase the signal over background ratio. In Chapter 4 the particles and observables that make up the WH final state, electrons, muons, $\not\!\!E_T$, and jets are presented. The CDF standard b-tagging algorithms to identify b jets, and the neural network flavor separator to distinguish them from other flavor jets are also described in Chapter 4.

The main background contributions are those coming from heavy flavor production processes, such as those coming from $Wb\bar{b}$, $Wc\bar{c}$ or Wc and $t\bar{t}$. The signal and background signatures are discussed in Chapter 5 together with the Monte Carlo generators that have been used to simulate almost all the events used in this thesis. The rest of the background events are modeled from the data.

WH candidate events have a high-p_T lepton (electron or muon), high missing transverse energy, and two or more than two jets (extra jets are coming from initial or final state radiation) in the final state. Chapter 6 describes the event selection applied in this analysis and the method used to estimate the background contribution.

The amount of WH signal events after the initial selection is much smaller than the uncertainty in the background prediction. Thus in this case, a method based in counting the total number of events only is hopeless. Then, a more sophisticated technique have to be used. The Matrix Element method, that was succesfully used in the single top discovery analysis and many other analyses within the CDF collaboration, is the multivariate technique used in this thesis to discriminante signal from background events. With this technique is possible to calculate a probability for an event to be classified as signal or background. These probabilities are then combined into a discriminant function called the Event Probability Discriminant, EPD, which increases the sensitivity of the WH process. This method is described in detailed in Chapter 7.

As no evidence for the signal has been found, the results obtained with this work are presented in Chapter 8 in terms of exclusion regions as a function of the mass of the Higgs boson, taken into acount the full systematics.

Finally, the conclusions of this work to obtain the PhD are presented in Chapter 9 including a complete overview of the analysis and the improvements that have been obtained in the search for the Standard Model Higgs boson in the mass range between the LEP limit and about 135 GeV, using 4.8 fb^{-1} of data colleted by the CDF experiment at the Tevatron collider. In this chapter, the contribution that this analysis has in the combination of the SM Higgs boson searches combination in the Tevatron is also presented.

Chapter 2

Standard Model (SM) and SM Higgs Physics

In this chapter an overview of the Standard Model (SM) is presented. It focuses on the Higgs boson searches at LEP, LHC, and Tevatron.

The outline of this chapter is as follows: in Section 2.1 we give a brief introduction to the Standard Model of particle physics, describing the elementary particles and its interactions. Section 2.2 contains in detailed the results and prospects for the Standard Model Higgs boson searches at LEP, the LHC, and the Tevatron, including the decay modes and production channels. There are some features that SM cannot explain, we will cover them in Section 2.3.

2.1 The Standard Model

The Standard Model (SM) of particle physics is a theory of three of the four known fundamental interactions, and the elementary particles that take part in these interactions. Elementary particle or fundamental particle is a particle not known to have substructure; it is one of the basic building blocks of the universe from which all other particles are made.

In the Standard Model, quarks, leptons, and gauge bosons are elementary particles. All elementary particles are either bosons or fermions, depending on their spin. Particles normally associated with matter are fermions, having half-integer spin; particles which obey Fermi-Dirac statistics. Particles associated with fundamental forces are bosons, having integer spin; which obey Bose-Einstein statistics.

Fermions

In the Standard Model there are two types of elementary fermions: quarks and leptons. In total, there are 24 different fermions; 6 quarks and 6 leptons, each one with a corresponding antiparticle. The fermions of the Standard Model are classified according to how they interact. The quarks come in six different flavors: up, down, charm, strange, top, and bottom; formally described by assigning flavor quantum numbers. The SM incorporates six leptons: the electron (e^-), the electron neutrino (ν_e), the muon (μ^-), the muon neutrino

(ν_μ), the tau (τ^-), and the tau neutrino (ν_τ). Pairs from each classification are grouped together to form a generation as shown in Table 2.1 which also contains the charges and masses of the particles. Each quark and each lepton has an associated antiparticle with the same mass but opposite charge. The antiquarks are denoted $\bar{u}$, $\bar{d}$, etc. The antiparticle of the electron is the positron (e^+).

Table 2.1: Charges and masses of the three generations of quarks and leptons [7].

Generation	First		Second		Third	
Quarks (spin = 1/2)						
Symbol	u	d	c	s	t	b
Charge	+2/3	-1/3	+2/3	-1/3	+2/3	-1/3
Mass (MeV/c^2)	1.5-3.3	3.5-6	(1.16-1.34)$\cdot 10^3$	70-130	(171.3±1.1±1.2)$\cdot 10^3$	(4.13-4.37)$\cdot 10^3$
Interaction	EM, Weak, Strong					
Leptons (spin = 1/2)						
Symbol	ν_e	e^-	ν_μ	μ^-	ν_τ	τ^-
Charge	0	-1	0	-1	0	-1
Mass (MeV/c^2)	$< 2 \cdot 10^{-6}$	0.511	<0.19	105.7	<18.2	1776.84
Interaction	Weak	EM, Weak	Weak	EM, Weak	Weak	EM, Weak

The three generations exhibit a striking mass hierarchy, the top quark having by far the highest mass. Understanding the deeper reason behind the hierarchy and generation structure is one of the open questions of particle physics.

The defining property of the quarks is that they carry color charge, and hence, interact via the strong interaction. Quarks also carry electric charge and weak isospin. Therefore they interact with other fermions both electromagnetically and via the weak nuclear interaction.

The leptons do not carry color charge. The three neutrinos do not carry electric charge either, so their motion is directly influenced only by the weak nuclear force, which makes them notoriously difficult to detect. However, by virtue of carrying an electric charge, the electron, muon, and tau all interact electromagnetically.

Each member of a generation has greater mass than the corresponding particles of lower generations. The first generation charged particles do not decay; hence all ordinary matter is made of such particles. Second and third generations charged particles, on the other hand, decay with very short half lives, and are observed only in very high-energy environments. Neutrinos of all generations also do not decay and pervade the universe, but rarely interact with baryonic, particles made of three quarks, matter.

Bosons

The known forces mediating particles described by the Standard Model have spin, in their case, the value of the spin is 1. All forces mediating particles are bosons. The different types of bosons are described below.

- Photons (γ) mediate the electromagnetic force between electrically charged particles. The photon is massless and is well described by the theory of quantum electrodynamics.

- The W$^+$, W$^-$, and Z gauge bosons mediate the weak interactions between particles of different flavors (all quarks and leptons): the $W^\pm$ mass is $M_W = (80.425 \pm 0.038)$ GeV/c^2 [7], and the Z^0, $M_Z = (91.1876 \pm 0.0021)$ GeV/c^2 [7]. The weak interactions involving the W$^\pm$ act on exclusively left-handed particles and right-handed antiparticles. Furthermore, the W$^\pm$ carry an electric charge of +1 and -1 and couple to the electromagnetic interactions. The electrically neutral Z boson interacts with both left-handed particles and antiparticles. These three gauge bosons along with the photons are grouped together which collectively mediate the electroweak interactions.

- The eight gluons mediate the strong interactions between color charged particles (the quarks). Gluons are massless. The eightfold multiplicity of gluons is labeled by a combination of color and an anticolor charge. Because the gluon has an effective color charge, they can interact among themselves. The gluons and their interactions are described by the theory of quantum chromodynamics, known as QCD.

Interactions

Interactions in physics are the ways that particles influence other particles. The forces of nature acting between quarks and leptons are described by quantized fields. The SM incorporates the electromagnetic force, the weak force, and the strong force which keeps nuclei stable. Gravitation is not included in the framework of the SM but rather described by the theory of general relativity. All particles with mass or energy feel the gravitational force. However, due to the weakness of gravitation with respect to the other forces acting in elementary particle reactions it is not further considered in this thesis.

The electromagnetic, weak and strong forces are described by so called quantum gauge field theories (see explanation below). Table 2.2 shows the charges and masses of the gauge bosons.

Table 2.2: Charges and masses of the gauge bosons.

Gauge Bosons (spin = 1)				
Symbol	Force	Coupling	Charge	Mass (GeV/c^2)
γ	EM	10^{-2}	0	0
W	Weak	10^{-13}	±1	80.4
Z	Weak	10^{-13}	0	91.2
g	Strong	1	0	0

Quarks participate in electromagnetic, weak and strong interactions. All leptons experience the weak force, the charged ones also feel the electromagnetic force. But leptons do not take part in strong interactions.

2.1.1 Electroweak Interactions

In quantum field theory quarks and leptons are represented by spinor fields Ψ which are functions of the continuous space-time coordinates x_μ. To take into account that the weak interaction only couples to the left-handed particles and right-handed antiparticles, left- and right-handed fields $\Psi_{\mathbf{L}} = \frac{1}{2}(1-\gamma_5)\,\Psi$ and $\Psi_{\mathbf{R}} = \frac{1}{2}(1+\gamma_5)\,\Psi$ are introduced. The left-handed states of one generation are grouped into weak-isospin doublets, the right-handed states form singlets:

$$\begin{pmatrix} u \\ d \end{pmatrix}_L \begin{pmatrix} c \\ s \end{pmatrix}_L \begin{pmatrix} t \\ b \end{pmatrix}_L \qquad \begin{pmatrix} \nu_e \\ e \end{pmatrix}_L \begin{pmatrix} \nu_\mu \\ \mu \end{pmatrix}_L \begin{pmatrix} \nu_\tau \\ \tau \end{pmatrix}_L$$

$$\begin{array}{cccccc} u_R & c_R & t_R & & & \\ d_R & s_R & b_R & e_R & \mu_R & \tau_R \end{array}$$

The weak-isospin assignment for the doublet is: up-type quarks (u,c,t) and neutrinos carry $T_3 = +\frac{1}{2}$; down-type quarks (d,s,b), electron, muon and tau lepton have $T_3 = -\frac{1}{2}$. In the original SM the right-handed neutrino states are omitted, since neutrinos are assumed to be massless. Experimental evidence [8–10], however, strongly indicates that neutrinos have mass and the SM needs to be extended in this respect.

The dynamics of the electromagnetic and weak forces follow from the free particle Lagrangian density

$$\mathcal{L}_0 = i\,\overline{\Psi}\,\gamma^\mu \partial_\mu\,\Psi \tag{2.1}$$

by demanding the invariance of $\mathcal{L}_0$ under local phase transformations:

$$\Psi_{\mathbf{L}} \longrightarrow e^{ig\alpha(x)\cdot\mathbf{T}+ig'\beta(x)Y}\,\Psi_{\mathbf{L}} \qquad \text{and} \qquad \Psi_{\mathbf{R}} \longrightarrow e^{ig'\beta(x)Y}\,\Psi_{\mathbf{R}}\,. \tag{2.2}$$

For historical reasons these transformations are also referred to as gauge transformations. In Eq. 2.2 the parameter $\alpha(x)$ is an arbitrary three-component vector and $\mathbf{T} = (T_1,\, T_2,\, T_3)^t$ is the weak-isospin operator whose components T_i are the generators of $SU(2)_L$ symmetry transformations. The index L indicates that the phase transformations act only on left-handed states. The matrix representations are given by $T_i = \frac{1}{2}\,\tau_i$ where the τ_i are the Pauli matrices. The T_i do not commute: $[T_i, T_j] = i\,\epsilon_{ijk}\,T_k$. That is why the $SU(2)_L$ gauge group is said to be non-Abelian. $\beta(x)$ is a one-dimensional function of x. Y is the weak hypercharge which satisfies the relation $Q = T_3 + Y/2$, where Q is the electromagnetic charge. Y is the generator of the symmetry group $U(1)_Y$. Demanding the Lagrangian $\mathcal{L}_0$ to be invariant under the combined gauge transformations of $SU(2)_L \times U(1)_Y$, see Eq. 2.2, requires the addition of terms to the free Lagrangian which involve four additional vector (spin 1) fields: the isotriplet $\mathbf{W}_\mu = (W_{1\,\mu}, W_{2\,\mu}, W_{3\,\mu})^t$ for $SU(2)_L$ and the singlet B_μ for $U(1)_Y$. This is technically done by replacing the derivative ∂_μ in $\mathcal{L}_0$ by the covariant derivative

$$D_\mu = \partial_\mu + i\,g\,\mathbf{W}_\mu \cdot \mathbf{T} + i\,g'\frac{1}{2}B_\mu Y \tag{2.3}$$

and adding the kinetic energy terms of the gauge fields: $-\frac{1}{4}\mathbf{W}_{\mu\nu}\cdot\mathbf{W}^{\mu\nu} - \frac{1}{4}B_{\mu\nu}{\cdot}B^{\mu\nu}$. The field tensors $\mathbf{W}_{\mu\nu}$ and $B_{\mu\nu}$ are given by $\mathbf{W}_{\mu\nu} = \partial_\mu\mathbf{W}_\nu - \partial_\nu\mathbf{W}_\mu - g\cdot\mathbf{W}_\mu \times \mathbf{W}_\nu$ and $B_{\mu\nu} =$

$\partial_\mu B_\nu - \partial_\nu B_\mu$. Since the vector fields $\mathbf{W}_\mu$ and B_μ are introduced via gauge transformations they are called gauge fields and the quanta of these fields are named gauge bosons. For an electron-neutrino pair, for example, the resulting Lagrangian is:

$$\begin{aligned}\mathcal{L}_1 \;&=\; i\,\overline{\begin{pmatrix}\nu_e\\ e\end{pmatrix}}_L\,\gamma^\mu\left[\partial_\mu + i\,g\,\mathbf{W}_\mu\cdot\mathbf{T} + i\,g'\,Y_L\,\frac{1}{2}\,B_\mu\right]\begin{pmatrix}\nu_e\\ e\end{pmatrix}_L +\\ &\quad i\,\bar{e}_R\,\gamma^\mu\left[\partial_\mu - g'\,Y_R\,\frac{1}{2}\,B_\mu\right]e_R - \frac{1}{4}\,\mathbf{W}_{\mu\nu}\cdot\mathbf{W}^{\mu\nu} - \frac{1}{4}B_{\mu\nu}\cdot B^{\mu\nu}\end{aligned} \tag{2.4}$$

This model developed by Glashow [11], Weinberg and Salam [12, 13] in the 1960s allows to describe electromagnetic and weak interactions in one framework. One therefore refers to it as unified electroweak theory.

2.1.2 The Higgs Mechanism

One has to note, however, that $\mathcal{L}_1$ describes only massless gauge bosons and massless fermions. Mass-terms such as $\frac{1}{2}M^2 B_\mu B^\mu$ or $-m\overline{\Psi}\Psi$ are not gauge invariant and therefore cannot be added. To include massive particles into the model in a gauge invariant way the Higgs mechanism is used. Four scalar fields are added to the theory in form of the isospin doublet $\mathbf{\Phi} = (\phi^+,\ \phi^0)^t$ where ϕ^+ and ϕ^0 are complex fields. This is the minimal choice. The term $\mathcal{L}_H = |D_\mu\Phi|^2 - V(\Phi^\dagger\Phi)$ is added to $\mathcal{L}_1$. The scalar potential takes the form $V(\Phi^\dagger\Phi) = \mu^2\ \mathbf{\Phi}^\dagger\mathbf{\Phi} + \lambda\ (\Phi^\dagger\Phi)^2$.

In most cases particle reactions cannot be calculated from first principles. One rather has to use perturbation theory and expand a solution starting from the ground state of the system which is in particle physics called the vacuum expectation value. The parameters μ and λ can be chosen such that the vacuum expectation value of the Higgs potential V is different from zero: $|\Phi_{\text{vac}}| = \sqrt{-\frac{1}{2}\,\mu^2/\lambda}$ and thus does not share the symmetry of V. The scalar Higgs fields inside Φ are redefined such that the new fields, $\xi(x) = (\xi_1(x), \xi_2(x), \xi_3(x))^t$ and $H(x)$, have zero vacuum expectation value. When the new parameterization of $\mathbf{\Phi}$ is inserted into the Lagrangian, the symmetry of the Lagrangian is broken, that is, the Lagrangian is not an even function of the Higgs fields anymore. This mechanism where the ground states do not share the symmetry of the Lagrangian is called spontaneous symmetry breaking. As a result, one of the Higgs fields, the $H(x)$ field, has acquired mass, while the other three fields, ξ, remain massless [14, 15].

Applying spontaneous symmetry breaking as described above to the combined Lagrangian $\mathcal{L}_2 = \mathcal{L}_1 + \mathcal{L}_H$ and enforcing local gauge invariance of $\mathcal{L}_2$, makes the three electroweak gauge bosons acquire mass. After all, this is the aim of the whole procedure. The massive bosons are, however, not the original fields $\mathbf{W}_\mu$ and B_μ but rather mixtures of those: the $W^\pm_\mu = (W^1_\mu \mp i\,W^2_\mu)/\sqrt{2}$, the Z^0 and the photon field A_μ:

$$\begin{pmatrix}A_\mu\\ Z_\mu\end{pmatrix} = \begin{pmatrix}\cos\theta_W & \sin\theta_W\\ -\sin\theta_W & \cos\theta_W\end{pmatrix}\begin{pmatrix}B_\mu\\ W^3_\mu\end{pmatrix} \tag{2.5}$$

The mixing angle θ_W is the Weinberg angle defined by the coupling constants $g'/g = \tan\theta_W$.

Spontaneous symmetry breaking also generates lepton masses if Yukawa interaction terms of the lepton and Higgs fields are added to the Lagrangian:

$$\mathcal{L}^{\text{lepton}}_{\text{Yukawa}} = -G_e \left[\bar{e}_R \left(\mathbf{\Phi}^\dagger \begin{pmatrix} \nu_e \\ e \end{pmatrix}_L \right) + \left(\overline{(\nu_e, e)}^t_L \mathbf{\Phi} \right) e_R \right] \tag{2.6}$$

Here the Yukawa terms for the electron-neutrino doublet are given as an example. G_e is a further coupling constant describing the coupling of the electron and electron-neutrino to the Higgs field. In this formalism neutrinos are assumed to be massless.

Quark masses are also generated by adding Yukawa terms to the Lagrangian. However, for the quarks, both the upper and the lower member of the weak-isospin doublet need to acquire mass. For this to happen an additional conjugate Higgs multiplet has to be constructed: $\Phi_c = i\tau_2\Phi^* = (\phi^{0^*}, -\phi^-)^t$. The Yukawa terms for the quarks are given by:

$$\mathcal{L}^{\text{quark}}_{\text{Yukawa}} = \sum_{i=1}^{3}\sum_{j=1}^{3} \tilde{G}_{ij}\ \bar{u}_{iR}\tilde{\Phi}^\dagger \begin{pmatrix} u_j \\ d_j \end{pmatrix}_L + G_{ij}\ \bar{d}_{iR}\ \Phi^\dagger \begin{pmatrix} u_j \\ d_j \end{pmatrix}_L + \text{ h.c.} \tag{2.7}$$

The u_j and d_j are the weak eigenstates of the up-type (u, c, t) and the down-type (d, s, b) quarks, respectively. Couplings between quarks of different generations are allowed by this ansatz. After spontaneous symmetry breaking the Yukawa terms produce mass terms for the quarks which can be described by mass matrices in generation space: $\overline{(u_1, u_2, u_3)}_R\ \mathcal{M}^u\ (u_1, u_2, u_3)^t_L$ and $\overline{(d_1, d_2, d_3)}_R\ \mathcal{M}^d\ (d_1, d_2, d_3)^t_L$ with $\mathcal{M}^u_{ij} = |\Phi_{\text{vac}}| \cdot \tilde{G}_{ij}$ and $\mathcal{M}^d_{ij} = |\Phi_{\text{vac}}| \cdot G_{ij}$. The mass matrices are non-diagonal but can be diagonalized by unitary transformations, which essentially means to change basis from weak eigenstates to mass eigenstates, which are identical to the flavor eigenstates u, c, t and d, s, b. In charged-current interactions ($W^\pm$ exchange) this leads to transitions between mass eigenstates of different generations referred to as generation mixing. It is possible to set weak and mass eigenstates equal for the up-type quarks and ascribe the mixing entirely to the down-type quarks:

$$\begin{pmatrix} d' \\ s' \\ b' \end{pmatrix}_L = \mathbf{V} \begin{pmatrix} d \\ s \\ b \end{pmatrix}_L = \begin{pmatrix} V_{ud} & V_{us} & V_{ub} \\ V_{cd} & V_{cs} & V_{cb} \\ V_{td} & V_{ts} & V_{tb} \end{pmatrix} \begin{pmatrix} d \\ s \\ b \end{pmatrix}_L \tag{2.8}$$

where d', s' and b' are the weak eigenstates. The mixing matrix $\mathbf{V}$ is called the Cabbibo-Kobayashi-Maskawa (CKM) matrix [16].

2.1.3 Strong Interactions

The theory of strong interactions is called quantum chromodynamics (QCD) since it attributes a color charge to the quarks. There are three different types of strong charges (colors): "red", "green" and "blue". Strong interactions conserve the flavor of quarks. Leptons do not carry color at all, they are inert with respect to strong interactions. QCD is a quantum field theory based on the non-Abelian gauge group $SU(3)_C$ of phase transformations on the quark color fields. Invoking local gauge invariance of the Lagrangian yields eight massless gauge bosons: the gluons. The gauge symmetry is exact and not broken as in the case of weak interactions. Each gluon carries one unit of color and one unit of anticolor. The strong force binds quarks together to form bound-states called hadrons. There are two groups of hadrons: mesons consisting of a quark and an antiquark, and baryons built of either three quarks or three antiquarks. All hadrons are color-singlet states. Quarks cannot exist as free particles. This experimental fact is summarised in the notion of quark confinement: quarks are confined to exist in hadrons.

2.2 The Standard Model Higgs Boson

One of the main challenges in high-energy physics is to understand electroweak symmetry breaking and the origin of mass. In the Standard Model (SM), the electroweak interaction is described by a gauge field theory based on the $\mathrm{SU}(2)_L \times \mathrm{U}(1)_Y$ symmetry group. Masses can be introduced by the Higgs mechanism as described above. In the simplest form of this mechanism, which is implemented in the SM, fundamental scalar "Higgs" fields fill the vacuum and acquire non-zero vacuum expectation values, and the $\mathrm{SU}(2)_L \times \mathrm{U}(1)_Y$ symmetry is spontaneously broken down to the electromagnetic $\mathrm{U}(1)_{\mathrm{EM}}$ symmetry. Gauge bosons and fermions obtain their masses by interacting with the vacuum Higgs fields. Associated with this description is the existence of massive scalar particles, Higgs bosons.

In the SM, the Higgs boson mass is given by $m_H = \sqrt{\lambda/2}\ v$, where λ is the Higgs self-coupling parameter and v is the vacuum expectation value of the Higgs field, $v = (\sqrt{2}G_F)^{-1/2} = 246$ GeV, fixed by the Fermi coupling G_F. Since λ is presently unknown, the value of the SM Higgs boson mass m_H cannot be predicted. However, besides the upper bound on the Higgs mass from unitarity constraints [17] [18], additional theoretical arguments place approximate upper and lower bounds on m_H [19]. There is an upper bound based on the perturbativity of the theory up to the scale Λ at which the SM breaks down, and a lower bound derived from the stability of the Higgs potential. If m_H is too large, then the Higgs self-coupling diverges at some scale Λ below the Planck scale. If m_H is too small, then the Higgs potential develops a second (global) minimum at a large value of the scalar field of order Λ. New physics must enter at a scale Λ or below, so that the global minimum of the theory corresponds to the observed $\mathrm{SU}(2)_L \times \mathrm{U}(1)_Y$ broken vacuum with $v = 246$ GeV. Given a value of Λ, one can compute the minimum and maximum allowed Higgs boson mass. Conversely, the value of m_H itself can provide an important constraint on the scale up to which the SM remains sucessful as an effective theory.

In particular, a Higgs boson with mass in the range 130 GeV $\leq m_H \leq$ 180 GeV is consistent with an effective SM description that survives all the way to the Planck scale, although the hierarchy problem between the electroweak scale and $\Lambda = M_{\mathrm{Pl}}$ still persists. The lower bound on m_H can be reduced to about 115 GeV, if one allows for the electroweak vacuum to be metastable, with a lifetime greater than the age of the universe.

The SM Higgs couplings to fundamental fermions are proportional to the fermion masses, and the couplings to bosons are proportional to the squares of the boson masses. In particular, the SM Higgs boson is a CP-even scalar, and its couplings to gauge bosons, Higgs bosons and fermions are given by:

$$g_{Hf\bar{f}} = \frac{m_f}{v}, \qquad g_{HVV} = \frac{2m_V^2}{v}, \qquad g_{HHVV} = \frac{2m_V^2}{v^2}$$

$$g_{HHH} = \frac{3m_H^2}{v} \qquad g_{HHHH} = \frac{3m_H^2}{v^2}$$

where $V = W$ or Z.

The cross sections for the production of SM Higgs bosons are summarized in Figure 2.1 for $p\bar{p}$ collisions at the Tevatron, and in Figure 2.2 for pp collisions at the LHC. The cross section for the $gg \to H+X$ process is known at next-to-next-to-leading order (NNLO) QCD, in the large top-mass limit, and at NLO in QCD for arbitrary top mass.

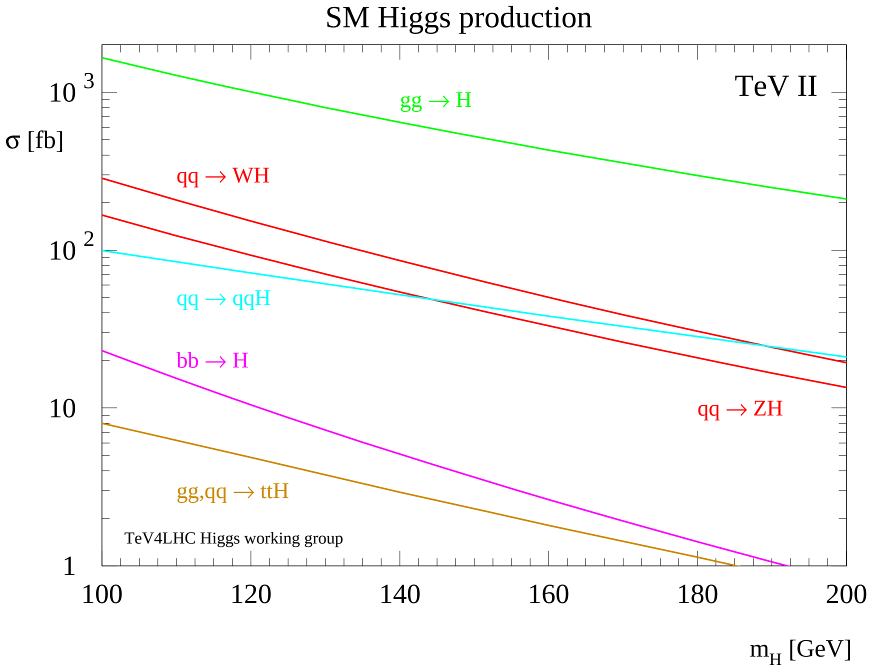

Figure 2.1: SM Higgs production cross sections for $p\bar{p}$ collisions at 1.96 TeV [20].

The branching ratios for the most relevant decay modes of the SM Higgs boson are shown in Figure 2.3 as functions of m_H. For masses below 135 GeV, decays to fermion pairs dominate, of which the decay $H \to b\bar{b}$ has the largest branching ratio. Decays to $\tau^+\tau^-$, $c\bar{c}$ and gluon pairs together contribute less than 15%. For such low masses, the total decay width is less than 10 MeV. For Higgs boson masses above 135 GeV, the WW decay dominates (below the WW threshold, one of the W bosons is virtual) with an important contribution from $H \to ZZ$, and the decay width rises rapidly, reaching about 1 GeV at $m_H = 200$ GeV and 100 GeV at $m_H = 500$ GeV. Above the $t\bar{t}$ threshold, the branching ratio into top-quark pairs increases rapidly as a function of the Higgs boson mass, reaching a maximum of about 20% at $m_H \sim 450$ GeV.

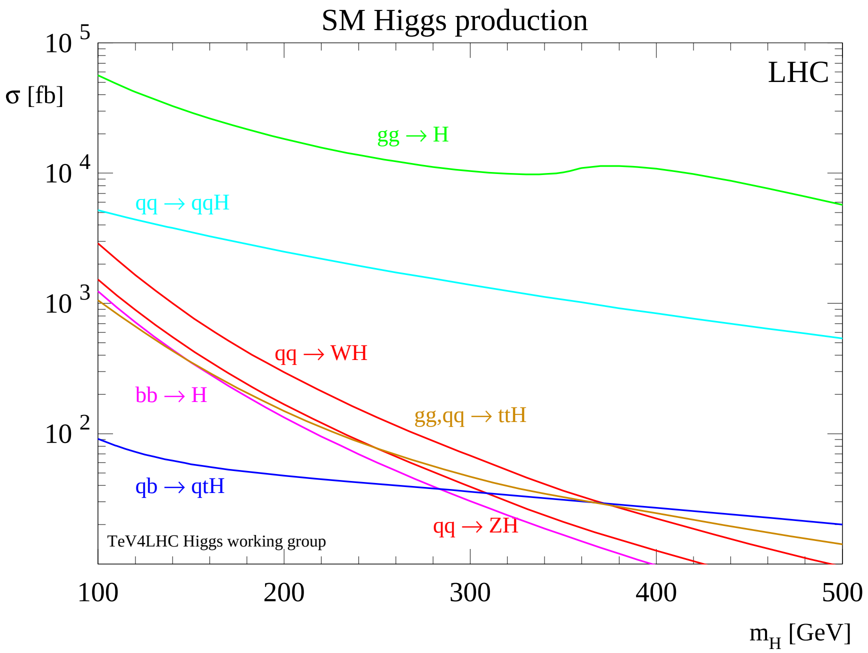

Figure 2.2: SM Higgs production cross sections for pp collisions at 14 TeV [20].

2.2.1 Searches for the SM Higgs Boson at LEP

The Large Electron Positron Collider (LEP) at CERN collided electrons and positrons at various center-of-mass energies from 1989 until 2000. LEP was a circular collider with a circumference of 27 kilometers, built in a tunnel in the border between Switzerland and France. When the LEP collider started operation in August 1989 it accelerated electrons and positrons to a total energy of 45 GeV each, to enable production of the Z boson. The accelerator was upgraded later to enable production of W boson pairs (LEP1 phase). LEP collider energy eventually topped at 209 GeV (LEP2 phase) at the end in 2000.

The principal mechanism for producing the SM Higgs boson in e^+e^- collisions at LEP energies is Higgs-strahlung in the s-channel, $e^+e^- \to ZH$. The Z boson in the final state is either virtual (LEP1), or on mass shell (LEP2). The SM Higgs boson can also be produced by WW and ZZ fusion in the t-channel, but at LEP these processes have small cross sections. The sensitivity of the LEP searches to the Higgs boson is primarily a function of the center of mass energy, $E_{\rm CM}$. For $m_H < E_{\rm CM} - m_Z$, the cross section is quite large, of order 1 pb or more, while for $m_H > E_{\rm CM} - m_Z$, the cross section is smaller by an order of magnitude or more.

Analysis

During the LEP1 phase, the ALEPH, DELPHI, L3 and OPAL collaborations analyzed over 16 million Z decays corresponding to an integrated luminosity around 600 pb^{-1} and set

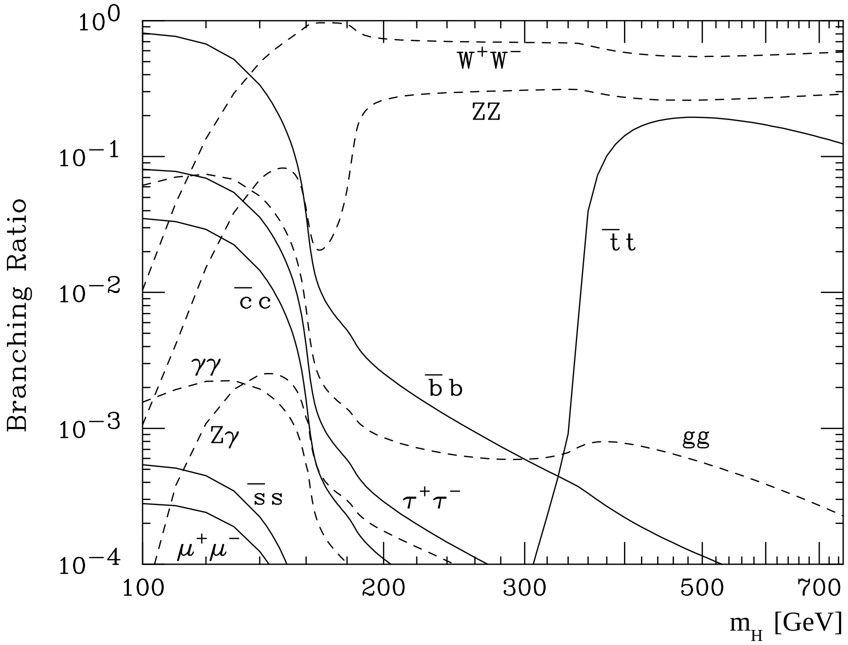

Figure 2.3: Branching ratios for the main decays of the SM Higgs boson [21].

lower bounds of approximately 65 GeV on the mass of the SM Higgs boson at a center of mass energies around 133 GeV. At LEP2, substantial data samples were collected at center of mass energies up to 209 GeV.

Each production and decay mode was analyzed separately. Data recorded at each center of mass energy were studied independently and the results from the four LEP experiments were then combined. The CL_s method [22] was used to compute the observed and expected limits on the Higgs boson production cross section as functions of the Higgs boson mass, and from that, a lower bound on m_H was derived.

Final State Topologies

Higgs bosons were sought in four final state topologies (ZH):

- The four-jet topology in which $H \to b\bar{b}$ and $Z \to q\bar{q}$.
- The final states with tau leptons: $H \to \tau^+\tau^-$ where $Z \to q\bar{q}$, and $H \to b\bar{b}$ with $Z \to \tau^+\tau^-$.
- The missing energy topology produced mainly in the process $H \to b\bar{b}$ with $Z \to \nu\bar{\nu}$.
- The leptonic states $H \to b\bar{b}$ with $Z \to e^+e^-, \mu^+\mu^-$.

At LEP1, only the modes with $Z \to \ell^+\ell^-$ and $Z \to \nu\bar{\nu}$ were used because the backgrounds in the other channels were prohibitive. For the data collected at LEP2, all decay modes were used. The LEP searches did not show any conclusive evidence for the production of a SM Higgs boson. However, in the LEP2 data, ALEPH reported an excess of about three standard deviations, suggesting the production of a SM Higgs boson with mass ∼ 115 GeV. Analyses of the data from DELPHI, L3, and OPAL did not show evidence for such an excess, but could not, however, exclude a 115 GeV Higgs boson at the 95% C.L. Not enough data was taken to improve the statistical significance of the excess. When the data of the four experiments are combined, the overall significance of a possible signal at $m_H = 115$ GeV is low, as given by the background-only p-value of 0.09. The same combination of the LEP data yields a 95% C.L. lower bound of 114.4 GeV for the mass of the SM Higgs boson. The median limit one would expect to obtain in a large ensemble of identical experiments with no signal present is 115.3 GeV. Figure 2.4 shows the observed production cross section limits, relative to the SM Higgs boson production rate (including vector-boson fusion), assuming SM Higgs boson branching ratios.

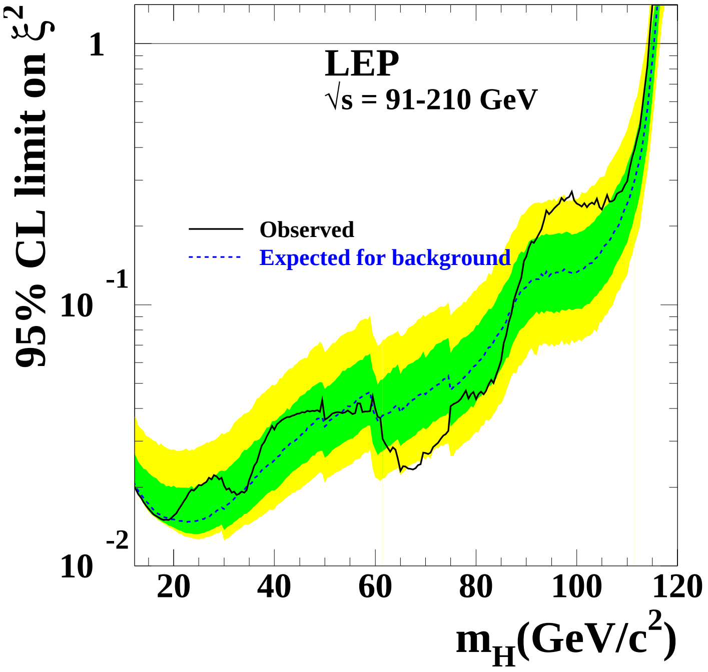

Figure 2.4: The 95% confidence level upper bound on the ratio $\xi^2 = (g_{\mathrm{HZZ}}/g^{\mathrm{SM}}_{\mathrm{HZZ}})^2$ [23]. The solid line indicates the observed limit, and the dashed line indicates the median limit expected in the absence of a Higgs boson signal. The dark and light shaded bands around the expected limit line correspond to the 68% and 95% probability bands, indicating the range of statistical fluctuations of the expected outcomes. The horizontal line corresponds to the Standard Model coupling. Standard Model Higgs boson decay branching fractions are assumed.

2.2.2 Prospects for the SM Higgs Boson Searches at the LHC

The LHC, Large Hadron Collider at CERN, will play an important role in the investigation of fundamental questions of particle physics. It is the world's largest and highest-energy particle accelerator, intended to collide proton beams at an energy of 7 TeV, about three times the energy applied to protons at Fermilab. It has been built in the LEP tunnel. It started working in September 2008, but was shut down when magnets used in the proton acceleration became damaged. The LHC restarted in November with an energy of its particle beams of 1.18 TeV. Currently the beam energy is setted to 3.5 TeV. It will be running with this energy through 2010 and 2011 until a 1 fb^{-1} of integrated luminosity is delivered. Only in 2013, the 7 TeV beams will be produced, until then the low mass Higgs searches will not be competitive with the low mass Higgs searches at Fermilab.

At the LHC, the main Standard Model Higgs boson production processes will be [24]:

- Gluon fusion ($gg \to H$).
- The vector boson fusion process (qqH or $q\bar{q}H$).
- Higgs boson production in association with a vector boson (WH or ZH).
- Higgs boson production in association with a top-quark pair ($t\bar{t}H$).

The cross-sections for WH, ZH and $t\bar{t}H$ production are one to two orders of magnitud below the gluon and vector boson fusion cross-sections. The most relevant Higgs boson branching ratios at the LHC are:

- $H \to \gamma\gamma$
- $H \to ZZ^{(*)} \to 4l (l = e, \mu)$
- $H \to \tau^+\tau^-$
- $H \to WW^{(*)} \to l\nu qq, l\nu l\nu$
- $H \to b\bar{b}$ (given the huge amount of background from $b\bar{b}$, this channel will be very difficult at the LHC)

This array of production and decay modes, together with a large integrated luminosity, allows for a variety of search channels. Search strategies have been explored in many analyses over the last years [3] [4].

The projections of the ATLAS and CMS collaborations show that, with an integrated luminosity of about 10 fb^{-1}, the SM Higgs boson is expected to be discovered if it exits and has a mass between 130 to 300 GeV. The discovery of a Higgs boson with a mass below 130 GeV is challenging [3]. If the Higgs boson's mass is in this range, a few years of running may be needed to discover it. If a SM Higgs boson is discovered, its properties could be studied at the LHC.

Indirectly, high precision electroweak data constrain the mass of the Higgs boson via their sensitivity to loop corrections. Assuming the overall validity of the Standard Model, a global fit, Figure 2.5, to all electroweak data leads to the 95% C.L. $m_H < 157$ GeV/c^2. The 95% C.L. lower limit obtained from LEP is not used in the determination of this limit. Including it increases the limit to 186 GeV. This is not a proof that the SM Higgs boson exists, but it does give a guideline in what mass range to look for it.

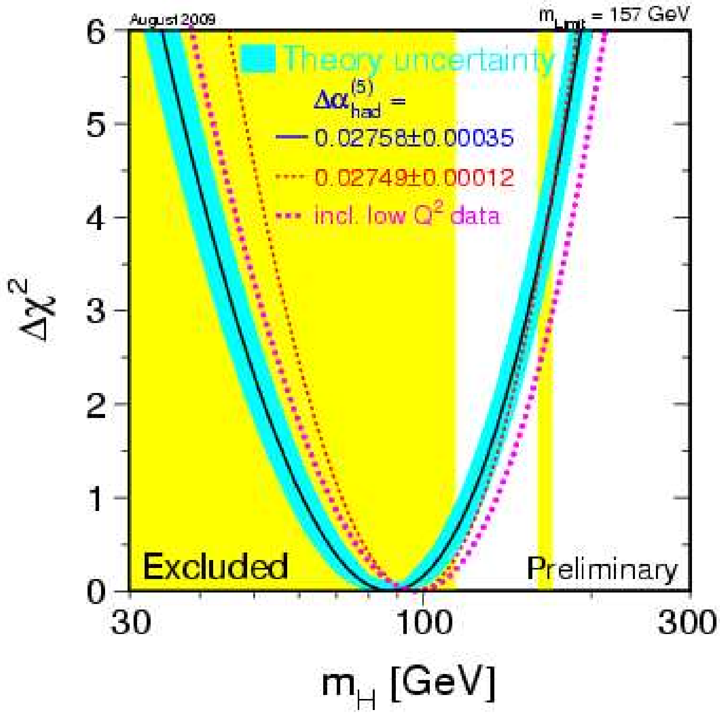

Figure 2.5: The figure shows the Delta-chi2 curve derived from precision electroweak data, performed at LEP and by SLD, CDF, and D0, as a function of the Higgs-boson mass, assuming the Standard Model to be the correct theory of nature. The yellow shaded region shows the exclusion by LEP and Tevatron direct Higgs search. The solid dark blue curve is the nominal fit, and the light blue band represents theoretical uncertainties on the fit.

2.2.3 Program of the SM Higgs Boson Searches at the Tevatron

Searching for the Standard Model Higgs Boson at low mass is the goal of this thesis. In this section an overview of the SM Higgs analyses done at the Tevatron is presented, including the one carried out in this thesis.

At the Tevatron, a $p\bar{p}$ collider at the Fermilab (see Chapter 3), the most important SM Higgs boson production processes are gluon fusion ($gg \to H$) and Higgs boson production in association with a vector boson (WH or ZH) [24]. For masses less than about 135 GeV, the most promising discovery channels are WH and ZH with $H \to b\bar{b}$. The contribution of $H \to W^{*}W$ is dominant at higher masses, $m_H > 135$ GeV. Both the direct $(gg \to H)$ and the associated production $(p\bar{p} \to WH$ or $ZH)$ channels are explored, and the results of both Tevatron experiments, CDF and DØ are combined to maximize the sensitivity to the Higgs boson.

The signal to background ratio is much smaller in the Tevatron searches than in the LEP analyses, and the systematic uncertainties on the estimated background rates are typically larger than the signal rates. In order to estimate the background rates in the selected samples more accurately, auxiliary measurements are made in data samples which are expected to be depleted in Higgs boson signal. These auxiliary samples are chosen to maximize the sensitivity to each specific background in turn. Then, Monte Carlo simulations are used to extrapolate these measurements into the Higgs signal regions.

Dominant Backgrounds

The dominant physics backgrounds such as top-pair, diboson, $Wb\bar{b}$ and single-top production are estimated by Monte Carlo simulations in this way, i.e. after having been tuned or verified by corresponding measurements in dedicated analyses, thereby reducing the uncertainty on the total background estimate. The uncertainties on the background rates diminish with increasing integrated luminosity because increasingly larger data samples are used to constrain them, and thus these uncertainties are not expected to be limiting factors in the sensitivity of the searches.

Low Mass Higgs Region

At masses below about 135 GeV, the searches for associated production, $p\bar{p} \to WH, ZH$ are performed in different channels:

- $p\bar{p} \to WH$, where the W decays leptonically and $H \to b\bar{b}$; such searches have been published by the CDF and DØ collaborations on ~ 2.7 fb^{-1} and ~ 1.05 fb^{-1} of data, respectively [25] [26]. Other results using higher integrated luminosities are public but have not been published yet, for example the result included in this thesis [27]. The Higgs boson production cross section limits obtained by the CDF collaboration is about five times higher than the SM expectation in this channel. These analyses use advanced analysis techniques such as neural networks to separate a potential signal from the background processes, and also to separate correctly identified b-jets from jets originating from gluons or from u, d, s or c quarks, mistakenly identified as b-jets.

- $p\bar{p} \to ZH$, where the Z decays into $\nu\bar{\nu}$ and $H \to b\bar{b}$, is also a very sensitive channel, but, since the final state is characterized by missing transverse energy and two b-jets, multijet backgrounds without Z bosons require special care. The sensitivity of this search is enhanced by WH events in which the charged lepton from the W decay escapes detection; these events have the same experimental signature as the $ZH \to \nu\bar{\nu}$ signal. The DØ collaboration has published a result in this channel with with 5.2 fb^{-1}

[28] and CDF with 2.1 fb^{-1} [29] using multivariate techniques and enhanced event reconstruction and selection, which increase the signal acceptance. The sensitivity is comparable to that obtained in the WH channel.

- $p\bar{p} \to ZH$, where the Z decays into charged leptons (e or μ), suffers from a smaller Z branching fraction, but has lower background, so its sensitivity is not much lower than that of the previous two channels. The both collaborations, CDF and DØ, has published results based on 2.7 fb^{-1} and 0.45 fb^{-1}, respectively, on the search for the Higgs boson in this channel [30] [31]. New updates will be ready soon.

The result of this thesis contributes to this low mass Higgs region.

High Mass Higgs Region

To probe masses above 135 GeV, the dominant $H \to WW^*$, the star indicates that below the $H \to W^+W^-$ threshold one of the W bosons is virtual, decay mode is best exploited in direct $gg \to H$ production, using the leptonic decays of the W which provide a clean, distinct final state. The WW pair issued from a Higgs boson decay has a spin correlation which is different from that of the dominant background, electroweak WW production. These spin correlations are transmitted to the distributions of observed leptons, providing a handle to separate the signal from the background. The invariant mass of the Higgs boson decay products cannot be reconstructed due to the undetected neutrinos, but the sensitivity is nevertheless significant.

Around $m_H = 135$ GeV, where all branching fractions are below 50%, no channel is dominant and the overall sensitivity is weaker. At these masses, the $WH \to WWW^*$ channel brings further sensitivity beyond the $b\bar{b}$ channel alone.

2.3 Physics Beyond the Standard Model

The Standard Model description of the different processes involving electroweak or strong interactions is extremely accurate. At the moment, no experiment has been able to find any clear deviation from the SM predictions. In spite of all its success, the Standard Model is not complete, many mysteries remain. The already mentioned non null mass of the neutrinos calls for an extension of the SM. The SM is unable to describe gravity, and cannot neither explain the existence of dark matter and dark energy without some extension. In addition, the model cannot explain which are the mechanisms to produce the matter-antimatter asymmetry observed in the universe or what is the relation between the strong and electroweak forces.

Another caveat of the SM that needs to be solved, related with the topic of this dissertation, is that the Higgs mass is subject to divergent quadratic radiative corrections that need to be somehow controlled in order for the Higgs mass to remain at the electroweak scale.

One possibility is that the radiative corrections are canceled by a new spectrum of particles at the electroweak scale: supersymmetric (SUSY) theories propose that to every SM particle corresponds a supersymmetric partner with different spin, so that radiative correction contributions to the Higgs mass from a particle is cancelled by the contribution from its supersymmetric partner. To SM fermions (bosons) correspond bosonic (fermionic) superpartners. For example, the superpartner of the top quark is called stop, the superpartner of the gluon is the gluino $\tilde{g}$, and the superpartner of the gauge bosons W and Z are the gauginos $\tilde{\chi}^0$, $\tilde{\chi}^{\pm}$. In SUSY, particles are combined into superfields and an operator generates the transformation of converting fermions to bosons and vice versa. SUSY requires additional Higgs fields in order to provide mass to both up and down families. The model with a minimal supersymmetric content in the Higgs sector is known as Minimal Supersymmetric Extension of the Standard Model, MSSM. In the MSSM, there are five Higgs bosons: h, H, A, and $\mathrm{H}^{\pm}$.

Recent fits on the electroweak precision observables, such as the effective leptonic weak mixing angle, $\sin^2\theta_{eff}$, seem to favor supersymmetric models over the SM. For example, the SM predictions for the M_W as a function of m_T are being compared with the predictions from the unconstrained Minimal Supersymmetric Standard Model (MSSM). The predictions within the two models give rise to two bands with only a relatively small overlap region. The allowed parameter region in the SM arises from varying the only free parameter of the model, the mass of the SM Higgs boson, from $\mathrm{M}_H = 114$ GeV/c^2 (upper edge of the band) to 400 GeV/c^2 (lower edge). For the MSSM area, SUSY masses close to their experimental limit are assumed for the upper edge, while the MSSM with large masses yields the lower edge of the blue area (dark-shaded). The 68% C.L. experimental results shown in Figure 2.6 slightly favours the MSSM over the SM.

Recently, the projections, using 1 fb^{-1} of the expected integrated luminosity at the LHC and 7 TeV, of the search for the MSSM Higgs boson in the τ τ channel at CMS has been made public, see Figure 2.7. These results improve the latest exclusion limits from the Tevatron [32].

Furthermore, some SUSY models predict the presence of a lightest supersymmetric particle, which is a candidate for dark matter in the universe, provided that it is neutral, weakly interacting and absolutely stable.

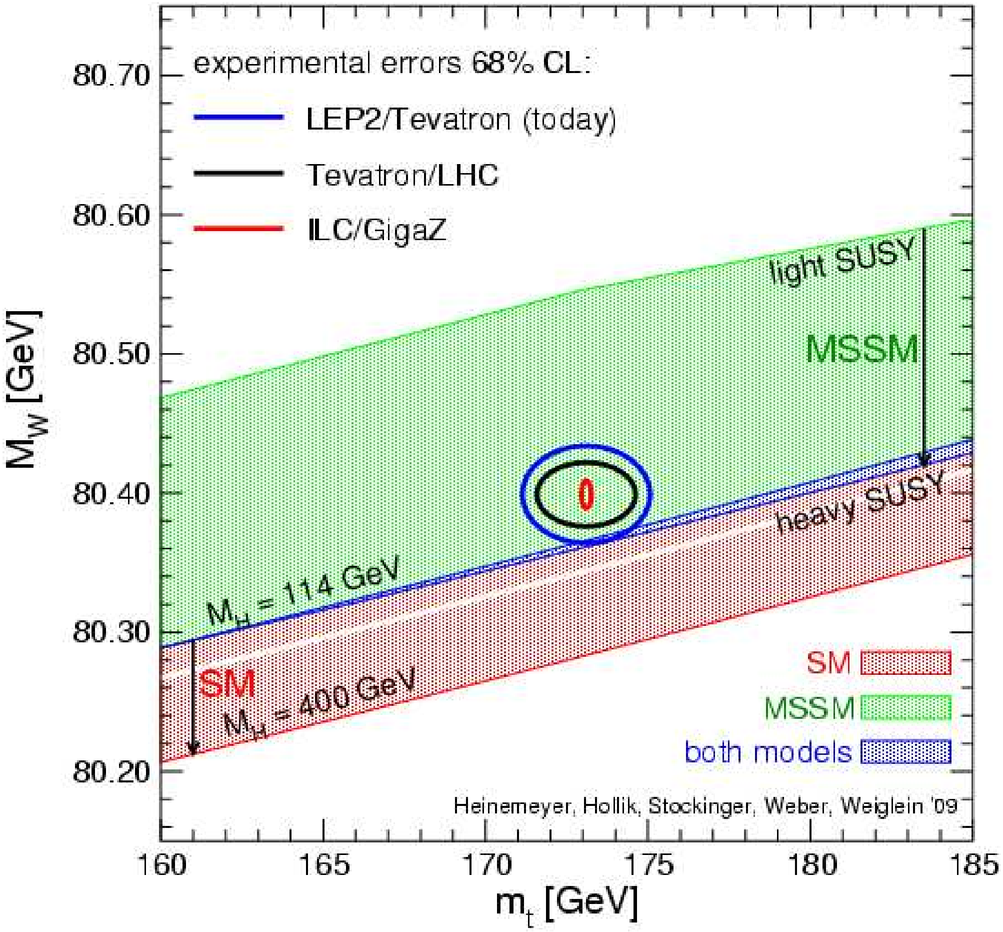

Figure 2.6: The 68% C.L. regions in the (m_T, M_W) plane: comparison of SM and MSSM. m_T = 173.1± 1.3 GeV, M_W = 80.399±0.023 GeV (the values from the Tevatron and the LEPEWWG). The SM prediction is giving in red (mediumshaded) and blue (dark-shaded) bands and the MSSM prediction in green (lightshaded) and blue (dark-shaded) bands.

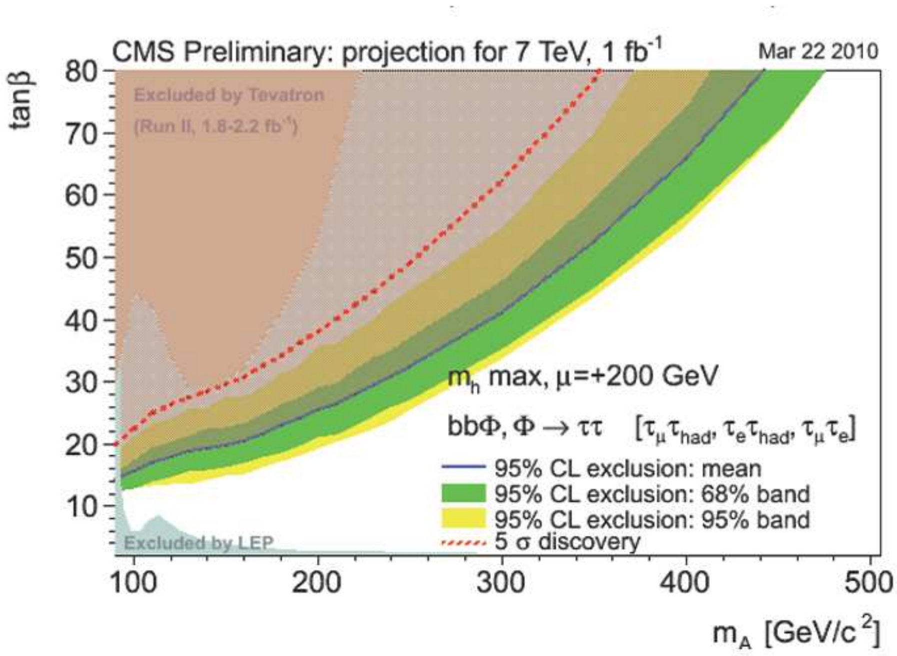

Figure 2.7: 95% confidence level exclusion limits on the cross section times branching ratio as a function of the Higgs boson mass translated into the MSSM Higgs sector parameter plane, tan β vs M_A.

Chapter 3

Experimental Apparatus

In proton-antiproton collisions the Higgs boson is expected to be produced, but with very low cross section. Around the two collision points of the Tevatron, two detectors are located to study the properties of these collisions. The relevant aspects of the collider apparatus and the CDF (Collider Detector at Fermilab) detector, used to collect the data presented in this thesis, are described in this chapter.

3.1 Fermilab

Founding Director Robert R. Wilson (1914-2000) envisioned a place of beauty and humanity. He built the world's highest-energy particle physics laboratory with the eye of an artist, the shrewdness of a banker, and the conscience of a human rights activist. Said Nobel Laureate Leon Lederman, who succeeded Wilson as director: "His spirit invades every corner of this great laboratory. He speaks to us through the surfaces of concrete, through the prairie restoration, through the style of openness, through the flags that grace the entry."

Fermilab research is exciting science. From dark matter in the universe, to new discoveries at the Tevatron, to neutrino physics deep underground. The future holds great promise. The startup of the Large Hadron Collider in Europe presents great physics opportunities as well. Fermilab is the host laboratory for U.S. efforts in the CMS experiment at the LHC. About 120 Fermilab scientists, postdocs, visiting students, engineers and technicians participate in the CMS collaboration.

Fermilab has a great past, a great present, and with the talent, the industry and the good of the people at the lab will have a great future as a world leader in particle physics.

3.2 The Fermilab Accelerator Complex

The Tevatron located at Fermilab (Fermi National Laboratory) in Batavia, Illinois (USA) is a proton-antiproton storage ring system with a center of mass energy of $\sqrt{s} = 1.96$ TeV and is the second highest energy particle collider in the world after the Large Hadron Collider (LHC). The first $p\bar{p}$ collisions have been produced in 1986. Since then, several extensive upgrades have been undertaken leading to major improvements of the overall performances. Run I went from 1992 to 1996 where the center of mass energy was 1.8 TeV. Between 1997 and 2001, both the accelerator complex and the collider detectors underwent major upgrades, mainly aimed at increasing the luminosity of the accelerator, and gathering data samples of 2 fb^{-1} or more (notice that at the moment more than 6fb^{-1} has been acquired by the CDF detector). The upgraded machine accelerates 36 bunches of protons and antiprotons, whereas the previous version of the accelerator operated with only 6. Consequently, the time between bunch crossings has been decreased from 3.5 μs for the previous version to 396 ns for the current collider. These parameters are summarized in Table 3.1. Run II is currently in progress where the collision center of mass energy is $\sqrt{s} = 1.96$ TeV and with a total delivered luminosity of around 8 fb^{-1} per experiment.

The collisions occur at two points on an underground ring, which has a radius of about 1 km. At these collision points there are two detectors: the Collider Detector at Fermilab (CDF) and DØ (see Figure 3.1).

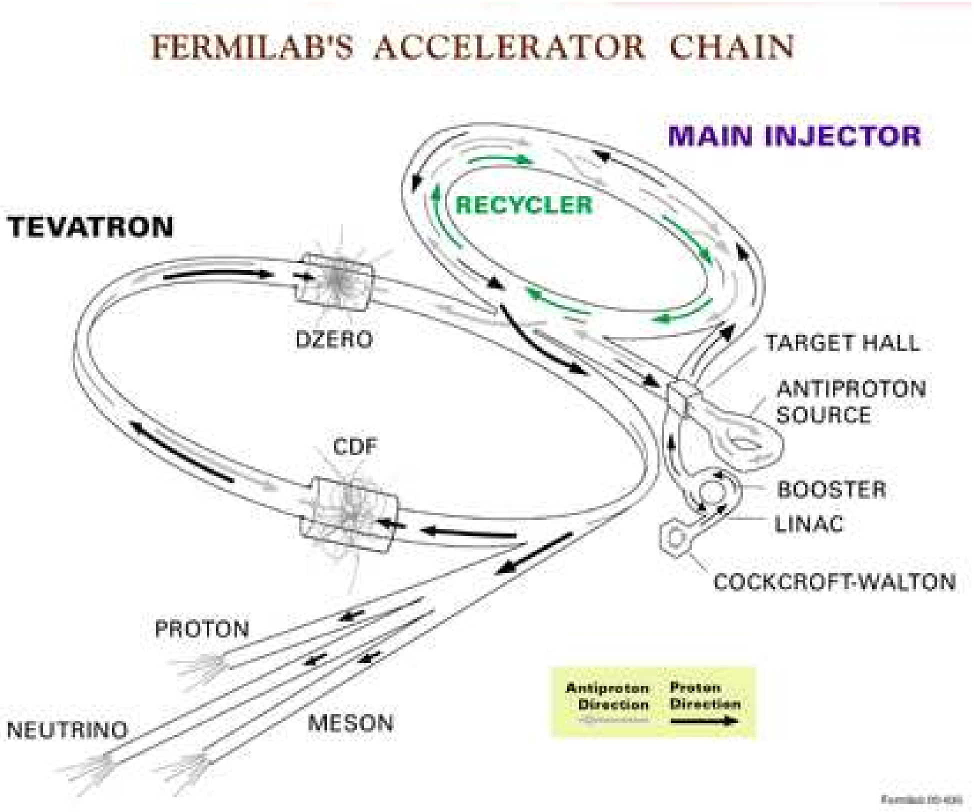

Figure 3.1: Layout of the Fermilab accelerator complex.

Production and acceleration of protons and antiprotons at Fermilab require a chain of accelerators, each one boosting particles to higher energies. Each step will be described in the following pages.

3.2.1 Proton Source

The protons used in the Tevatron are originally extracted from very pure hydrogen gas. Hydrogen gas is moved between two electrodes and a spark ionizes the hydrogen into electrons and H^+ ions. The positive ions strike a cathode made of cesium, which has a low work function and thus loses electrons easily, and occasionally pick up two electrons and form H^- ions. An electrostatic extractor sends them to the pre-accelerator.

3.2.2 Cockcroft-Walton

The Cockcroft-Walton [33] pre-accelerator is a electrostatic generator that accelerates the H^- ions from the proton source through successive potential differences to a final energy of 750 keV. The pre-accelerator produces 750 keV hydrogen ions every 66 ms. The H^- ions are focus by magnets and steered to the Linac.

3.2.3 Linac

The H^- ions enter a linear accelerator (abbreviated Linac) [34], approximately 150 m long, where they are accelerated to 400 MeV using radio frecuency (RF) cavities, method of accelaration used by all accelerators at the Fermilab complex. The oscillating electric field of the RF cavities groups the ions into bunches. This acceleration is also done every 66 ms (with an offset to catch the ions from the pre-accelerator). The 400 MeV H^- ions are then injected into the Booster [34].

3.2.4 Booster

The Booster is a circular synchrotron where the protons circulate through a circular vacuum chamber in a tunnel filler with bending magnets. The electrons are stripped off the H^- ions at injection by passing the H^- through a carbon foil leaving bare protons. The protons are accelerated from 400 MeV to 8 GeV by a series of "kicks" applied by RF cavities. The Booster is the first synchroton in the Tevatron complex. It is composed of a series of magnets with 18 RF cavities inside, located around the ring. This stage of production is also operated at 66 ms, with sufficient phase offset to catch the ions from the Linac.

A set of fast kicker magnets extracts the proton beam from the Booster. Some of the protons are sent to the Mini Booster Neutrino Experiment (MiniBooNE) [35]; the rest go into a transfer line that leads to the Main Injector.

3.2.5 Main Injector

It is a 3 km long circular accelerator, completed in 1999. It is composed of 18 accelerating RF cavities and can accelerate protons and antiprotons to a total energy of up to 150 GeV. The Main Injector can be used in other different operation modes:

- Antiproton production: it produces 120 GeV protons which are then used to strike the antiproton source and create antiprotons. This process is called "stacking pbars".
- Proton and antiproton boosting, before injection into the Tevatron in collider mode.
- Antiproton deceleration, in order to recover antiprotons after a Tevatron collision run.
- Proton and antiproton acceleration for fixed target experiment, either directly or as a booster for the Tevatron.

3.2.6 Antiproton Production

In order to produce antiprotons, a pulse of $5 \cdot 10^{12}$ protons at 120 GeV is extracted from the Main Injector and focused into a nickel target. In the collisions with the target, about 1 antiproton are produced for each 10^5 protons, with a mean kinetic energy of 8 GeV. The antiprotons produced by the collision are collected by a lithium lens, separated from other particle species by a pulsed magnet and then focus down a transfer line to the Debuncher.

3.2.7 Debuncher

The Debuncher is a triangular storage ring. Its main purpose is to "debunch" the particle beam, removing the RF bunch structure. Before the antiprotons can be used in the narrow beams needed in the collider, the differences in kinetic energy between the different particles need to be reduced. Since this process reduces the spread of the kinetic energy spectrum of the beam, it is referred to as "cooling" the beam.

New batches of antiprotons are initially cooled in the Debuncher Ring, collected and further cooled using stochastic cooling [36] in the 8 GeV Accumulator (also a rounded triangular synchrotron). The principle of stochastic cooling is to sample a particles motion with a pickup sensor and correct its trajectory later with a kicker magnet.

It takes between 10 and 20 hours to build up a "stack" of antiprotons which is then used in collisions in the Tevatron. Antiproton availability is the most limiting factor for attaining high luminosities.

Roughly once a day, the stacked antiprotons (36 bunches of about 3×10^{10} antiprotons per bunch) are injected back into the Main Injector.

3.2.8 Accumulator

It is a long-term antiproton storage ring. The antiprotons are kept in this storage ring for several hours, that is, until there are about 10^{12} accumulated antiprotons. This storage ring also uses stochastic cooling to produce a dense core of antiprotons near the inner radius of the Accumulator. This 8 GeV beam is subsequently injected backwards to the Main Injector, accelerated to 150 GeV together with 36 bunches of roughly 3×10^{11} protons, and injected into the TeVatron.

3.2.9 Recycler Ring

The Recycler Ring lies in the same tunnel as the Main Injector and, contrarily to the other rings at Fermilab, it is built with permanent magnets. Permanent magnets, not being prone to the most common causes of failure (such as power loss and lightning) provide a very stable repository for up to $3 \cdot 10^{12}$ antiprotons at a time.

Not all antiprotons in a given store are used up by the collisions. Recycling the unused antiprotons and reusing them in the next store significantly reduces the stacking time. The tasks of the Recycler are when the Accumulator reaches its maximum optimal capacity, its antiprotons are passed into the Recycler collecting them until the Tevatron is ready to injection, and to receive antiprotons from a Tevatron store, cool them and re-integrate them into the stack, so that they can be used in the next store.

3.2.10 Tevatron

The Tevatron is the last stage of Fermilab's accelerator chain. It is a circular synchroton with a 1 km radius, composed of eight accelerating cavities, quadrupole and dipole focusing magnets. The Tevatron is cryogenically cooled by liquid helium to 4.2 K, and the accelerating cavities are made of superconducting materials. It is desirable to use superconducting magnets because the very large fields necessary to maintain TeV-scale energies would require currents so large that it is more cost effective to use superconducting magnets than ordinary resistive magnets.

The Tevatron receives 150 GeV protons and antiprotons from the Main Injector or the Recycler (for antiprotons) and accelerates them to 980 GeV in 85 s. Since the antiprotons and protons are oppositely charged, they circle in opposite directions in the magnetic field, housed in the same ring. Electrostatic separators produce a strong electric field that keeps the two beams from touching except at the "collision points". The beams are brought to collision at two collision points, B0 and D0. The two collider detectors, the Collider Detector at Fermilab (CDF II) and DØ are built around the respective collision points. The Tevatron can then sustain both beams for hours at a time (called a "store").

The Tevatron is not a perfect circle. There are six sectors (A-F) and each one has five service buildings (0-4). The "0" sections have large straight sections. A0 is where the Tevatron tunnel connects to the injection point. It also contains one of two beam aborts. B0 contains CDF (which will be described below), and the D0 detector is aptly named for it's place along the ring. At B0 and D0, the colliding beams are focused into very narrow beamlines of order 32 μm, and the beams then collide. C0 is the location of the other beam abort (protons only). E0 used to be the site of the old Main Ring transfer to the Tevatron, but now it is unused. F0 houses the RF stations which "kick" the beam back into position if it has wandered off its axis. It is also where the transfer lines from the Main Injector connect with the Tevatron.

The Tevatron can also be used in fixed-target mode: it can accelerate up to $3 \cdot 10^{13}$ protons at a time to an energy of 800 GeV and deliver single bunches to be used in proton, meson and neutrino experiments.

3.2.11 Luminosity

The number of collisions per second is described by the "luminosity", $\mathcal{L}$. Making use of the upgrades in the rest of the accelerator chain, the Tevatron can provide an initial luminosity of 10^{32} cm^{-2}s^{-1}. During a collider store, instant luminosity slowly decreases. In the early stage of the store, the most important cause for this decrease is intrabeam scattering; some hours later, the depletion of antiprotons during collisions becomes more relevant. Luminosity is expected to decrease to 50% in about seven hours, and to $1/e$ in twelve hours.

The luminosity of collisions can be expressed as:

$$\mathcal{L} = \frac{f N_B N_p N_{\bar{p}}}{2\pi(\sigma_p^2 + \sigma_{\bar{p}}^2)} F\left(\frac{\sigma_l}{\beta^*}\right), \tag{3.1}$$

where f is the revolution frequency in Hz, N_B is the number of bunches, $N_{p(\bar{p})}$ is the number of protons (antiprotons) per bunch, and $\sigma_{p(\bar{p})}$ is the protons (antiprotons) RMS beam size at the interaction point. This is multiplied by a form factor, F, that depends on the ratio of the bunch longitudinal RMS size, σ_l, and the beta function at the interaction point, β^*, which is a measure of the transverse beam width and it is proportional to the beam's x and y extent in phase space. Table 3.1 shows a comparison of Run I and design Run II [37] accelerator parameters. Figure Fig. 3.2 shows the total luminosity collected by CDF as of March 2010.

Table 3.1: Accelerator parameters for Run I and Run II configurations.

Parameter	Run Ib	Run II
Number of bunches (N_B)	6	36
Protons/bunch (N_p)	2.3×10^{11}	2.7×10^{11}
Antiprotons/bunch ($N_{\bar{p}}$)	5.5×10^{10}	3.0×10^{10}
Total antiprotons	3.3×10^{11}	1.1×10^{12}
β^* [cm]	35	35
Bunch length [m]	0.6	0.37
Bunch spacing [ns]	3500	396
Interactions/crossing	2.5	2.3
Energy [GeV/particle]	900	980
Integrated luminosity [pb^{-1}]	112	8000
Peak luminosity [cm^{-2}s^{-1}]	2×10^{31}	3.6×10^{32}

However, the luminosity is not determined from this formula, but from the measured rate of some reference physical processes. The measurement of the luminosity delivered by the Tevatron to the CDF experiment is described in Sec. 3.10.

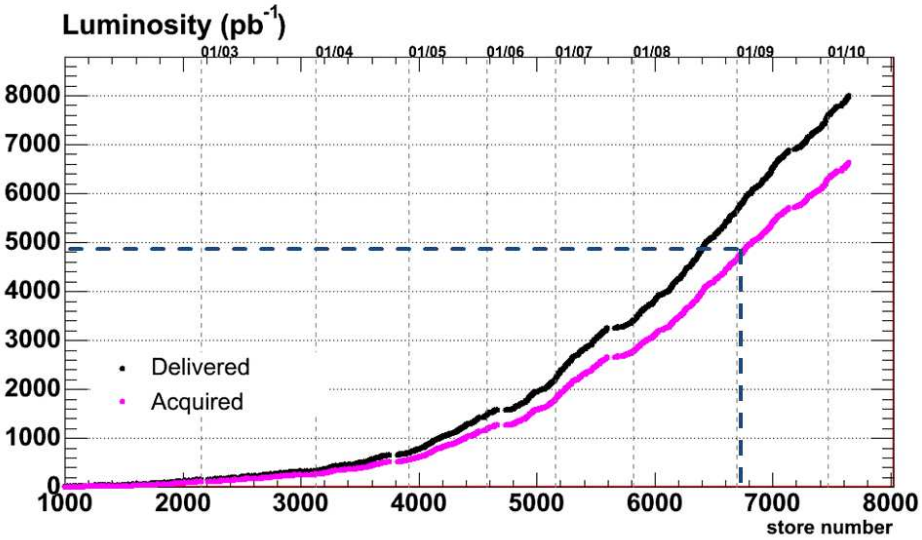

Figure 3.2: Total luminosity acquired by the CDF detector by March 2010. The black curve is the luminosity delivered and the pink curve is the luminosity written to tape by CDF. The blue dashed line corresponds to 4.8 fb^{-1}, that is the integrated luminosity used in this thesis.

3.3 The CDF II Detector

The CDF II Detector [38,39] is a general purpose detector designed to study the physics of $p\bar{p}$ collisions, in many cases I will refer to it as "CDF" only. The design is not geared toward one particular physics measurement, but rather optimized toward extracting a number of different properties about all particle species created in the particle interactions. It is a substantial upgrade of the original CDF Detector [40].

The detector has both azimuthal and forward-backward symmetry, and consists of 3 primary subsystems: the innermost part of the detector is the tracking system, which contains a set of silicon strips and an open-cell drift chamber inside of a solenoid to detect charged particles, measure their momenta and displacements from the point of collision (primary interaction vertex). Outside of the solenoid are the calorimeters, which measure the energy of particles that shower when interacting with matter. Finally, outside of the calorimeters are the muon chambers, which detect and measure the momenta of muons. When interacting with matter, muons act as "minimal ionizing particles", they only deposit small amounts of ionization energy in the material.

A diagram of the CDF II Detector is shown in Figure 3.3. A quadrant of the detector is cut out to expose the different subdetectors. Protons enter the detector from the west side

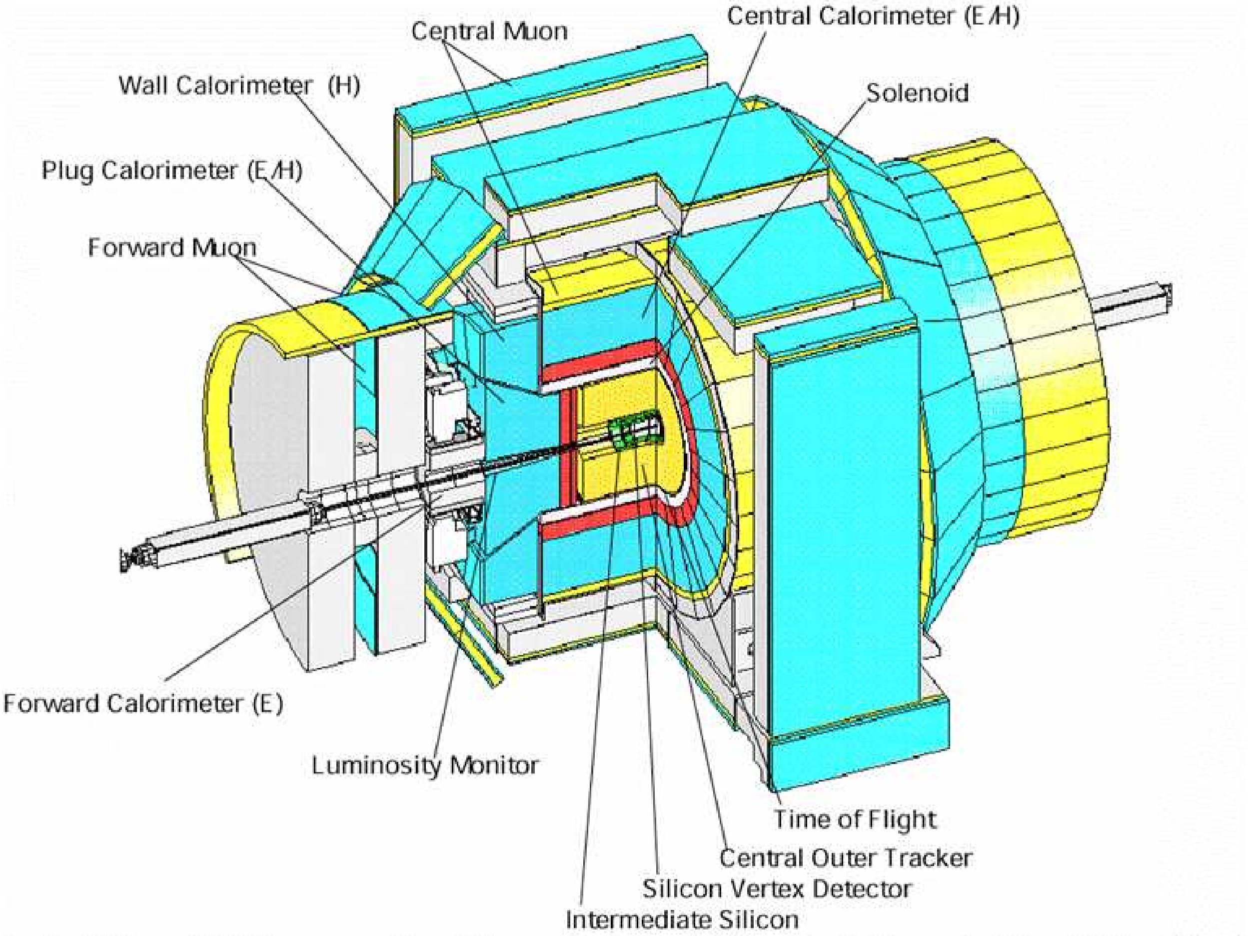

Figure 3.3: The CDF II Detector with quadrant cut to expose the different subdetectors.

and antiprotons enter from the east side.

The subdetectors are described in more detail in the following sections together with the Time of Flight system, designed to provide particle identification for low-momentum charged particles, and the Cherenkov Luminosity Counter (CLC) measures the rate of interactions near the beam used for luminosity measurements.

All these systems surround the “beam pipe”, a vacuum tube of diameter 2.2 cm located at the innermost part of the detector and where the proton and antiproton beams travel and collide. The beam pipe is made of beryllium because this metal has the best mechanical qualities, yet lowest nuclear interaction cross section of all materials.

More detailed information on each system can be found in the Technical Design Report of the CDF II Detector [38].

3.4 CDF Coordinate System

Figure 3.4 shows an elevation view of the detector. Because of its barrel-like detector shape CDF generally uses a combination of cylindrical (r, ϕ, z) and spherical (ϕ, θ) coordinates to describe locations and directions, as follows:

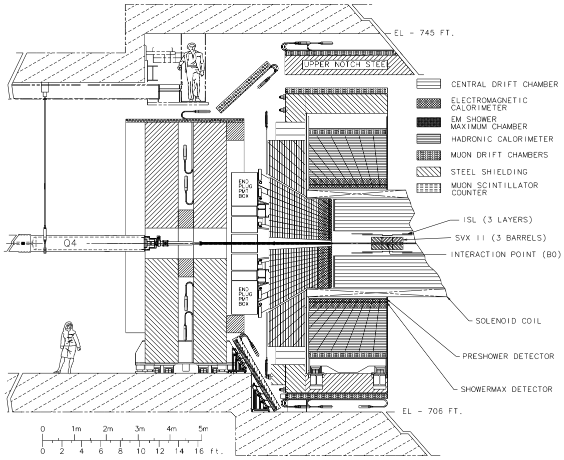

Figure 3.4: Elevation view of the Collider Detector at Fermilab. West (East) corresponds to the right (lef) side of the picture.

- The z axis lies along the beamline, with the +z direction defined as the direction of proton travel (east) and the -z direction the direction of $\bar{p}$ travel (west). Longitudinal refers to components along the z axis, and transverse refers to components perpendicular to the z axis.
- x and y are not commonly used: the +x direction is north, while the +y direction is up (away from the ground).
- r is the radial distance from the beamline (r = $\sqrt{(x^2+y^2)}$).
- θ is the polar angle from the beamline: tan θ = r/z.
- ϕ is the azimuthal angle around the beamline: tan ϕ = y/x.

However, θ is not a good variable to use in this case because it is not a Lorentz invariant. Due to the fact that the proton (and antiproton) is an extended object, the actual constituent partons will not be travelling at 980 GeV. Thus, the number of particles per unit angle ($dN/d\theta$) will not be the same for particles with different velocity.

Instead, we use the concept of the *rapidity*, defined as

$$Y \equiv \frac{1}{2} \ln \frac{E + p_z}{E - p_z} \tag{3.2}$$

where E is the energy and p_z is the z component of the momentum of the particle. For the high energy particles, $p \gg m$ so $E \sim p$ and the rapidity is approximated by the *pseudo-rapidity*, defined as

$$\eta \equiv -\ln \tan\left(\frac{\theta}{2}\right). \tag{3.3}$$

In this case, the number of particles per unit rapidity ($dN/d\eta$) is invariant under boosts in the z direction.

Typically, the position of objects (such as detector components) is described with r, z, and ϕ coordinates. The direction of particles is usually measured in (η, ϕ).

For a particle with momentum p and energy E, we define the transverse momentum p_T and the transverse energy E_T as $p \cdot sin\theta$ and $E \cdot sin\theta$, respectively; the two-dimensional vector transverse momentum is simply the x and y components of the momentum vector: $\vec{p_T}$ = (p_x, p_y). The quantity R is often used to measure distances in $\eta - \phi$ space; it is defined as

$$\Delta R = \sqrt{(\Delta\eta^2 + \Delta\phi^2)} \tag{3.4}$$

3.5 Tracking Systems

The detector has a cylindrical tracking system immersed in a 1.4 T solenoidal magnetic field to enable measurement of charged particle momenta. We will describe this system starting from the devices closest to the beam and moving outwards. The innermost tracking device is a silicon strip vertex detector, which consists of three subdetectors: Layer 00 (L00), the Silicon Vertex Detector (SVX-II) and the Intermediate Silicon Layers (ISL). Figure 3.5 shows a view in the $r - \phi$ plane of the three subsystems. Surrounding the silicon detector is

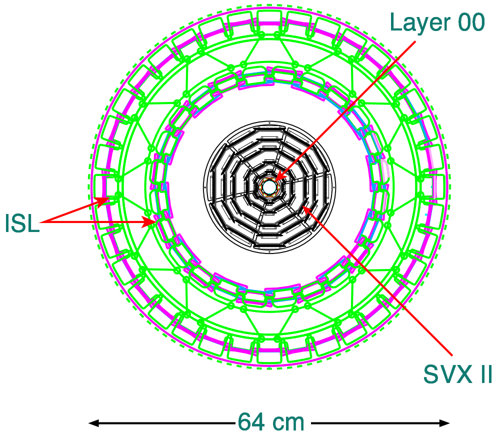

Figure 3.5: Transversal view of the Silicon Vertex Detector at CDF showing the different layers and parts of the detector.

the Central Outer Tracker (COT), a 3.1 m long cylindrical open-cell drift chamber covering radii from 43.4 to 132.3 cm. Figure 3.6 shows the coverage of the whole tracking system.

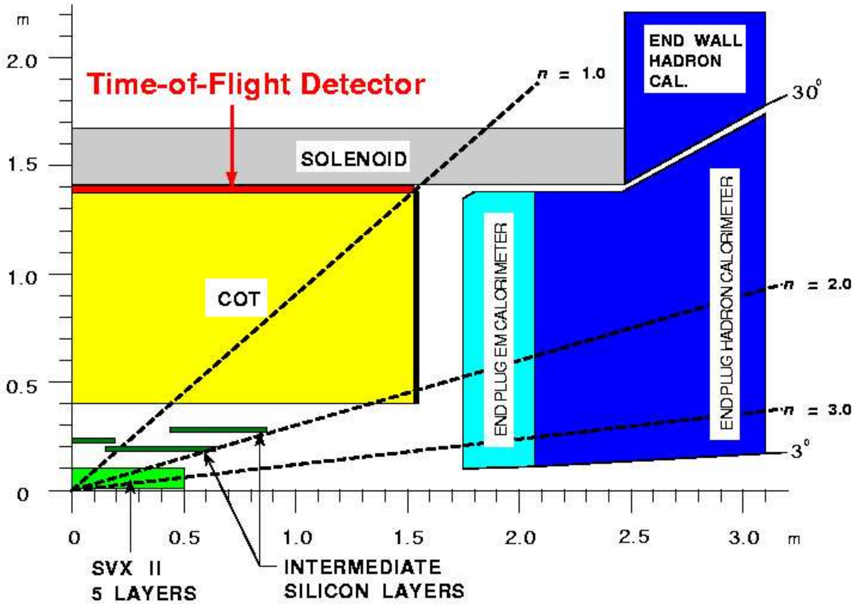

Figure 3.6: The CDF II tracker layout showing the different subdetector systems.

The silicon detectors provide excellent impact parameter, azimuthal angle and z resolution. They are also instrumental in vertexing. The COT provides excellent resolution of the curvature, ϕ and η. Together they provide very accurate measurements of the helical paths of charged particles.

3.5.1 Silicon Tracking Detectors

Silicon tracking detectors are used to obtain precise position measurements of the path of a charged particle. A silicon tracking detector is fundamentally a reverse-biased p-n junction. When a charged particle passes through the detector material, it causes ionization. In the case of a semiconductor material, this means that electron-hole pairs will be produced. Electrons drift towards the anode, and holes drift toward the cathode, where the charge is gathered. The amount of charge is, to first order, proportional to the path length traversed in the detector material by the charged particle.

By segmenting the p or n side of the junction into "strips" and reading out the charge deposition separately on every strip, we obtain sensitivity to the position of the charged particle. All the CDF II silicon tracking detectors are implemented as microstrip detectors. The typical distance between two strips is about 60 μm. Charge deposition from a single particle passing through the silicon sensor will be read out on one or more strips. This charge deposition is called a "cluster". There are two types of microstrip detectors: single and double-sided. In single-sided detectors only one (p) side of the junction is segmented into strips. Double-sided detectors have both sides of the junction segmented into strips. The benefit of double-sided detectors is that while one (p) side has strips parallel to the z direction, providing $r-\phi$ position measurements, the other (n) side can have strips at an angle (stereo angle) with respect to the z direction, which will give z position information.

Layer 00

The innermost layer, L00 [41], is a radiation-hard, single-sided silicon detector installed directly onto the beryllium vacuum beam pipe. L00 is the most recent addition to the CDF II tracker. The geometry of L00 is such that there are two overlaping hexagonal structures at radii between 1.35 and 1.62 cm from the beam. Figure 3.7 shows a detailed view of the L00. It only provides $r-\phi$ measurements. Being so close to the interaction point, L00 improves noticeably the spacial resolution up to ≈15 μm per hit.

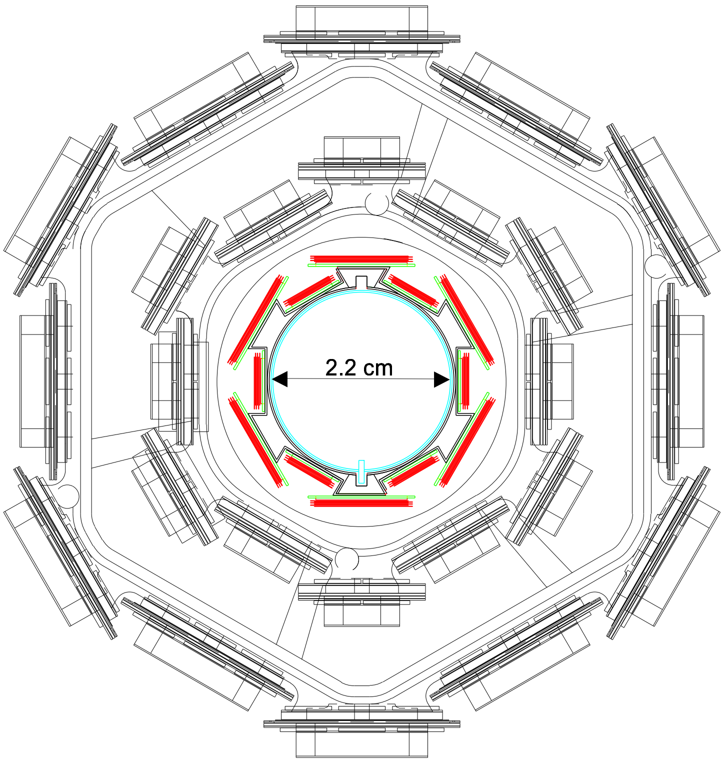

Figure 3.7: Detailed view of the Silicon L00 detector along with the two innermost layers of the SVX detector.

SVX-II

The L00 is followed by the SVX-II [42]. It consists of five concentric layers of double-sided silicon sensors. One side of each sensor provides measurements in the transverse plane (axial strips); the other side's strips deliver 3D information. SVX-II extends radially from 2.5 to 11 cm, and along z up to 45 cm on either side of the interaction point. The spacial resolution of the SVX-II is $\approx$20 μm.

ISL

The Intermediate Silicon Layers (ISL) [43] are the outermost silicon subdetector systems, consisting of one double-sided silicon, similar to those on SVX-II, placed at a radius of 22 cm in the central region ($|\eta| < 1$), and two forward layers ($1 < |\eta| < 2$) at radii 20 and 28 cm from the beam line. Together with SVX-II, the ISL makes it possible to reconstruct tracks in the forward regions, which lie beyond the acceptance region of the outer tracker.

The silicon tracking system is used in stand-alone mode to provide an extension of tracking down to 2.8 in pseudorapidity.

3.5.2 Central Outer Tracker

The Central Outer Tracker (COT) [44] is a multiwire drift chamber. The active volume of the COT begins at a radius of 43.4 cm from the nominal beamline and extends out to a radius of 132.2 cm and it is 3.1 m long. The COT contains eight "superlayers", as inferred from the end plate section shown in Figure 3.8. Four superlayers (axial superlayers) provide $r - \phi$ measurements and are alternated with the remaining four that provide 2° stereo measurements (stereo superlayers).

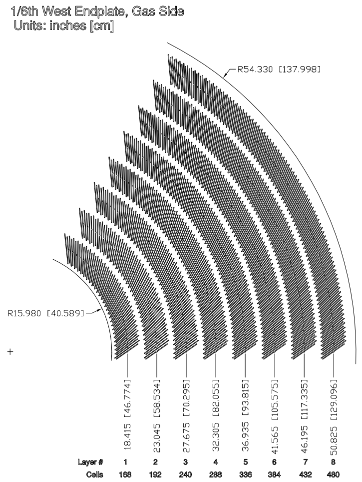

Figure 3.8: Layout of wire planes on a COT endplate.

The entire COT contains 30,240 sense wires. Approximately half the wires run along the z direction ("axial"). The other half are strung at a small angle (2°) with respect to the z direction ("stereo"). Particles originating from the interaction point, which have $|\eta| < 1$, pass through all 8 superlayers of the COT. Particles which have $|\eta| < 1.3$ pass through 4 or more superlayers.

The COT drift chamber provides accurate information in the $r-\phi$ plane for the measurement of transverse momentum, p_T, and substantially less accurate information in the $r-z$ plane for the measurement of the z component of the momentum, p_z.

The COT is filled with an Argon-Ethane gas mixture and Isopropyl alcohol (49.5:49.5:1). The mixture is chosen to have a constant drift velocity across the cell width. This allows a maximun drift time of 177 ns with a drift velocity of 100 μm/ns. This prevents pileup of events in the drift chamber from the previous event.

When a charged particle passes through, the gas is ionized. Electrons drift towards the sense wires. The electric field in a cylindrical system grows exponentially with decreasing radius. As a result, the electric field very close to the sense wire is large, resulting in an avalanche discharge when the charge drifts close to the wire surface.

Signals on the sense wires are processed by the ASDQ (Amplifier, Shaper, Discriminator with charge encoding) chip, which provides input protection, amplification, pulse shaping, baseline restoration, discrimination and charge measurement [45]. The charge measurement is encoded in the width of the discriminator output pulse, and is used for particle identification by measuring the ionization along the trail of the charged particle (dE/dx). The pulse is sent through $\sim$ 11 m of micro-coaxial cable, via repeater cards to Time to Digital Converter (TDC) boards in the collision hall. Hit times are later processed by pattern recognition (tracking) software to form helical tracks, particles moving through a homogeneous solenoidal magnetic field follow helical trajectories. The hit resolution of the COT is about 140 μm. The transverse momentum resolution has been measured using cosmic ray events to be

$$\frac{\sigma_{p_T}}{p_T^2} = 0.17\% \ [\mathrm{GeV/c}]^{-1}. \tag{3.5}$$

3.6 Time of Flight

Outside the tracking system CDF II has a Time of Flight (TOF) [46] system. The TOF system was added in 2001, during the accelerator and detector upgrades, to improve the particle identification capability. It is designed to distinguish low momentum pions, kaons and protons by measuring the time it takes these particles to travel from the primary vertex of the $p\bar{p}$ collision to the TOF system. The system consists of 216 bars of scintillating material, roughly 3 m in length and with a cross section of 4×4 cm^2. The bars are arranged into a barrel around the COT cylinder, at a radius of $\sim$1.5 m. The pseudo-rapidity coverage of the system is about $|\eta| < 1$. The scintillating material is Bicron 408, which has a short rise time and a long (380 cm) attenuation length.

Particles passing through the scintillating material of the bars deposit energy causing small flashes of visible light. This light is detected by photomultiplier (PMT) tubes which are attached at both ends of each bar and provide time and pulse height measurements. The signal from the photomultiplier tube is processed by a pre-amplifier circuit mounted directly onto the tube. The readout electronics perform both time and amplitude digitalization of the signal. The TDC (Time to Digital Converter) information is a digitalization of the time when the signal pulse reaches a fixed discriminator threshold. This time depends on the amplitude of the pulse, since a large pulse crosses the threshold earlier (time walk). The digitalization of the pulse amplitude is needed to correct for this effect. After correcting for time walk effects, the timing resolution of the TOF system is about 110 ps for particles crossing the bar exactly in front of one of the photomultiplier tubes. The timing resolution varies with displacement from the photomultiplier tube. A more detailed description can be found in [47].

With a time of flight resolution around 110 ps the TOF system can provide at least a two standard deviation separation between charged kaons and charged pions for momentum $p < 1.6$ GeV, an information complementary to the dE/dx measurement from COT. A separation power for TOF is shown in Figure 3.9 together with the dE/dx separation power for kaon and pion from COT superimposed.

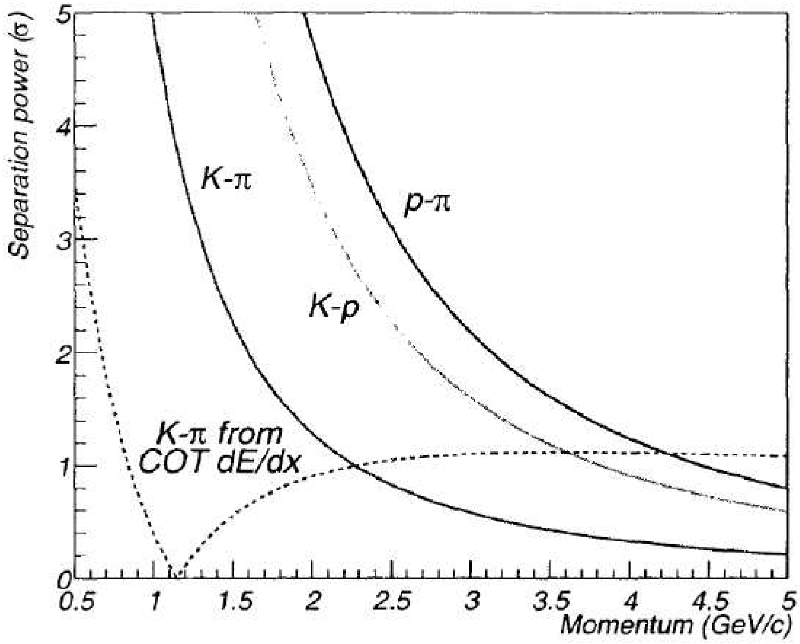

Figure 3.9: Separation power of TOF for different particles at CDF.

During my thesis, as a member of Universidad de Oviedo and IFCA, I have been in charge of the Time of Flight detector offline calibrations and validations. Every time a new period of data is avaible we have to check it, verify that the system is working properly, and produce new TOF calibration parameters into the database whenever there is a change in the hardware. These parameters are included with the rest of the parameters from the other detectors and will be later used in the offline processing of the CDF data.

3.7 The Solenoid

The tracking and the TOF systems are enclosed in a superconducting solenoid which provides a nearly uniform magnetic field of up to 1.4 T parallel to the beamline.

It is made of an aluminium-stabilized Nb Ti superconductor and runs at a current of about 4650 A, and operating at liquid helium temperature.

3.8 Calorimeters

In addition to tracking information, which determines the trajectory and momentum of a particle, detectors also must measure a particle's energy and that is the role of the calorimeters in the CDF II detector.

Each calorimeter samples particle energies using a sandwich of absorbing material and plastic scintillator. Incident particles interact with the absorbing layers and develop into a shower of many particles. The scintillator layers produce light as charged shower particles pass through. Photo-multiplier tubes read out the light from the scintillators in the sampling layers. The size of the shower inside the calorimeter indicates the energy of the incident particle. Each calorimeter has two components with different absorber materials designed to produce showers from either electromagnetic or hadronic objects.

The calorimeter is divided into separate electromagnetic (large number of radiation lenghts X_0 and small number of interaction lenghts λ for photon and electron identification and energy measurement) and hadronic (large number of interaction lenghts for hadron energy measurement) sections.

The entire calorimeter is segmented into "projective towers". This means that it is segmented in η and ϕ "towers" that point to the interaction region. The coverage of the calorimetry system is 2π in ϕ and $|\eta| < 3.6$ in pseudorapidity.

The calorimeter system is divided into three regions: central, plug and forward. Each calorimeter tower consists of an electromagnetic shower counter followed by a hadron calorimeter. This allows for comparison of the electromagnetic and hadronic energies deposited in each tower, and therefore separation of electrons and photons from hadrons.

The pseudorapidity coverage, resolutions, thickness and absorber material for the different electromagnetic and hadron calorimeters are given in Table 3.2. The details of each calorimeter are based on the specific physics needs and are discussed below.

3.8.1 Central Calorimeters

The central region of the detector is covered by the Central Electromagnetic (CEM) [48] and Central Hadronic (CHA) [49] calorimeters, in the pseudorapidity ranges $|\eta| < 1.1$ and $|\eta| < 0.9$, respectively.

Table 3.2: Pseudorapidity coverage, energy resolution and thickness for the different calorimeter subdetectors of the CDF II Detector. The $\oplus$ symbol means that the constant term is added in quadrature to the resolution. λ_0 signifies interaction lengths and X_0 radiation lengths.

System	η coverage	Energy Resolution (%)	Thickness	Absorber
CEM	$\|\eta\| < 1.1$	$13.5/\sqrt{E_T} \oplus 2$	$18X_0$	3.18 mm lead
PEM	$1.1 < \|\eta\| < 3.6$	$16/\sqrt{E_T} \oplus 1$	$21X_0$	4.5 mm lead
CHA	$\|\eta\| < 0.9$	$50/\sqrt{E_T} \oplus 3$	$4.5\lambda_0$	2.5 cm steel
WHA	$0.7 < \|\eta\| < 1.3$	$75/\sqrt{E_T} \oplus 4$	$4.5\lambda_0$	5 cm steel
PHA	$1.3 < \|\eta\| < 3.6$	$80/\sqrt{E_T} \oplus 5$	$7.0\lambda_0$	5.08 cm steel

Central Electromagnetic Calorimeter

The CEM is a sampling device made of layers of polystyrene scintillator, alternated with layers of aluminum-clad lead. The CEM is divided into four arches (North-West, South-West, North-East and South-East) made of identical 15° modules, each of them being segmented into 10 projective towers. Thus each tower covers a solid angle of 0.1 by 15° in $\eta \times \phi$ space.

The Central EM Max Detector (CES) [48] is a strip chamber designed to provide a measurement of charged tracks very close to the calorimeter, with very little material in between. This is done to distinguish electrons from photons, which otherwise look very similar in the detector. They are located between the 8^{th} lead layer and the 9^{th} scintillator layer (counting outward), which is the expected position of shower maximum ($\approx 6X_0$, including tracking and solenoid material).

The CEM is also equipped with a pre-shower detector (CPR), useful in discriminating between hadrons and photons/electrons. The CPR is a set of multi-wire proportional chambers with wires parallel to the beam providing transverse measurements and strip cathodes providing z information, with a resolution of the order of a few milimeters.

Central Hadronic Calorimeter

The CHA is a sampling hadronic calorimeter surrounding the CEM, following the same segmentation (0.1 by 15° in $\eta \times \phi$). The Wall Hadronic Calorimeter (WHA) [49] extends the CHA coverage and uses the same technology as the CHA. Altogether, a wedge contains 12 towers, 6 of which are fully in the CHA, 3 in the WHA and 3 are shared between the two. The CHA is made of 32 layers of 2.5 cm thick steel absorber and 1.0 cm thick scintillator. The WHA is made of 15 layers of 5.0 cm thick steel absorber and 1.0 cm thick scintillator. Two PMT's per tower are linked to the scintillators by a wavelength shifter and a light guide. The Wall Hadronic Calorimeter fills the gap between the CHA and the PHA in the pseudorapidity range $0.7 < |\eta| < 1.3$.

3.8.2 Plug Calorimeters

In the forward region, the Plug Calorimeters, shown in Figure 3.10, cover the η region between 1.1 and 3.64, corresponding to polar angles between 37° and 3°.

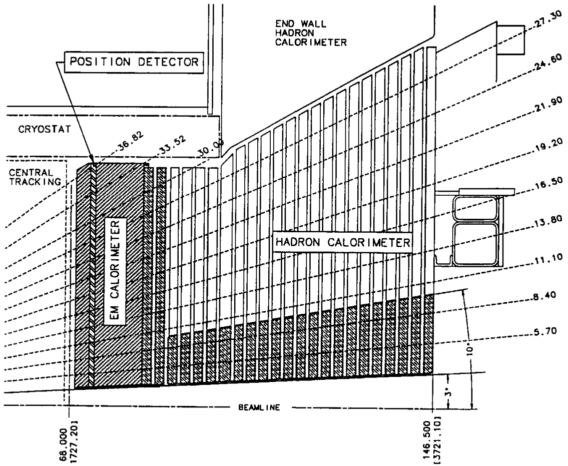

Figure 3.10: View of the Plug Calorimeters (PEM and PHA).

The Plug Calorimeters consist of an electromagnetic (PEM) and hadronic (PHA) calorimeter with the same projection segmentation. Figure 3.11 shows the segmentation patern of a 15° module and also shows how towers are combined for the purpose of being used by the trigger system.

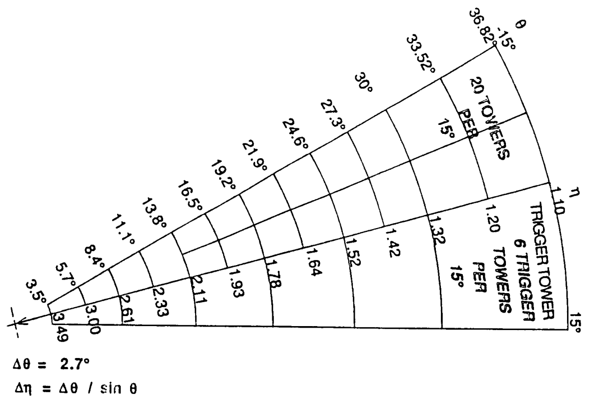

Figure 3.11: Segmentation of the Plug Calorimeters (PEM and PHA).

The PEM is made of 22 layers of 4.5 mm lead and 4 mm thick scintillator tiles. Each scintillator tile is read by a single PMT. In front of the 22 sampling layers is a 1 cm thick scintillator tile read out by a multi-anode photomultiplier (MAPMT) which is used as a pre-shower detector.

As in the Central Calorimeters, a shower maximum detector (PES) is also embedded in the PEM. Figure 3.12 shows the inner detector and CES, PPR and PES locations. It is made of two sets of scintillating strips that provide precise 2D shower position measurement (resolution ≈1 mm).

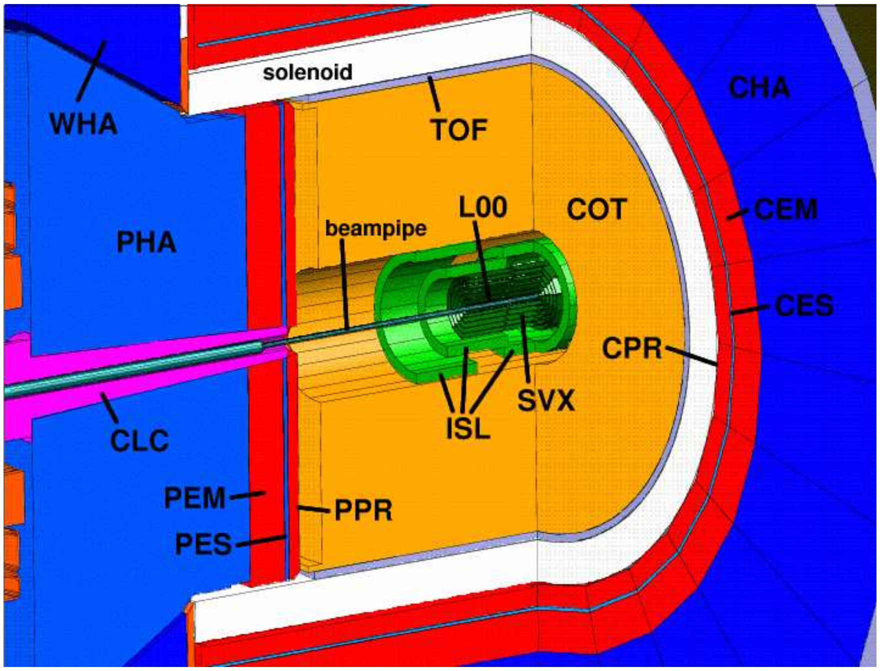

Figure 3.12: CDF Inner Detector (cutaway view).

The PHA is made of 23 layers of 5.08 cm thick steel absorber and 6 mm thick scintillator.

3.9 Muon Systems

We expect that the calorimeters will absorb nearly all particles produced in $p\bar{p}$ collisions. Neutrinos are, of course, expected to escape the detector completely undetected, but muons are also expected to pass through the calorimeters, as muons produced with energies typical of $p\bar{p}$ collisions are minimum-ionizing particles and lose little energy to bremsstrahlung. Consequently, CDF has additional drift chambers and scintillators located outside the calorimeter to detect and measure these muons. Muon detection systems are therefore placed radially outside the calorimeters, being the outermost component of CDF.

The muon detectors at CDF make use of single wire drift chambers as well as scintillator counters for fast timing. The various subsystems are the Central Muon Detector (CMU), the Central Muon uPgrade Detector (CMP), the Central Scintillator uPgrade (CSP), the Central Muon eXtension Detector (CMX), the Central Scintillator eXtension (CSX), the Toroid

Scintillator Upgrade (TSU), the Barrel Muon Upgrade (BMU) and the Barrel Scintillator Upgrade (BSU).

The CMU, CMP and CSP cover $|\eta| < 0.6$, the CMX and CSX cover $0.6 < |\eta| < 1.0$ and the TSU, BMU and BSU cover $1.0 < |\eta| < 2.0$. Table 3.3 summarizes the information on the muon subsystem.

Table 3.3: Parameters of the Muon Detectors at CDF.

	CMU	CMP/CSP	CMX/CSX
η coverage	0 - 0.6	0 - 0.6	0.6 - 1.0
Min p_T [GeV/c]	1.4	2.2	1.4
Drift Tubes			
Thickness [cm]	2.68	2.5	2.5
Width [cm]	6.35	15	15
Length [cm]	226	640	180
Max drift time [μs]	0.8	1.4	1.4
Scintillators			
Thickness [cm]	N/A	2.5	1.5
Width [cm]	N/A	30	30 - 40
Length [cm]	N/A	320	180

The first muon system built at CDF, the CMU [50], is placed just outside the CHA. It provides roughly 5.5 interaction lengths for pions, absorbing more than 99% of the outgoing charged hadrons. The p_T threshold of the CMU is 1.4 GeV/c. It is cylindrical in geometry with a radius of 350 cm, arranged into 12.6° wedges. Each wedge contains three modules (stacks) with four layers of four rectangular drift cells. The cells have 50 μm sense wires at the center of the cell, parallel to the z direction. The system is filled with an Argon-Ethane gas mixture and alcohol (49.5:49.5:1) as the COT.

A second set of chambers, the CMP, is situated outside an additional layer 60 cm thick of steel to act as an absorber, which is 3.5 additional interaction lenghts (for a total of $9.0\lambda_0$). The p_T threshold of the CMP is 2.2 GeV/c. It is rectangular in geometry, consisting in four layers of single-wiredrift cells, staggered by one half cell per layer.

On the other surface of the CMP lies the CSP [51], a single layer of rectangular scintillator tiles, with a waveguide to move the scintillated light into a PMT. This provides a fast detection mechanism used in triggering muons.

The CMX is located on either side of the detector straddling the beamline. It is a conical geometry of drift tubes with drift chambers, similar to the CMP, and scintillators on both sides. The CSX is another scintillator array similar to the CSP. The CMX cover 360° in ϕ. The segmentation is in 15° wedges in azimuthal angle. Each wedge consists of eight layers of rectangular tubes in the radial direction, also offset to provide better resolution.

Using the timing information from the drift cells of the muon systems, short tracks (called "stubs") are reconstructed. Tracks reconstructed in the COT are extrapolated to the muon systems. Based on the projected track trajectory in the muon system, the estimated errors on the tracking parameters and the position of the muon stub, a χ^2 value of the track-stub match is computed. To ensure good quality of muons, an upper limit is placed on the value of χ^2_ϕ, the χ^2 of the track-stub match in the ϕ coordinate.

3.10 The Cherenkov Luminosity Counter

The Cherenkov Luminosity Counter (CLC) [52, 53] was designed for the Tevatron Run II in order to achieve a precision measurement of the instantaneous luminosity up to $\approx 2{\cdot}10^{32}$ cm^{-2}s^{-1} and to cope with the 396 ns bunch-spacing.

The detector, located in the 3° gap between the plug calorimeters and the beam pipe as shown in Figure 3.13, is made of two identical CLC modules installed at small angles, inside the Plug Calorimeters, on each side of the interaction point.

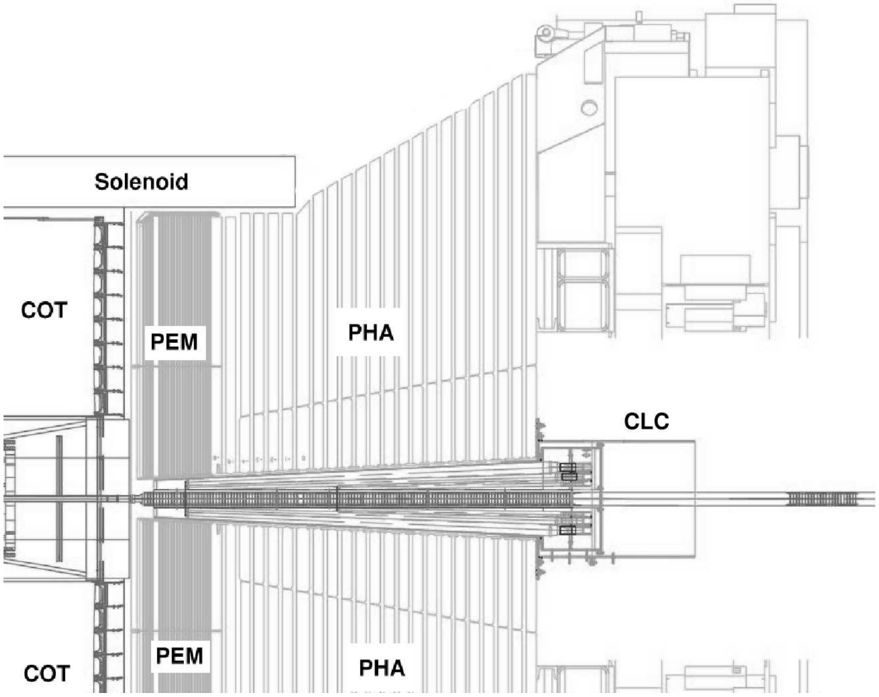

Figure 3.13: Location of the CDF Cherenkov Luminosity Counter in the 3° gap between the plug calorimeter and the beam pipe.

Each module is composed of 48 thin, long, conical, gaseous Cherenkov counters pointing toward the interaction point and covering the pseudorapity range $3.7 < |\eta| < 4.7$. The counters are arranged around the beam pipe in three concentric layers, with 16 counters each. The cones in the two outer layers are about 180 cm long and the inner layer counters (closer to the beam pipe) have a length of 110 cm; their diameter varies from 2 to 6 cm. At the widest end of each one (the furthest away from the interaction point), a conical mirror collects the Cherenkov light into 2.5 cm diameter photomultiplier tubes. The tubes have a concave-convex, 1 mm thick, quartz window for efficient collection of the ultraviolet part of Cherenkov spectra and operate at a gain of $2 \cdot 10^6$. The modules are filled with isobutane at atmospheric pressure; it is however possible to increase the pressure up to 2 atm, in order to increase the yield of Cherenkov light. The Cherenkov angle is 3.1° and the momentum threshold for light emission is 9.3 MeV/c for electrons and 2.6 GeV/c for pions.

Because of the narrow shape and the orientation of the cones, particles produced by $p\bar{p}$ interactions close to the center of the detector are likely to go through a large portion of the CLC, producing an important light yield (several hundred photo-elelectrons), while particles from the beam halo or from secondary interactions traverse the detector at large angle, and have lower energy, hence producing a much smaller light signal. Thus the background is easily rejected by requiring a certain minimal light yield threshold in each channel; the number of particles is measured from the total yield in the module. Thanks to the CLC's excellent time resolution (less than 100 ps), it is also possible to select hits from prompt particles by requiring time coincidence between hits in the two different modules.

At hadron collider experiments the beam luminosity can be expressed as a function of the number of hits per bunch-crossing as follows:

$$L = \frac{f_{bc}}{\sigma_{in} \cdot \epsilon} \cdot \mu \,, \tag{3.6}$$

where L is the instantaneous luminosity, f_{bc} is the rate of bunch-crossings in the Tevatron, σ_{in} is the inelastic scattering cross section, ϵ is the acceptance times efficiency of the CLC for inelastic scattering events and μ is the (measured) average number of interactions per bunch-crossing.

In Eq. 3.6, f_{bc} and ϵ are known and the total inelastic cross section was measured in several experiments. The inelastic scattering cross section at 1.96 TeV is 61.7 ± 2.4 mb. Therefore, we just need to know the number of hits per bunch-crossing in order to calculate the luminosity. And this is what the CLC was designed for by measuring the number of particles and their arrival time in each bunch-crossing.

A precision of 5.9% [54] on the luminosity is achieved with the CLC.

3.11 Trigger

The trigger plays an important role in hadron collider experiments because the collision rate is much higher than the rate at which the data can be stored on tape. Collisions happen at a rate of 2.5 MHz, roughly 2.5 millions of collision per second, while the tape writing speed will be less than 50 Hz. The trigger role is efficiently extract the most interesting physic events from the large number of minimum bias events.

The readout of the full detector produces an event the size of 250 kB, saving the full output of the detector for all events would be prohibitively impractical. There is no medium available which is capable of recording data this quickly, nor would it be practical to analyze all these data later on. The CDF II trigger system is a three-layer system which progressively reduces the event rate to a much smaller rate suitable for saving events to tape. Many different trigger paths are defined to collect events for the different analyses performed at CDF.

The CDF II trigger system is designed based on three conditions. The first condition is that the trigger has to be deadtimeless. This means that the trigger system has to be quick enough to make a decision for every single event, before the next event occurs. The second condition is imposed by the Tevatron, and it is the time between collisions, 396 ns. The last condition is that the data logging system can write about 30-50 events per second to tape, because of limited resources. In short, the trigger has to be fast enough to analyze every collision, and it has to figure out which 50 of 2.5 million events it should save in a given second.

3.11.1 Trigger System Levels

Each level of the trigger is given a certain amount of time to reach a decision about accepting or rejecting an event. At the first level of the trigger, only very rough and quick pattern recognition and filtering algorithms are used. In order to do this in time, the Level 1 and Level 2 triggering mechanisms are implemented with custom electronics. The third level of the trigger, Level 3, is implemented with a PC farm with about 300 CPUs.

The delay necessary to make a trigger decision is achieved by storing detector readout information in a storage pipeline.

Level 1 uses costum designed hardware to find physics objects based on a subset of the detector information and makes a decision based on simple counting objects. The Level 2 trigger uses costum hardware to do a limited event reconstruction which can be processes in programmable processors. The Level 3 uses the full detector resolutions to fully reconstruct events in a processor farm.

The block diagram for the trigger system is presented in Figure 3.14.

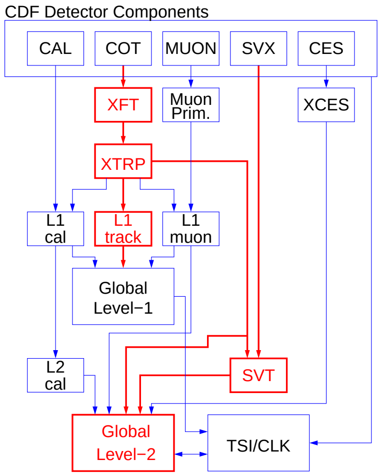

Figure 3.14: Block diagram of the Level 1 and Level 2 trigger paths.

The input of the Level 1 hardware comes from the calorimeters, tracking chamber, and muon detectors. The decision to retain an event for further processing is based on the number and energies of electron, muon, and jet candidates as well as the missing transverse energy in the event. A Level 1 accept can also be generated based on the kinematic properties of observed track pairs. Events accepted by the Level 1 system are processed by the Level 2 hardware. All the information used in the Level 1 decision is available to the Level 2 system, but higher precision. In addition, data from the central calorimeter showermax detector allows improved identification of electrons and photons. Jet reconstruction is provided by the Level 2 cluster finder; secondary-vertex information is produced by the SVT. A Level 2 accept initiated full detector readout for the event.

A set of requirements that an event has to fulfill at Level 1, Level 2 and Level 3 constitutes a trigger path. The CDF II trigger system implements about 100 trigger paths. An event will be accepted if it passes the requirements of any one of these paths.

3.11.2 Online Monitoring

The CDF detector consists of many detector subsystems and runs a high rate large bandwidth data transfer environment. To take data with high efficiency and high quality, it is necessary to quickly spot problems with one of these subdetectors in real time. Multiple event monitor programs are attached to the DAQ system [55, 56].

The online monitoring programs are called Consumers, where a Consumer is defined as a process which receives events from Consumer Server Logger (CSL) in real time. CSL sends the data to the computer center where they are written to tape and forwards copies of a subset of the data to the online monitoring programs. Figure 3.15 shows a schematic view of the CDF online monitoring system (Consumer Framework).

The task of the Consumers is to analize and monitor the event data and to make histograms and tables. These results could be viewed by the display browser via a server in real time. Results of the monitor are also stored as data files periodically during a run, and also archived systematically.

The display browser provides a GUI to view the online monitored results, while also providing some basic utilities to do comparisons with previously stored results. By separating the two tasks of monitoring and displaying, we remove CPU bound associated with displaying graphics from the machine which runs the consumers. During the data taking, multiple consumer processes run in parallel, receiving event data with the desired trigger types from the CSL. Communication between consumers and run control, which controls the overall CDF DAQ system, is handled by the error Receiver. Severe errors detected by a consumer monitor program are forwarded to run control to take necessary actions. The state manager watches the state of consumers.

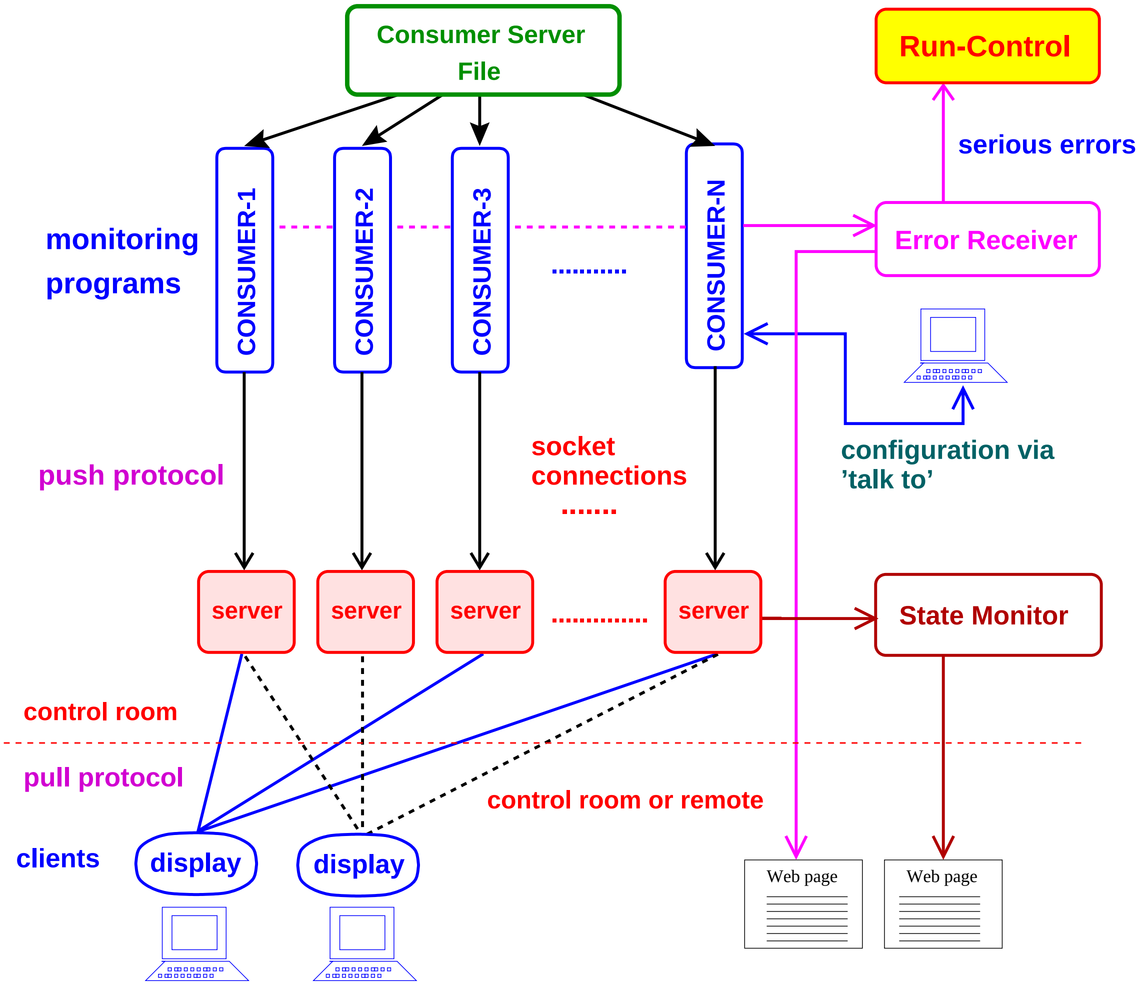

Figure 3.15: Design of the CDF online consumer framework.

Chapter 4

High P_T Objects Reconstruction

After an event has been accepted by the CDF trigger system, full event reconstruction is performed offline; at this stage, raw tracks and clusters are identified as electrons, muons, jets, or other objects.

The analysis presented in this thesis is strongly based on high-p_T electrons and muons, jets, and missing transverse energy ($\not{E}_T$). These objects are defined in the following sections.

4.1 Lepton Identification

This section describes the standard requirements used for electron and muon identification at the CDF experiment.

4.1.1 Electrons

High-p_T electrons traversing the CDF detector are expected to leave a track in both the silicon detector as well as the COT. Then, electrons, having a relatively low mass and being electrically charged, will deposit most of their energy into the central (CEM) and plug (PEM) electromagnetic calorimeters. An electromagnetic cluster with a reconstructed track pointing to it is essentially the starting point for electron identification. Clusters are made of small, contiguous groups of calorimeter towers with energy deposits.

The types of electrons used in this analysis are CEM electrons, tight central electrons, with $|\eta| < 1.1$, and PHX electrons, tight forward electrons, which rely on silicon tracking with $1.2 < |\eta| < 2.0$. Table 4.1 contains the electron identification cuts.

The meaning of the identification variables is as follows:

- E_T is the transverse energy of the cluster. The trigger requires $E_T >$18 GeV, but requiring $E_T >$20 GeV ensures that the trigger is fully efficient.
- E_{HAD}/E_{EM} is the ratio of energy which is deposited in the hadronic (CHA or WHA) calorimeter with respect to the energy deposited in the electromagnetic (CEM or PEM) calorimeter.

Selection	Central (CEM)	Plug (PHX)
E_T	> 20 GeV	> 20 GeV
E_{HAD}/E_{EM}	$\leq (0.055 + (0.00045 \cdot E))$	≤ 0.05
Isolation	≤ 0.1	≤ 0.1
Track z_0	≤ 60 cm	≤ 60 cm
Track p_T	≥ 10 GeV/c	
COT Axial Segments	≥ 3	
COT Stereo Segments	≥ 2	
Silicon Hits		≥ 3
L_{shr}	≤ 0.2	
E/p	≤ 2.0 for $p_T \leq 50$ GeV/c	
χ^2	≤ 10.0	≤ 10.0
$Q \cdot \Delta x$	$-3.0 \leq Q \cdot \Delta x \leq 1.5$	
$\lvert\Delta z\rvert$	≤ 3.0 cm	
ΔR		≤ 3.0 cm
Phoenix Match		TRUE

Table 4.1: Electron identification cuts

- Isolation is the ratio of the additional transverse energy in a cone of radius $R = \sqrt{(\Delta\phi)^2 + (\Delta\eta)^2} = 0.4$ around the cluster to the transverse energy of the cluster itself.

- Track z_0 is the longitudinal (z) position of the track where it intersects the beamline.

- Track p_T is the transverse component of the momentum which is measured explicitly using the track curvature.

- COT Axial and Stereo Segments are, respectively, the number of axial and stereo superlayers in the COT which have at least 5 hits associated with this track.

- Silicon Hits is the number of hits in the silicon detector associated with a specific track. The maximum number of hits is 8 (for L00, SVX, and ISL combined).

- L_{shr} is a variable that measures how close the energy distribution in the CEM towers adjacent to the cluster seed is to the electron hypothesis.

- E/p is the ratio of the cluster's energy and the track's momentum.

- χ^2 is the χ^2 of the fit to electron test beam data for shower-maximum profile.

- $Q \cdot \Delta x$: the quantity Δx is the signed difference in x between the track and the cluster when the track is extrapolated to the position of the shower max. Q is the measured charge of the particle.

- $|\Delta z|$ is the absolute value of the difference in z position between the cluster and the extrapolated track.

- ΔR is the distance in the $\eta - \phi$ plane between the position of the reconstructed cluster in the PEM calorimeter and the PES shower maximum detector.
- Phoenix Match: PHX electrons must have a track that is matched to the PEM cluster and event vertex.

4.1.2 Muons

Muons are minimum ionizing particles which can traverse the entire CDF II detector. Muons are characterized by the track they leave in the tracking system, very little energy deposited in the calorimeter which they pass through, and in cases where they are fiducial to muon chambers they will also leave track, often called a stub, in these detectors.

The types of muons used in this analysis are:

- CMUP: central muon which has hits in both the CMU and CMP muon detectors, $|\eta| < 0.6$.
- CMX: muon which has hits in the CMX detector, $0.65 < |\eta| < 1.0$.
- BMU: muon which has hits in the forward, $1.0 < |\eta| < 1.5$, barrel muon chambers.
- CMU only and CMP only¿ muon candidates that have tracks in the CMU and CMP chambers, respectively, but not in the corresponding overlaping CMP and CMU chambers.
- CMIO and SCMIO: muons with isolated tracks matched to calorimeter clusters that do not point towards a muon detector or that point towards a non-fiducial part of a muon detector, respectively. These tracks are required to be matched to a COT track and a low energy calorimeter cluster consistent with the criteria of minimum ionizing particles.
- CMXNT: muon which leaves tracks in the most forward region of the CMX detector, which is not triggerable due to the limited COT geometry. They have the same quality requirements as the CMX muon sample.

Table 4.2 and 4.3 contains the muon identification cuts. The meaning of each identification variables is given below.

- Track d_0 is the impact paremeter of the tracks defined as the distance of the closest approach of the fitted track to the beamline.
- $CM(U|P|X)$ and BMU FidX, FidZ: the extrapolation of the track to the relevant muon detector is required to be fiducial to the detector and, in the case of CMX, must also not be within 3 cm in FidZ of the edge of the detector.
- $|\Delta X_{CMU|P|X}|$ and $|\Delta X_{BMU}|$ is the distance between the actual stub in a given muon detector and the track position extrapolated to that detector.

- $|\rho_{COT}|$ is the radius at which the track appears to leave the COT. This value is required to ensure that these muons are a type which can be triggered on by the CMX trigger track requirements.

The rest of the variables are defined in the previous section 4.1.1.

	CMUP	CMX
p_T	> 20 GeV	
E_{em}	$\leq 2.0\ +\ max(0, 0.0115(p-100))$ GeV	
E_{had}	$\leq 6.0\ +\ max(0, 0.0280(p-100))$ GeV	
$Isolation$	< 0.1	
Track z_0	< 60 cm	
Track d_0	< 0.2 cm (0.02 cm w/ silicon hits)	
NAxL	≥ 3	
NStL	≥ 2	
χ^2	< 2.3 (2.75 if run < 190697 & !BMU)	
CMU FidX	< 0 cm	—
CMU FidZ	< 0 cm	—
CMP FidX	< 0 cm	—
CMP FidZ	$<$ -3 cm	—
CMX FidX	—	< 0 cm
CMX FidZ	—	$<$ -3 cm
BMU FidX	—	—
BMU FidZ	—	—
$\|\Delta X_{CMU}\|$	< 7 cm	—
$\|\Delta X_{CMP}\|$	≤ 5 cm	—
$\|\Delta X_{CMX}\|$	—	< 6 cm
$\|\Delta X_{BMU}\|$	—	—
$\|\rho_{COT}\|$	—	> 140 cm

Table 4.2: Muon identification requirements

The CEM, PHX, CMUP, CMX leptons are the so called tight leptons from events of the high-p$_T$ lepton triggered coverage, and the rest of leptons used in this analysis are muons collected by the $\not\!\!E_T$+jets trigger called extended muon coverage (EMC). A detailed explanation of these triggers is given in Chapter 6.

4.2 Jet Identification

Jets consist of a shower of particles originate from the production of high energetic quarks or gluons. The jets used in this analysis are defined by using the JETCLU [57] algorithm. JETCLU is a cone algorithm, which searches for clusters of deposited energy in the calorimeters. The cone algorithm searches for such clusters placed inside a cone with

	BMU	CMU	CMP	CMIO	SCMIO	CMXNT
p_T	> 20 GeV					
E_{em}	$\leq 2.0\ +\ max(0, 0.0115(p-100))$ GeV					
E_{had}	$\leq 6.0\ +\ max(0, 0.0280(p-100))$ GeV					
$Isolation$	< 0.1					
Track z_0	< 60 cm					
Track d_0	< 0.2 cm (0.02 cm w/ silicon hits)					
NAxL	COT Hit Frac.> 0.6	≥ 3				
NStL		≥ 2				
χ^2	< 2.3 (2.75 if run < 190697 & !BMU)					
$E_{em} + E_{had}$	—	—	—	> 0.1GeV	> 0.1GeV	—
CMU FidX	—	< 0 cm	$\geq$ 0 cm	≥ 0 cm	—	—
CMU FidZ	—	< 0 cm	$\geq$ 0 cm	≥ 0 cm	—	—
CMP FidX	—	$\geq$ 0 cm	< 0 cm	≥ 0 cm	—	—
CMP FidZ	—	$\geq$ -3 cm	$<$ -3 cm	$\geq$ -3 cm	—	—
CMX FidX	—	—	—	≥ 0 cm	—	< 0 cm
CMX FidZ	—	—	—	$\geq$ -3 cm	—	$<$ -3 cm
BMU FidX	< 0 cm	—	—	≥ 0 cm	—	—
BMU FidZ	$<$ -3 (-13 if $\lvert\eta\rvert <$ 1.25)	—	—	$\geq$ -3 (-13)	—	—
$\lvert\Delta X_{CMU}\rvert$	—	< 7 cm	—	—	—	—
$\lvert\Delta X_{CMP}\rvert$	—	—	≤ 5 cm	—	—	—
$\lvert\Delta X_{CMX}\rvert$	—	—	—	—	—	< 6 cm
$\lvert\Delta X_{BMU}\rvert$	≤ 9 cm	—	—	—	—	—
$\lvert\rho_{COT}\rvert$	—	—	—	—	—	—

Table 4.3: Extended Muon Coverage identification requirements

radius $\Delta R = \sqrt{(\Delta\phi)^2 + (\Delta\eta)^2}$ in the η-ϕ plane. If there is a lepton, which falls into the cone of the jet, the energy of this lepton is neglected for the determination of the jet energy.

The energy of the measured jet is corrected to scale it back to the energy of the final state particle level jet. Additionally, there are corrections to associate the measured jet energy to the parent parton energy, see Figure 4.1. The energy of the jets is corrected in several steps to accomodate different effects [58]:

- Relative Energy Corrections: the non-uniformity of the detector in η is accounted for. This results from the difference in clustering performance between the central and plug calorimeters, and from inefficiencies due to cracks between sections of the calorimeter. Since the central calorimeters are better calibrated and understood, this correction scales the forward calorimeters to the central calorimeter scale. This correction is obtained using Pythia and data di-jet events. Both data and Monte Carlo events are given η dependent corrections to make the jet energy response uniform across the detector.

- Multiple Interaction Corrections: this correction takes into account the fact that ener-

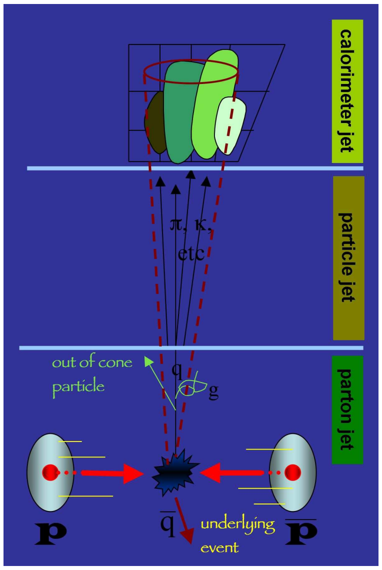

Figure 4.1: A diagram from the parton level jet to the measured jet in the detector.

gies originating from different $p\bar{p}$ collisions in the same bunch increase the measured jet energy because the energies falls inside the jet cluster. For a luminosity of 10^{32} cm^{-2}s^{-1} the average number of collisions is three. The correction is derived from minimum bias data and is parameterized as a function of the number of vertices in the event.

- Absolute Energy Corrections: corrects the calorimeter energy for non-linearities and un-instrumented parts of the detector. The correction is obtained mapping the total p_T of the hadron-level jet to the p_T of the calorimeter-level jet. The hadron-level jet consists of particles within a cone of the same size as and within $\Delta R < 0.4$ of the calorimeter-level jet. The result of this correction is assumed to be the energy on particle level after the fragmentation process. The main systematic uncertainties on the absolute scale are obtained by propagating the uncertainties on the single particle response (E/p) and the fragmentation. Figure 4.2 shows the absolute energy corrections and its systematic uncertainties.

- Underlying Energy Corrections: subtracts the energy estimated from the underlying event. Underlying events can occur in the same $p\bar{p}$ collision originating from an interaction of other partons of the proton.

- Out of Cone Corrections: corrects the particle energy to parton energy. This correction adds the energy of particles produced during the fragmentation, that are not placed inside the cone of the clustering.

For the selection of jets in this analysis we use absolute energy corrections.

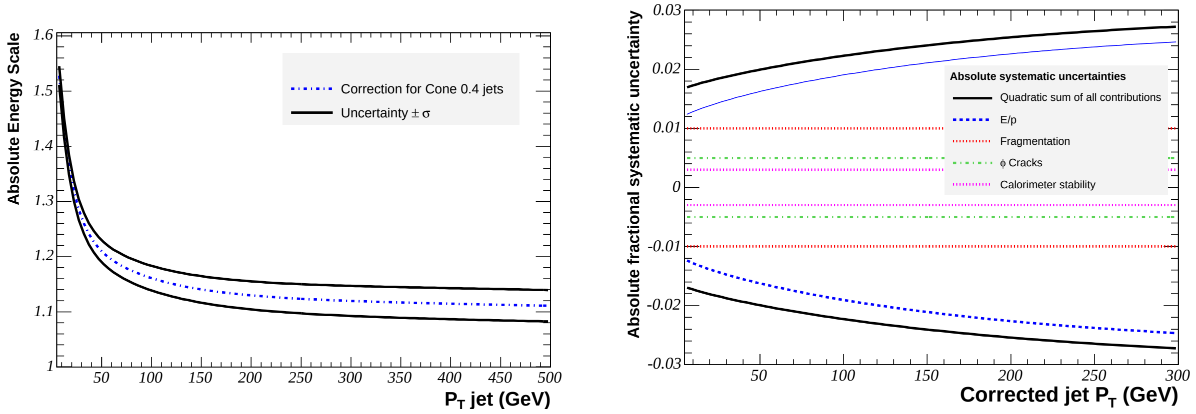

Figure 4.2: Absolute jet energy corrections as a function of calorimeter jet p_T for a cone size of 0.4 (left) and the systematic uncertainties of the jet energy scale due to the calorimeter calibration and simulation (right). The solid line shows the total untertainty and the other lines the individual contributions.

In the WH channel we expect to have two b-quarks forming jets. Jets are required to have $E_T > 20$ GeV after jet corrections have been applied and have $|\eta| < 2.0$. We classify events according to the their number of jets.

4.3 Missing Transverse Energy

The presence of neutrinos in an event is inferred by an imbalance of transverse energy in the detector. The missing transverse energy, $\not\!\!E_T$, is defined as:

$$\not\!\!E_T = -\sum_i [E_{T,i}cos(\phi_i), E_{T,i}sin(\phi_i)],$$

where $E_{T,i}$ is the transverse energy of the calorimeter tower i calculated with respect to the z coordinate of the event, ϕ_i is its azimuthal angle, and the sum is over all calorimeter towers. The trigger hardware calculates the $\not\!\!E_T$ assuming the primary vertex of the event is at the center of the CDF detector and using only calorimeter information. We correct offline $\not\!\!E_T$ for the z-position of the primary vertex, for the corrected jet energies, and for the momentum of any minimum ionizing high-p_T muons, by subtracting the transverse momentum of the muon track and adding back the transverse energy in the calorimeter towers traversed by the muon.

4.4 b-tagging Algorithms

Since the signal events that we are looking for are characterized by the presence of two b-jets, see Section 5.2, identifying b-jets is one of the main keys of this analysis. Fortunately,

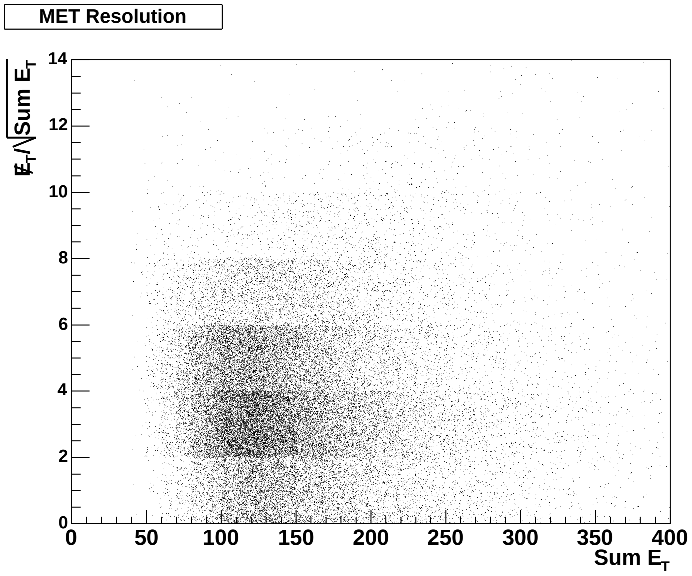

Figure 4.3: Missing E_T resolution.

the b-hadrons have long lifetimes, of the order of picoseconds. Therefore, they travel several millimeters in the detector before decaying into other particles. In this case, we use this information to distinguish the b-hadrons from the rest of the particles that come from the primary vertex.

Two CDF standard b-tagging algorithms are used in this analysis to identify heavy flavor content in jets: the secondary vertex (SECVTX) and the JET PROBABILITY (JP) algorithms, both of them explained below.

4.4.1 SECONDARY VERTEX b-Tagging

The CDF secondary vertex (SECVTX) [59] detection algorithm looks for displaced secondary vertices with respect to the primary event vertex, to identify the long-lived hadrons, as shown in Figure 4.4. The primary vertex location in a given event can be found by fitting well-measured tracks to a common point of origin.

The SECVTX algorithm runs on a per jet basis, where only tracks within the jet cone are considered for each jet in the event. The algorithm starts by considering silicon tracks within each jet ($\Delta R < 0.4$). The silicon tracks must be confirmed by a track in the COT. SECVTX uses a two pass approach to find secondary vertices. In the first pass, applying loose track selection criteria ($p_T > 0.5$ GeV/c and $|\frac{d_0}{\sigma d_0}| > 2.5$ cm), it attemps to reconstruct a secondary vertex which includes at least three tracks (at least one of the tracks must have $p_T > 1$ GeV/c). If no secondary vertex is found, it makes tighter track selection requirements ($p_T > 1$ GeV/c and $|\frac{d_0}{\sigma d_0}| > 3.0$ cm) and attempts to recontruct a two track vertex in a second pass.

All tracks are required to satisfy the "baseline" cuts shown in Table 4.4 to reject poorly

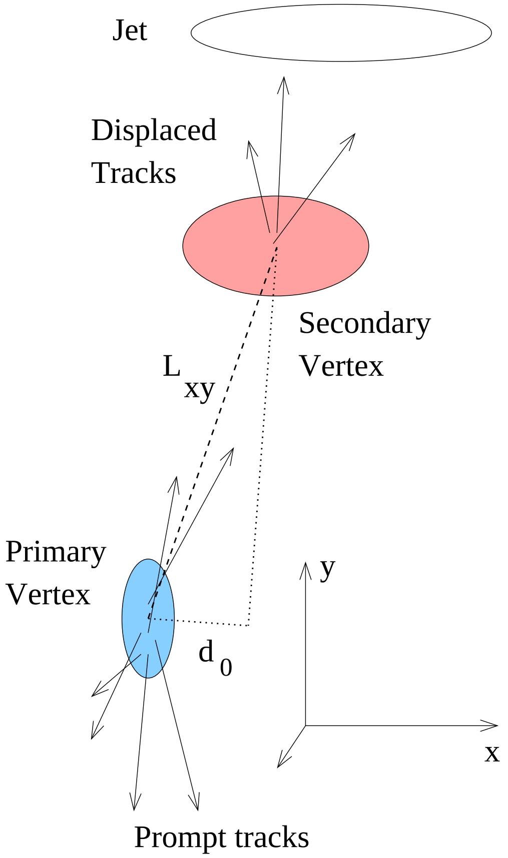

Figure 4.4: A diagram of a secondary vertex tag.

reconstructed tracks. d_0, the impact parameter of the tracks, is corrected to the primary vertex, and z_{pvtx} is the z-position of the event primary vertex. Only jets with at least two of these good tracks can produce a displaced vertex. A jet is defined as SecVtx taggable if it has two good tracks.

Table 4.4: Selection criteria for tracks used by the SecVtx algorithm.

Variable	Cut
p_T	$> 0.5\,\mathrm{GeV/c}$
$\lvert d_0 \rvert$	< 0.3 cm
$\lvert z_{trk} - z_{pv} \rvert$	< 5 cm

In addition to this baseline cuts, SecVtx makes specific requirements on the number and type of COT and SVX hits accociated with the tracks, the track fit χ^2 and other track qualities that can discriminate fake tracks.

The selected tracks are ordered in p_T, and a secondary vertex is sought among these tracks. The algorithm uses the two dimensional decay length of the vertex with respect to the primary vertex, L_{xy} (shown also in Figure 4.4), as its principal to discriminante b-jets. Finally the vertex is demanded to have $S_{L_{xy}} > 7.5$, where $S_{L_{xy}}$ is the two dimensional decay length significance defined as $S_{L_{xy}} = \frac{L_{xy}}{\sigma_{L_{xy}}}$.

If the vertex satisfies all the above criteria, a secondary vertex is defined to have been found and the jet is said to be SecVtx tagged. L_{xy} is defined to be positive when the secondary vertex is displaced in the same direction as the jet, and the jet is positively tagged. A negative value of L_{xy} indicates an improper assignment of a b-tag due to improperly reconstructed tracks, in this case the tag is called negative. These negative tags are useful for estimating the rate of fake b-jets, explained in sub-section 4.4.4.

4.4.2 Jet Probability b-Tagging

The Jet Probability b-tagging algorithm [60] can be used to determine whether a jet has been produced from the hadronization process of a light parton or a heavy parton. The latter result in long-lived hadrons whose decay gives rise to tracks displaced from the primary interaction vertex. This algorithm uses tracks associated with a jet to determine the probability for these tracks to come from the primary vertex of the interaction. The calculation of the probability is based on the impact parameters (d_0) of the tracks in the jet and their uncertainties. The impact parameter is assigned a positive or negative sign depending on the position of the track's point of the closest approach to the primary vertex with respect to the jet direction, as shown in Figure 4.5. By construction, the probability for tracks originating from the primary vertex is uniformly distributed from 0 to 1. The distribution for a jet coming from heavy flavor hadronization peaks at 0.

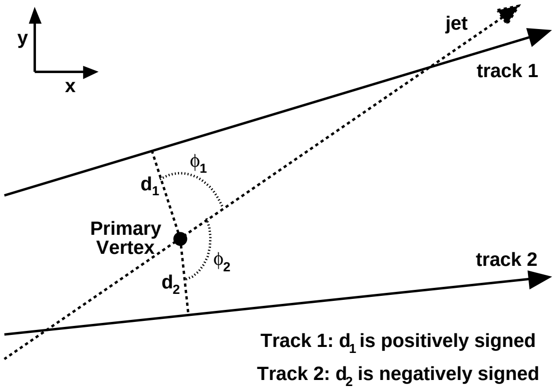

Figure 4.5: The sign of the impact parameter of a track. The impact parameter is positive (negative) if the angle ϕ between the jet axis and the line connecting the primary vertex and the track's point of the closest approach to the primary vertex itself is smaller (bigger) than $\pi/2$.

The particles in a jet coming from a light parton originate at the primary vertex, but these tracks are reconstructed with a non-zero impact parameter due to the finite tracking resolution. They have an equal probability of being positively or negatively signed. Jets which originate from a heavy parton contain long lived hadrons giving rise to tracks from secondary vertices that will bias toward positive impact parameters. The width of the negative impact parameter distribution is solely due to the tracking detector resolution, beam spot size, and multiple scattering.

We parameterize the impact parameter significance, S_{d_0} (ratio of the impact parameter to its uncertainty), for tracks satisfying the quality criteria listed in Table 4.5 that are associated with jets with $E_T > 7$ GeV and $|\eta| < 2.5$. Tracks passing this selection are called jet probability tracks. Jets are required to have at least two jet probability tracks with positive impact parameter to be Jet Probability taggable.

Table 4.5: Selection criteria for tracks used by the Jet Probability algorithm

Variable	Cut
p_T	$> 0.5\,\mathrm{GeV/c}$
$\|d_0\|$	< 0.1 cm
$N_{\mathrm{SVX\ axial}}$	≥ 3 and ≤ 5
$N_{\mathrm{COT\ axial}}$	≥ 20
$N_{\mathrm{COT\ stereo}}$	≥ 17
$\|z_{trk} - z_{pv}\|$	< 5 cm

Figure 4.6 shows the distribution of the impact parameter significance of tracks in an inclusive jet sample with at least 5 good SVX hits, $p_T > 5$ GeV/c and $|\eta| < 0.6$.

The Jet Probability P_J that a jet is consistent with a zero lifetime hypothesis is defined as

$$P_J = \prod \times \sum_{k=0}^{N_{trk}-1} \frac{(-ln \prod)^k}{k!}, \tag{4.1}$$

where

$$\prod = \prod_{l=1}^{N_{trk}} P_{tr} \tag{4.2}$$

and N_{trk} is the number of jet probability tracks with positive impact parameter. The individual track probabilities, $P_{tr}(S_{d_0})$, are expressed as a function of the impact parameter significance,

$$P_{tr}(S_{d_0}) = \frac{\int_{-\infty}^{-|S_{d_0}|} R(S)dS}{\int_{-\infty}^{0} R(S)dS} \tag{4.3}$$

where R(S) is the impact parameter resolution, S_{d_0} and S are signed impact parameter significance. We obtain the resolution parameterization from fitting tracks in jet data. The fit uses only negative signed impact parameter tracks, and assumes a symmetric distribution for positive signed impact parameters in light flavor jets. We define positive (negative)

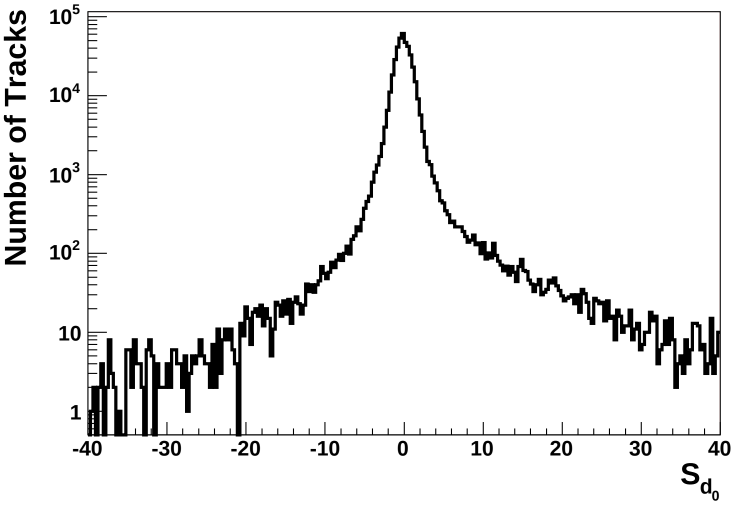

Figure 4.6: Distribution of the impact parameter significance for tracks in an inclusive jet sample with at least 5 good SVX hits, $p_T > 5$ GeV/c, and $|\eta| < 0.6$.

tagged jets as those jets whose positive (negative) P_J is less than a cutoff, the value for P_J used in this analysis is 5%. Positive tagged jets are expected to be enriched in heavy flavor.

In Figure 4.7 the right plot shows the JET PROBABILITY distributions observed in two different data sets of jets. The first sample is enriched in heavy flavor content by requiring the jets to contain a soft momentum electron. The second set consists of generic QCD jets selected by requiring events with at least one jet with $E_T > 50$ GeV. The left plot shows the JET PROBABILITY distributions for b, c, and light jets in MC samples.

4.4.3 Tagging Efficiency for Heavy Quark Jets

The efficiency for identifying a heavy flavor jet is different in simulated events and in data. The ratio of data tagging efficiency to Monte Carlo simulation tagging efficiency is called the tagging scale factor (SF).

Figure 4.8 shows the efficiency, for SECVTX, to tag jets in top quark Monte Carlo samples which have been matched to b-quarks. The efficiency is obtained by multiplying the tag rate for such jets in the Monte Carlo by data/MC scale factors.The bands represent the systematic error on the data/MC scale factors. The decrease in efficiency at high jet E$_T$ is due to declining yield of good silicon tracks passing the quality cuts.

The tagging scale factors used in this analysis are summarized in Table 4.6 for $P_J < 5\%$, and SECVTX. The uncertainties shown are statistical and systematic.

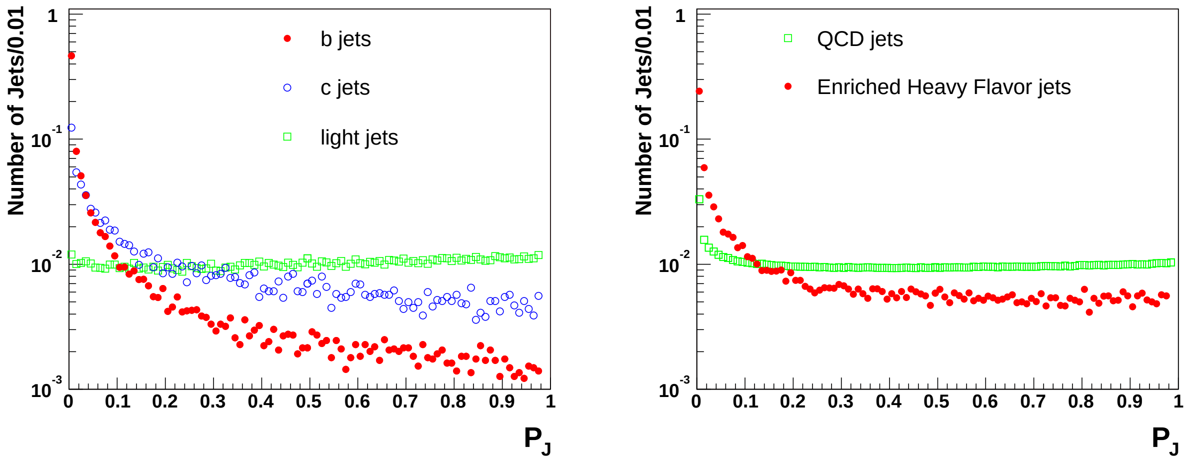

Figure 4.7: Left: Jet Probability distributions for jets matched to b (full circles), c (empty circles) and light (empty squares) quarks in Monte Carlo simulated events. Right: Jet Probability distributions for electron jets in inclusive electron data (full circles) and for generic QCD jets in Jet50 data (empty squares).

Table 4.6: Tagging scale factors for $P_J < 5\%$, and SecVtx

	$P_J < 5\%$	SecVtx
SF	0.806 ± 0.038	0.95 ± 0.04

4.4.4 Mistag Rate

The probability of identifying a light jet as a heavy flavor jet ("mistag") is closely related to the rate of negatively tagged jets. The tagging scale factor accounts for the fact that Monte Carlo over-estimates the tagging efficiency of jets originating from heavy flavor quarks. The mistag matrix corrects the Monte Carlo for an under-estimate of the number of mis-tagged light flavor jets.

Figure 4.9 shows displaced tracks from a light jet creating a secondary vertex with a negative value of L_{xy} (bottom) compared with a real b-jet secondary vertex with a positive value of L_{xy} (top).

It is assumed that the negative tags are due to detector resolution effects only, while the positive tag rate has an additional contribution from real heavy flavor in the jets. Under this assumption, the mistag rate is equal to the negative tag rate, although there is a small contribution from heavy flavor jets to the negative tag rate and there are contributions from K's, Λ's and nuclear interactions with the detector material to the positive tag rate that are also taken into account as asymmetry corrections.

The tag rate has a dependence on jet kinematics. To properly understand mistags requires

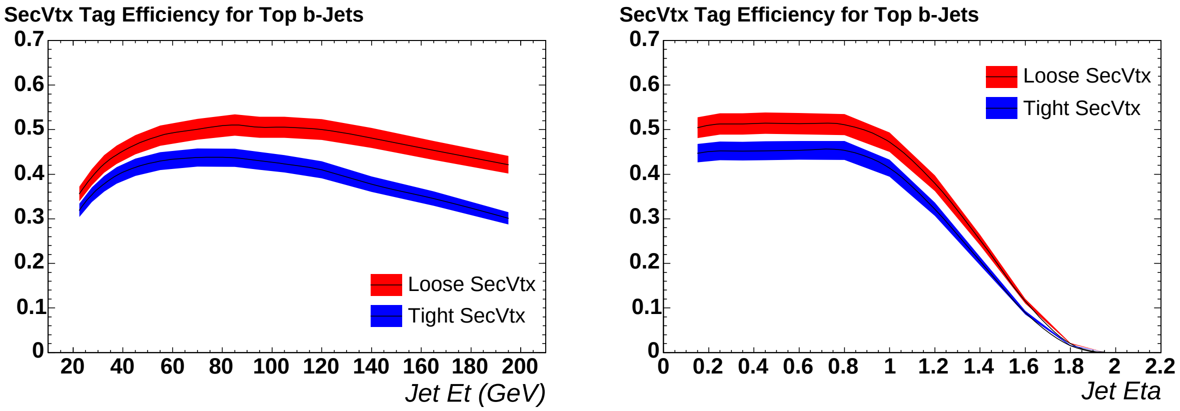

Figure 4.8: SecVtx efficiency to tag jets in top quark Monte Carlo.

a 6 dimensional mistag matrix, which is a parameterization of the mistag rate as a function of these variables: transverse energy of the jet (E_T), the number of tracks in the jet (N_{trk}), the sum of the transverse energies of all jets in the event ($\sum E_T^{jet}$), pseudorapidity of the jet (η), the number of reconstructed vertices in the event (N_{vtx}), and the z-position of the primary vertex (z_{vtx}). Figure 4.10 shows the false positive tag rate (including asymmetry corrections). These have been measured from inclusive jet data.

4.5 Neural Network Flavor Separator

After the event selection, see Chapter 6, and applying b-tagging, several of the sizable backgrounds in this analysis do not have a b-quark in the final state (as demonstrated in Table 6.2 and Table 6.3), but are falsely identified as such. This happens either because a light quark jet is falsely identified to have a displaced secondary vertex due to tracking resolution (mistag) or because real heavy charm quark decays happen to have a sufficiently long life-time to be tagged by the secondary vertex tagger. Therefore, it would be desirable to have better separation of b-quark jets from charm or light quark jets. In this analysis, a Neural Network flavor separator [61] is used to achieve this separation.

The Neural Network flavor separator is a continuous variable, result of a Neural Network training that uses a broad range of variables in order to identify b-quark jets with high purity. It is only defined for SecVtx tagged jets. A variety of variables is suitable to exploit lifetime, mass, and decay multiplicity of b-hadrons. Many of them are related to the reconstructed secondary vertex, some are reflected by the properties of the tracks in the SecVtx tagged jet. To account for the probability of semileptonic b-hadron decays, the number and momenta of leptons in the jet are useful quantities. For example, the most significant variables in the training are: the number of tracks with the impact paramenter significance ($|\frac{d_0}{\sigma d_0}|$) greater than 3, the lifetime signed impact parameter significance of the three most energetic tracks in each tagged jet, and the invariant mass of the vertex. Distributions that have different

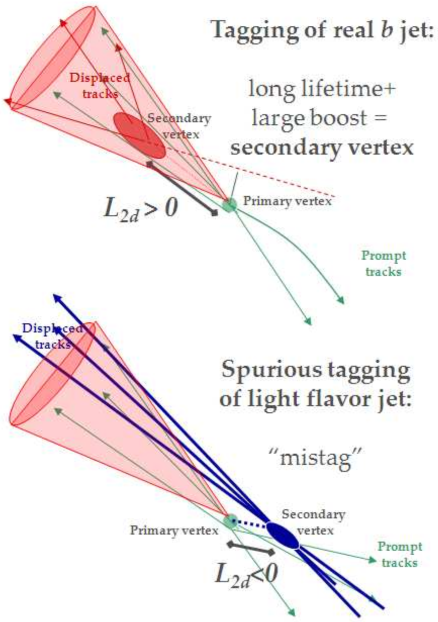

Figure 4.9: Top (bottom): a true (fake) b-jet with a positive (negative) value of L_{xy}.

behaviour for the different jet flavors, and give some separation betweem b, c, and light jets.

Left plot of Figure 4.11 shows the Neural Network flavor separator output for b-jets signal and non b-jets background. Both distributions are very well separated. In this analysis we include the Neural Network flavor separator by using its output as a b-jet probability in the discriminant, for more details see Section 7.3. This is motivated by the right plot of Figure 4.11, which shows that larger values of the Neural Network output corresponds with also larger signal purity therefore the jet is most probable to be a b-jet.

The Neural Network flavor separator was succesfully used in the single top discovery analyses [62], where it has proven to be an important quantity to reject events not containing any b-quarks.

The ouput of the flavor separator for different type of jets is displayed in Figure 4.12.

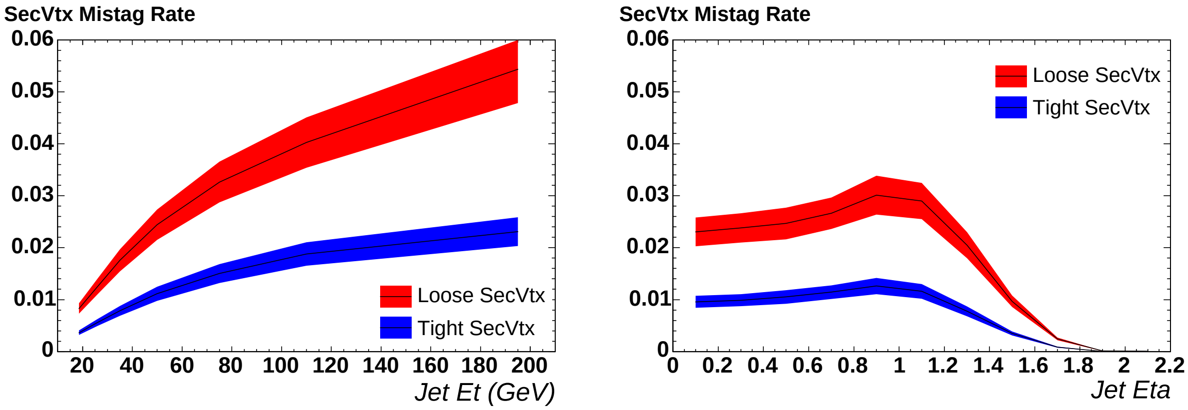

Figure 4.10: False positive tag rate (including asymmetry corrections) for SECVTX. These have been measured from inclusive jet data.

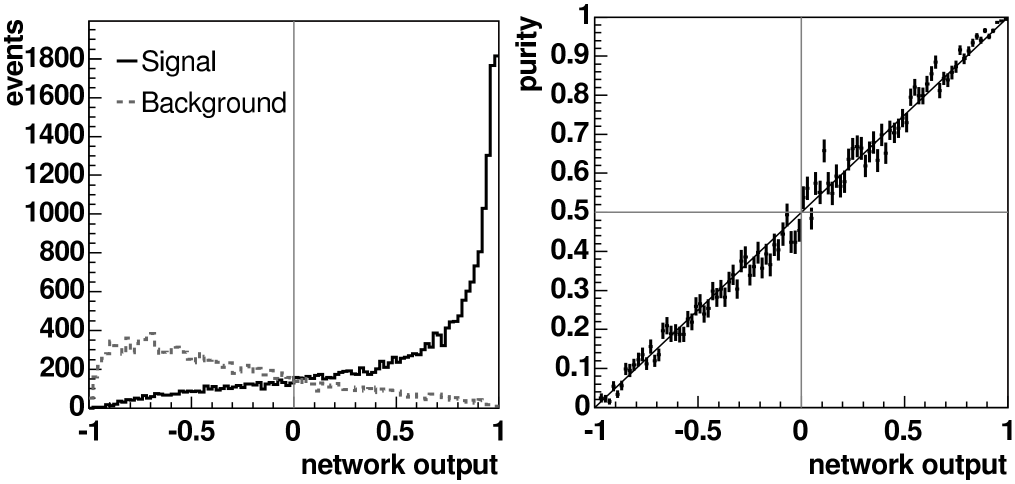

Figure 4.11: Left: Neural network flavor separator output for b-jets signal and non b-jets background. Right: shows the signal purity versus the Neural Network b-tag output and illustrates the expected linear dependence [61].

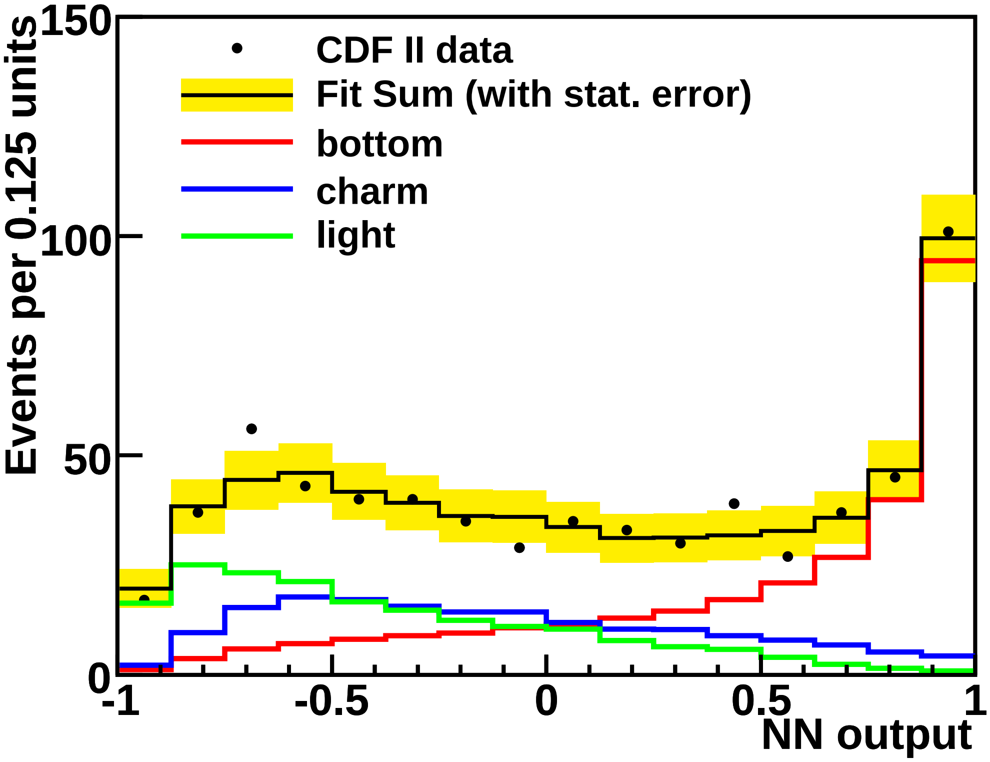

Figure 4.12: Fit of the Neural Network flavor separator output templates to the observed output distribution. The output of the b-tagged jet with the largest $\not{E}_T$ is used. The uncertainty on the fit result is statistical only.

Chapter 5

Signal and Background Simulation

Particle physics analyses are statistical in nature. To perform an analysis we need to produce millions of simulated events in order to understand the behavior of different physics processes. There are several physics processes which can mimic the signal signature, and thus need to be considered as potential background. We use a variety of Monte Carlo generators to simulate signal and background events. In this chapter we give an overview of the signal and background signatures that are used in this analysis with a previous explanation of the Monte Carlo generators to model the signal and background samples.

5.1 Monte Carlo Simulation

Standard Model processes are modeled using simulated events from several Monte Carlo (MC) generators which are then passed through the full `GEANT3` [63] based CDF II detector simulation. Simulation is essential to be able to predict the composition of the final state distributions and the contributions of not-yet-observed processes. The understanding of acceptances, efficiencies and backgrounds relies on detailed simulation of physics processes and detector response.

The description of a typical high-energy event is as follows:

- Parton Distribution Functions: initially two beam particles are coming in towards each other. Each particle is characterized by a set of parton distributions, which describe the probability to find a parton inside a beam particle, with the parton carrying a fraction of the total momentum. Actually, parton distributions also depend on some momentum scale Q^2 that characterizes the hard process.
- Generation of the initial-state partons: one shower initiator parton from each beam starts off a sequence of branchings.
- One incoming parton from each of the two showers enters the hard process, where then a number of outgoing partons are produced (usually two). It is the nature of this process that determines the main characteristics of the event.

- Generation of the parton level final state: the outgoing partons may branch, just like the incoming did.
- In addition to the hard process considered above, further semihard interactions may occur between the other partons of two incoming hadrons.
- Fragmentation: the outgoing partons, quarks and gluons, are not observable, but instead fragment to colour neutral hadrons.
- Hadronization: most of the hadrons produced during the fragmentation are unstable particles and decay to final and stable particles, jets (see Figure 4.1), which finally deposit their energy in the detector.

5.1.1 Event Generators

An event generator can be used in many different ways. We typically used it as a tool to optimize the signal to background conditions and as a method to calculate the detector corrections that have to be applied to data. The event generators used in this analysis are described below.

Signal Generator

The signal Monte Carlo is generated using `PYTHIA v6.2` [64] as are several of the background processes. The `PYTHIA` Monte Carlo is a general-purpose event generator. This generator employs leading order matrix elements for the hard parton scattering. The generator is used with the `CTEQ5L` parton distribution functions (PDF) [65]. The program is intended to generate complete events. It is used to perform the parton shower and hadronization.

Background Generators

Estimates of backgrounds from W and Z bosons produced in association with jets are derived using the `ALPGEN` generator [66]. The advantage of using `ALPGEN` is that it models accurately events with multiple jets. It is designed specifically for processes whose final state contains an electroweak boson and several radiated quarks and gluons, a major background in this analysis.

The backgrounds from electroweak (WW, ZZ, and WZ) and top pair ($t\bar{t}$) processes are studied using `PYTHIA`, and the single top production uses `MADEVENT` [67], designed to produce events at parton level. It is used for diagrams in which the polarization of the top quark is an important part of the event kinematics. The top mass is assumed to be 175 GeV/c^2 in the modeling of both $t\bar{t}$ and the single top production.

The QCD multijet background is not modeled using events generated by Monte Carlo, the model is based on data events.

5.1.2 Parton Showering and Hadronization

All events are passed to `PYTHIA` for a parton showering, to simulate gluon radiation, and hadronization effects. The showering procedure generates initial- and final-state gluon radiation for each event and allows them to decay to quark pairs, increasing the number of particles in the final state of the event. More particles may be added from effects of beam remnants or multiple interactions. This gives the final set of particles that are passed to the hadronization routine.

Since the hadronization of quarks and gluons, which describes the formation of jets, takes place at low Q^2 and large α_s, perturbation theory cannot be applied. The phenomenologic models, used to describe hadronization in the absence of any firm theoretical understanding are different for distinct Monte Carlo generators.

Table 5.1 summarized the Monte Carlo programs used to generate events for signal and background processes.

Process	Generator
WH	`PYTHIA`
Dibosons	`PYTHIA`
$t\bar{t}$	`PYTHIA`
W/Z+jets	`ALPGEN`+`PYTHIA`
single top	`MADEVENT`+`PYTHIA`

Table 5.1: Monte Carlo generators used for signal and background processes

5.1.3 Detector Simulation

The CDF II detector simulation reproduces the response of the detector and uses the same detector geometry database as the event reconstruction. Particle interactions through matter are performed with `GEANT3` [63]. Charge deposition in the silicon detectors is calculated using a simple geometrical model based on the path length of the ionizing particle and an unrestricted Landau distribution. The drift model for the COT uses a parametrization of a `GARFIELD` [68] simulation with parameters tuned to match COT collider data [44]. The calorimeter simulation uses the `GFLASH` [69] parametrization package interfaced with `GEANT3`. No parameterization is used in the muon system. More details on the CDF II simulation can be found in reference [70].

5.1.4 Monte Carlo Validation

One of the responsabilities I had, was to check the Monte Carlo samples for the top group after they were regenerated using a new detector simulation or other MC generator, making sure everything was in good shape and the differences were understood. This tool is still available, thanks to it, a few bugs were detected on time to be fixed before making the samples available.

Hundreds of plots are produced per sample, and are carefully checked. The distributions are, for example, event quantities, track, jet, and lepton information like the missing transverse energy, number of tracks, electrons, muons, and jets per event, the p_T of the tracks, the impact parameter (d_0), number of silicon hits, etc.

Since this analysis is highly reliant on Monte Carlo simulation we need to validate that Monte Carlo samples correctly model the data. In order to do that we compare the signal and background Monte Carlo modeling versus the observed data. This comparison is done for all the kinematic varaibles used in this analysis (Appendix C and Appendix D) and for other related variables after we estimate the contribution before and after requiring any b-tagging.

5.2 Signal Samples

The process discussed in this thesis is $WH \rightarrow l\nu b\bar{b}$. In this channel the Higgs boson is produced via associated production with a W boson. The Higgs is assumed to decay into a b-quark pair, the W boson into a charged lepton and a neutrino as mentioned in section 2.2.3 when searching for a low mass Higgs boson. The leading order Feynman diagram is shown in Figure 5.1.

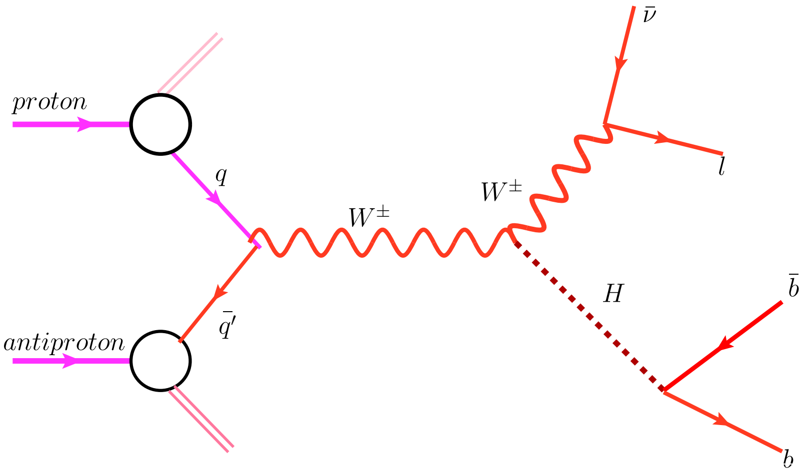

Figure 5.1: Feynman diagram of the W-Higgs production.

The final state for WH is made of two b-quarks (b and $\bar{b}$), a neutrino, and a charged lepton. In this analysis the charged lepton can be an electron or a muon, a tau can only be detected in the case it decays to an electron or a muon. Events with this final state form the so called lepton+jets sample.

Signal samples are generated for $100 < m_H < 150$ GeV/c^2 in 5 GeV/c^2 increments using `PYTHIA`. In `PYTHIA` the Standard Model Higgs production, where the Higgs is reasonably light and narrow, can be considered as a resonance. A list of the cross section (σ) at each mass point can be seen in Table 5.2.

Higgs Mass (GeV/c^2)	$\mathcal{BR}$ ($H \rightarrow b\bar{b}$)	σ (pb)	σ x $\mathcal{BR}$ ($H \rightarrow b\bar{b}$) (pb)
100	0.812	0.286	0.232
105	0.796	0.253	0.201
110	0.770	0.219	0.169
115	0.732	0.186	0.136
120	0.679	0.153	0.104
125	0.610	0.136	0.083
130	0.527	0.120	0.063
135	0.436	0.103	0.045
140	0.344	0.086	0.030
145	0.256	0.078	0.020
150	0.176	0.070	0.012

Table 5.2: SM branching ratios ($H \rightarrow b\bar{b}$) and cross sections for all Higgs masses

5.3 Background Samples

There are two types of backgrounds: physical processes, which are modeled by Monte Carlo (MC), and instrumental backgrounds. The background candidates are dominated by W-boson production, $Wb\bar{b}$, $Wc\bar{c}$, and Wc production, called W+heavy flavor. Other background candidates considered in this analysis are top pair production ($t\bar{t}$), single top production (s-channel and t-channel), Z+jets, and dibosons.

The instrumental backgrounds originate from mis-tagged W+jets events (W events with light-flavor jets, i.e. with u, d, s-quark and gluon content, misidentified as heavy-flavor jets) and from non-W events (QCD multi-jet events where one jet is erroneously identified as a lepton), predicted from data.

All the background processes considered in this analysis are given in Table 5.3 along with their theoretical cross sections. The diboson cross sections are taken from the NLO calculations with MCFM [71]. For the Z+jets background, the CDF inclusive $Z \rightarrow l^+l^-$ cross section measurement is used [72]. Predictions based on NLO calculations are also used for the $t\bar{t}$ and single top backgrounds [73] [74]. The W+jets and non-W background cross sections are obtained from the data. For a detailed discussion of the background estimation see Chapter 6.

Process	Theoretical Cross Section (pb)
s-channel	0.88 ± 0.11
t-channel	1.98 ± 0.25
WW	11.66 ± 0.7
WZ	3.46 ± 0.3
ZZ	1.51 ± 0.2
$t\bar{t}$	6.7 ± 0.8
Z+jets, Z$\rightarrow e, \mu, \tau$	787.4 ± 85
W+jets	-
non-W	-

Table 5.3: Background Monte Carlo samples and theoretical cross sections. The W+jets and non-W cross sections are obtained from the data.

5.3.1 W+jets

The largest background contribution to the signal is W+jets events which have the same final state as the WH sample and a much larger cross section. W+jets production are simulated using a combination of `ALPGEN` matrix element generation and `PYTHIA` parton showering.

This background consists of a real W boson in association with either quarks or gluons. The gluon can split into a pair of heavy flavor quarks producing W + heavy flavor events ($Wb\bar{b}$, $Wc\bar{c}$, Wc) or it can happen that the gluon or the initial quark hadronizes into a jet which is mis-tagged producing W + light flavor mistag events.

The W+jets samples are generated with a specific number of partons in the matrix element; for example, the $W+b\bar{b}$ contribution includes samples with $W+bb+0p$, $W+bb+1p$, and $W+bb+2p$. In order to get the total $W+b\bar{b}$ contribution, we must add up these three subsamples. However, we must avoid double-counting, since it is possible that additional jets can be created during the parton shower, so overlaps are removed following the MLM prescription [75]. As an example of the W+jets processes, a couple of Feynman diagrams are shown in Figure 5.2.

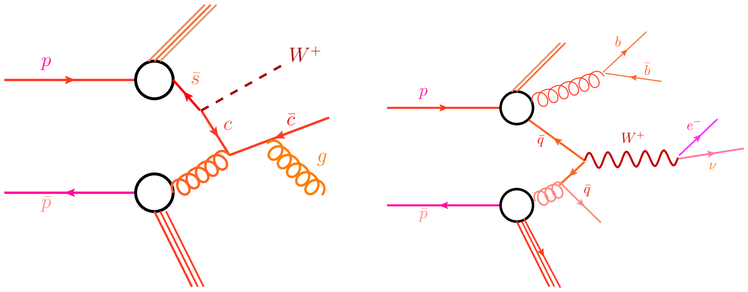

Figure 5.2: Feynman diagrams of the Wc (left), and $Wb\bar{b}$ (right) production.

Similarly, because heavy flavor can be produced in the parton shower of W+light events or light flavor jets can be produced in the parton shower of $Wb\bar{b}$, $Wc\bar{c}$, and Wc, we also must order the flavors using a jet-based heavy flavor overlap removal algorithm [76]. After the overlap removal, the subsamples are then added together (W+bottom, W+charm, and W+light) with each subsample weighted by the cross section for that subprocess times the acceptance.

5.3.2 Top Pair Production

For $t\bar{t}$ production simulated events generated with `PYTHIA` are used. Events of $t\bar{t}$ production contribute as background candidates in the case that one W boson decays leptonically, to a lepton and a neutrino, and the decay products of the other W are lost due to detector acceptance. The leading order Feynman diagram is shown in Figure 5.3.

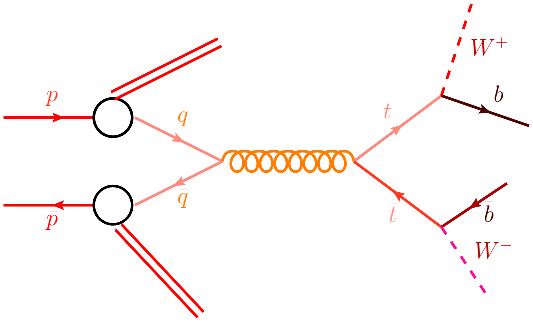

Figure 5.3: Feynman diagram of the $t\bar{t}$ production.

The contribution of $t\bar{t}$ events in the lepton+jets sample increases in the 3 and 4 jet bin compared with the 2 jet bin, as shown in Figure 5.4, and in the final background estimate tables, Tables 6.2 and 6.3.

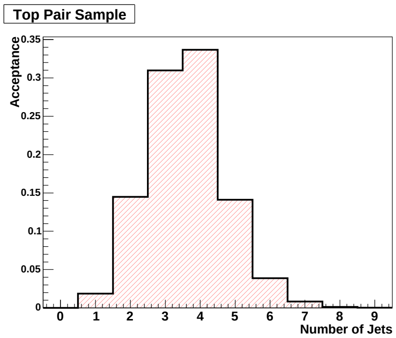

Figure 5.4: Acceptance of $t\bar{t}$ events as a function of jet multiplicity.

5.3.3 Single Top Production

The final state of single top production events have a W boson that decays leptonically like the top pair production explained above, and two quarks, at least one of them is a b-quark (two in the s-channel). The events are generated using `MADEVENT`, but the parton showering is done with `PYTHIA`. Both single top contributions, s-channel and t-channel (see Feynman diagrams in Figure 5.5), are considered in this analysis.

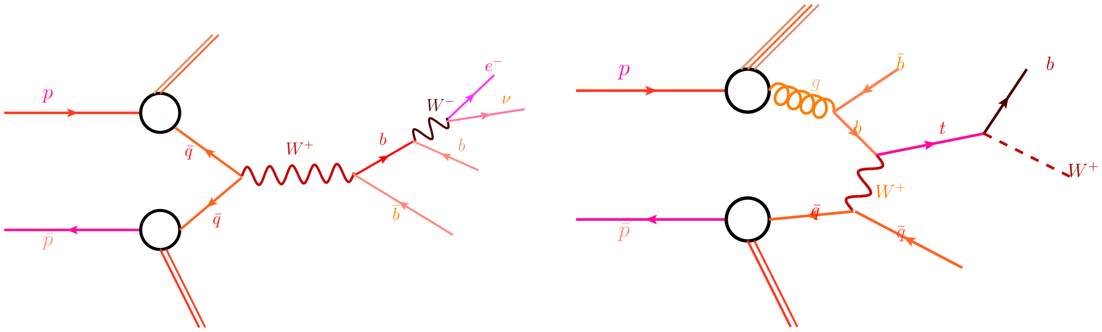

Figure 5.5: Feynman diagrams of the s-channel (left), and t-channel (right) production.

5.3.4 Z+jets Production

Z+jets production is simulated using a combination of `ALPGEN` matrix element generation and `PYTHIA` parton showering (same as for W+jets events). Z+jets candidates only contribute when one of the two leptons, from the Z boson, is lost to detection, see Figure 5.6.

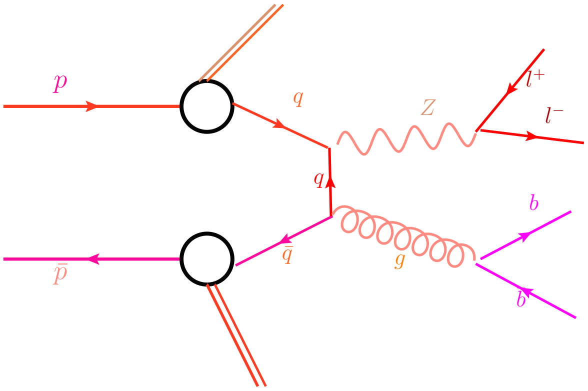

Figure 5.6: Feynman diagram of the Z+jets production.

5.3.5 Disoson Production

The electroweak disobon samples are WW, WZ, and ZZ. The events are generated with `PYTHIA`. In WW and WZ events, the W boson decays to a lepton and a neutrino and the other W boson and the Z boson decay hadronically, to two quarks. However, ZZ events happen to have a Z boson decaying to two quarks and a Z boson that decays to a lepton and the other lepton is lost like in Z+jets events. Feynman diagrams are shown in Figure 5.7.

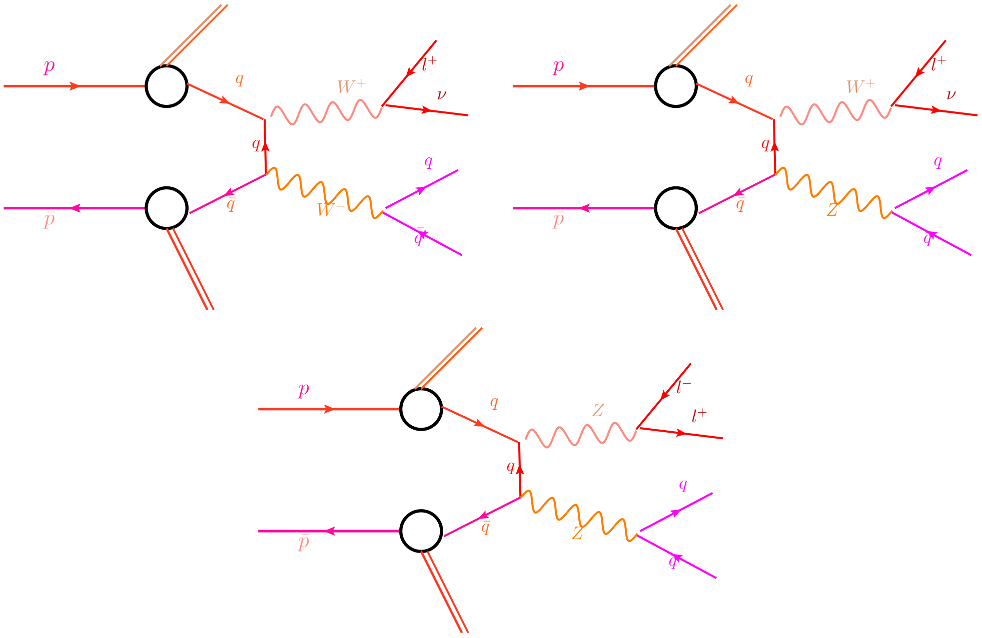

Figure 5.7: Feynman diagrams of the WW (top left), WZ (top right), and ZZ (bottom) production.

5.3.6 non-W QCD Multi-jet

The only background process that is not modeled by Monte Carlo is the non-W QCD. We use a non-W model based on data events. These background events arise when the events do not contain a real W boson. These non-W events come from direct $\bar{b}b$ production, a lepton from a semileptonic b decay or from strong gluon production, when a jet is erroneously identified as an isolated lepton, see Feynman diagrams in Figure 5.8. For details on the estimation of this background see section 6.5.

We use different types of non-W model for central leptons events, for forward electrons and for extended muons events. Three types of data events are used for these models: anti-electrons, jet-electrons, and non-isolated muons.

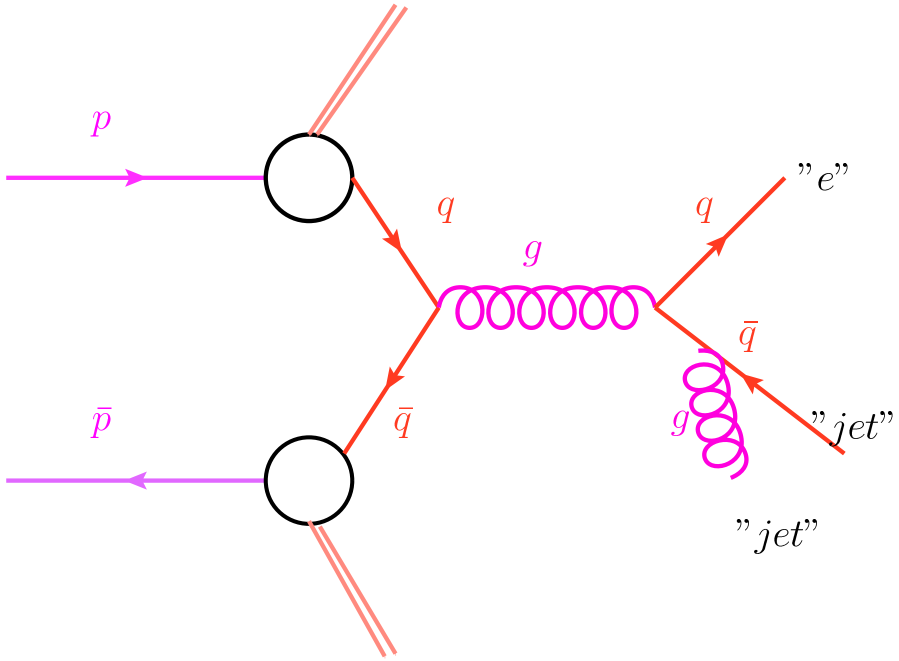

Figure 5.8: Feynman diagram for non-W QCD production.

- Anti-electron events come from the central electron sample (6.1.1): events where a jet fired the electron trigger, passed the electron kinematic cuts, but failed two of the cuts on these variables: E_{HAD}/E_{EM}, χ^2, L_{shr}, $Q \cdot \Delta x$, and $|\Delta z|$. All the electron cuts are summarized in Table 4.1.
- Jet-electrons are events that pass a generic jet trigger where one jet looks similar to an electron. They must have a transverse energy $E_T > 20$ GeV and a fraction of energy deposited in the electromagnetic calorimeter between 80% and 95%. The jet is also required to have at least four tracks, effectively removing events that may have a real electron.
- Non-isolated muons pass the MET+jets trigger (6.1.5) and contain a muon passing all identification requirements but fails the isolation requirement. The isolation is the ratio of the transverse energy surrounding the muon to the transverve energy of the muon.

There are also a number of samples needed to evaluate our systematic uncertainties where various parameters have been changed to reflect our uncertainty in modeling a particular aspect of WH events; these are discussed in more detailed in Chapter 8.

5.4 Kinematics

A set of varibales have been chosen to compare the different kinematic distributions in the lepton+jets sample for signal and background processes. Figure 5.9 shows some of the variables that describe the events like the corrected jet energy, jet η, lepton η, missing transverse energy for WH signal ($m_H = 115$ GeV/c^2), W+jets, Top ($t\bar{t}$, and single top), Z+jets, dibosons (WW, WZ, and ZZ), and non-W samples.

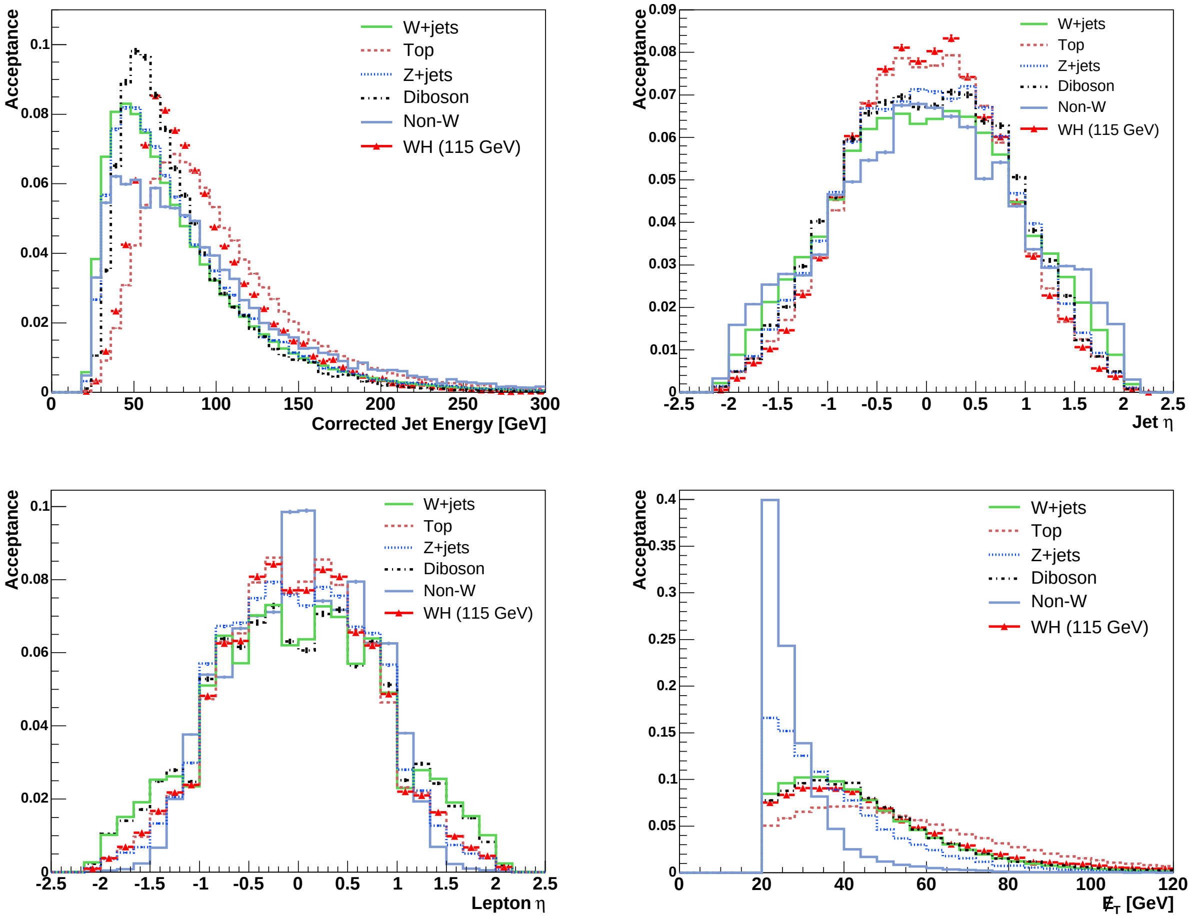

Figure 5.9: From top left to bottom right: corrected jet energy, jet η, lepton η, and missing transverse energy for WH signal $m_H = 115$ GeV/c^2 (red), W+jets (green), Top (maroon), Z+jets (blue), dibosons (black), and non-W (light blue) background processes. All histograms are normalized to unity. These plots show the different kinematic distributions between signal and background processes.

Chapter 6

Signal Event Selection and Background Estimation

The process $WH \to l\nu b\bar{b}$ is the most promising channel at the Tevatron in the search for the SM Higgs Boson at low mass (Higgs mass below 135 GeV/c^2). The leptonically decaying W causes a specific signature in the detector allowing to trigger the candidate events. The event selection is done in two steps: online and offline, both described in this chapter together with the background estimation method.

The method to estimate the backgrounds used in this analysis has been used for several published results, for example, $t\bar{t}$ cross section measurement [77], the single top search [62], and the measurement of the diboson production cross section [78].

6.1 Online Event Selection: Triggers

Candidate events for this analysis are selected by requiring a W + 2 or 3 jet event topology where the W decays leptonically, either to an electron $W \to e\nu_e$ or a muon $W \to \mu\nu_\mu$. To select this type of events this analysis uses two electron triggers, two muon triggers, one for the CMU and CMP detectors and the other for the CMX detector, and a missing transverse energy ($\not\!\!E_T$) trigger (MET+jets trigger).

Electron events are triggered by the high p_T CEM trigger as well as through the MET+PEM20 trigger. Muon events are triggered by the high p_T CMUP and CMX trigger. An additional trigger, which requires significant $\not\!\!E_T$ plus at least two high-p$_T$ jets, is also used to add candidate events with non-triggered leptons.

Each trigger is a composite of the three levels in the CDF trigger system see Section 3.11, with tighter requirements imposed at each level. The specific trigger requirements are given in the following sub-sections.

Because some triggers have prescales, and some have not been active for as long as others, the collected luminosity is different for each trigger. The luminosity for each trigger path is summarized in Table 6.1 .

Trigger	Integrated luminosity (pb^{-1})
Central electrons	4780.35
Plug electrons	4780.35
Central muons	4771.34
Forward muons	4727.11
Untriggered muons	4352.04

Table 6.1: Integrated Luminosity used by each trigger

6.1.1 CEM Trigger

The central electron trigger used is ELECTRON_CENTRAL_18. This trigger selects high-E_T electrons in the CEM detector.

The CEM trigger requires, at Level 1, a COT track with $\mathrm{p}_T > 8$ GeV/c, a calorimeter trigger tower with $\mathrm{E}_T > 8$ GeV, and a ratio of electromagnetic to hadronic energy $\mathrm{E}_{had}/\mathrm{E}_{EM} < 0.125$. At Level 2, the calorimeter clustering is performed, and the requirement is a cluster with $\mathrm{E}_T > 16$ GeV matched to a track with $\mathrm{p}_T > 8$ GeV/c. Finally, at Level 3, the final reconstructed transverse energy of the electron is required to be $\mathrm{E}_T > 18$ GeV with a matching track of $\mathrm{p}_T > 9$ GeV/c.

The effciency of this trigger is evaluated from a sample of W→ eν events requiring an electron and missing transverse energy. The CEM trigger is found to be about 96% efficient.

6.1.2 PHX Trigger

The plug electron trigger used is MET_PEM. The MET_PEM trigger is designed to trigger on events with a high-energy electromagnetic object in the forward calorimeter region, such as an electron or photon, and $\not\!\!E_T$.

The requirements for each trigger level are: at Level 1, requires at least a central or plug calorimeter cluster with $\mathrm{E}_T > 8$ GeV, $\mathrm{E}_{had}/\mathrm{E}_{EM} < 0.0625$, and $\not\!\!E_T > 15$ GeV. At Level 2, $\mathrm{E}_T > 20$ GeV, $\mathrm{E}_{had}/\mathrm{E}_{EM} < 0.125$, and $1.1 < |\eta| < 3.6$. Level 3 requirements are the same as in Level 2, but with fully reconstructed clusters and tracks.

To measure the efficiency of the calorimeter energy requirement, a sample of Z bosons that decay to electrons is used, with one electron triggered in the central electron trigger and the other detected in the plug calorimeter. Requiring that these electrons come from a Z boson makes this sample very pure. The average efficiency of this trigger is 94%.

Figure 6.1 shows the coverage of the CDF high p_T electron triggers in the $\eta - \phi$ plane, CEM and PHX events are shown in red and black, respectively.

6.1.3 CMUP trigger

The CMUP trigger is MUON_CMUP18 and it selects high-p_T muons in the CMU and CMP detectors. At Level 1, the CMUP trigger requires hits in both the CMU and CMP

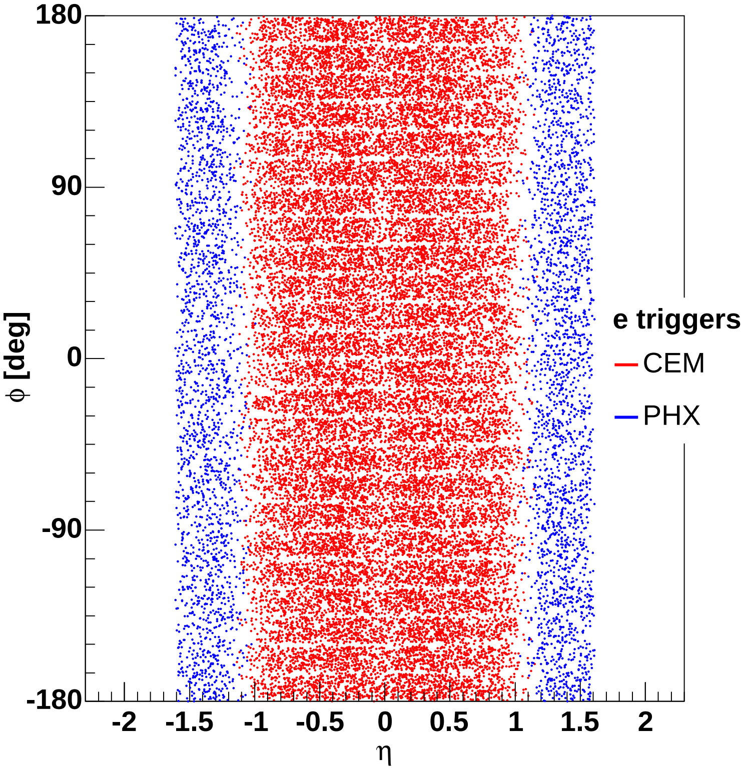

Figure 6.1: Coverage of the CDF high p_T electron triggers in the $\eta - \phi$ plane. CEM and PHX events are shown in red and black, respectively.

consistent with a muon of $p_T > 6$ GeV/c and a matching track with $p_T > 4$ GeV/c. At Level 2, the calorimeter cluster corresponding to the stubs must have an energy consistent with that of a minimum ionizing particle, and a track with $p_T > 15$ GeV/c. At Level 3, requires a COT track with $p_T > 18$ GeV whose extrapolation matches hits in the CMU and CMP detectors within a $\Delta x_{CMP} < 20$ cm (difference in x between the track and the cluster) and $\Delta x_{CMU} < 10$ cm.

In $Z \rightarrow \mu\mu$ events where one muon passes the trigger requirements, the second muon can be used to evaluate the trigger efficiency. The CMUP trigger is about 88% efficient. Similar to CEM events, the offline momentum threshold is raised to 20 GeV/c to avoid the effect of a trigger turn-on.

6.1.4 CMX trigger

The trigger for muons in the more forward CMX subsystem is MUON_CMX18_DPS. The CMX trigger selects high-p_T muons in the CMX detector. The CMX trigger operates very similarly to the CMUP trigger, but requires a track of $p_T > 8$ GeV/c at Level 1 matched to a CMX stub. The efficiency is about 91%.

6.1.5 EMC trigger (MET+jets trigger)

The trigger paths for the EMC trigger have been changed several times. The paths that we are using for this analysis are: MET35_&_TWO_JETS, MET35_&_CJET_&_JET, MET35_&_CJET_&_JET_LUMI_190, MET35_&_CJET_&_JET_DPS.

The basic selection of this trigger is two jets and at least 35 GeV of missing transverse energy. The trigger selection requirements at each level are: at Level 1, events with $\not\!\!E_T >$ 15 GeV, and calorimeter towers with $E_T >$ 1 GeV. At Level 2, there must be a calorimeter cluster with $E_T >$ 10 GeV, two or more jets, and it is also required the calorimeter towers with $E_T >$ 1 GeV. The Level 3 requirement is simply $E_T >$ 35 GeV.

Events passing this selection are required to fulfill a few offline selection criteria so that the trigger is fully efficient at Level 2: events must contain two jets with $E_T >$ 25 GeV, one must be central ($|\eta| <$0.9), and the distance between the two jets in $\eta - \phi$ space (ΔR) must be greater than 1.

Figure 6.2 shows on the left the coverage of the CDF high p_T muon triggers in the $\eta - \phi$ plane, CMUP and CMX coverage in green and blue; and on the right shows events with the muons, mentioned in Chapter 4, collected with the MET+jets trigger.

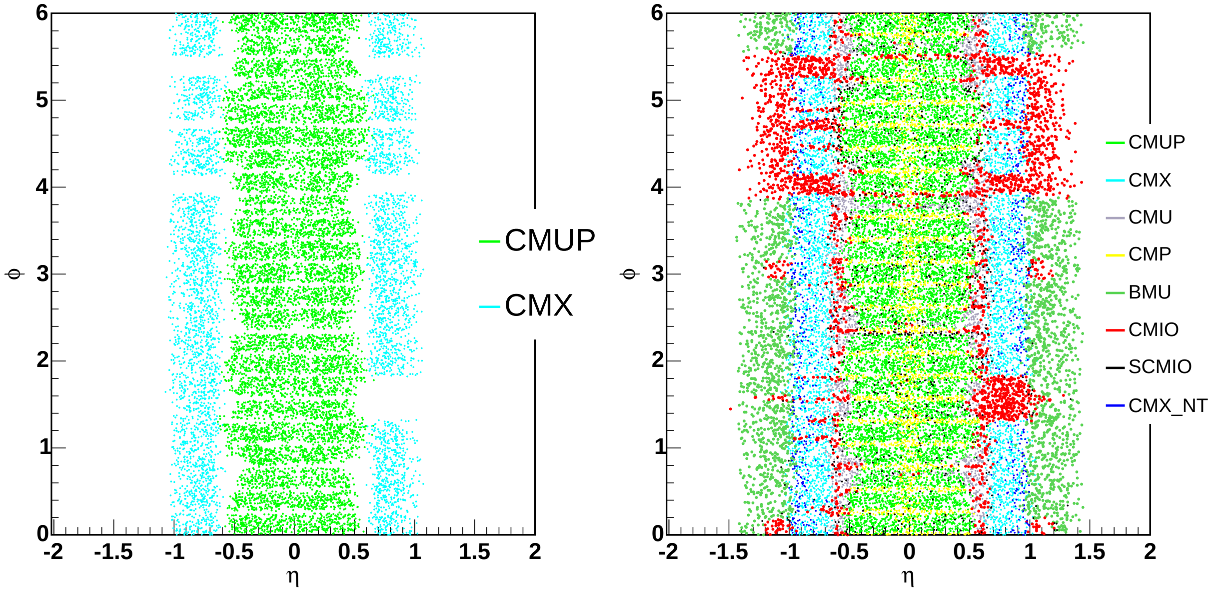

Figure 6.2: Left plot: coverage of the CDF high p_T muon triggers in the $\eta - \phi$ plane. CMUP and CMX coverage in green and blue. Right plot: includes the extended muon coverage (EMC) muons collected with the MET+jets trigger.

6.2 Offline Event Selection

We require events to contain an isolated electron or muon with offline transverse energy, $E_T > 20$ GeV, or transverse momentum, $p_T > 20$ GeV/c and $\not{E}_T > 20$ GeV (25 GeV for forward electrons).

WH events are expected to have two b-quarks forming jets. Jets are clustered with a cone size of $\Delta R < 0.4$ and are required to have $|\eta| < 2.0$ and $E_T > 20$ GeV after jet corrections. At least one of the tight jets should be identified as a b-jet using the secondary vertex (SECVTX) algorithm. If two or more jets are SECVTX tagged, we call the event SVSV; otherwise if only one jet is tagged by SECVTX but another one is tagged by JET PROBABILITY (5%), we call it SVJP; and, finally, if any other jet is tagged by SECVTX we call the event SVnoJP.

We veto:

- Dilepton events, events with more than one lepton.
- Z-boson events, events where the invariant mass of the lepton and a second track falls in the Z-boson mass window $76 < m_Z < 106$ GeV/c^2.
- Leptons from photon conversion events: electrons traversing the detector can emit photons due to bremsstrahlung radiation from the interaction with detector material. These photons can then convert to electron-positron pairs which are characterized by two tracks with a small opening angle and a vertex far from the primary interaction point. Events which contain such a conversion are identified and removed from the data sample.
- QCD multi-jet events: we use a rather tight QCD veto implementation which limits the amount of non-W QCD multi-jet events (see next sub-section).

6.2.1 QCD Veto

The implementation of the veto is described in detail in [79] and it is only applied to single tag (SVnoJP) events and all events with Phoenix electrons. Basically, we require:

- for central electrons (CEM):
  - $m_T(W) > 20$ GeV
  - METsig $\geq -0.05 \times m_T(W) + 3.5$
  - METsig $\geq 2.5 - (2.5/0.8) \times \Delta\phi(\not{E}_T,\text{jet2})$,
- for plug electrons (PHX):
  - $\not{E}_T > 25$ GeV
  - $m_T(W) > 20$ GeV, METsig > 2
  - $\not{E}_T > 45 - 30 \times \Delta\phi(\not{E}_T,\text{jet1})$

- $\not{E}_T > 45$ - $30\times\Delta\phi(\not{E}_T$,jet2)

- and for muons: $m_T(W) > 10$ GeV

where METsig is:

$$MET sig = \frac{\not{E}_T}{\sqrt{\sum_{jets} C^2_{JES}\ cos^2(\Delta\phi_{jet,\not{E}_T})\ +\ cos^2(\Delta\phi_{vtz,corr})}} \tag{6.1}$$

where C_{JES} is the jet energy correction factor, and $\phi_{vtz,corr}$ is the azimuthal angle between corrected and uncorrected missing transverse energy.

In order to estimate the remaining non-W background, we use the anti-electron and jet electron data samples for the tight leptons and non-isolated muons for the extended muon coverage (EMC), as described in 5.3.6.

6.3 Background Estimate Introduction

This method assumes that the lepton+jets data sample consists of electroweak, top (single top, and $t\bar{t}$), QCD multi-jet production (non-W), and W+jets processes. The first step is to calculate the Monte Carlo based (MC-based) processes. We use measured or theoretical cross sections, the integrated luminosity of our dataset, and Monte Carlo derived efficiencies (ε) to calculate each normalization. Electroweak, single top, and $t\bar{t}$ proccesses are the so called MC-based processes; their normalizations are calculated in this manner for both pretag and tagged samples:

$$N^i_{p\bar{p}\to X} = \sigma_{p\bar{p}\to X}\cdot\varepsilon\cdot\int dt\cdot\mathcal{L}. \tag{6.2}$$

The non-W QCD fraction is the next step. Of all processes in our sample, QCD is by far the least understood and the most poorly predicted. Because of this, a large uncertainty is assigned to the normalization of this process. We use a fit to the $\not{E}_T$ spectrum to estimate the fraction of our sample that is from entirely QCD processes. To get the normalization, the non-W QCD fraction is then simply applied to the amount of data in our signal region. This is also done in both pretag and tagged samples.

$$N^i_{QCD} = F_{QCD}\cdot N_i \qquad i = pretag\ or\ tag \tag{6.3}$$

Finally, what is not QCD, electroweak, or top is considered W+jets. In the pretag sample, we simply subtract the MC-based processes and the non-W QCD events from data and whatever is left is considered W+jets.

$$N^{pretag}_{W\ +\ Jets} = N_{pretag}\cdot(1 - F^{pretag}_{QCD}) - N^{pretag}_{ewk} - N^{pretag}_{top}. \tag{6.4}$$

6.4 MC-Based Background Estimate

Several electroweak processes and top processes contribute to the lepton+jets sample. They are WW, WZ, ZZ, Z+jets, $t\bar{t}$ and single top events. The numbers in our sample are estimated using the theoretical or measured (Z+jets) cross sections shown in Table 5.3, the integrated luminosity of our dataset, trigger efficiency, and an overall selection efficiency derived from Monte Carlo simulation of each processes. The calculated number in our sample is given by

$$N_{p\bar{p}\to X} = \sigma_{p\bar{p}\to X} \cdot \varepsilon_{event} \cdot \varepsilon_{tag} \cdot \int dt \cdot \mathcal{L} \tag{6.5}$$

where $\sigma_{p\bar{p}\to X}$ is the theoretical or measured cross section, $\int dt \cdot \mathcal{L}$ is the total integrated luminosity used in this analysis, ε_{event} is the selection efficiency, before requiring any tagging. ε_{event} is derived from Monte Carlo and includes the efficiency for lepton identification, triggers, the z vertex cut ($|z| < 60$ cm fiduciality), and all of the acceptance cuts. ε_{tag} is the tagging selection efficiency. For the pretag sample ε_{tag} is equal to one.

Because Monte Carlo simulations do not model tagging correctly, a tagging scale factor and mistag matrix must be integrated into the tagging efficiency calculation. Each event is then weighted by a probability of the event being tagged as opposed to using the Monte Carlo to count tags. The probability that an event is tagged is:

$$P^{tag}_{event} = 1 - \prod_{i}^{jets}(1 - p^{i}_{tag}). \tag{6.6}$$

For jets matched to heavy flavor p^{jet}_{tag} is the tagging scale factor if the jet is tagged and zero if it is not tagged. If the jet is matched to light flavor p^{jet}_{tag} is the mistag probability. The calculation of the tagging efficiency is shown in equation 6.7.

$$\varepsilon_{tag} = \frac{\sum_{j}^{events} P^{tag}_{j}}{N_{pretag}}. \tag{6.7}$$

The calculation for the tagging efficiency for double tags is performed with the same methodology only the combinatorics is slightly more complicated. The uncertainty in the normalizations from the tag scale factor and the mistag matrix are calculated by fluctuating these values by $\pm 1\sigma$ within the nominal values and then performing the entire procedure.

6.5 Non-W Background Estimate

To estimante the non-W fraction in both the pretag and tagged sample, we fit the $\not{E}_T$ spectrum in pretag and tagged data to a sum of the background $\not{E}_T$ shapes. The pretag non-W fraction is used to estimate the heavy flavor (W+Heavy Flavor) and light flavor (W+Light Flavor) fractions.

The fit of the $\not{E}_T$ distribution for CEM, CMUP, CMX, and EMC is performed from 0 to 120 GeV and from 15 to 115 GeV for PHX. The fit includes the region below the analysis $\not{E}_T$ cut, which is enriched in QCD events.

The fit has one fixed component and two templates whose normalizations can float. The fixed component is coming from the MC-based processes. The normalization of this template is explained above. The two floating templates are a Monte Carlo W+jets template and a non-W template. The non-W template is different depending on the lepton category and it is determined with data events as explained in Section 5.3.6: the anti-electron sample is used for CEM, CMUP, and CMX; the jet-electron sample is used for PHX; and the non-isolated muon sample is used for EMC.

The templates are fitted to the $\not{E}_T$ distribution of pretag and tagged data events using a binned likelihood fitter. Examples of these fits can be found in Figure 6.3 for pretag events and in Figure 6.4 for double tagged (SVSV) events, the arrow indicates the $\not{E}_T$ cut applied in this analysis. From the fits we extract the QCD fraction which is the fraction of QCD events that pass the $\not{E}_T$ cut over the number of data events that also pass the $\not{E}_T$ cut.

Once the QCD fraction is calculated the number of QCD multi-jet events is simply:

$$N_{QCD}^{pretag} = F_{QCD} \cdot N_{pretag} \tag{6.8}$$

for pretag events, and:

$$N_{QCD}^{tag} = F_{QCD} \cdot N_{tag} \tag{6.9}$$

for tagged events.

A conservative 40% uncertainty is taken on the QCD normalization.

6.6 W+jets Background Estimate

The W+jets normalization is calculated by subtracting the MC-based processes and the QCD events from data as shown in equation 6.4. In the tagged sample, W+jets is broken into two subcategories: heavy flavor and light flavor (mistags). Each of these processes produce a tagged jet very differently and therefore requires different treatment in calculating the normalization.

6.6.1 W+Heavy Flavor

The W+heavy flavor (W+HF) normalization is calculated by applying a data-corrected heavy flavor fraction ($F_{HF} \cdot K$) and a tagging efficiency to the W+jets pretag estimate. The contribution of this background to our signal region is calculated by equation 6.10.

$$N_{W+\,HF}^{tag} = (N_{pretag} \cdot (1 - F_{QCD}^{pretag}) - N_{ewk}^{pretag} - N_{top}^{pretag}) \cdot F_{HF} \cdot K \cdot \varepsilon_{tag}. \tag{6.10}$$

The number of events predicted in QCD, electroweak, single top, and $t\bar{t}$ are subtracted from the pretag sample, leaving an estimate for the number of events with a W-boson. The fraction of these events with jets matched to heavy flavor quarks, F_{HF}, is calculated from a detailed Monte Carlo simulation `ALPGEN` [66], which includes all possible processes contributing to the production of a single real W-boson. This fraction is corrected by a scale factor, K, which is a correction to the Monte Carlo heavy flavor fraction. The K-factor is calculated in the 1 jet bin and applied to the rest of the sample. ε_{tag} is the tagging efficiency as described in section 6.4. Only the heavy flavor fraction relies on Monte Carlo, the absolute normalization is derived from the pretag sample in data.

6.6.2 W+Light Flavor

Once we know the W+jets heavy flavor content and the normalizations for all the other processes, we can isolate the number of W+light flavor events in our pretag sample. A data-based mistag matrix is applied to the pretag data to calculate the fraction of W+light flavor events that will be mistagged (N_{-}/N_{pretag}). This fraction is applied to the W+light flavor pretag estimate to produce a normalization for the tagged sample. The predicted number of background events from W+light flavor (W+LF) processes is calculated by equation 6.11.

$$N^{tag}_{W\,+\,LF} = (N_{pretag} \cdot (1 - F^{pretag}_{QCD}) - N^{pretag}_{ewk} - N^{pretag}_{top} - N^{pretag}_{W\,+\,HF}) \cdot \frac{N_{-}}{N_{pretag}}. \tag{6.11}$$

The predicted amount of $t\bar{t}$, QCD, W+HF, electroweak, and single top background events is subtracted from the total pretag sample leaving an estimate for the W+LF fraction. The predicted number of mistagged W+LF events is the W+LF fraction multiplied by the predicted amount of mistag events in the pretag sample. The uncertainy on the mistag rate is calculated by re-performing this calculation with the mistag matrix values for each jet fluctuated within $\pm 1\sigma$ of the uncertainty.

6.7 Signal Estimate

As explained in section 5.2, the signal samples were generated for $100 < m_H < 150$ GeV/c^2 in 5 GeV/c^2 increments using `PYTHIA`. We estimate the expected number of signal events at each Higgs boson mass point using equation 6.12.

$$N_{p\bar{p}\to WH} = \sigma_{p\bar{p}\to WH} \cdot \mathcal{BR}\ (H \to b\bar{b}) \cdot \varepsilon_{event} \cdot \varepsilon_{tag} \cdot \int dt \cdot \mathcal{L} \tag{6.12}$$

where the $\sigma_{p\bar{p}\to X} \cdot \mathcal{B}\ (H \to b\bar{b})$ for each Higgs mass is given by Table 5.2, the rest of the terms where explained above, in section 6.4.

6.8 Event Yield Summary

The event yields using 4.8 fb^{-1} for events with 2 and 3 jets are shown in Tables 6.2 and 6.3, respectively. They include the contribution from the 3 b-tagging categories used in the analysis: SVSV, SVJP, and SVnoJP. Figure 6.5 shows the information from the tables given by one signal (m_H = 115 GeV/c^2) sample and all background samples compared to data.

Process	**SVSV**	**SVJP**	**SVnoJP**
All pretag. Cand.	103564	103564	91545
WW	0.76 ± 0.17	2.80 ± 1.10	90.48 ± 11.26
WZ	7.06 ± 0.99	5.29 ± 0.84	30.03 ± 3.34
ZZ	0.26 ± 0.04	0.22 ± 0.04	1.18 ± 0.18
$t\bar{t}$ lepton+jets	40.22 ± 6.64	32.17 ± 5.85	175.64 ± 24.36
$t\bar{t}$ dilepton	24.11 ± 3.93	17.07 ± 2.86	68.02 ± 9.39
t-channel	5.40 ± 0.93	5.36 ± 1.13	98.96 ± 14.25
s-channel	22.46 ± 3.67	15.72 ± 2.63	56.46 ± 7.82
Z+jets	3.63 ± 0.60	4.40 ± 1.12	68.34 ± 10.43
Total MC	**103.90 ± 13.09**	**83.02 ± 12.66**	**589.10 ± 50.94**
$Wb\bar{b}$	121.91 ± 39.11	103.40 ± 33.52	834.96 ± 251.86
$Wc\bar{c}$ / Wc	11.85 ± 4.05	39.08 ± 14.48	817.84 ± 252.20
Total HF	**133.75 ± 42.88**	**142.48 ± 46.99**	**1652.80 ± 502.04**
W+ LF	4.07 ± 1.30	16.10 ± 9.23	818.71 ± 119.41
Non-W	14.82 ± 5.93	25.91 ± 10.36	250.28 ± 100.11
Total Prediction	**256.55 ± 45.25**	**267.51 ± 50.60**	**3310.90 ± 528.13**
WH (100 GeV/c^2)	5.07 ± 0.59	3.53 ± 0.45	13.40 ± 1.06
WH (105 GeV/c^2)	4.70 ± 0.55	3.22 ± 0.41	12.08 ± 0.95
WH (110 GeV/c^2)	4.10 ± 0.48	2.85 ± 0.36	10.56 ± 0.83
WH (115 GeV/c^2)	3.47 ± 0.41	2.39 ± 0.30	8.79 ± 0.69
WH (120 GeV/c^2)	2.77 ± 0.32	1.92 ± 0.24	6.91 ± 0.55
WH (125 GeV/c^2)	2.27 ± 0.27	1.59 ± 0.20	5.64 ± 0.45
WH (130 GeV/c^2)	1.77 ± 0.21	1.23 ± 0.16	4.38 ± 0.35
WH (135 GeV/c^2)	1.28 ± 0.15	0.91 ± 0.11	3.16 ± 0.25
WH (140 GeV/c^2)	0.87 ± 0.10	0.61 ± 0.08	2.11 ± 0.17
WH (145 GeV/c^2)	0.60 ± 0.07	0.43 ± 0.05	1.45 ± 0.11
WH (150 GeV/c^2)	0.38 ± 0.04	0.27 ± 0.03	0.91 ± 0.07
Observed	**245**	**263**	**3313**

Table 6.2: Number of expected signal and background events, in the 2 jet bin, in 4.8 fb^{-1} of CDF data, passing all the event selection requirements

Process	**SVSV**	**SVJP**	**SVnoJP**
All pretag. Cand.	18858	18858	16406
WW	0.85 ± 0.17	2.24 ± 0.80	28.10 ± 3.38
WZ	1.94 ± 0.28	1.66 ± 0.30	8.03 ± 0.90
ZZ	0.16 ± 0.03	0.13 ± 0.03	0.50 ± 0.08
$t\bar{t}$ lepton+jets	160.58 ± 26.37	137.65 ± 24.83	430.84 ± 59.60
$t\bar{t}$ dilepton	21.72 ± 3.53	15.53 ± 2.63	49.19 ± 6.81
t-channel	4.76 ± 0.80	4.24 ± 0.78	22.37 ± 3.15
s-channel	7.59 ± 1.24	5.84 ± 0.99	16.67 ± 2.32
Z+jets	2.52 ± 0.43	3.43 ± 0.91	25.40 ± 3.73
Total MC	**200.12 ± 29.55**	**170.73 ± 28.66**	**581.10 ± 65.28**
$Wb\bar{b}$	41.69 ± 13.63	40.66 ± 13.52	220.65 ± 66.91
$Wc\bar{c}$ / Wc	6.10 ± 2.12	19.62 ± 7.36	202.17 ± 62.36
Total HF	**47.79 ± 15.56**	**60.28 ± 20.32**	**422.83 ± 128.42**
W+ LF	2.80 ± 0.93	9.48 ± 5.14	221.17 ± 32.72
Non-W	9.77 ± 3.91	17.78 ± 7.11	86.47 ± 34.59
Total Prediction	**260.48 ± 33.63**	**258.27 ± 36.21**	**1311.56 ± 151.72**
WH (100 GeV/c^2)	1.23 ± 0.14	0.94 ± 0.13	2.88 ± 0.23
WH (105 GeV/c^2)	1.21 ± 0.14	0.90 ± 0.13	2.76 ± 0.22
WH (110 GeV/c^2)	1.10 ± 0.13	0.83 ± 0.12	2.57 ± 0.21
WH (115 GeV/c^2)	0.99 ± 0.12	0.73 ± 0.10	2.20 ± 0.18
WH (120 GeV/c^2)	0.81 ± 0.09	0.61 ± 0.08	1.81 ± 0.15
WH (125 GeV/c^2)	0.69 ± 0.08	0.51 ± 0.07	1.54 ± 0.12
WH (130 GeV/c^2)	0.58 ± 0.07	0.42 ± 0.06	1.23 ± 0.10
WH (135 GeV/c^2)	0.43 ± 0.05	0.32 ± 0.04	0.93 ± 0.08
WH (140 GeV/c^2)	0.30 ± 0.04	0.22 ± 0.03	0.65 ± 0.05
WH (145 GeV/c^2)	0.21 ± 0.02	0.16 ± 0.02	0.46 ± 0.04
WH (150 GeV/c^2)	0.14 ± 0.02	0.10 ± 0.01	0.30 ± 0.02
Observed	**273**	**267**	**1271**

Table 6.3: Number of expected signal and background events, in the 3 jet bin, in 4.8 fb^{-1} of CDF data, passing all the event selection requirements

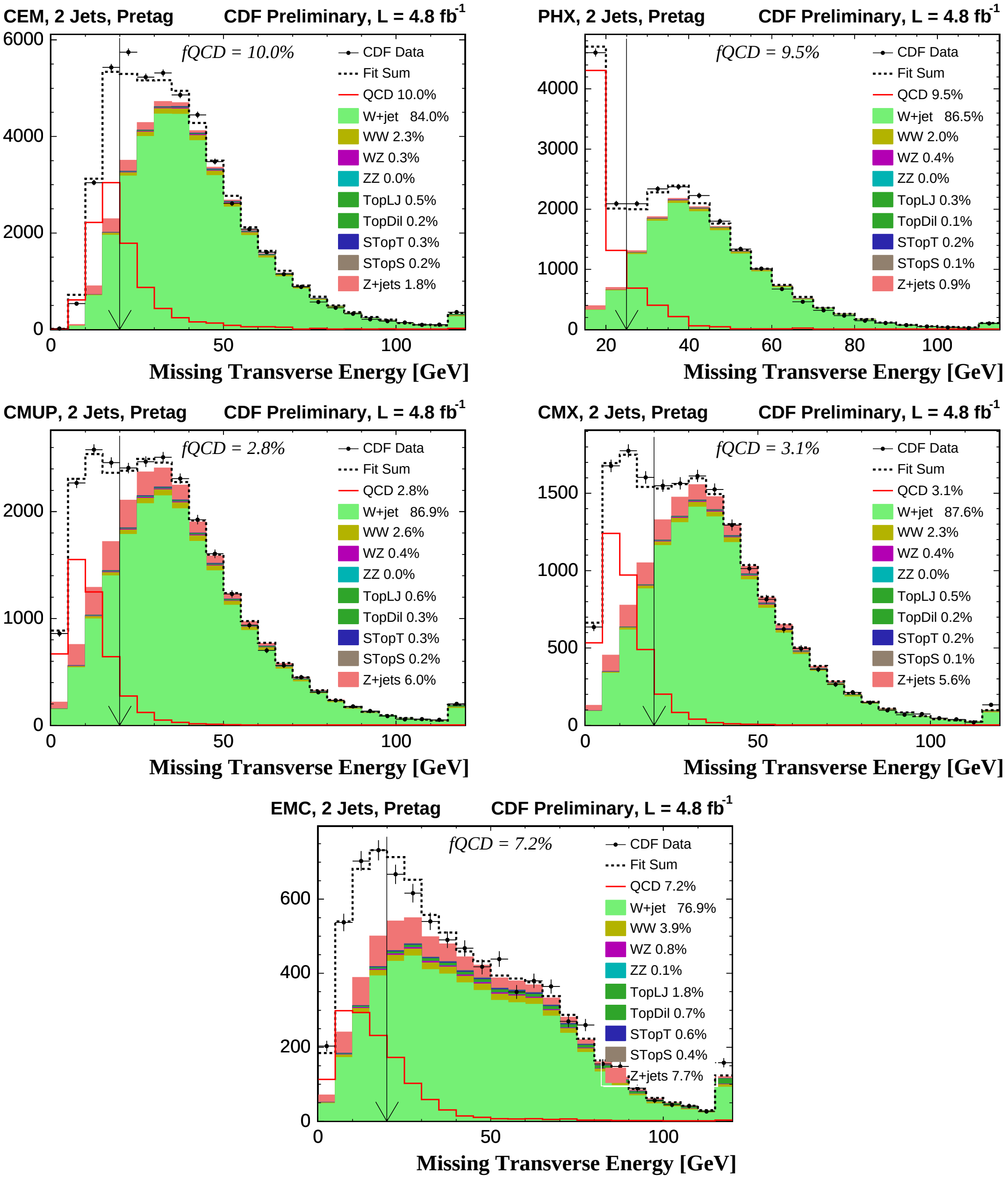

Figure 6.3: non-W QCD fits for pretag CEM, PHX, CMUP, CMX, and EMC events in the 2 jet bin. The QCD fraction is shown as fQCD inside the plot.

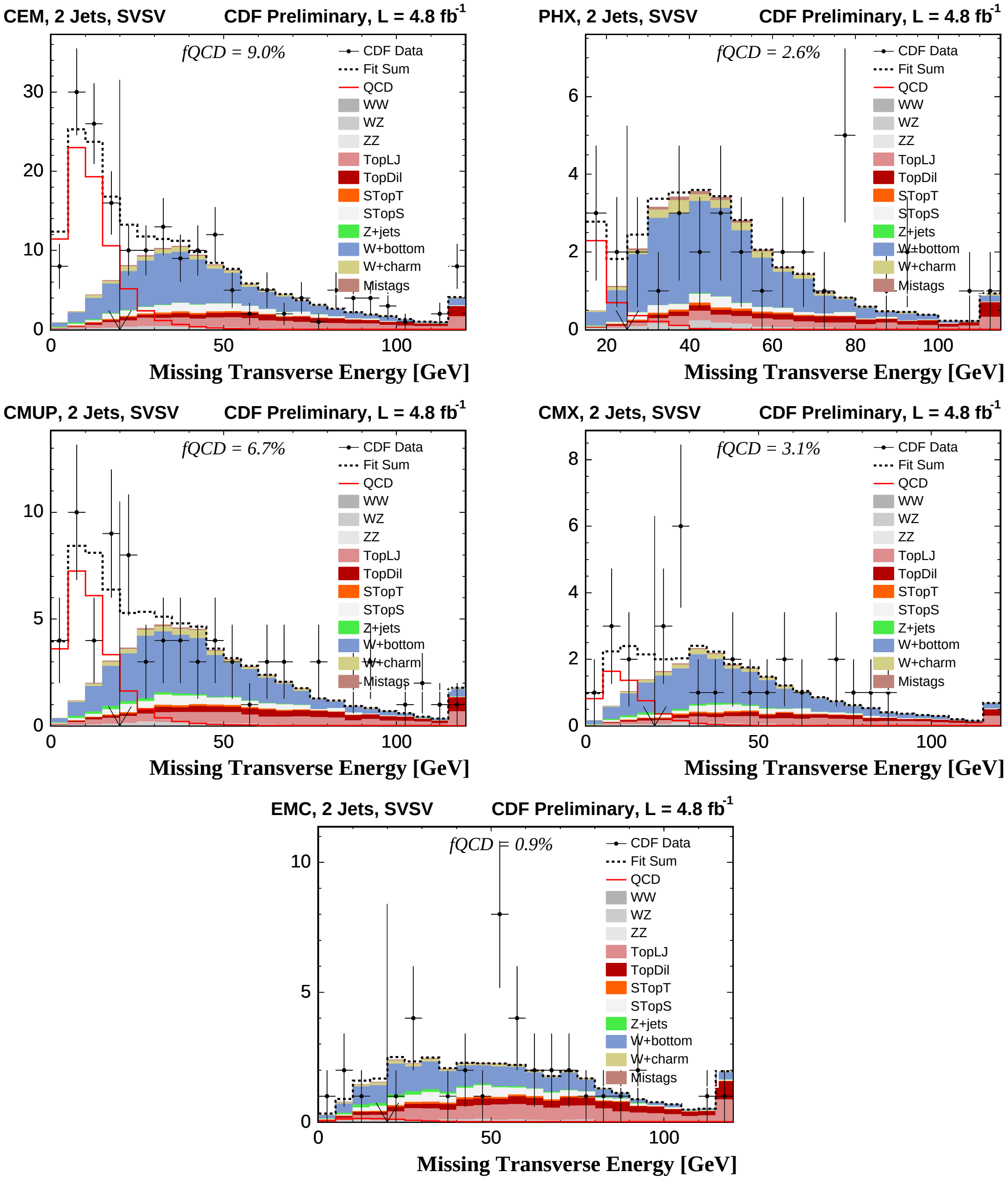

Figure 6.4: non-W QCD fits for SVSV CEM, PHX, CMUP, CMX, and EMC events in the 2 jet bin. The QCD fraction is shown as fQCD inside the plot.

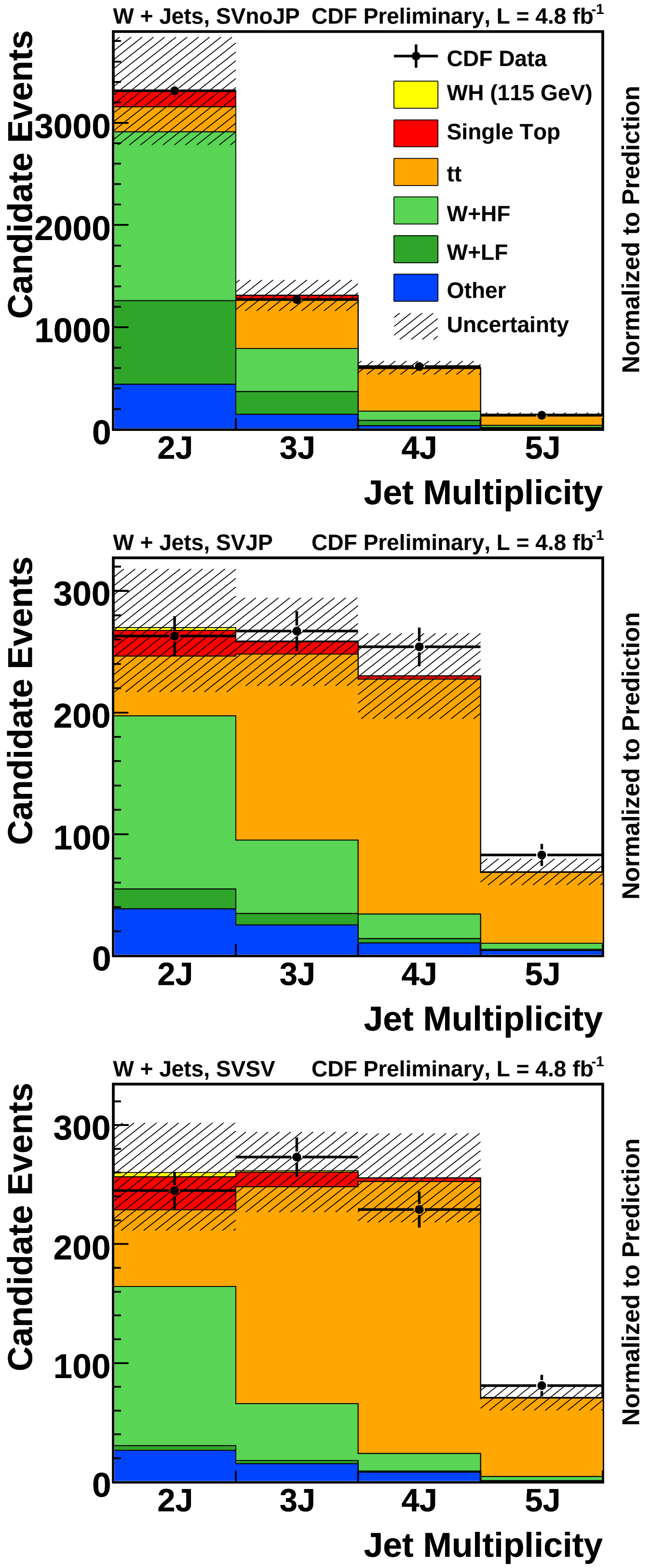

Figure 6.5: Jet multiplicity of SVnoJP (top), SVJP (middle), and SVSV (bottom) signal and background events compared with the CDF data.

Chapter 7

Matrix Element Method

Finding a Standard Model Higgs boson produced in association with a W boson is very challeging since it is rarely produced in comparison with other processes that have the same final state like, for example, W+jets events. As shown in Chapter 6, the signal to background ratio is really tiny, typically on the order of S/B∼1/400. Cases like this where the signal is much smaller than even the uncertainty on the background estimation, even counting experiments are not useful at all.

The invariant mass distribution of the two leading jets in the event, see Figure 7.1, is the most powerful variable in this analysis, but still a better discrimination of signal and background events needs to be used. This can be achieved by using more information to characterize each event.

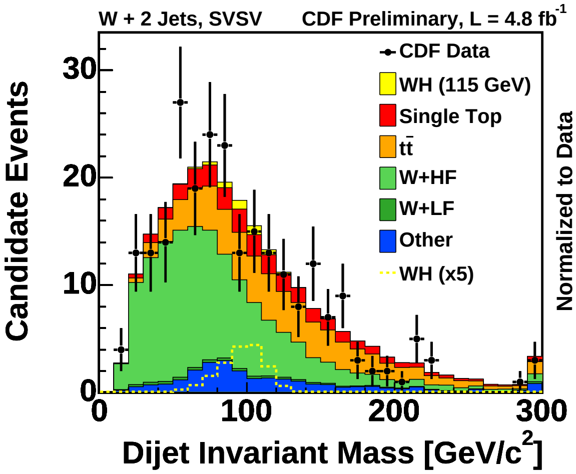

Figure 7.1: Invariant mass distribution of the two leading jets in W + 2jets SVSV events.

To distinguish the small amount of signal events from the overwhelming backgrounds, the analysis described here employs a matrix element technique which is used to calculate, for each event, event probability densities (commonly called event probabilities) for signal and background hypothesis. The ratio of signal and background event probabilities is then used as a discriminant variable. The goal is to maximize the use of all kinematic information contained in each event analyzed.

7.1 Event Probability Densities

The matrix element analysis relies on the evalution of the event probability densities for the signal and background processes based on the Standard Model differential cross-section calculation.

In general a differential cross-section is given by [7]:

$$d\sigma = \frac{(2\pi)^4|M|^2}{4\sqrt{(q_1 \cdot q_2)^2 - m_{q_1}^2 m_{q_2}^2}} \, d\Phi_n(q_1 + q_2; p_1, .., p_n) \tag{7.1}$$

where $|M|$ is the Lorentz invariant matrix element; q_1, q_2 and m_{q_1}, m_{q_2} are the four momenta and masses of the incident particles, and $d\Phi_n$ is the n-body phase space given by [7]:

$$d\Phi_n(q_1 + q_2; p_1, .., p_n) = \delta^4(q_1 + q_2 - \sum_{i=1}^{n} p_i) \prod_{i=1}^{n} \frac{d^3p_i}{(2\pi)^3 2E_i} \tag{7.2}$$

Since the CDF detector is not 'ideal', several effects have to be considered: the initial state interaction is initiated by partons inside the proton and antiproton, neutrinos in the final state are not identified directly, and the energy resolution of the detector can not be ignored. To address the first point, the differential cross section is folded over the parton distribution functions. To address the second and third points, we integrate over all particle momenta which we do not measure (e.g. p_z of the neutrino), or do not measure very well, due to resolution effects (e.g. jet energies). The integration reflects the fact that we want to sum over all possible particle variables (y) leading to the observed set of variables (x) measured with the CDF detector. The mapping between the particle variables (y) and the measured variables (x) is established with the transfer function, $W(y, x)$. After incorporating the effects mentioned above, the event probability can be written as:

$$P(x) = \frac{1}{\sigma} \int d\sigma(y) dq_1 dq_2 f(y_1) f(y_2) W(y, x) \tag{7.3}$$

where $d\sigma(y)$ is the differential cross section in terms of the particle variables; $f(y_i)$ are the particle distribution functions (PDFs), with y_i being the fraction of the proton momentum carried by the parton ($y_i = E_{q_i}/E_{beam}$); and $W(y, x)$ is the transfer function, explained in detailed in sub-section 7.1.1. Substituting Equation 7.1 and 7.2 into Equation 7.3, and considering a final state with four particles (n=4), the event probability becomes:

$$P(x) = \frac{1}{\sigma} \int 2\pi^4 |M|^2 \frac{f(y_1)}{|E_{q_1}|} \frac{f(y_2)}{|E_{q_2}|} W(y, x) d\Phi_4 dE_{q_1} dE_{q_2} \tag{7.4}$$

where the masses and transverse momenta of the initial partons are neglected (i.e. $\sqrt{(q_1 \cdot q_2)^2 - m_{q_1}^2 m_{q_2}^2} \simeq 2E_{q_1}E_{q_2}$).

The matrix element ($|M|^2$) for the event probability density at leading order perturbation theory are calculated by using the HELAS (HELicity Amplitude Subroutines for Feynman Diagram Evaluations) package [80]. The correct subroutines for a given process are automatically generated by the MadGraph program [81].

In this thesis, event probability densities for events with two and three jets in the final state are calculated.

Two jets final state

For events with two jets event probability densities for the WH signal, as well as for the s-channel and t-channel single top, $t\bar{t}$, $Wb\bar{b}$, $Wc\bar{c}$, Wcg, Mistags (Wgj, and Wgg) and diboson (WW, WZ) background processes are calculated. Figures in Appendix B show the different Feynman diagrams used for each channel.

Three jets final state

The WH channel is mainly procuded in two jet events, but it can happen that an ISR or FSR jet is identified as the third jet of the event. Including three-jet events add more acceptance and help to gain sensitivity in the final result. Figure 7.2 shows the acceptance of WH events as a function of jet multiplicity in the event.

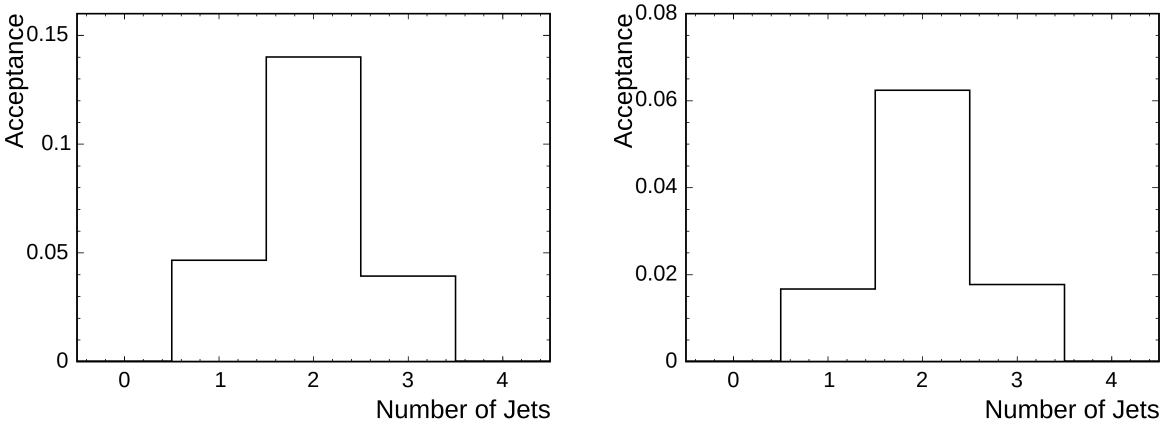

Figure 7.2: Acceptance of WH events as function of jet multiplicity. The plot on the left shows the sample before b-tagging requirements. The plot on the right shows the distribution with exactly one SecVtx tagged jet.

In the case of events with three jets in the final state we do not calculate the same event probabilities as in the two-jet events. For events with three jets, event probability densities for the WH signal, as well as for the s-channel and t-channel single top, $t\bar{t}$, $Wb\bar{b}$, and $Wc\bar{c}$ processes are calculated. The WH Feynman diagrams include only those with initial and final state radiation, and exclude those in which a ggh coupling is present as these contributes less than 1% to the total cross section, but increase the computation time by more than 20%. Figures in Appendix B show the different Feynman diagrams used for each channel with three jets in the final state.

7.1.1 Transfer Function W(y,x)

The transfer function, $W(y,x)$, provides the probability of measuring the set of observable variables (x) that correspond to the set of production variables (y). The set (y) represents all final state particle momenta at the particle level, while the set (x) represents the measured momenta (of the corresponding object) with the CDF detector. The general idea of the transfer functions is to introduce a relation between the parton level objects and the measured objects. In the case of well-measured objects, $W(y,x)$ is taken as a δ-function (i.e. the measured momenta are used in the differential cross section calculation). When the detector resolution cannot be ignored, $W(y,x)$ is taken as a Gaussian-type function. For unmeasured quantities, like the momenta of the neutrino, the transfer function is unity (the transverse momenta of the neutrino, however, can be inferred from energy and momentum conservation).

Lepton momenta are well-measured with the CDF detector and δ-functions are assumed for them (first factor of Equation 7.5). The jet angular resolution of the calorimeter is also well measured (on the order of $\sigma_{\Delta_R} \simeq 0.07$) and δ-functions are assumed for the transfer function of the jet directions (second factor of Equation 7.5). The resolution of the measured jet energies, however, is not negligible and the transfer function needs to be derived. Using these assumptions, $W(y,x)$ takes the following form for the four final state particles considered in the WH search (lepton, neutrino and two jets):

$$W(y,x) = \delta^3(\vec{p_l}^{\,y} - \vec{p_l}^{\,x}) \prod_{i=1}^{2} \delta^2(\Omega_i^y - \Omega_i^x) \prod_{j=1}^{2} W_{jet}(E_{parton_j}, E_{jet_j}) \tag{7.5}$$

where $\vec{p_l}^{\,y}$ and $\vec{p_l}^{\,x}$ are the produced and measured lepton momenta, Ω_i^y and Ω_i^x are the produced quark and measured jet angles, and E_{parton_j} and E_{jet_j} are the produced quark and measured jet energies.

The mapping between parton and jet energies is determined by the transfer function $W_{jet}(E_{parton}, E_{jet})$. The standard CDF jet energy corrections (see section 4.2) correct the energies of the jets in a way that the means of the corrected jet energies and the original parton energies are equal. Such corrections, however, do not account for the shape of the difference in energies: the shape of the $\delta_E = (E_{parton} - E_{jet})$ distribution. This distribution is asymmetric and features a significant tail at positive δ_E, as shown in Figure 7.3 for different flavor jets b, c, light jets and gluons.

The δ_E distribution is parameterized as a sum of two Gaussian functions: one to account for the sharp peak and one to account for the asymmetric tail:

$$W_{jet}(E_{parton}, E_{jet}) = \frac{1}{\sqrt{2\pi}(p_2 + p_3 p_5)} (exp\frac{-(\delta_E - p_1)^2}{2p_2^2} + p_3\ exp\frac{-(\delta_E - p_4)^2}{2p_5^2}). \tag{7.6}$$

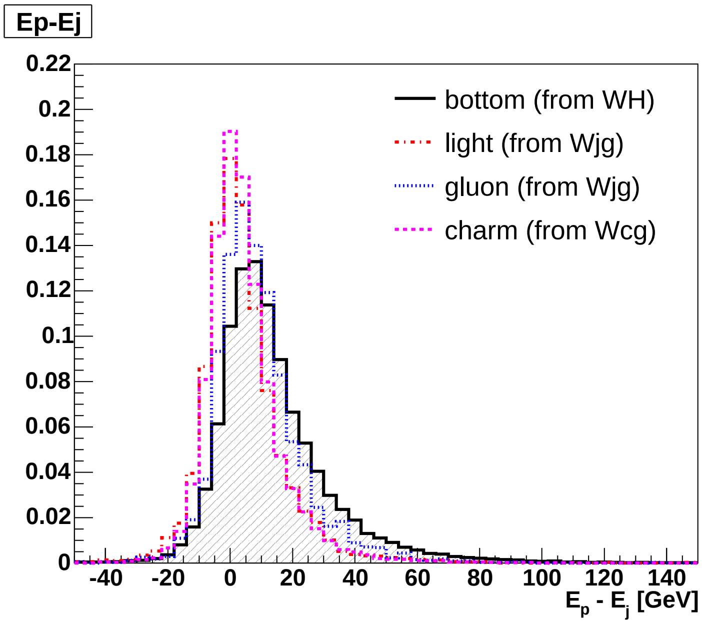

Figure 7.3: δ_E distribution for matched jets to partons in WH with a Higgs mass of 115 GeV (b-jets), W_{jg} (light-jets and gluons), and W_{cg} (c-jets) Monte Carlo events (passed through full detector simulation).

A study of the parameters p_i as a function of E_{parton} showed a linear dependence on E_{parton}, we therefore use a simple linear form as:

$$p_i = a_i + b_i E_{parton}. \tag{7.7}$$

A total of 10 parameters $(a_1, b_1, .., a_5, b_5)$ are therefore required to specify $W_{jet}(E_{parton}, E_{jet})$.

After specifying the transfer function, we can apply the general event probability of Equation 7.4 to the case of the WH analysis, but before getting into that, an explanation about the way to get the transfer function parameters is shown below.

Parameters for TF

The light, b, c jets, and gluons transfer funcions are parameterized in a different way due to the different kinematics as shown in Figure 7.3.

One of the novelties of this analysis is that, in order to better reproduce the real parton energy (E$_{parton}$), a neural network output (NN_{output}) is used instead of the measured jet energy (E$_{jet}$). So W(E$_{parton}$, E$_{jet}$) is substitued for W(E$_{parton}$, NN$_{output}$), it is commonly referred to Neural Network Transfer Function (NN TF).

The NN_{output} used in the analysis are the result of training 23 Neural Networks (NNs) using the Stuttgart Neural Network Simulator (SNNS) [82]. The SNNS is a neural network simulator developed at the University of Stuttgart since 1989 and maintained at the University of Tubingen. For this analysis an interface built at CDF allows us to create and train neural networks using ROOT Trees fed to SNNS (ROOTSNNS v3.0).

Each NN is trained for a different type of jet (b, c, light and gluons) and a different physic process (WH [100-150] GeV/c^2, $Wb\bar{b}$, $t\bar{t}$, s-channel, t-channel, $Wc\bar{c}$, Wcg, Wjg, Wgg, WW, and WZ) as shown in Table 7.1. Summing together the 11 Higgs masses and all the other physic processes makes a total of 23 NNs.

Process	b jets	c jets	light jets	gluons
WH (11 Higgs masses)	X			
$Wb\bar{b}$	X			
$Wc\bar{c}$		X		
$t\bar{t}$	X			
s-channel	X			
t-channel	X		X	
Wcg		X		X
Wjg			X	X
Wgg				X
WW-WZ			X	

Table 7.1: Type of jet used to train the different NNs for each process

The trainings of the NN$_{is}$ are based in MC events. The MC events used for the trainings are the remaining events after applying the analysis event selection (see Chapter 6) and matching the reconstructed jets to their corresponding partons. The partons are required to be aligned within a cone of $\Delta R < 0.4$ (radius used for the jets in the event selection) around the reconstructed jet-axes in order to be considered "matched". The events that have two partons matching to the same jet are removed, that only corresponds to a ~2% of the total number of events.

The most common type of artificial neural network consists of three layers of units: a layer of "input" units is connected to a layer of "hidden" units, which is connected to a layer of "output" units, as shown in Figure 7.4. The activity of the input units represents the raw information that is fed into the network. For this analysis seven input variables related to the jet kinematics are used. The activity of each hidden unit is determined by the activities of the input units and the weights on the connections between the input and the hidden units. The behaviour of the output units depends on the activity of the hidden units and the weights between the hidden and output units.

All the NN trainings have the same architecture; the same input variables, hidden layers and nodes, number of epochs, and learning function. Seven input variables related to the jet kinematics have been used:

- E$_j$ is the total energy of the jet corrected.
- SumE is the ratio between the sum of the transverse momentum of the tracks in the jet and the seno of the η of the tracks:

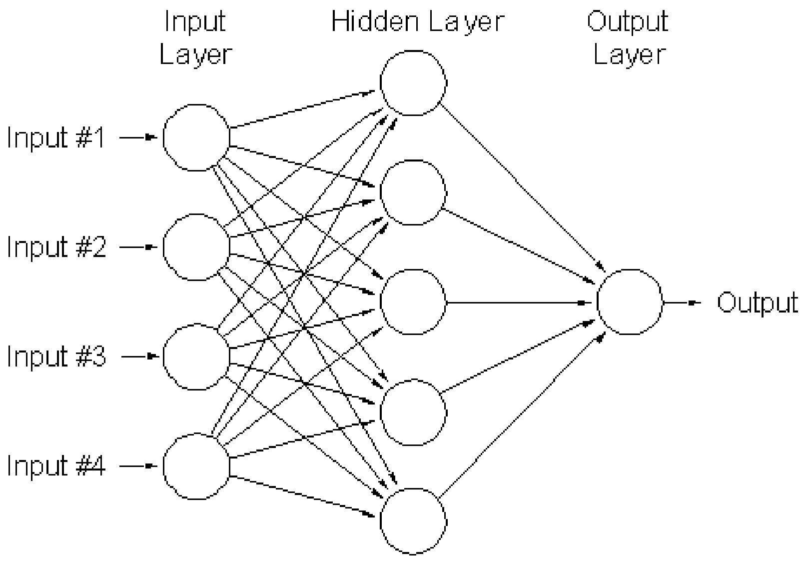

Figure 7.4: An example of a typical artificial neural netwrok architecture.

$$\text{SumE} = \Sigma^{tracks} \frac{p_{T\ track}}{sin(2 \cdot atan(e^{-\eta_{track}}))},\ \eta = -\tfrac{1}{2} \cdot ln(tan\ \theta) \Rightarrow \text{SumE} = \Sigma^{tracks} \frac{p_{T\ track}}{sin(\theta)}.$$

- p_T is the raw (measured) transverse momentum of the jet.
- ϕ is the azimuthal angle of the jet.
- η is the pseudorapidity of the jet.
- RawE_j is the raw (measured) energy of the jet.
- Ejcone7 is the energy of the jet corrected with cone size 0.7 (16% of the times there are no jets of cone size 0.7 available. In this case, the energy of the jet of cone size 0.4 is used).

Figure 7.5 shows the data-MC comparison of the seven input variables for the first leading jet in 2-jet events where at least one of the jet is tagged by SecVtx (see Section 6). The same distributions for the first leading jet in 2-jet untag events (event with 0 b-tags), and for the second leading jet in 2-jet untag and tagged events can be found in Appendix C.

For each training one hidden layer with 13 hidden nodes is used. The training is done over 900 epochs.

The NNs have one output variable that is an estimate of the parton energy (E_{parton}).

Figure 7.6 shows the difference between the parton energy and the measured jet energy corrected (black histogram) and between the parton energy and the NN_{output} (red solid histogram) for four different physic processes (WH, diboson (WW, WZ), $Wb\bar{b}$, and Wgg). It is clear that, in all cases, the NN_{output} is closer to the parton energy than the Level 5 corrected jet energies and that the distributions are also narrower. Therefore, since the

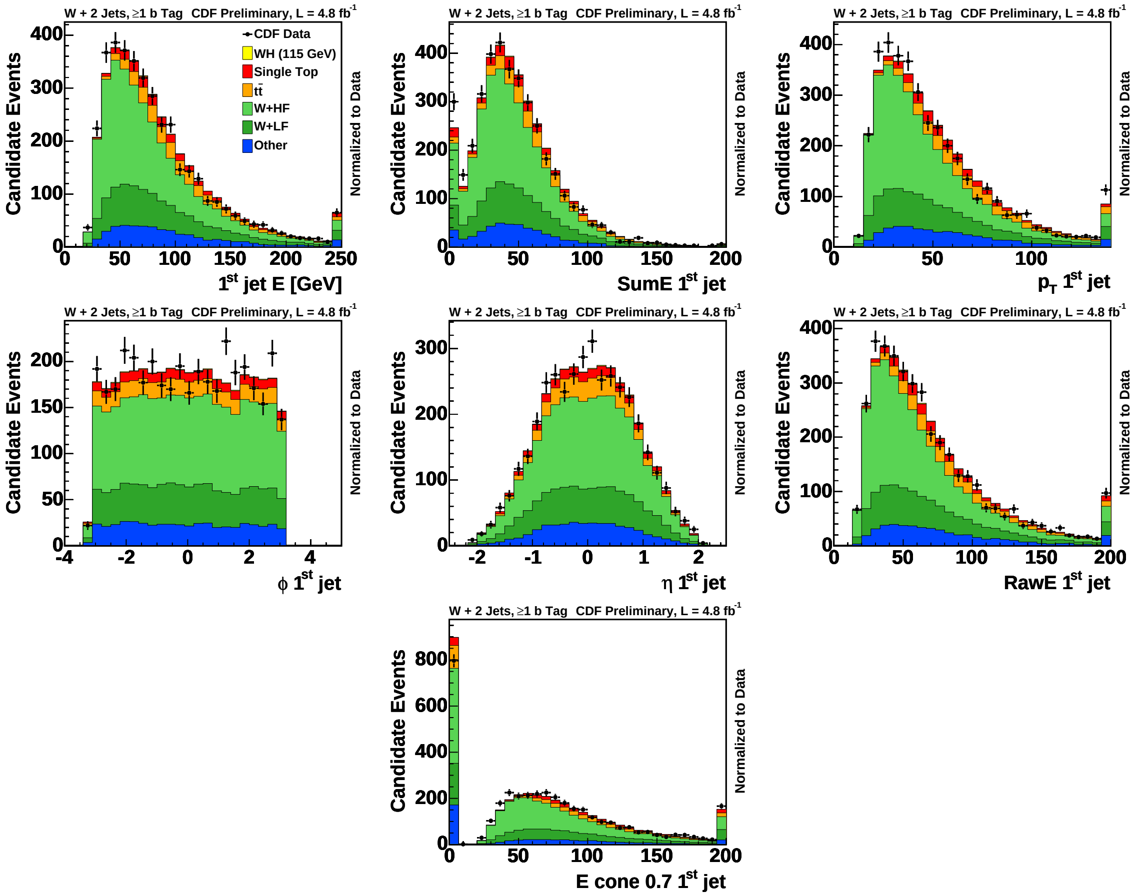

Figure 7.5: Data-MC comparison for the seven input variables used to train the NN for events with at least on SecVtx tagged jet.

NN$_{output}$ provides a better jet resolution, using it as input of the transfer function should help to improve the performance of the transfer function.

If n$(NN_{output}, E_{parton})dNN_{output}dE_{parton}$ is the number of jets with NN_{output} between NN_{output} and $NN_{output}+dNN_{output}$, and parton energies between E_{parton} and $E_{parton}+dE_{parton}$ in the sample, then

$$n(NN_{output}, E_{parton})dNN_{output}dE_{parton} = n(E_{parton})dE_{parton}W_{jet}(E_{parton}, NN_{output})dNN_{output} \tag{7.8}$$

where $n(E_{parton})dE_{parton}$ is the number of particles with an energy between E_{parton} and $E_{parton} + dE_{parton}$. The parameters of $W_{jet}(E_{parton}, NN_{output})$ are determined such to maximize the agreement in Equation 7.8. This is done performing an un-binned maximum likelihood fit to the selected events. More details can be found in [83] (Chapter 4.2).

The functional form used to parameterize δ_E is the same one described in Sect. 7.1.1, that is a sum of two Gaussian functions given by Eq. 7.6. The parameteres used for the NN TF of WH (m$_H$ = 115 GeV/c^2) can be found in Table 7.2.

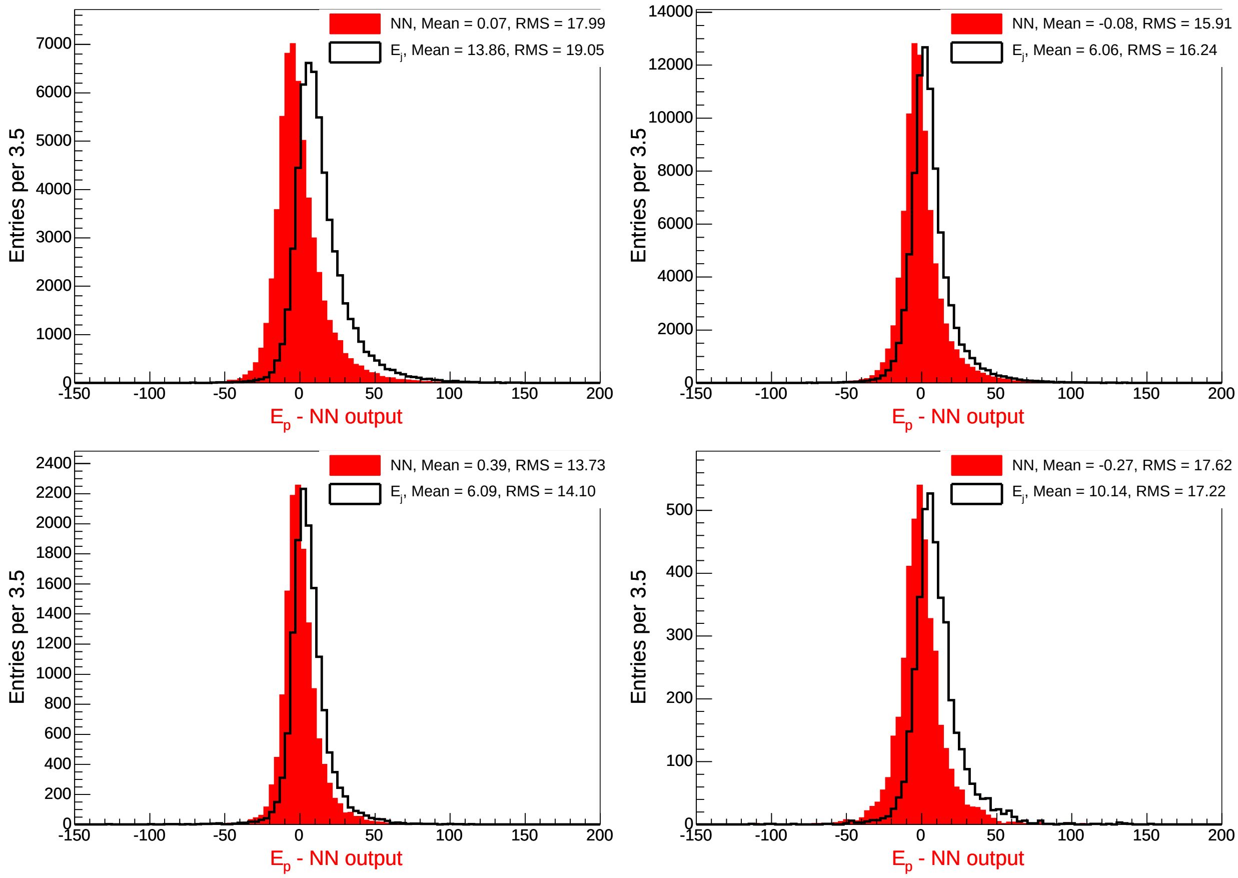

Figure 7.6: Difference between the parton energy and the measured jet energy (black) and the NN$_{output}$ (red). From top left to bottom right: b-jets in WH (m$_H$ = 115 GeV/c^2) events, b-jets in $Wb\bar{b}$ events, light jets in diboson events, andWgg events for gluon.

a$_i$	b$_i$
8.568166	-0.058203
1.295644	0.088275
0.528380	0.000000
21.707869	-0.286853
2.883938	0.154726

Table 7.2: Parameteres used for the NN transfer function of WH (m$_H$ = 115 GeV/c^2)

Performance of the $W_{jet}(E_{parton}, NN_{output})$

The performance of the parameterization can be checked by comparing the original distribution in (E$_{parton}$, NN$_{output}$) with the prediction using the transfer function and n(E$_{parton}$). Since it is very hard to compare quantitatively in 2-D, 1-D projections are done, see Figure 7.7, in terms of δ_E in parton energy slides. The figures show a good agreement between the $\delta_E \equiv E_p - NN_{output}$ distribution (black histogram) compared to the prediction from the NN TF (solid blue line) for four different physic processes (WH, diboson (WW, WZ), $Wb\bar{b}$, and Wgg). The TF prediction is calculated integrating Equation 7.8:

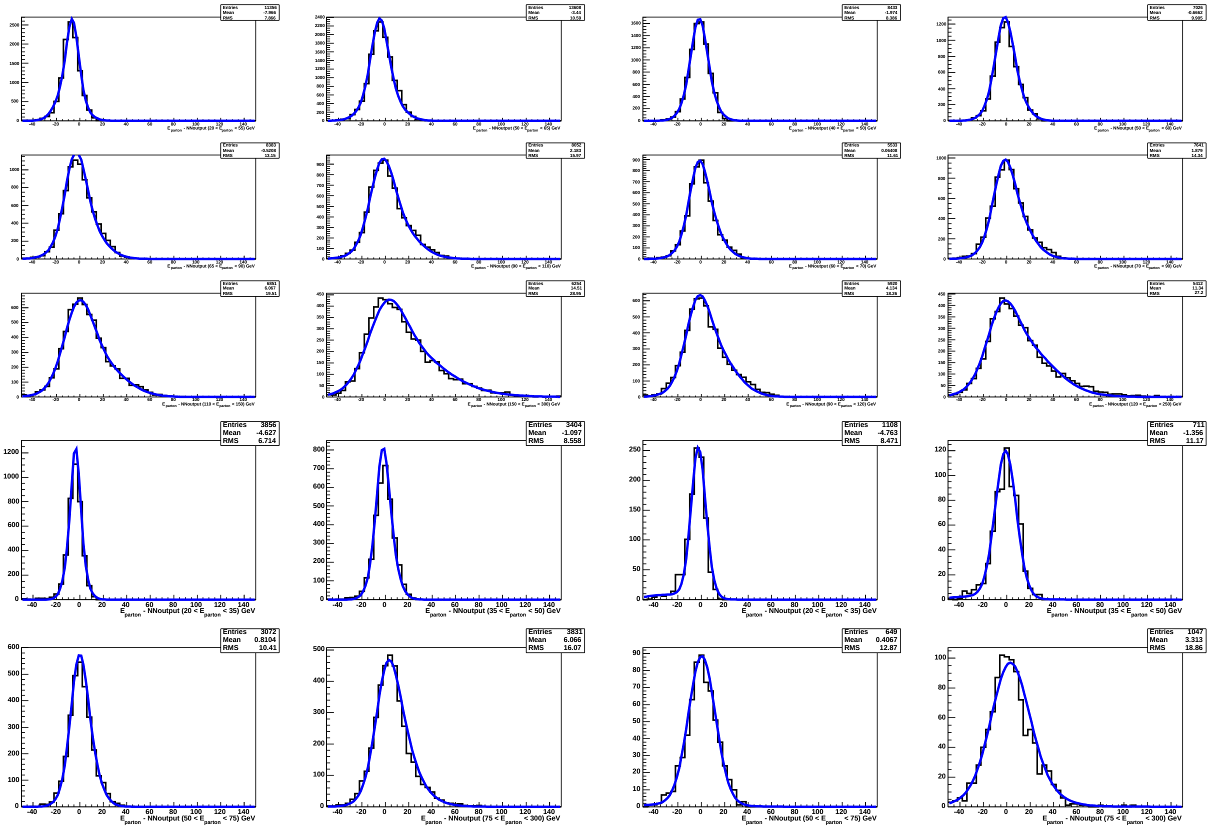

Figure 7.7: Distributions of δ_E in different E$_{parton}$ ranges of WH (m$_H$= 115 GeV/c^2) (top left), $Wb\bar{b}$ (top right), diboson (bottom left), Wgg (bottom right) MC events. The solid blue line corresponds to the NN TF prediction.

$$H(\delta_E) = \int_{E_{parton}1}^{E_{parton}2} n(E_{parton}) dE_{parton} W_{jet}(E_{parton}, E_{parton} - \delta_E). \tag{7.9}$$

The n(E$_{parton}$) distribution is parameterized as a sum of two gaussians and an exponencial:

$$n(E_{parton}) = p_1(exp\frac{-(E_{parton} - p_2)^2}{2p_3^2}) + p_4(exp\frac{-(E_{parton} - p_4)^2}{2p_6^2}) + p_7(exp(E_{parton} - p_8)). \tag{7.10}$$

Figure 7.8 shows the n(E$_{parton}$) distribution. The red solid line is the result of the fit using the sum of the two gaussians and an exponencial from Equation 7.10.

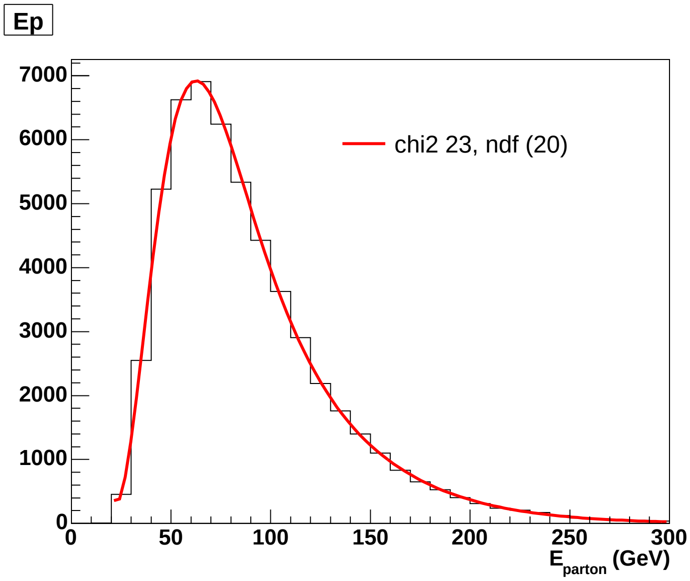

Figure 7.8: n(E_{parton}) distribution of the WH sample for a Higgs mass of 115 GeV/c^2.

Cross-check of the output of the NN

The output of the Neural Network is used to correct the measured energy of all the jets from the events that pass the analysis selection. As a cross-check, we compare the invariant mass resolution of the dijet system in WH signal events before and after applying this correction. A way to do this is to fit the invariant mass distributions to a gausian function and compare the resolution, defined as the sigma divided by the mean of the fit, for all Higgs masses; the result is shown in Figure 7.9 (left). As expected, the invariant mass resolution is laeger (smaller sigma) after correcting by the NN_{output}.

The linearity of the correction is also checked, see Figure 7.9 (right). Both functions are linear, the only difference is that the reconstructed invariant mass is closer to the generated one once the correction is applied. This could give a big improvement in the final sensitivity, but the backgrounds are also being corrected in the same way that the signal is; so, at the end, this improvement is not that significant.

7.2 Calculate the Event Probabilities

Once everything (PDFs, Matrix Elements, and the transfer functions) is in place, we can go ahead and calculate the event probability densities per event using Equation 7.4. This provides good discrimination between signal and background.

The event probability density makes use of all measured quantities to specify each event, i.e the only information that is needed from the events are the four-vectors of the lepton and the jets (E, p_x, p_y, and p_z). The level of agreement between data and Monte Carlo simulation is checked for all the input variables in the twelve signal regions as well as in

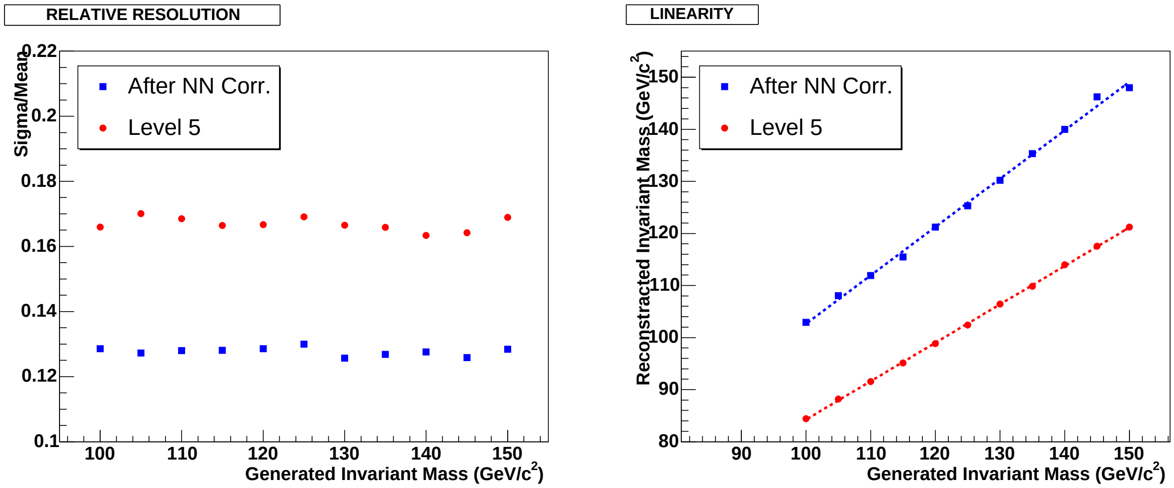

Figure 7.9: Left (right): Relative resolution of the invariant mass (reconstructed vs generated invariant mass) before and after apply the NN correction to the measured jets.

different control regions. Figure 7.10 show the input distributions to the event probability calculation of the lepton for 2 and 3-jet untag events. The distributions of the lepton for 2 and 3-jet tagged events, and of the jets for 2 and 3-jet untag and tagged events are shown in Appendix D.

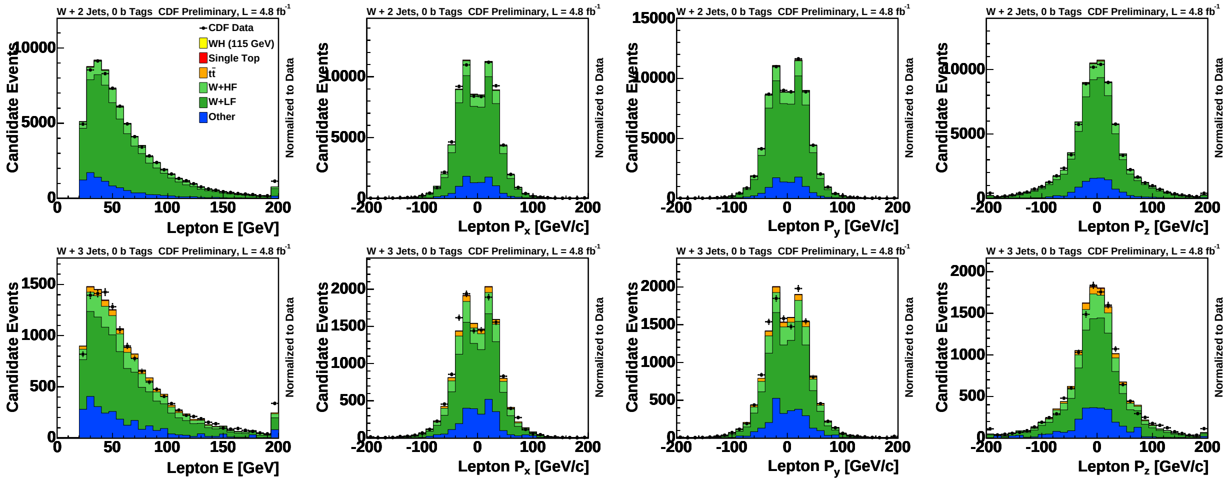

Figure 7.10: Top (bottom): The four-vector of the lepton for 2-jet (3-jet) untag events.

The result of the signal event probabilities obtained are shown in Figure 7.11. The event probability distributions of the rest of the processes calculated in this thesis are shown in Appendix E.

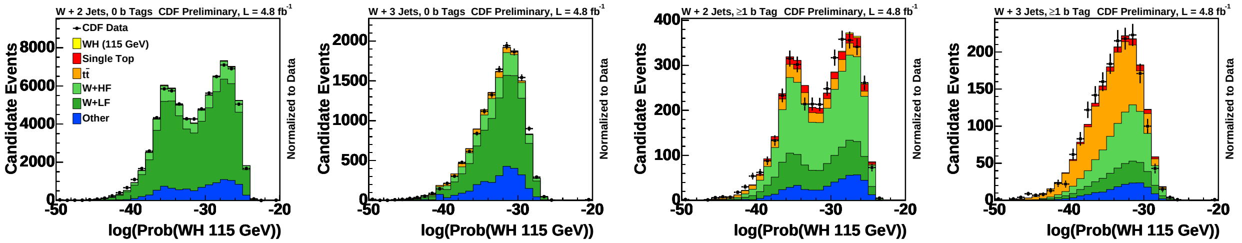

Figure 7.11: Data-MC comparison of the event probability densities for signal WH (m$_H$=115 GeV/c^2). From left to right: 2-jet untag, 3-jet untag, 2-jet tagged and 3-jet tagged events are shown.

7.3 Event Probability Discriminant: EPD

The next step is to build the final discriminant. The event probability densities are used as inputs to build an Event Probability Discriminant (EPD), i.e. a distribution which separates signal from background.

The most intuitive discriminant is the ratio of signal probability over signal plus background probability, $EPD = P_{signal}/(P_{signal} + P_{background})$, and, basically, this is what is used in this analysis. By construction, this discriminant is close to zero for background-like events and close to unity for signal-like events. Expresions 7.11 and 7.12 are the definition of the Event Probability Discriminants used in this thesis:

$$EPD \equiv \frac{b \cdot \hat{P}_{WH}}{b \cdot (\hat{P}_{WH} + \hat{P}_{Wb\bar{b}} + \hat{P}_{t\bar{t}} + \hat{P}_{schan} + \hat{P}_{tchan}) + (1-b) \cdot (\hat{P}_{Wc\bar{c}} + \hat{P}_{Wcj} + \hat{P}_{W+l} + \hat{P}_{Wgg} + \hat{P}_{dib})} \tag{7.11}$$

$$EPD = \frac{b_1 \cdot b_2 \cdot \hat{P}_{WH}}{b_1 \cdot b_2 \cdot (\hat{P}_{WH} + \hat{P}_{Wb\bar{b}} + \hat{P}_{t\bar{t}} + \hat{P}_{schan}) + b_1 \cdot (1-b_2) \cdot \hat{P}_{tchan} + (1-b_1) \cdot (1-b_2) \cdot (\hat{P}_{Wc\bar{c}} + \hat{P}_{Wcj} + \hat{P}_{W+l} + \hat{P}_{Wgg} + \hat{P}_{dib})} \tag{7.12}$$

where $\hat{P}_i$ = C$_i$*P$_i$, P$_i$ is the event probability of a given physic process (WH, s-channel, W$b\bar{b}$, ...), C$_i$ its optimized coefficient, and b is a transformation of the output of the neural network flavor separator (KNN), see Section 4.5.

Extra non-kinematic information is introduced into the Event Probability Discriminant by using KNN, and some additional coefficients (C$_i$). These C$_i$ coefficients are artificially included into the EPD, one coefficient per event probability, and optimized to increase the discrimination power between signal and background. The goal is to obtain a set of coefficients that increases the sensitivity of the analysis. This has been succesfully used in the measurement of the WW+WZ production cross section [84]. The optimization of the coefficients is done using only Monte Carlo templates and the total number of expected signal and background events calculated previously. The optimization is performed using a maximum likelihood fit to extract β, being β the ratio between the WH cross section and the predicted WH cross section. The likelihood used is:

$$\mathcal{L}(\beta) = \sqrt{\sum_{k=1}^{n_{bin}} \frac{(\beta S_k)^2}{\beta S_k + B_k + (\beta \Delta S_k)^2 + (\Delta B_k)^2}}, \tag{7.13}$$

where S_k and B_k are the expected number of signal and background events in the kth bin. Δ S_k and Δ B_k are the statistical unvertainty on S_k and B_k, respectively.

The procedure to obtain the optimized coefficients is described as follows:

- Create the EPD templates with a set of random coefficients.
- Calculate the figure of merit (F.O.M.) of these new background and signal EPDs. The F.O.M. is one over the error on β, shown in Equation 7.14:

$$F.O.M. = \frac{1}{\sigma_\beta} \tag{7.14}$$

This is done over ~ 2000 iteration. Finally, the set of coefficients with the best F.O.M. is saved and used in the analysis.

The optimized coefficients used in this analysis for the EPD of Higgs mass of 115 GeV/c^2 are given in Table 7.3.

Process	SVnoJP and SVJP	SVSV
s-channel	$9.7{\cdot}10^6$	$6.4{\cdot}10^6$
t-channel	$7.1{\cdot}10^4$	$4.2{\cdot}10^5$
$Wb\bar{b}$	$1.2{\cdot}10^7$	$3.3{\cdot}10^6$
$Wc\bar{c}$	$6.9{\cdot}10^4$	$2.6{\cdot}10^5$
Wc	$1.3{\cdot}10^6$	$4.4{\cdot}10^4$
Wjg	$2.5{\cdot}10^5$	$3.1{\cdot}10^4$
Wgg	$5.4{\cdot}10^4$	$1.2{\cdot}10^4$
$t\bar{t}$	$1.2{\cdot}10^3$	$3.2{\cdot}10^2$
WW	$8.9{\cdot}10^5$	$1.1{\cdot}10^6$
WZ	$1.4{\cdot}10^7$	$4.0{\cdot}10^6$
WH	$1.0{\cdot}10^{10}$	$5.5{\cdot}10^9$

Table 7.3: Coefficients for the EPD of a Higgs mass of 115 GeV/c^2

As mentioned before, the b variable used in the EPD is a transformation of the KNN:

$$b = 0.5 \cdot (1 + KNN). \tag{7.15}$$

As a result of this transformation, b can only vary between 0 and 1. Including this factor, helps to discriminate signal from background events and improves the final sensitivity.

The Event Probability Discriminants are defined for all the MC events that pass the analysis selection, see Section 6, including events with at least one jet tagged by SecVtx.

Ideally, that would be enough MC statistics except for W+light and non-W events, so in these cases events with no tagged jets are also included.

The EPDs, for MC events, are defined independently of the tagging category of the event, but later on, when making the final templates, the events are weighted by the corresponding tagging probability. These tagging probabilities are function of the flavor of the quark, the b-tagging scale factor and the mistag matrix as explained in Section 6.4, equation 6.6. On the other hand, for data, tagging is required and the events are not weighted by any tagging probability.

Therefore, since the flavor separator, KNN, is defined only for SecVtx tagged jets, we have to be careful how we use this variable. KNN is used for each type of event, in the cases where the jet is not tagged the value of the KNN is randomized using a light or non-W flavor separator template. Following, it is an explanation of all the cases in this analysis where KNN is used and needs to be defined:

- For events with two or more SecVtx tagged jets: KNN is the flavor separator of one of the jets randomly chosen. KNN_1 and KNN_2 are the flavor separators of two of the tagged jets, randomly ordered. Figure 7.12 shows the flavor separator for the two jets in SVSV events.

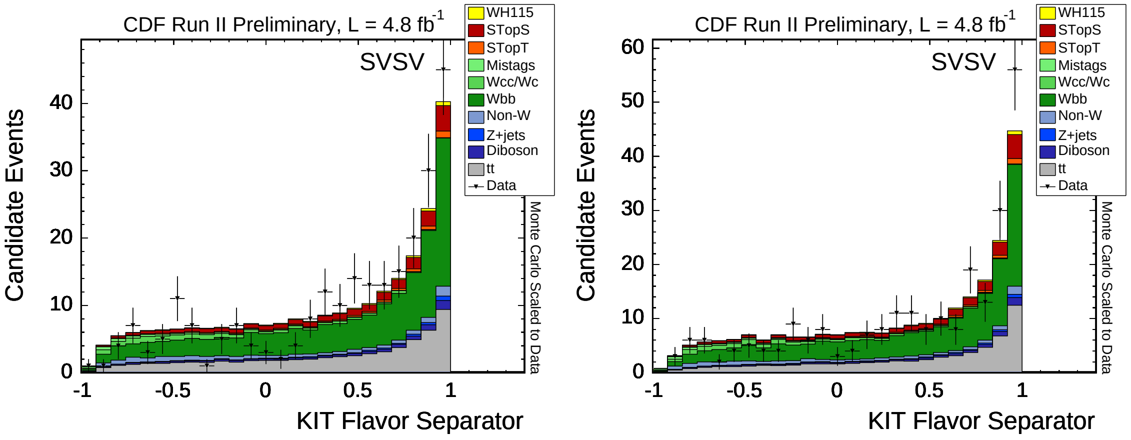

Figure 7.12: Data-MC comparison of the flavor separator for SVSV events.

- For events with one SecVtx tagged jet: KNN is the flavor separator of the tagged jet. KNN_1 and KNN_2, one is the flavor separator of the tagged jet and the other is a random value from the non-W template for non-W events or a random value from the light flavor separator template for the rest of events. Figure 7.13 shows the flavor separator for the SecVtx tagged jet in SVJP (left plot) and SVnoJP (right plot) events.

- For events with no SecVtx tagged jets (that is only the case for W+light and non-W events): KNN, KNN_1, and KNN_2 are a random value from the light flavor separator template for W+light events or from the non-W template for non-W events. The non-W template is a mixture of the bottom, charm and light templates (45:40:15).

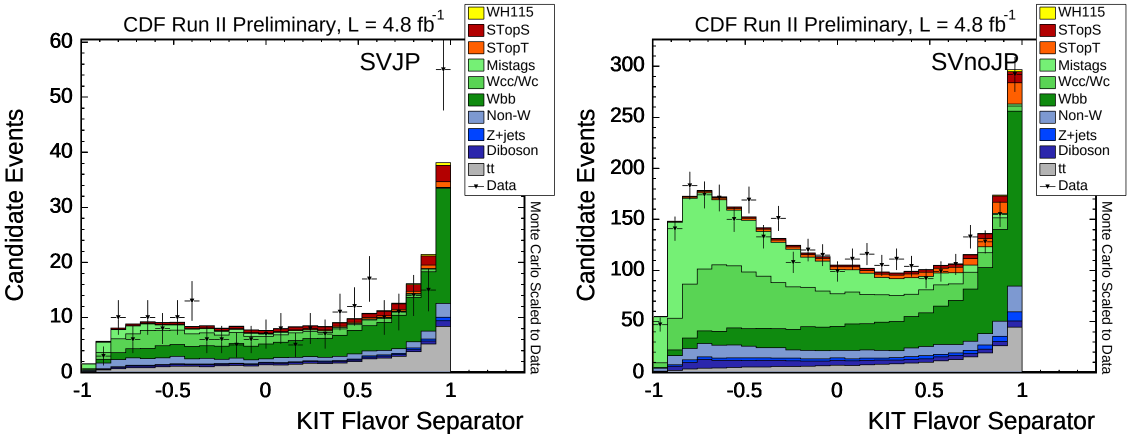

Figure 7.13: Left (Right): Data-MC comparison of the flavor separator for the SecVtx tagged jet in SVJP (SVnoJP) events.

In the search for SM Higgs production, we create twelve separate EPD discriminants for each Higgs mass point, given by the different b-tag categories, the number of jets in the final state, and the type of leptons (tight and EMC). This gives us the ability to tune the discriminants independently.

7.3.1 Validation of the EPD

As mentioned before, the data-MC agreement is checked for all the input variables in the twelve signal regions as well as in different control regions. In addition to the validation of the input variables, the discriminants are validated in the control region of 2 and 3 jets with no b-tags (W + light flavor dominant). The Event Probability Discriminants for 2 and 3-jets events in the control region are shown in Figure 7.14.

7.3.2 EPD in the Signal Regions

The EPD discriminant, in all the b-tag channels and all the Higgs masses, is used as the final discriminant for the WH search. Figure 7.15 (7.16) shows this comparison for a Higgs mass of 115 GeV/c^2 for 2 (3) jet events.

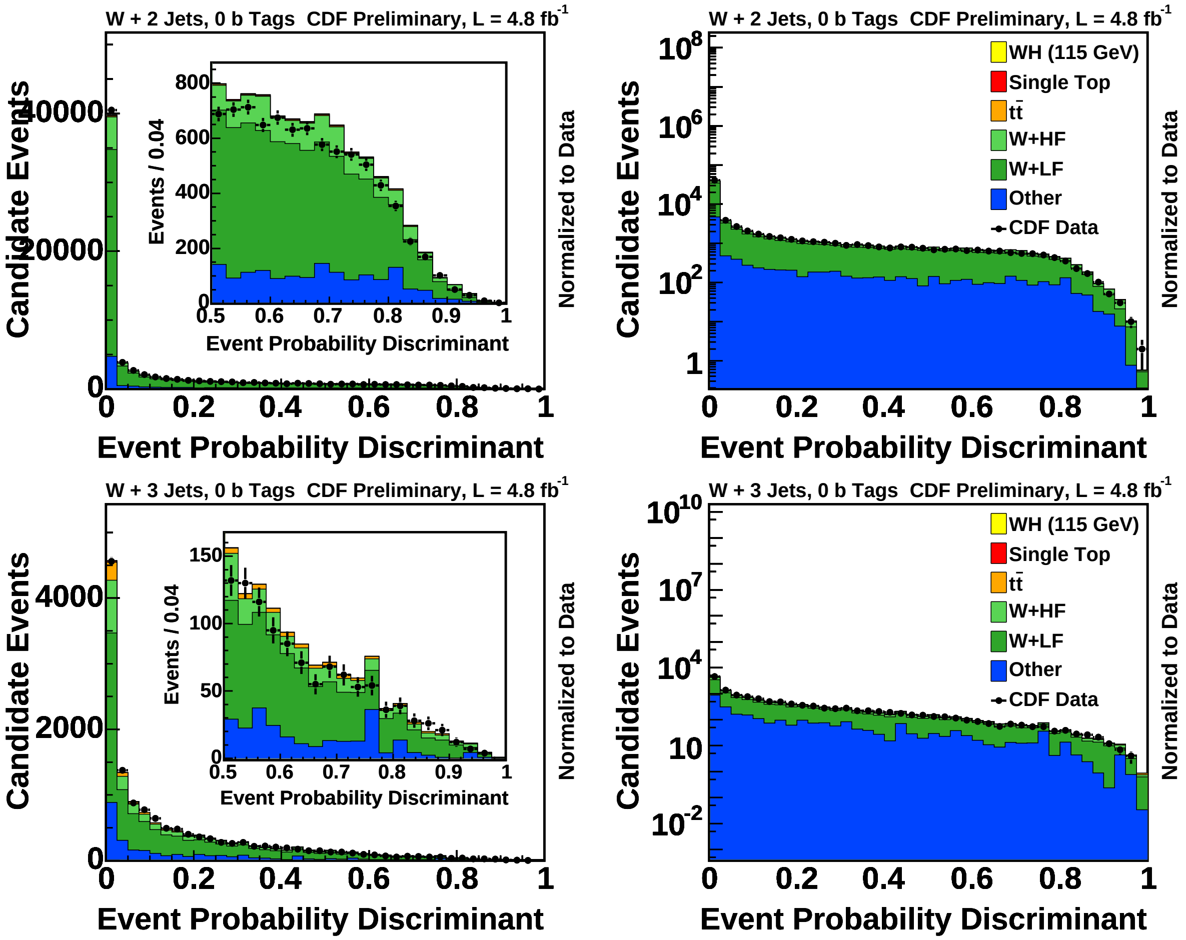

Figure 7.14: Data-MC comparison of the EPD distributions ($m_H = 115\ GeV/c^2$). Top (bottom): EPD applied in the W + 2 (3) jets untag sample.

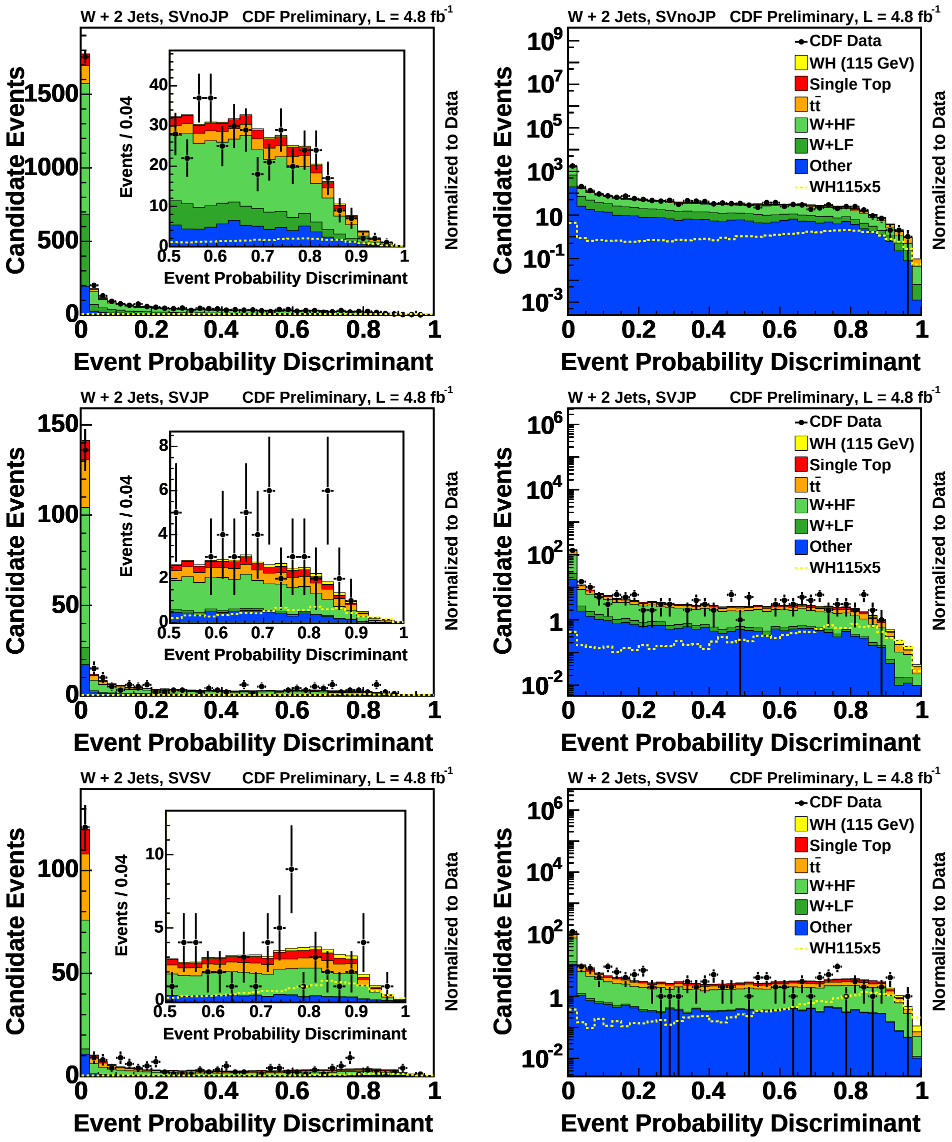

Figure 7.15: EPD output distributions for lepton + 2 jets data compared to the Monte Carlo prediction for WH (m_H = 115 GeV/c^2) signal and background. From top to bottom: SVnoJP, SVJP, and SVSV tagged data events.

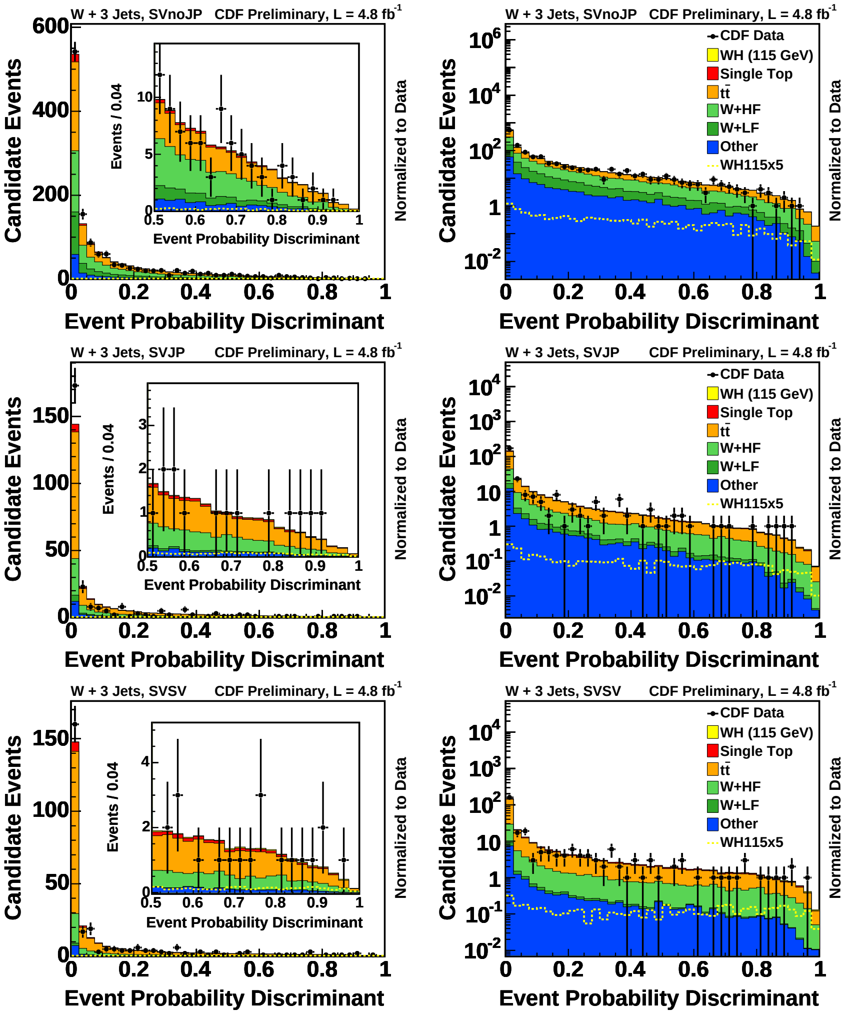

Figure 7.16: EPD output distributions for lepton + 3 jets data compared to the Mont e Carlo prediction for WH (m_H = 115 GeV/c^2) signal and background. From top to bottom: SVnoJP, SVJP, and SVSV tagged data events.

Chapter 8

Results

We search for an excess of Higgs signal events in the EPD distributions, but we find no evidence of a signal excess in the CDF observed data. This chapter describes the binned likelihood technique used to set an upper limit on SM Higgs boson production associated with a W boson for 11 values of m_H, $100 \leq \mathrm{m}_H \leq 150$ GeV/c^2 in 5 GeV/c^2 steps. The limits are calculated for all lepton and b-tagging categories together, for the 2 and 3 jet events separately and combined. They are given as a ratio to the Standard Model cross section times branching ratio $(\sigma(p\bar{p} \rightarrow WH) \cdot B(H \rightarrow b\bar{b}))$.

8.1 Systematic Uncertainties

Systematic uncertainties can bias the outcome of this analysis and have to be incorporated into the result. There are many sources of possible uncertainty that can influence both the expected event yield (normalization) and the shape of the discriminant distribution. Both types of systematic uncertainties, rate and shape uncertainties, are addressed in this analysis. Sources of uncertainty applied for signal and backgrouns processes are presented in Table 8.1.

Process	JES rate	JES shape	ISR/FSR/PDF	Lumi	Lepton ID	b-tagging SF	Background cross sections
signal, WH	X	X	X	X	X	X	
W+jets	X	X					X
$t\bar{t}$	X	X		X	X	X	X
single top				X	X	X	X
Z+jets				X	X	X	X
Diboson				X	X	X	X
non-W							X

Table 8.1: Systematic Uncertainties.

8.1.1 Rate Systematics

Rate uncertainties affect only the expected contribution of the signal and background samples. We address rate systematic uncertainties from several different sources:

- Jet energy scale (JES)
- Initial state radiation (ISR)
- Final state radiation (FSR)
- Parton distribution functions (PDF)
- Luminosity
- b-tagging SF
- Lepton ID
- Background cross sections

Normalization uncertainties are estimated by recalculating the acceptance using Monte Carlo samples altered due to a specific systematic effect. The WH normalization uncertainty is the difference between the systematically shifted acceptance and the default one.

The effects of systematic uncertainty from the same source are considered to be fully correlated. The effects of different sources of systematic uncertainty are considered to be uncorrelated.

Jes Energy Scale

The effect of the uncertainty in the Jet Energy Scale is evaluated by applying jet-energy corrections that describe $\pm 1\sigma$ variations to the default correction factor. As mentioned in Chapter 4, the JES used in this analysis is Absolute jet energy scale, the variations in this case, are on the order of 2-3%, as shown in Figure 8.1. This leads to the systematic uncertainties shown in Table 8.2.

The kinematic properties of each event are affected, and some events are re-categorized as having a different number of jets, as jets change their $\not{E}_T$. Jet Energy Scale rate systematic is applied to the signal sample, and to $t\bar{t}$ and W+jets.

Inital and Final State Radiation

Systematic uncertainties due to the modeling of ISR and FSR are obtained from dedicated Monte Carlo samples for WH signal events where the strength of ISR/FSR was increased and decreased in the parton showering to represent $\pm 1\sigma$ variations [85]. The effects of variations in ISR and FSR are treated as 100% correlated with each other. The ISR/FSR rate systematic is only applied to the signal sample.

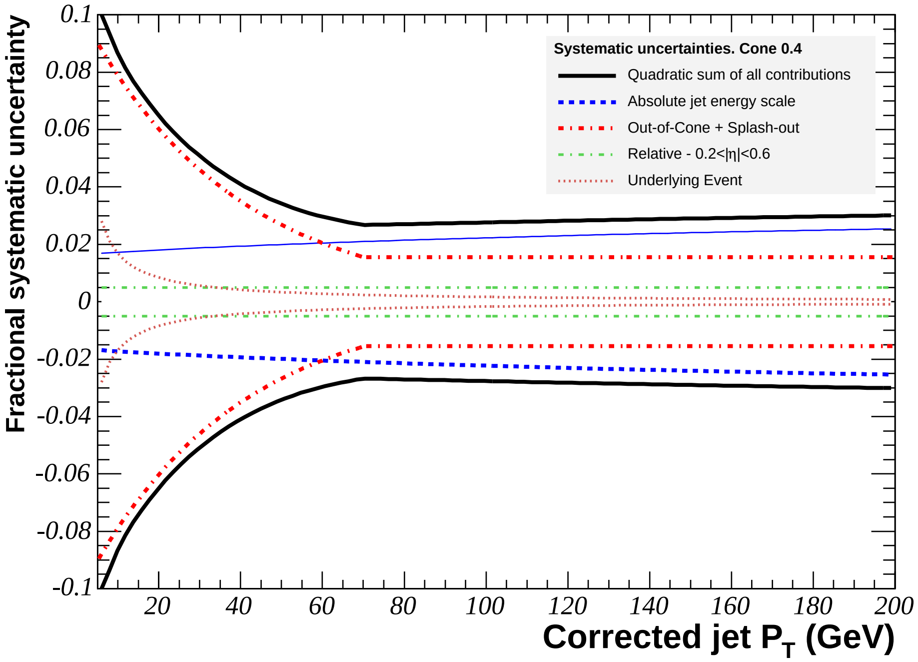

Figure 8.1: The total systematic uncertainties in the central calorimeter ($0.2 < |\eta| < 0.6$).

Parton Distribution Functions

To evaluate the uncertainty associated with the specific choice of parton distribution functions events are reweighted based on different PDF schemes. We vary of the twenty independent eigenvectors of the CTEQ PDFs and compare to the MRST PDFs.We sum in quadrature the uncertainty from the CTEQ and MRST PDF uncertainty if the difference between the CTEQ and MRST PDFs is larger than the CTEQ uncertainty. As well as the Inital and Final State Radiation rate systematics, the Parton Distribution Functions rate is only applied to the signal sample. Table 8.2 summarizes the ISR/FSR + PDF and JES rate uncertainties on WH acceptance.

Luminosity

For all Monte Carlo based samples a systematic is applied for the uncertainty in the CDF luminosity measurement of 6% which is correlated across all samples and channels. This does not apply to the W+jets and non-W samples since they are obtained from the data. This uncertainty includes the uncertainty in the $p\bar{p}$ inelastic cross section as well as the uncertainty in the acceptance of CDF's luminosity monitor [52, 53]. The requirement that the primary vertex position in z is within ±60 cm of the origin causes a small acceptance uncertainty that is also included.

2 jet		
Channel	ISR/FSR + PDF	JES
SVnoJP	3.1%	2.0%
SVSV-SVJP	5.6%	2.0%
3 jet		
Channel	ISR/FSR + PDF	JES
SVnoJP	13.1%	15.8%
SVSV-SVJP	21.4%	13.5%

Table 8.2: WH ISR/FSR + PDF and JES rate systematic uncertainties for each channel.

b-tagging SF

The predicted rates of Monte Carlo based background processes and the signals are affected by the b-tagging efficiency. The uncertainty on the efficiency of the b-tagging algorithm is a source of uncertainty for each sample that uses these factors, it 4.2% for SecVtx tags and 4.7% for JetProbabilty tags. These uncertainties lead to a systematic uncertainty of 3.5% for SVnoJP and 8.4% for SVJP and SVSV. The rate uncertainties differ by sample and by channel but are correlated. No b-tagging SF uncertainty is assigned to the W+jets and non-W sample since they are derived from the data. We estimate the systematic uncertainty on the event tagging efficiency by varying the tagging scale factor and mistag prediction by $\pm 1\sigma$.

Lepton ID

The estimate of the lepton ID uncertainty is a result of varying the lepton ID scale factors. The results are then compared to the nominal prediction for an estimate of the fractional uncertainty. All lepton ID scale factors are varied either all up or all down simultaneously. The yield is then calculated for each sample and compared to the nominal prediction. The lepton ID systematic uncertainty is $\sim 2\%$ in all the cases. No lepton ID uncertainty is assigned to the W+jets and non-W sample since they are derived from the data.

Background Cross Sections

The normalization uncertainties for all backgrounds are represented by the uncertainty on the predicted number of background events and are incorporated in the analysis as Gaussian constraints in the likelihood function. The systematic uncertainty, per physic process, on the cross section is given by the Table 8.3.

The total rate systematic uncertainty is 8.1 (21.8)% for 2 (3)jet SVnoJP signal events and 12.1 (23.3)% for 2 (3)jet SVSV and SVJP signal events. The main source of systematic uncertainty comes from the b-tagging SF in 2 jet events and from ISR/FSR and PDF in 3 jet events.

Process	Uncertainty (%)
W+HF	30
non-W	40
Z+jets	15
Diboson	10
$t\bar{t}$	15.3
single-top	14.5
W+LF	9

Table 8.3: Background cross section systematic uncertainty.

8.1.2 Shape Systematics

Uncertainties in the jet energy scale lead to uncertainties both on WH event detection efficiency and kinematic distributions. The jet energy scale uncertainty is also consider as a shape uncertainty in the Event Probability Discriminant (EPD) for the 2 and 3 jet events and for all channels. It has been only applied to the WH signal sample, and W+jets and $t\bar{t}$ background samples.

The jet energy corrections are varied up and down corresponding to their $\pm 1\sigma$ uncertainties. Variations of the jet energy scale for 2 and 3 jet WH signal events are shown in Figure 8.2. In the top plots of Figure 8.2 the variations of 1 σ up (down) jet energy correction in the EPD are shown in red (blue). Bottom plots show the relative difference of 1 σ up (down) jet energy correction with respect to the nominal correction.

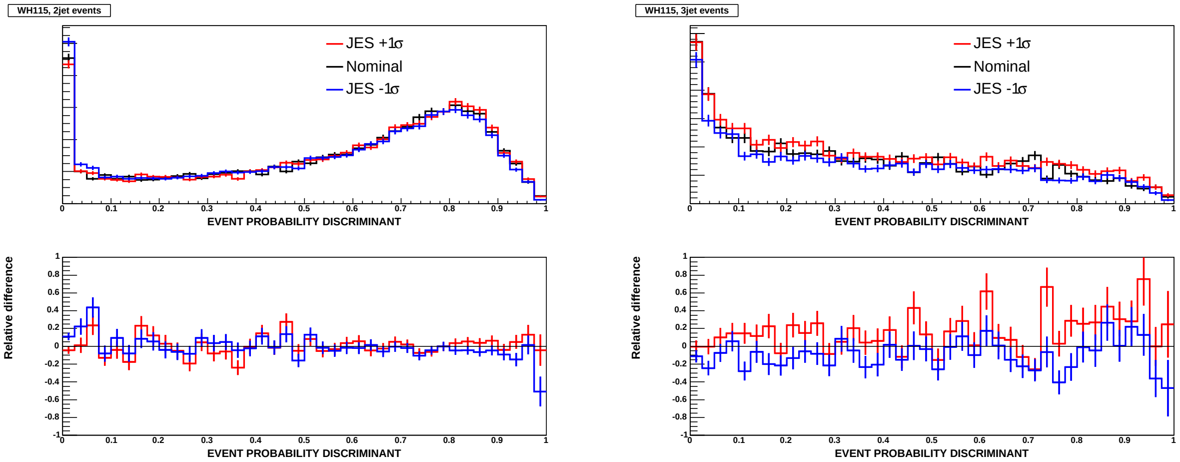

Figure 8.2: WH (m_H = 115 GeV/c^2) Jet Energy Scale shape systematic for 2 (left) and 3 (right) jet events. The bottom plots show the relative difference of 1 σ up (down) jet energy correction with respect to the nominal correction.

Variations of the jet energy scale for 2 and 3 jet events for background events, W+jets and $t\bar{t}$, are shown in Appendix F.

The shape uncertainty effect is very small compared with the normalization uncertainties. When computing limits including the shape uncertainties there is no noticeable difference in the final result.

8.2 Binned Likelihood Technique

In this analysis a binned likelihood is used where the likelihood is given by a product of Poisson probabilities:

$$\mathcal{L} = \prod_{k=bin} \frac{e^{-\mu_k} \cdot \mu_k^{n_k}}{n_k!} \tag{8.1}$$

where μ_k is the expected number of events in the k-th bin and n_k the number observed events in that bin. The expected number of events is represented as the sum of signal and background events:

$$\mu_k = s_k + b_k \tag{8.2}$$

where b_k is the number of expected background events in the k-th bin and s_k the number of expected signal events.

The likelihood function, $\mathcal{L}$, is defined such that it expresses the joint probability of observing the N data events at their respective values of the EPD output. The values of the Poisson means at which $\mathcal{L}$ achieves its maximum, corresponds to the most probable estimate for the true signal and background content in the data sample.

We perform a binned likelihood fit to the EPD output distributions. To make it easier to compare the different fit parameters, we define the fit parameter as $\beta_j = \sigma_j^{Fit}/\sigma_j^{SM}$ where β_j is unity when the fit result corresponds to the expected number of events obtained from the independent signal/background estimate:

$$\mathcal{L} = \prod_{j=2}^{6} G_j(\beta_j; \sigma_j) \prod_{k=bin} \frac{e^{-\mu_k} \cdot \mu_k^{n_k}}{n_k!} \tag{8.3}$$

The Gaussian constraints to the backgrounds are given by:

$$G_j(\beta_j; \sigma_j) = \frac{1}{\sqrt{2\,\pi \cdot \sigma_j^2}} \exp\left[-\frac{1}{2} \cdot \left(\frac{\beta_j - 1.0}{\sigma_j} \right)^2 \right] \tag{8.4}$$

The index k runs over the bins of the fitted histogram. The template histograms are normalized to the predicted number of events as shown in Table 6.2 for 2 jet events and in Table 6.3 for 3 jet events.

In addition, the prediction in each bin needs an additional Gaussian uncertainty due to the limitations of Monte Carlo statistics. Each bin is allowed to fluctuate according to the total uncertainty in that bin, which is the sum in quadrature of the weight of each event. This prevents us from overestimating our sensitivity due to a fluctuation in Monte Carlo.

$$\mathcal{L}(\beta_1, \ldots, \beta_6; \delta_1, \ldots, \delta_{11}) = \underbrace{\prod_{k=bin} \frac{e^{-\mu_k} \cdot \mu_k^{n_k}}{n_k!}}_{Poisson\ term} \cdot \underbrace{\prod_{j=2}^{6} G(\beta_j|1, \Delta_j)}_{Gauss\ constraints} \cdot \underbrace{\prod_{i=1}^{11} G(\delta_i, 0, 1)}_{Systematics} \tag{8.5}$$

All systematic normalization and shape uncertainties are incorporated in the analysis into the likelihood as nuisance parameters, conform with a fully Bayesian treatment [86]. We take the correlation between normalization and shape uncertainties for a given source into account. The relative strength of a systematic effect due to the source i is parameterized by the nuisance parameter δ_i in the likelihood function, constrained to a unit-width Gaussian (last term in Equation 8.5).

We marginalize the likelihood function by integrating $\mathcal{L}(\beta_1, ..., \beta_N, \delta_1, ..\delta_S)$ over all nuisance parameters for many possible values of the WH cross-section $\beta_1 = \beta_{WH}$. The resulting reduced likelihood $\mathcal{L}(\beta_{WH})$ is a function of the WH cross-section β_{WH} only. We use the MCLIMIT package for our statistical treatment [87] [88].

8.3 Results with 4.8 fb^{-1} of CDF II Data

We apply the analysis to 4.8 fb^{-1} of CDF Run II data. We compare the EPD output distributions of our data candidate events with the sum of predicted WH signal and background events for all Higgs masses. Figure 7.15 (7.16) shows this comparison for a Higgs mass of 115 GeV/c^2 for 2 (3) jet events. In order to extract the most probable WH signal content in the data we perform the maximum likelihood method described in Section 8.2. We perform marginalization using the likelihood function of Equation 8.5 with all systematic uncertainties included in the likelihood function. The posterior p.d.f is obtained by using Bayes' theorem:

$$p(\beta_1|data) = \frac{\mathcal{L}^*(data|\beta_{WH})\pi(\beta_{WH})}{\int \mathcal{L}^*(data|\beta'_{WH})\pi(\beta'_{WH})d\beta'_{WH}}$$

where $\mathcal{L}^*(data|\beta_{WH})$ is the reduced likelihood and $\pi(\beta_{WH})$ is the prior p.d.f. for β_{WH}. We adopt a flat prior, $\pi(\beta_{WH}) = H(\beta_{WH})$, in this analysis, with H being the Heaviside step function.

To set an upper limit on the WH production cross-section, we integrate the posterior probability density to cover 95% [7]. In this analysis events from three different b-tagging categories: with two or more jets SecVtx (SVSV) tagged, with one jet SecVtx and other jetprob (SVJP) tagged, and with only one jet SecVtx (SVnoJP) tagged; from two type of leptons: tight leptons and extended muon coverage; and from the 2 and the 3 jet bin are used. That makes a total of twelve different channels per Higgs mass (11 Higgs masses are used in this analysis). The observed and expected results (after combining the twelve analysis channels) are shown in Table 8.8 and in Figure 8.4.

8.3.1 Upper Limits for 2 jet events

The results from the 2 jet bin are expected to be more sensitive compared with the 3 jet bin, because most of the signal events have 2 jets in its final state. Table 8.4 represents the expected and observed limits for each Higgs mass for 2 jet events, including all b-tagging categories and all type of leptons, for an integrated luminosity of 4.8 fb^{-1}. The left plot on Figure 8.3 shows the expected and observed 95% confidence level upper limits normalized to the Standard Model expectation as a function of the Higgs mass.

σ / SM	100	105	110	115	120	125	130	135	140	145	150
Exp.	3.0	3.1	3.4	3.9	5.1	5.9	7.7	10.2	15.6	21.0	32.1
Obs.	3.7	3.8	3.9	4.4	5.4	7.3	8.2	13.5	19.8	25.0	38.7

Table 8.4: Expected and observed upper limits for 2-jet events for 4.8 fb^{-1}.

8.3.2 Cross Check using the M$_{jj}$ as discriminant for 2 jet events

As mentioned in Chapter 7, the invariant mass of the two leading jets (M$_{jj}$) in 2 jet events, see Figure 7.1, is the most discriminanting variable of this analysis. We compare the results using M$_{jj}$ as the discriminant variable instead of the EPD distribution to check the improvement that this multivariate technique gives.

Using M$_{jj}$ in events that have 2 jets in their final state as the discriminant we obtain the expected and observed limits shown in Table 8.5. As expected, the Event Probability Discriminant, which uses all the kinematic information available in the event, is a better discriminator between signal and background events. It is ~20% more sensitive than the M$_{jj}$ alone as you can see comparing the results in Tables 8.4 and 8.5.

σ / SM	100	105	110	115	120	125	130	135	140	145	150
Exp.	3.7	4.0	4.5	5.2	6.5	7.8	9.9	13.6	20.0	28.8	44.9
Obs.	5.6	6.2	6.8	7.1	8.0	10.0	12.8	20.1	31.3	41.0	69.1

Table 8.5: Expected and observed upper limits for 2-jet events for 4.8 fb^{-1} using M$_{jj}$ as discriminant.

8.3.3 Upper Limits for 3 jet events

Table 8.6 summarizes the expected and observed limits for each Higgs mass for 3 jet events. The limits, as well as the limits for 2 jet events, are computed including all b-tagging categories and all type of leptons, for an integrated luminosity of 4.8 fb^{-1}. The right plot on Figure 8.3 shows the expected and observed 95% confidence level upper limit normalized to the Standard Model expectation as a function of the Higgs mass.

This is the first time that 3 jet events have been used in the search for the Standard Model Higgs boson production in association with a W boson in CDF.

σ / SM	100	105	110	115	120	125	130	135	140	145	150
Exp.	13.4	14.0	15.1	16.7	21.5	24.7	30.3	42.2	59.8	83.8	129.7
Obs.	6.4	6.6	9.4	9.8	11.7	13.9	18.1	25.6	35.6	46.2	85.2

Table 8.6: Expected and observed upper limits for 3-jet events for 4.8 fb^{-1}.

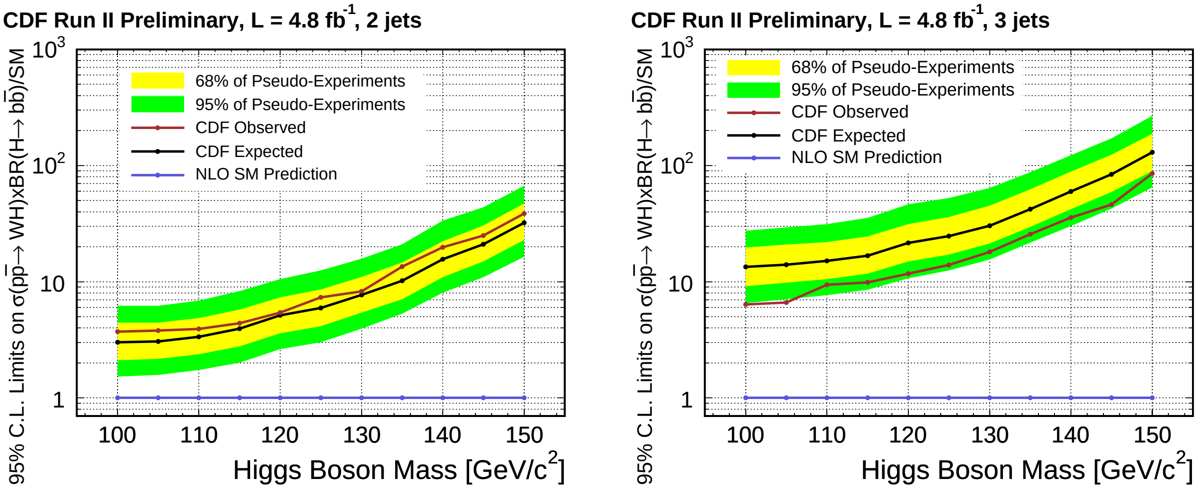

Figure 8.3: Expected and observed upper limits on Higgs production as a ratio to the Standard Model cross section times branching ratio for 2 (left) and 3 (right) jet events.

8.3.4 Upper Limits with no Systematic Uncertainties

To estimate the effect of the systematic errors used in this search, we calculate the upper limits for 2 and 3 jets combined together with no systematic uncertainties. The expected limits in this case are shown in Table 8.7.

σ / SM	100	105	110	115	120	125	130	135	140	145	150
Exp.	2.3	2.4	2.7	3.2	4.0	4.6	5.9	8.0	12.0	16.2	25.5

Table 8.7: Expected upper limits for 2-jet events for 4.8 fb^{-1} using M$_{jj}$ as discriminant.

8.3.5 Upper Limits for 2 and 3 jet events

The expected and observed 95% confidence level upper limits combining events from all jet bins, 2 and 3 jet events, all b-tagging categories, SVSV, SVJP, and SVnoJP, and all type of leptons, tight leptons (TL) and extended muon coverage (EMC), for an integrated luminosity of 4.8 fb^{-1} are shown in Table 8.8 and represented in Figure 8.4 as a ratio to the Standard Model cross section times branching ratio ($\sigma(p\bar{p} \to WH) \cdot B(H \to b\bar{b})$), in SM units, per Higgs mass.

Combining the events with 2 and 3 jets in the final state the limit improves by 3 to 10%, depending on the Higgs mass, with the respect to the result using 2 jet events only.

σ / SM	100	105	110	115	120	125	130	135	140	145	150
Exp.	2.9	3.0	3.2	3.8	4.7	5.6	7.1	9.2	14.4	19.3	29.8
Obs.	2.9	2.9	3.1	3.3	3.9	5.4	7.1	10.7	13.9	20.5	31.4

Table 8.8: Expected and observed upper limits for 2 and 3 jet events for 4.8 fb^{-1}.

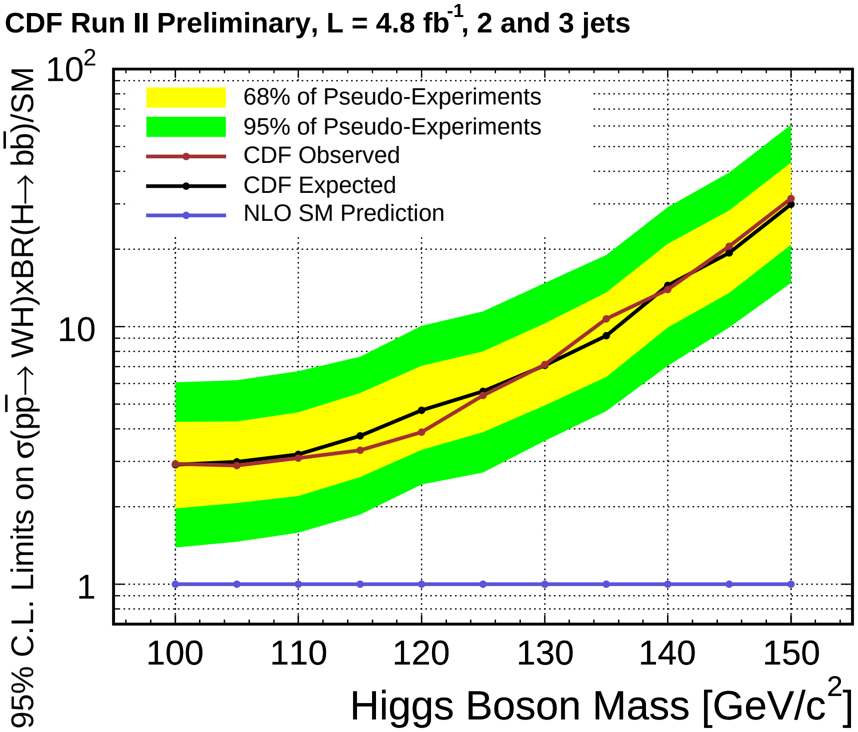

Figure 8.4: Expected and observed limits on Higgs production as a ratio to the SM cross section times branching ratio for 2 and 3 jet events.

This final result, the limits for 2 and 3 jet events, are 13 to 20 %, depending on the Higgs mass, less sensitive than the limits estimated with no systematic uncertainties, this difference is due to the effect that the systematic errors have in the limit calculation.

8.3.6 Upper Limits Splitting in Tagging Categories

The previuos results are obtained computing the three b-tagging categories together. Splitting the b-tagging categories give us the knowledge of which of the categories is the most powerful in the final result. Events with two or more SecVtx tagged jets, SVSV events, have the best signal to background ratio with respect to the other b-tagging categories.

Table 8.9 shows the expected and the observed limits splitting the limits in the three tagging categories, SVSV, SVJP, and SVnoJP, for 2 and 3 jet events combined together. As expected the SVSV category is the most sensitivy one, giving the best upper limit with respect to the SVJP and SVnoJP categories, that have similar sensitivities.

2 and 3 jets											
σ / SM	100	105	110	115	120	125	130	135	140	145	150
SVSV											
Exp.	4.6	4.3	4.8	5.7	7.0	8.4	10.3	14.2	21.5	28.4	44.5
Obs.	4.7	3.7	3.9	4.6	5.4	6.5	8.5	11.7	17.8	22.3	35.2
SVJP											
Exp.	5.6	6.0	6.7	7.6	9.6	11.1	14.2	18.7	28.2	39.1	60.6
Obs.	6.6	7.9	9.7	10.8	13.5	16.5	18.4	23.4	35.2	46.1	65.8
SVnoJP											
Exp.	5.8	6.4	6.8	8.0	10.2	12.0	15.4	20.2	29.3	41.7	64.0
Obs.	4.7	5.7	5.7	5.9	8.3	11.9	15.9	26.5	35.3	36.0	107.2

Table 8.9: Expected and observed upper limit cross sections, in SM units, for different Higgs mass points in 2- and 3-jet events for each tagging category.

Chapter 9

Conclusions and Outlook

In this thesis, a direct search for the Standard Model Higgs boson production in association with a W boson is presented. The final state of this channel, WH, is given by the Higgs boson decaying to two b quarks and the W decaying leptonically.

WH is the most promising channel in the region of low mass Higgs searches, $\mathrm{m}_H < 135$ GeV, at the Tevatron. What makes this channel so powerful is the combination between the production cross section and the branchig ratio. The largest branching ratio at low mass Higgs, see Figure 2.3, is the decay of $H \to b\bar{b}$. If the Higgs is produced via gluon fusion, $gg \to H$, the QCD background is overwhelming. So then, in order to have a cleaner signal, the presence of a lepton has been required in the final state from a W or Z boson, i.e. a Higgs boson is produced in association with a W or a Z boson. The advantage of the WH channel with respect to ZH is that the production cross section is larger as shown in Figure 2.1.

The data used in this thesis has been collected between February 2002 and May 2009 by the CDF detector and corresponds to 4.8 fb^{-1} of integrated luminosity as shown in Figure 3.2. For these kind of analyses, we need the whole detector up and running, from the tracking system, the most inner part, to the muon chambers, the outermost. Five different triggers of central and forward leptons have been used. The trigger with large missing transverse energy and no lepton required in the final states has increased the acceptance by 15% translated into a 10% increase in the final sensitivity with respect to using only high p_T lepton triggers. Different triggers, that explores some other regions of the detector (ϕ or η gap triggers), will be included to increase the acceptance.

The selection of the events has been done by requiring a high p_T lepton, large missing tranverse energy ($\not{E}_T > 20$ GeV), and two or three energetic and central jets in the final state. Including events with three jets in the final state has increased the acceptance and improved the sensitivity by 3% to 11%, depending on the Higgs mass considered. The selection cuts can be softened to also improve the acceptance, but further studies are needed to check the new signal acceptance over background acceptance, and the data versus Monte Carlo comparisons. This second statement is important because this thesis relies on accurate Monte Carlo modeling of signal and background processes.

Identifying jets as b jets is absolutely essential for this analysis to reduce the amount of background events and to improve the signal over background ratio. Three signal regions has been used in this analysis, SVSV, SVJP, and SVnoJP. The advantage of doing so is that each region has different kinematics and background contributions. This strategy improves the final sensitivity by 8% with respect to only having two signal regions.

Physics processes in which a W boson is produced in association with several jets can be misidentified as WH since they have the same signature. Background contributions coming from heavy flavor production processes, such as $Wb\bar{b}$, $Wc\bar{c}$ or Wc, misidentified W bosons, electroweak processes, $t\bar{t}$, single top production, and mistagged jets have been estimated using a combination of Monte Carlo calculations and independent measurements in control data samples.

Given the fact that the amount of signal events after the event selection is much smaller than the uncertainty in the background prediction, and, to achieve maximal sensitivity, this search has been performed using a Matrix Element Technique in which event probability densities for the signal and background hypothesis are calculated. In the event probability calculation we need to consider some effects: the partons colliding are inside protons, the neutrino is not measured by the detector, and the energy resolution of the detector. A transfer function has been used to account for the energy resolution effect. The transfer function is a mapping between the parton energy (E_p) and the jet energy (E_j) to correct the measured energy of the jet to closer values of the real parton energy, Figure 7.3 shows the different between the parton energy and the jet energy. To better reproduce the energy of the parton, and improve the energy resolution, a new transfer function has been built using a neural network output (NN_{output}). Figure 7.6 shows the difference between E_p and E_j (in black) and the NN_{output} (in red). The NN_{output} is closer to the E_p than E_j, the result is a new transfer function closer to zero and also narrower. Including this new transfer function translates in an improvement in the final sensitivity of 3% to 7%, depending on the Higgs mass. Once the event probability densities for all the events in the analysis have been calculated, they are combined to create a powerful discriminator called the Event Probability Discriminant, EPD.

Unfortunately, no evidence for a Higgs boson signal has been observed in an integrated luminosity of 4.8 fb^{-1} of CDF Run II data. We set 95% confidence level upper limits on the WH production cross section. To extract the most probable WH content in data, the signal and background EPD distributions have been fitted to the CDF data using a maximum likelihood technique. All sources of systematic uncertainties are included in the likelihood function. The upper limits on the WH production cross section times the branching ratio, in SM units, of the Higgs boson to decay to a $b\bar{b}$ pair are given by $\sigma(p\bar{p} \rightarrow WH) \times BR(H \rightarrow b\bar{b})/SM < 2.9$ to 31.4 for Higgs boson masses between $m_H = 100$ GeV/c^2 and $m_H = 150$ GeV/c^2. The expected sensitivity estimated in pseudo experiments is 2.9 to 29.8 at 95% C.L. This result, for 11 values of m_H, $100 \leq m_H \leq 150$ GeV/c^2 in 5 GeV/c^2 steps, is summarized is Table 9.1 and Figure 9.1.

As a cross check the limits, in 2 jet events, using the invariant mass distribution of the two leading jets as the discriminant, instead of the Event Probability Discriminant, has been calculated. The conclusion in this case is that using the Matrix Element Method improves the result by 20% with respect to the invariant mass distribution. Therefore, it is worthwhile to use this complicated multivariate technique.

σ / SM	100	105	110	115	120	125	130	135	140	145	150
Exp.	2.9	3.0	3.2	3.8	4.7	5.6	7.1	9.2	14.4	19.3	29.8
Obs.	2.9	2.9	3.1	3.3	3.9	5.4	7.1	10.7	13.9	20.5	31.4

Table 9.1: Expected and observed upper limits on the $\sigma(p\bar{p} \to WH) \times BR(H \to b\bar{b})/SM$ for 2 and 3 jet events for 4.8 fb^{-1}

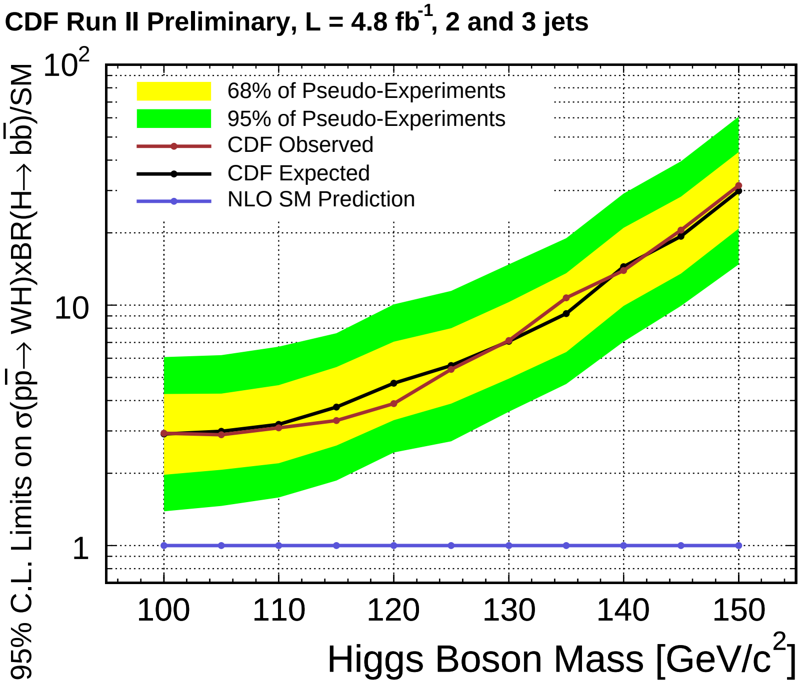

Figure 9.1: Expected and observed limits on Higgs production as a ratio to the Standard Model cross section times branching ratio for 2 and 3 jet events combined.

Being one of the most sensitive channels at the Tevatron at low mass Higgs, the WH channel alone will not be sensitive enough to discover the mechanism of the electroweak symetry breaking even with the full Tevatron data of approximately 10 to 12 fb^{-1} expected at the end of 2011. The Tevatron has improved the SM sensitivity by combining analysis channels and combining the data from the two experiments. At the moment, the latest combined results from CDF and DØ [89] on direct searches for a SM Higgs boson exclude the presence of the Higgs boson at 95% C.L. in a mass range of $162 < \text{m}_H < 166$ GeV/c^2. This result is shown in Figure 9.2, where the LEP exclusion is also included.

An update of the theoretical predictions for the production cross sections of the Standard Model Higgs boson at the Tevatron, focusing on the two main search channels, the gluon-gluon fusion mechanism, $gg \to H$, and the Higgs-strahlung processes, $q\bar{q} \to VH$ with $V = W/Z$, has been presented. It has been found that while the cross sections are well

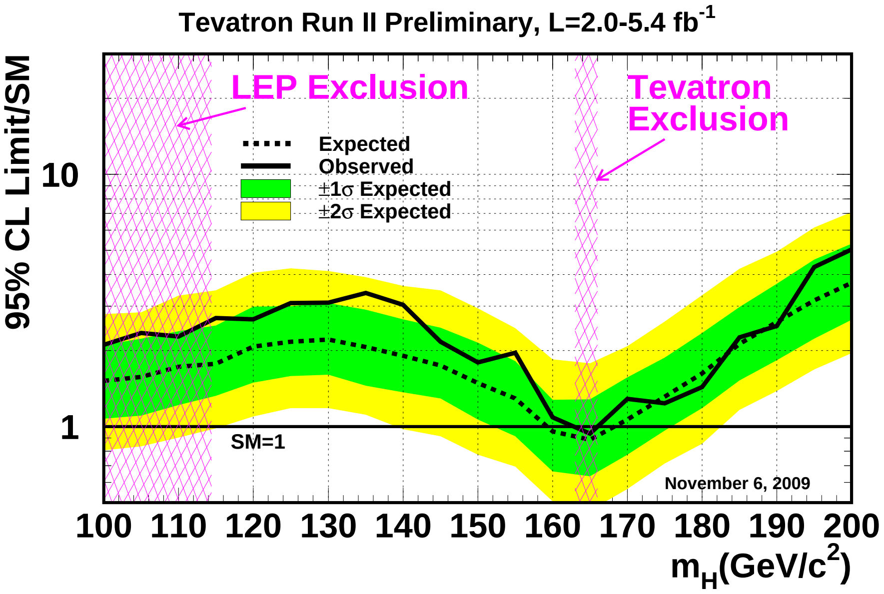

Figure 9.2: Observed and expected 95% C.L. upper limits on the ratios of the SM cross sections, as a function of the Higgs boson mass for the combined CDF and DØ analyses. The solid curve shows the observed upper bound, the dashed black curve shows the expected upper bound assuming no signal is present, and the colored bands show the 68% and 95% probability bands around the expected upper bound. The limits displayed in this figure are obtained with the Bayesian calculation.

under control in the Higgs-strahlung processes, the theoretical uncertainties are rather large in the case of the gluon-gluon fusion channel, possibly shifting the central values of the next-to-next-to-leading order cross sections by more than ≈ 40%. These uncertainties are thus significantly larger than the ≈ 10% error assumed by the CDF and D0 experiments in their recent analysis that has excluded the Higgs mass range m_H = 162-166 GeV/c^2 at the 95% confidence level. These exclusion limits should be, therefore, reconsidered in the light of these large theoretical uncertainties [90].

For a Standard Model Higgs boson of m_H = 115 GeV/c^2 the limits are getting very close to the SM expectation. The expected (observed) limit is 1.78 (2.70) times higher than the expected SM production cross section. This result includes the previous version of this analysis that we did using 4.3 fb^{-1}. The result of this thesis will be included in the next CDF, and CDF and DØ combinations like the 4.3 fb^{-1} result was included in the November 2009 combination as shown in Figure 9.3.

Overall, the combined CDF and DØ analyses are expected to test, at the 95% C.L.

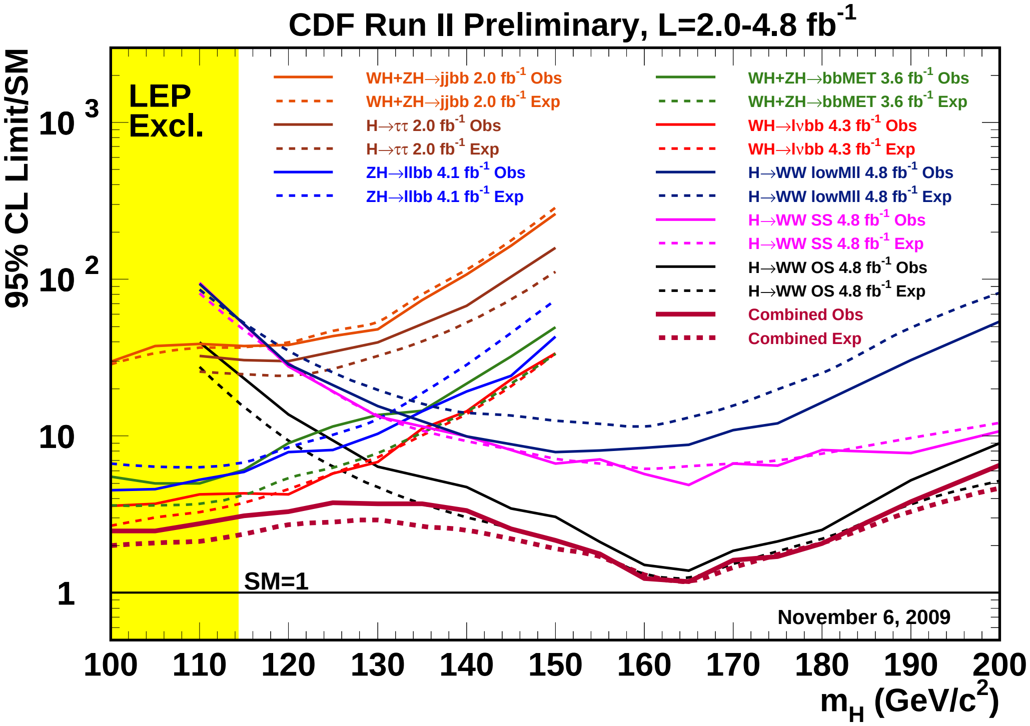

Figure 9.3: Expected and observed 95% confidence level upper limits on different channels of Higgs production in CDF, expressed as a ratio to the Standard Model cross section expectation times branching. The limits are obtained using integrated luminosities from 2.0 to 4.8 fb^{-1}. The dashed line indicates the expected limit and the solid line the observed limit. All the separate channel results are combined to obtain the CDF combination (maroon).

or better, the SM Higgs boson predictions for masses between the LEP limit and about 185 GeV before the end of Run II. With the projected improvements in analysis sensitivity, and the accumulation of more integrated luminosity, the Higgs boson is expected to be probed at the Tevatron. The comparison of the achieved expected limits by CDF multiplied by $1/\sqrt{2}$, to approximate the contribution of DØ assuming identical peformance, and the $1/\sqrt{L}$ extrapolations are shown in Figure 9.4 for $\text{m}_H = 115$ GeV/c^2. Tevatron could exclude a Higgs boson of $\text{m}_H = 115$ GeV/c^2 with 10 fb^{-1}.

These are very exciting times for the Higgs searches. The low mass Higgs boson searches are very challenging at the LHC, the channels used at the Tevatron for Higgs masses below 130 GeV are different from those dominant at the LHC. Few years of data collection will be needed for the LHC to get the same sensitivity that the Tevatron has right now.

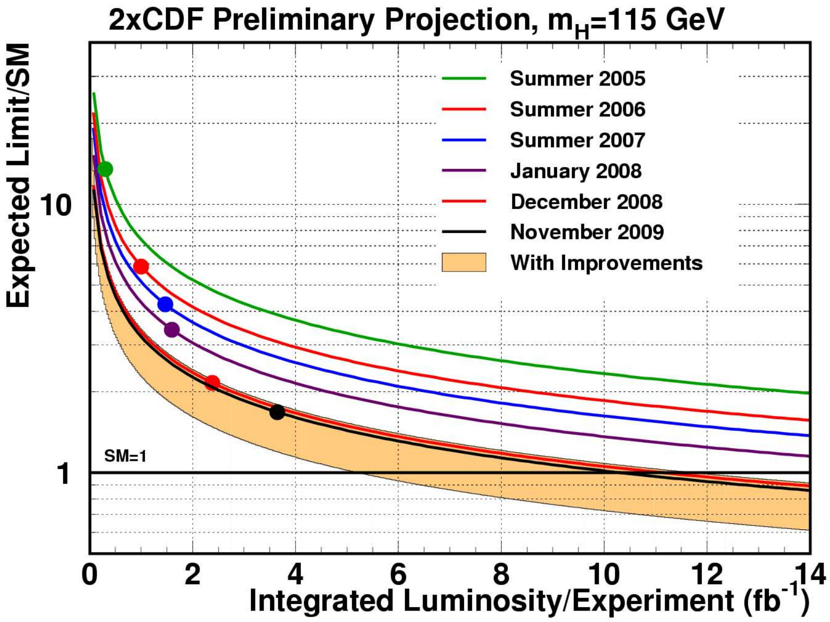

Figure 9.4: Projected median expected upper limits on the SM Higgs boson cross section, scaling CDF performance to twice the luminosity. The solid lines are $1/\sqrt{L}$ projections, as functions of integrated luminosity per experiment and each analysis update corresponds to a new point with a new curve. The top of the orange band corresponds to the Summer 2007 performance expected limit divided by 1.5, and the bottom of the orange band corresponds to the Summer 2007 performance expected limit divided by 2.25. This plot is shown for m_H = 115 GeV/c^2

Appendix A

Resumen y Conclusiones en Castellano

Introducción

El bosón de Higgs es una partícula fundamental predicha por el Modelo Estándar de la física de partículas que, hasta la fecha (Marzo 2010) aún no ha sido observada experimentalmente. Desempeña un papel fundamental en la explicación del origen de la masa de otras partículas elementales.

En esta tesis se presenta el resultado de la búsqueda directa del bosón de Higgs del Modelo Estándar usando 4.8 fb^{-1} de datos recogidos por el detector CDF (Collider Detector at Fermilab). El canal que se estudia en este análisis es aquel en el que el bosón Higgs se produce asociado con un bosón W (canal WH), donde el W se desintegra leptónicamente dando lugar a un leptón cargado de alto momento y a un neutrino, y el Higgs se desintegra produciendo dos quarks b. Este estado final se conoce como "leptón+jets". La identificación de jets b es un aspecto fundamental en este análisis. La señal de WH se ve mejorada notablemente con respecto a los fondos al identificar jets b, jets provenientes de quarks b.

Modelo Estándar

El Modelo Estándar de la física de partículas es una teoría, desarrollada entre 1970 y 1973, que describe las relaciones entre las interacciones fundamentales conocidas y las partículas elementales . Muchos físicos participaron en el desarrollo, basándose además en numerosas teorías anteriores.

El Modelo Estándar postula que la materia está formada por unos pocos constituyentes básicos, puntuales y sin estructura llamados partículas fundamentales. Aparte de sus antipartículas asociadas, el Modelo Estándar explica un total de doce tipos diversos de partículas de materia. Éstos se clasifican como quarks y como leptones. Los quarks se presentan en seis sabores diferentes: up (u), down (d), charm (c), strange (s), top (t) y bottom (b); y están ligados por la interacción fuerte. Los seis leptones son: electrón (e^-), muón

(μ^-), tau (τ^-), neutrino electrónico (ν_e), neutrino muónico (ν_μ), y neutrino tauónico (ν_τ). Ambos son fermiones y tienen spin 1/2. Los quarks y leptones se pueden agrupar en tres generaciones como se muestra en la Tabla 2.1, donde se muestra también la carga y masa de estas partículas. Cada quark y leptón lleva asociado su antipartícula con la misma masa pero carga opuesta. Los antiquarks se denotan por $\bar{u}$, $\bar{d}$, etc. La antipartícula del electrón es el positrón (e^+).

Las fuerzas en la física son la forma en que las partículas interaccionan recíprocamente y se influencian mútuamente. El Modelo Estándar explica las fuerzas de la naturaleza como el resultado del intercambio de otras partículas por parte de las partículas de materia, conocidas como partículas mediadoras de la fuerza. Las partículas mediadoras de fuerza descritas por el Modelo Estándar también tienen spin, pero en su caso, el valor del spin es 1, significando que todas las partículas mediadoras de fuerza son bosones. La Tabla 2.2 muestra la carga y la masa de estos bosones.

El Modelo Estándar incorpora:

- La fuerza electromagnética, responsable de la emisión de luz por parte de los átomos excitados. El mediador de la fuerza electromagnética es el fotón (γ) que es una partícula sin masa.

- La fuerza débil, la causante, por ejemplo, de la desintegración nuclear beta. Los masivos $W^\pm$, $M_W = (80.425 \pm 0.038)$ GeV/c^2 [7], y el Z^0, $M_Z = (91.1876 \pm 0.0021)$ GeV/c^2 [7] son los mediadores de la fuerza débil.

- La fuerza fuerte, que mantiene a los núcleos estables, es mediada por los ocho gluones (g), partículas sin masa.

La gravitación no está incluida en el marco del Modelo Estándar sino en la teoría general de la relatividad. Todas las partículas con masa o energía sienten la fuerza gravitacional. Sin embargo, debido a la debilidad de la gravitación con respecto a las otras fuerzas que actúan en reacciones de partículas elementales, no se considera en esta tesis.

Los quarks pueden experimentar interacción electromagnética, débil, y fuerte. Todos los leptones experimentan la interacción débil y los cargados también la electromagnética, pero no toman parte en interacciones fuertes.

Bosón de Higgs del Modelo Estándar

Uno de los retos de la física de altas energías es entender la ruptura espontánea de simetría y el origen de la masa de las partículas elementales. Uno de los mecanismos posibles para producir la ruptura espontánea de simetría electrodébil, sin destruir la invariancia gauge de la teoría, es el mecanismo de Higgs. En un espacio vacío, el campo de Higgs adquiere un valor esperado de vacío diferente de cero que permanece constante en el tiempo y en todo lugar del universo. Este valor esperado de vacío es igual a 246 GeV. La existencia de un valor esperado de vacío no nulo tiene una importancia fundamental: da una masa a cada partícula elemental, incluyendo al mismo bosón de Higgs. En particular, la adquisición espontánea de un valor esperado de vacío diferente de cero rompe la simetría gaugiana electrodébil, un fenómeno conocido como el mecanismo de Higgs. Este es el mecanismo más simple capaz de dar masa a un bosón de gauge que es también compatible con la Teoría de campo de gauge.

Hay otras alternativas al mecanismo de Higgs para la ruptura espontánea de simetría electrodébil. Todas las otras alternativas usan una dinámica que interactúa fuertemente para producir un valor esperado del vacío que rompa la simetría electrodébil.

La masa del bosón de Higgs (m_H) no viene determinada por el Modelo Estándar. Aunque aún no se ha logrado ninguna observación de dicho bosón, sí se han realizado experimentos indirectos que nos permiten saber, al menos, en qué intervalo está su masa con cierta precisión. Actualmente se puede descartar un valor inferior a 114.4 GeV con un intervalo de confianza al 95%, región excluida por LEP. Por supuesto, ciertas ideas teóricas permiten valores inferiores a 100 GeV pero con un bosón de Higgs que interactúa de forma exótica con el resto del Modelo Estándar y que está alejado de lo normalmente entendemos por bosón de Higgs. La Figura 2.5 muestra la curva de $\Delta\chi^2$ derivada de datos de alta precisión realizados en LEP, SLD, CDF, y DØ en función de la masa del bosón de Higgs, asumiendo que el Modelo Estándar es la teoría correcta de la naturaleza. Los datos predicen una masa de Higgs menor que 157 GeV, que asciende a 186 GeV si se incluye la exclusión de LEP. El valor preferido para su masa, correspondiente al mínimo de la curva, es 87 GeV, con una incertidumbre experimental de +35 -26 GeV (correspondiente al nivel de confianza del 68%).

Los experimentos del Tevatron, DØ y CDF, llevan a cabo la búsqueda del bosón en todos los posibles canales de producción. El resultado combinado más reciente permite excluir una región de masa de 162 GeV a 166 GeV con un nivel de confianza del 95%. En esta tesis se presenta la búsqueda del bosón de Higgs en uno de estos canales, en el cual el Higgs se produce asociado con un bosón W (canal WH). Este es el canal más sensible, y probablemente, el más prometedor, para una masa menor a unos 135 GeV.

Las proyecciones de la colaboración ATLAS, muestran que, con un luminosidad integrada de alrededor de 10 fb^{-1}, el bosón de Higgs del Modelo Estándar, se espera que sea descubierto en el LHC (Large Hadron Collider) si tiene una masa de 130 a 300 GeV. El descubrimiento del bosón de Higgs con una masa menor de 130 GeV, es un reto [3]. Si la masa del bosón de Higgs está en este rango, unos pocos años de funcionamiento puede ser necesaria para descubrirlo. Si se descubre el bosón de Higgs, sus propiedades podrían ser estudiadas en el LHC.

Tevatron y CDF

El Fermilab (Laboratorio Nacional Fermi) es un laboratorio de física de altas energías, llamado así en honor al físico Enrico Fermi, pionero en física de partículas. Se encuentra localizado en Batavia, Illinois. Dos componentes muy importantes del Modelo Estándar fueron descubiertos en el Fermilab: el quark bottom (1977) y el quark top (1995). En 2000, los investigadores del Fermilab anunciaron la primera observación directa del neutrino tauónico, la última partícula fundamental en ser observada.

En el Fermilab está instalado el que fuera durante un largo tiempo el acelerador de partículas más potente del mundo, el Tevatron, con una energía en centro de masas de 1.96 TeV y sólo superado en la actualidad por el LHC. La aceleración ocurre en un número de etapas. El Tevatron es la última etapa de este proceso de aceleración.

- La primera etapa ocurre en el pre-acelerador Cockcroft-Walton, que ioniza átomos de hidrógeno y acelera los iones negativos (H^-) hasta una energía de 750 KeV, usando un voltaje positivo.
- Los iones pasan al acelerador lineal (Linac) de 150 metros de largo, que utiliza cavidades de radio frecuencia para acelerar los iones hasta 400 MeV. Una vez alcanzada esa energía, los iones negativos pasan al Booster.
- El Booster es un acelerador magnético circular pequeño en el cual los iones pasan a través de una hoja del carbón, para deshacerse de los electrones. Los protones restantes giran hasta 20.000 veces dentro del Booster antes de lograr una energía de unos 8 GeV.
- Los protones con una energía de 8 GeV pasan al Main Inyector (inyector principal). El Main Inyector tiene varias tareas: acelerar los protones hasta 150 GeV; recolectar protones de 120 GeV para la creación de antiprotones; aumentar la energía de los antiprotones hasta 120 GeV e inyectar los protones y los antiprotones en el Tevatron.
- Los antiprotones son creados por la Fuente de Antiprotones. Protones de 120 GeV se chocan con una blanco del níquel produciendo partículas, incluido antiprotones, que se recogen y almacenan en el anillo del Acumulador. Del anillo los antiprotones pasan al Main Inyector.
- El Tevatron es un complejo acelerador-colisionador de partículas de 6 kilómetros de longitud. Acelera los haces de protones y antiprotones, que llegan del Main Inyector, hasta una energía de 980 GeV y cruza sus trayectorias en dos puntos del acelerador. Dos detectores de propósito general están situados en estos dos puntos: DØ y CDF. Los haces colisionan cada 396 ns. La Figura 3.1 muestra toda la cadena de acelaración.

El análisis presentado en esta tesis utiliza los datos recogidos entre Febrero del 2002 y Junio del 2009 de colisiones protón-antiprotón producidas por el Tevatron y observadas por el detector CDF. CDF es un detector de partículas de carácter general. Está diseñado con el fin de detectar las partículas generadas en las colisiones protón-antiprotón y medir sus propiedades. Un diagrama del detector CDF se muestra en la Fig. 3.3. Como se ve, el detector consta de tres subsistemas primarios: el sistema de trazas, el de calorimetría y el de muones.

La parte más interna corresponde al sistema de trazas. Se trata de varios subsistemas (Layer00, Silicon Vertex Detector, Intermediate Silicon Layers y COT) con simetría cilíndrica y forma de barril. Está diseñado para detectar partículas cargadas, medir su momento y desplazamientos respecto del vértice de la colisión. Las partículas cargadas ionizan átomos del detector, lo cual, tras una amplificación, crea trazas que señalan el camino seguido por las partículas. Bajo el efecto de un campo magnético, esas trayectorias se curvan; de la curvatura que adquieren se puede obtener el momento de la partícula. El sistema de trazas está rodeado por el detector de tiempo de vuelo, diseñado para proporcionar una buena identificación de partículas a bajo momento transverso. Estos dos sistemas se encuentran inmersos dentro de un solenoide superconductor capaz de generar un campo magnético de 1.4 T. Este imán está rodeado por el sistema de calorimetría, que consta de un calorímetro electromagnético y otro hadrónico. Su tarea consiste en medir energías de las partículas que interaccionan con la materia que lo forma. El calorímetro electromagnético se encarga de los electrones y fotones, y el hadrónico, de protones, neutrones o mesones. En la parte más externa del detector, rodeando al resto de los subsistemas, se encuentran las cámaras de detección de muones.

En el Tevatron se producen aproximadamente 2.5 millones de colisiones por segundo, pero la capacidad para escribir en cinta es de 50 sucesos por segundo así que el sistema de trigger tiene un papel muy importante en los experimentos de colisión de hadrones. El objetivo del triger, además de reducir el número de sucesos recogidos de 2.5 millones a 50 por segundo, es coger aquellos sucesos que tengan algún aspecto físico interesante lo suficientemente rápido. El sistema está diseado basado en tres condiciones. La primera condición es que no debe existir tiempos muertos en la toma de datos. El triger tiene que ser lo suficientemente rápido para tomar la decisión de cada suceso antes de que el siguiente ocurra. La segunda, impuesta por el Tevatron, es que el tiempo entre colisiones es de 396 ns. La última condición es que el sistema pueda escribir entre 30 a 50 sucesos por segundo en cinta.

Sucesos de Señal

Para realizar este análisis necesitamos producir millones de sucesos de simulación con el fin de comprender el comportamiento de los distintos procesos físicos. Usamos una gran variedad de generadores de Monte Carlo para simular los sucesos de señal, en este caso WH, y los sucesos de fondo.

El proceso de estudio en esta tesis es $WH \rightarrow l\nu b\bar{b}$. En este proceso físico, el bosón de Higgs se produce asociado a un bosón W. En la Figura 2.1 se puede ver la sección eficaz de producción de este suceso canal y del resto de los canales que se pueden producir en el Tevatron. El bosón de Higgs se desintegra en dos quarks b, y el bosón W en un leptón (electrón o muón) cargado y un neutrino. El diagrama de Feynman para este proceso se muestra en la Figura 5.1. El estado final al que nos vamos a referir es conocido como leptón+jets, un leptón y dos o tres jets en el estado final. La contribución de sucesos de señal con tres jets es considerablemente menor que para sucesos de dos jets, como se muestra en la Figura 6.5, pero incluyendo estos sucesos se ayuda a mejorar el resultado final.

Para este análisis se generan once muestras de señal con m$_H$ entre $100 \leq m_H \leq 150$ GeV/c^2 en saltos de 5 GeV usando el generadore de Monte Carlo `PYTHIA`.

Reconstrucción de los Sucesos

El análisis presentado en esta tesis se basa fundamentalmente en objetos de alto momento: electrones, muones, jets, y energía transversal faltante.

Los datos utilizados vienen de colisiones $p\bar{p}$, con una energía de centro de masas de $\sqrt{s}$ = 1.96 TeV, recogidos por el detector CDF II desde Febrero del 2002 hasta Junio del 2009. Esta muestra de datos corresponde con una luminosidad integrada de 4.8 fb^{-1} (Figura 3.2).

Para la selección del electrón pedimos, básicamente, una deposición de energía aislada en el calorímetro central con $E_{\mathrm{T}} > 20\,\mathrm{GeV}$ y asociada a una traza con $p_{\mathrm{T}} > 10\,\mathrm{GeV}/c$. Por su parte, los muones candidatos han de tener una traza en la cámara de deriva (COT) con $p_{\mathrm{T}} > 20\,\mathrm{GeV}/c$ y que esté asociada a una traza en las cámaras de muones. Para mejorar la pureza de la selección de leptones se aplican otros cortes que se muestran en las Tablas 4.1 y 4.2.

Los jets son reconstruidos en el calorímetro utilizando un algoritmo de cono [57] con un radio R $\leq$0.4. La energía de los jets es corregida [58] por la dependencia con la pseudo-rapidez de la respuesta del calorímetro, por la dependencia temporal del calorímetro y por extra E_T debida a interacciones múltiples. Los jets que utilizamos tienen energía corregida E_T > 20 GeV y detector $|\eta|$ < 2.0. Detector η es la pseudo-rapidez del jet calculada con respecto al centro del detector.

La presencia de neutrinos en un suceso se deduce a partir de un desajuste en la energía transversa en el detector. La energía transversa perdida, $\not\!\!E_T$, se define como $-\sum_i[E_{T,i}cos(\phi_i), E_{T,i}sin(\phi_i)]$, donde $E_{T,i}$ es la energía transversa de la torre i del calorímetro calculada con respecto a la coordenada z del suceso, ϕ_i es su ángulo azimutal y la suma es sobre todas las torres del calorímetro. La $\not\!\!E_T$ está corregida restando el momento transverso de la traza del muón y añadiendo en las torres del calorímetro atravesadas por el muón.

El conocimiento de la aceptancia, eficiencias y fondos se basa en simulaciones detalladas de procesos físicos y de respuesta del detector. La aceptancia del detector para sucesos WH se modela utilizando `PYTHIA` [64]. La simulación del detector CDF II reproduce la respuesta del detector y utiliza la misma geometría que en la reconstrucción del suceso. Las interacciones de las partículas al atravesar la materia se simulan con `GEANT3` [63]. El modelo de deriva en la COT utiliza una parametrización de `GARFIELD` [68]. Y la simulación del calorímetro utiliza la parametrización de `GFLASH` [69] junto con `GEANT3`.

Algoritmos de Etiquetado de Jets b

Uno de los aspectos fundamentales de este análisis es la identificación de jets b, dado que el estado final de la señal WH contiene dos quarks b, que se miden en el detector como jets b. Afortunadamente los hadrones B viajan en el detector unos pocos segundos (del orden de pico segundos) antes de desintegrarse en otras partículas, produciendo vértices secundarios, y eso es una ventaja para poder diferenciarlos de jets más ligeros que vienen de vértices primarios. En CDF hay dos algoritmos estándar de etiquetado de jets b los cuales usan en este análisis: vértice secundario (SecVtx) [59] y Jet Probability [60].

- El algoritmo de SecVtx busca vértices secundarios desplazados con respecto al vértice primario para identificar hadrones con una vida media larga. Figura 4.4 ilustra esa idea, donde las trazas de un jet, que ha viajado por el detector unos milímetros antes de desintegrarse en otras partículas, apuntan a un vértice secundario desplazado con respecto al vértice primario.

- El algortimo de Jet Probability usa las trazas asociadas a un jet para calcular la probabilidad de que esas trazas vengan del vértice primario de la interacción. Esta probabilidad se basa en el parámetro de impacto (d_0) de las trazas y sus incertidumbres. La Figura 4.5 muestra cuando el parámetro de impacto es positivo o negativo dependiendo del ángulo entre el jet (apuntando al vértice primario) y las trazas de dicho jet. La distribución de que un jet se haya producido por un hadrón pesado pica en 0. La figura de la izquierda en la Figura 4.7 muestra la distribución de la variable Jet Probability para jets b (círculos rojos), c (círculos vacíos) y jets ligeros (cuadrados vacíos) para sucesos de Monte Carlo.

Después de identificar jets como provenientes de quarks b, todavía existe un 50% de los sucesos de fondo que no contienen jets b en el estado final. Esto ocurre porque quarks ligeros han sido erróneamente identificados con un vértice secundario debido a la resolución del tracking o porque quarks c se desintegran con una vida media lo suficientemente larga como para producir un vértice secundario. Necesitamos una herramienta para poder separar quarks c, y quarks ligeros de quarks b. En este análisis se utiliza un separador de sabores, algoritmo que es capaz de distinguir los sabores de los diferentes jets con una cierta probabilidad. Este algoritmo se ha usado con éxtio en el análisis de la observación del proceso de single top quarks [62]. La Figura 4.12 muestra la variable separador de sabor para quarks b (bottom), quarks c (charm), y quarks ligeros (light), esta variable puede interpretarse como la probabilidad de que un jet haya sido etiquetado como un jet b.

Selección del suceso

Como ya se ha mencionado antes, los sucesos WH se caracterizan por la presencia de un electrón o muón de alto momento transverso, gran energía transversa perdida y dos jets energéticos. La selección básica de sucesos requiere la presencia de un electrón o muón, $\not{E}_T > 20$ GeV y jets con energía transversa corregida $E_T > 20$ GeV y $|\eta| < 2$.

Además de la selección básica, con el fin de mejorar la pureza de la muestra, realizamos algunos cortes adicionales. Se rechazan sucesos:

- con más de un leptón identificado,

- consistentes con $Z \to l^+l^-$ si un leptón y un segundo objeto forman una masa invariante en el rango [76, 106] GeV/c^2,

- cuyo vértice del suceso está en una posición z mas allá de 5 cm de la z de la traza del leptón,

- donde la posición z del vértice del suceso está a más de 60 cm del centro del detector, para asegurarnos una buena reconstrucción del suceso.

Los sucesos seleccionados con este criterio están dominados por producción QCD de bosones W asociados a jets. Para mejorar el cociente de señal sobre fondo para sucesos WH pedimos que haya, al menos, un jet en el suceso que sea identificado como jet b. Se espera que un suceso WH presente dos jets en el estado final pero, debido a la radiación de gluones, solapamiento de jets en el calorímetro e ineficiencias en la reconstrucción de jets, este número puede ser diferente. Por tanto, utilizamos también los sucesos con tres jets.

Los sucesos que pasan el criterio de selección descrito hasta ahora, a excepción del etiquetado de jet b, forman lo que se llama muestra "pretag". La muestra de sucesos se divide en tres regiones. Después de pedir la presencia de dos jets identificados con el algoritmo SECVTX, este tipo de sucesos se llaman SVSV, cuando un jet es identificado con SECVTX y otro con JET PROBABILITY el suceso se conoce como SVJP y cuando sólo un jet es identificado con SECVTX entonces se llama SVnoJP. El corte que se usa en esta análisis para JET PROBABILITY es 5%.

Sucesos de Fondo

Existen varios procesos físicos que contribuyen en la muestra de sucesos candidatos de leptón+jets y que hay que considerarlos como posibles fondos. Hay dos tipos de fondos: fondos físicos modelados por Monte Carlo, y fondos instrumentales. Los fondos dominantes son aquellos que tienen un bosón W en su estado final, $W+$ jets de sabor fuerte ($Wb\bar{b}$, $Wc\bar{c}$, y Wc). Otros fondos que se consideran como posibles candidatos son pares de quarks top ($t\bar{t}$), producción de single top quarks (s-channel y t-channel), Z+jets, y dibosones (WW, WZ, y ZZ).

Los fondos instrumentales son sucesos W+jets de quarks ligeros donde un jet es falsamente etiquetado como un jet b y producción directa de QCD de quarks con sabor fuerte sin un bosón W asociado (non-W QCD).

Todos los fondos que se consideran en este análisis vienen dados en la Tabla 5.3 con sus respectivas secciones eficaces. La secciones eficaces de W+jets y non-W se estiman de los datos. De la Figura 5.2 a la Figura 5.8 se muestran los diagramas de Feynman para cada uno de estos procesos.

Estimación de los Sucesos de Fondos

La estimación de estos fondos se realiza utilizando tanto datos recogidos por el detector CDF como simulaciones Monte Carlo. El método para estimar los fondos utilizado en este análisis se ha utilizado anteriormente para varios resultados que han sido publicados, como por ejemplo, para la medida de la sección eficaz de $t\bar{t}$ [77], para la observación del proceso de single top quark, y para la medida de la sección de producción de dibosones [78]. Este método asume que los sucesos que contribuyen al estado final de leptón+jets consisten en procesos electrodébiles (dibosones, pares de quarks top, single top quarks y Z+jets), producción de QCD, y W+jets.

Procesos Basados en MC

Todos los procesos electrodébiles y de top ($t\bar{t}$ y single top quarks) se estiman utilizando muestras de Monte Carlo. Los sucesos de $t\bar{t}$ pueden contribuir a la muestra de señal cuando un bosón W se desintegra leptónicamente y el otro W no es detectado por el detector. Los sucesos de single top quarks contienen un W que se desintegra leptónicamente y dos quarks, al menos unos de ellos es un quark b. Los sucesos de dibosones (WW, WZ y ZZ) pueden contribuir si uno de los bosones se desintegra leptónicamente y el otro lo hace dando lugar a quarks pesados. El proceso $Z \to \tau^+\tau^-$ también puede contribuir debido a desintegraciones leptónicas del tau.

Los números de sucesos estimados para estos procesos se calculan en base a su sección eficaz teórica, la luminosidad total integrada y las aceptancias y efficiencias de etiquetado calculadas a partir de la simulación Monte Carlo.

Non-W

El fondo de non-W consiste en sucesos para los cuales la signatura de leptón+energía perdida ($\not{E}_T$) no es debida a la desintegración de un bosón W. La principal contribución en este tipo de fondo se debe a producción QCD de jets donde un jet es mal identificado como electrón y la energía perdida es debida a malas medidas de la energía de los jets.

Para estimar este fondo se ajusta la distribución de energía transversal faltante ($\not{E}_T$) a la suma de señal y de todos los fondos y se extrae la fracción de QCD. La fracción de QCD corresponde al cociente del número de sucesos de non-W que pasan el corte de $\not{E}_T$ entre el número de sucesos observados que pasan el corte de $\not{E}_T$. La Figura 6.3 muestra un ejemplo del ajuste para sucesos antes de identificar jets como jets b y la Figura 6.4 para sucesos donde los dos jets son jets b, la flecha indica el corte de $\not{E}_T$ que se aplica en el análisis.

Una vez calculada la fración de QCD el número de sucesos de non-W se puede calcular utilizando las ecuaciones 6.8 y 6.9 para sucesos antes y después de etiquetar jets como jets b, respectivamente.

$W+$ jets de sabor fuerte

Esta es la principal fuente de sucesos de fondo en este análisis. Este fondo consiste en sucesos que presentan un bosón W real asociado a quarks con sabor fuerte. Estos se pueden originar bien en sucesos $q_1\bar{q}_2 \to W + g$ donde el gluon da lugar a pares $b\bar{b}$ o $c\bar{c}$ o bien en sucesos $gq \to Wc$.

La contribución de sucesos de $W+$ jets de sabor fuerte se calcula utilizando la fracción de sabor fuerte en la producción de bosones W asociados con partones y las eficiencias de etiquetado para estos procesos, y normalizando por el número de sucesos observados en la muestra pretag menos las contribuciones de procesos electrodébiles, de top y non-W también en la muestra pretag (ecuación 6.10).

$W+$ jets de sabor ligero

Sucesos en los que un jet de sabor ligero es identificado como jet de sabor fuerte también contribuyen a la muestra de señal. El número de sucesos en la muestra pretag con etiquetados negativos podría ser una estimación de este fondo, pero presenta el problema de tener una gran incertidumbre estadística. En vez de esto, se cuentan los sucesos en la muestra pretag y se pesan por la probabilidad de tener, al menos, un jet mal identificado. Esta probabilidad se calcula aplicando la matriz de etiquetado negativo a todos los jets "taggable" de la muestra. Taggable jets son aquellos jets que tienen al menos dos trazas reconstruidas que pasan los cortes de calidad.

Una vez hecha esta estimación, se escala por el número de sucesos observados en la muestra pretag menos las contribuciones de procesos electrodébiles, de top, de non-W, de $W+$ jets de sabor fuerte también en la muestra pretag, como muestras la ecuación 6.11.

Las predicciones finales para sucesos con dos (tres) jets en el estado final se muestran en la Tabla 6.2 (Tabla 6.3).

Método de Elementos de Matriz

La búsqueda del bosón de Higgs no es tarea fácil. Uno de las mayores desventajas del canal WH es que la sección eficaz de producción es varios órdenes de magnitud menor que la de los fondos. Se dice que buscar el bosón de Higgs es como buscar una aguja en un pajar, muy difícil. Para eso no basta con una sola variable discriminatoria, como la masa invariante de los dos jets de mayor energía del suceso, véase Figura 7.1, sino que se necesita una herramienta más sofisticada que contenga toda la información del suceso.

En este análisis se usa el método de elementos de matriz. La idea general es que se calcula la probabilidad de que un suceso dado sea un suceso de señal o de fondo. La probabilidad es función de los cuadro-momentos del leptón y de los jets del estado final, es decir es función de toda la información que se conoce del suceso. Pero además hay que incluir varias aspectos ya que el detector no es perfecto. Hay que tener en cuenta el hecho de que los partones que colisionan están contenidos dentro de protones y antiprotones, así que hay que incluir las funciones de distribución de los partones (PDF), también hay que tener en cuenta que el neutrino no es medido por el detector así que hay que integrar sobre el momento del neutrino, y hay que incluir la resolución en energía del detector. Finalmente, la probabilidad viene dada por esta ecuación:

$$P(x) = \frac{1}{\sigma} \int 2\pi^4 |M|^2 \frac{f(y_1)}{|E_{q_1}|} \frac{f(y_2)}{|E_{q_2}|} W(y,x) d\Phi_4 dE_{q_1} dE_{q_2} \tag{A.1}$$

donde σ es la sección eficaz de un proceso dado, $|M|^2$ es el elemento de matriz del proceso, en este análisis se ha calculado usando el paquete HELAS (HELicity Amplitude Subroutines for

Feynman Diagram Evaluations) [80], $f(y_i)$ son las funciones de distribución de los partones, E_{qi} son las energías de los partones, $W(y,x)$ es la función de transferencia y $d\Phi_4$ es el espacio de fase para cuatro elementos en el estado final.

La función de transferencia es una parametrización de la diferencia entre la energía del partón y la energía del jet medido (E_p - E_j), véase Figura 7.3 para conocer el tipo de función a la que nos referimos. La distribución es asimétrica, tiene una cola para valores positivos de esta diferencia. Para parametrizar esta función se usa la suma de dos funciones gausianas, una de ella modela el pico de la distribución y la otra la cola. La ecuación 7.6 corresponde a esta parametrización.

Una de las mejoras de este análisis ha sido usar el output de una red neural (NN_{output}) en vez de la E_j para obtener un valor más aproximado de E_p. La Figura 7.6 muestra la diferencia entre la energía del partón y la energía medida (en negro) y entre la energía del partón y el output de la red neural (en rojo) para sucesos de WH ($\mathrm{m}_H = 115$ GeV/c^2), $Wb\bar{b}$, dibosones, y Wgg. Como se puede ver la E_p - NN_{output} es más estrecha y está más centrada en cero que E_p - E_j, esto mejora el resultado final entre un 3% y un 7%, dependiendo de la masa del bosón de Higgs.

Las probabilidades que se calculan para esta tesis son: WH [100-150] GeV/c^2, $Wb\bar{b}$, $t\bar{t}$, s-channel, t-channel, $Wc\bar{c}$, Wcg, Wjg, Wgg, WW, and WZ para sucesos con dos jets y todas las anteriores menos Wcg, Wjg, Wgg, WW, and WZ para sucesos con tres jets. Después se convinan en un discriminante (EPD, que viene del término en inglés Event Probability Discriminant), que es el cociente de la probabilidad de señal (P_s) entre la probabilidad de señal junto con la suma de todas las probabilidades de los fondos (P_f), $EPD = P_s/(P_s + \sum_i P_{fi})$. Además de las probabilidades, en este discriminante también se incluye información no cinemática del suceso. Cada probabilidad lleva asociado un coeficiente que se optimiza, para cada masa de Higgs, para mejorar el cociente entre señal y fondo. La otra variable no cinemática que se incluye en el discriminante es el separador de sabor, mencionado anteriormente, que se utiliza como un peso por suceso expresando la probabilidad de que los jets de un suceso dado sean identificados como un jet b.

Los discriminantes que se utilizan en este análisis vienen dados por las ecuaciones 7.11 y 7.12. Hay dos tipos de EPD: el primero (7.11) para sucesos con sólo un jet SecVtx, donde se utiliza el separador de sabor del jet b, y el segundo (7.12) para sucesos con dos jets SecVtx, donde se utilizan los separadores de sabor de los dos jets b.

Resultados

Finalmente, se busca un exceso de sucesos de señal de Higgs en las distribuciones del discriminante (EPD) construido con las probabilidades de que un suceso dado sea señal o de fondo, pero no se ha encontrado ninguna evidencia de tal exceso en los sucesos observados por CDF. Así que se calculan los límites para sucesos que pasan la selección, sucesos que contienen un leptón (electrón o muón) y dos o tres jets, con al menos uno de ellos identificado como un jet b, en el estado final.

Las Figuras 7.15 and 7.16 muestran las distribuciones del discriminante EPD, para dos y tres jets respectivamente, aplicado a las muestras de sucesos observados comparado con las distribuciones esperadas.

Para extraer el valor más probable de WH del contenido en los datos, las distribuciones del EPD para la señal y para los fondos se ajustan a los sucesos observados por CDF usando una técnica de máxima verosimilitud. La función de verosimilitud utilizada viene dada por el producto de las probabilidades Poissonianas de cada bin de cada histograma de la variable discriminante en cada región de señal (hay 12 regiones de señal: 3 categorías de etiquetado, dos tipos de leptones y dos y tres jets). Las probabilidades de Poisson son función del número de sucesos n_k observados y de las predicciones μ_k en cada bin k dadas en la ecuación 8.1. Todas las fuentes de errores sistemáticos se incluyen en la función de verosimilitud, y esto complica un poco la expresión de verosimilitud, ecuación 8.5. Las fuentes de errores sistemáticos que se tienen en cuenta en este análisis son las incertidumbres en:

- la escala de energía de los jets (JES),
- la cantidad de radiación en el estado inicial (ISR),
- la cantidad de radiación en el estado final (FSR),
- los errores en las funciones de distribución de los partones (PDF),
- la luminosidad,
- las efficiencias de etiquetado de jets,
- la identificación de leptones.

Cuando una fuente de incertidumbre afecta tanto a la forma como a la normalización, ambos efectos son tratados como 100% correlacionados. Por último, las incertidumbres estadísticas debido al limitado tamaño de las muestras de Monte Carlo son tenidas en cuenta bin a bin.

Los límites se calculan para once valores de m_H, de $100 \leq m_H \leq 150$ GeV/c^2 en saltos de 5 GeV. Los límites vienen dados como la sección eficaz de producción de WH multiplicada por el cociente de desintegración, en unidades del Modelo Estándar, $(\sigma(p\bar{p} \to WH) \times BR(H \to b\bar{b})/SM)$. Los resultados finales pueden verse en la Section 8, Tablas 8.4, 8.6, y 8.8.

Conclusiones

En esta tesis se presenta la búsqueda directa del bosón de Higgs del Modelo Estándar producido en asociación con un bosón W, en un estado final donde el bosón de Higgs se desintegra en dos jets b, y el W se desintegra leptónicamente. Este canal es el más prometedor para la búsqueda del bosón de Higgs a baja masa, es decir cuando la masa es menor que 135 GeV. Hay otros canales que complementan al WH para la búsqueda a baja masa, por ejemplo, aquellos en donde el bosón de Higgs es producido en asociación con un bosón Z, pero el producto de la sección eficaz de producción por el cociente de desintegración es más favorable para sucesos de WH.

La selección de sucesos viene dada por el estado final del bosón de Higgs asociaciado con un bosón W, en el que tenemos un leptón (electrón o muón) de alto momento, energía transversal faltante para contar con el neutrino y dos o tres jets con al menos uno de ellos identificado con jet b para aunmentar la pureza de la muestra.

Dado que la cantidad de señal después de la selección de sucesos es mucho menor que la incertidumbre en la predicción de los fondos, para alcanzar una máxima sensibilidad, esta búsqueda se realiza utilizando una técnica de elementos de la matriz. Con esta técnica se calculan las probabilidades de que un suceso sea señal y fondo y se utilizan para crear una discriminante (EPD). Para extraer el valor más probable de WH del contenido en los sucesos observados, las distribuciones del EPD para la señal y para los fondos se ajustan a los sucesos observados por CDF usando una técnica de máxima verosimilitud. Todas las fuentes sistemáticas e incertidumbres se incluyen en la función de verosimilitud.

Analizando 4.8 fb^{-1} de los datos recogidos por el detector CDF, no se observa evidencia de señal del bosón de Higgs. Así que se procede a estimar los límites superiores con un nivel de confianza del 95%. Los límites superiores esperados para la sección eficaz de producción de WH multiplicada por el cociente de desintegración, en unidades del Modelo Estándar ($\sigma(p\bar{p} \to WH) \times BR(H \to b\bar{b})/SM$), para masas de Higgs entre 100 y 150 GeV son menores que 3.0 a 32.2, con un nivel de confianza del 95%, dependiendo de la masa del bosón Higgs. Lo que significa que se ha excluido la existencia del bosón de Higgs con $\sigma(p\bar{p} \to WH) \times BR(H \to b\bar{b})/SM$ mayor que dichos valores.

Para comprobar la mejora que este método de elementos de matriz tan complicado nos da con respecto al hecho de usar una sola variable discriminatoria, se calculan los límites usando la masa invariante de los dos jets de mayor energía del sucesos (M_{jj}) en vez del EPD. Se elige M_{jj} ya que es la variable con mayor poder de discriminación de este análisis. La conclusión en este caso es que merece la pena usar este método que utiliza toda la información cinemática del suceso ya que mejora el resultado final en un 20% con respecto a M_{jj}.

Está planeado correr el Tevatron durante todo 2011, eso supondrá un aumento de luminosidad integrada más del doble de la luminosidad que se usa en este análisis. Muchas mejoras quedan por incorparar a este análisis a parte de las que ya hemos incluido hasta ahora como por ejemplo nuevos triggers que aún no han sido usados en este análisis, diferente regiones de señal depediendo del tipo de jets b, también se puede aumentar la aceptancia de los sucesos de señal reduciendo los cortes de la selección básica de sucesos. Estas mejoras junto con el incremento en luminosidad harán que se obtengan límites mucho más cercanos a las predicciones dadas por el Modelo Estándar. Figura 9.4 muestra las projecciones de los límites superiores esperados para una masa de Higgs de 115 GeV/c^2 en función de la luminosidad integrada. Combinando los resultados de DØ y CDF podremos excluir un bosón de Higgs de 115 GeV/c^2 con una luminosidad integrada entre 10 y 12 fb^{-1}.

Estamos viviendo momentos muy emociaonantes en lo que concerne a la búsqueda del bosón de Higgs y sobre cuanto tiempo más debe seguir el Tevatron funcionando, ya que el LHC no será competivo en sus primeros años de funcionamiento si el bosón de Higgs tiene una masa menor a 130 GeV.

Appendix B

Feynman Diagrams

In this appendix are shown the Leading order Feynman diagrams for signal and background used in this analysis. In Figures B.1 to B.6 are the Feynman diagrams for 2-jet events, in Figures B.7 to B.10 are the ones for 3-jet events.

B.1 Two jets final state

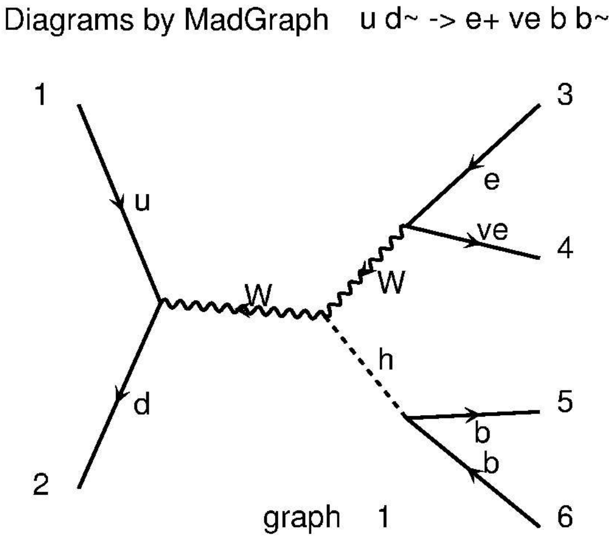

Figure B.1: Leading order Feynman diagram for Higgs production in association with a W boson for 2-jet events. The Higgs boson is set to decay into a pair of bottom quarks.

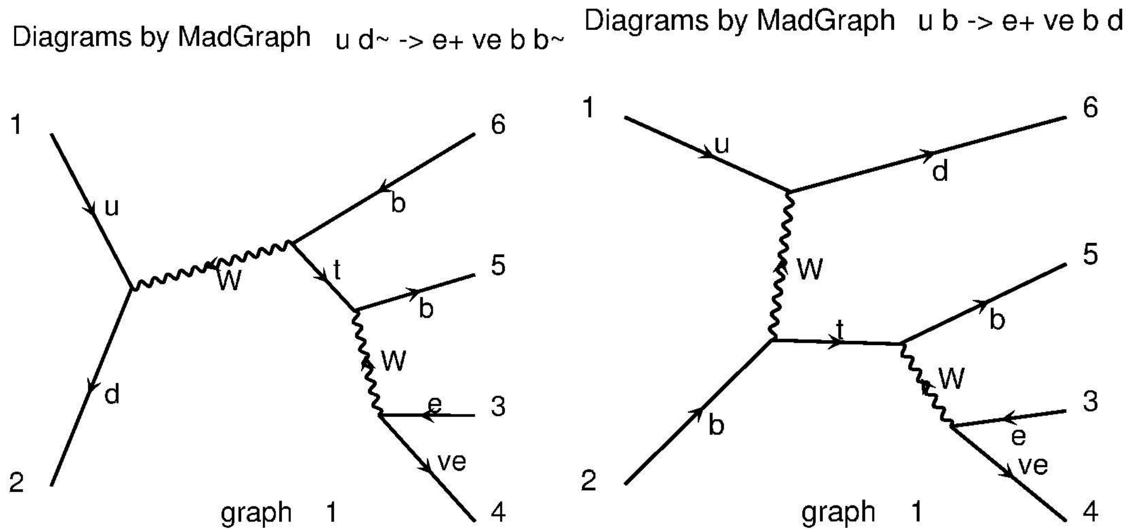

Figure B.2: Leading order Feynman diagram for s-channel (left) and t-channel (right) single top quark production and decay used in the calculation of the single top event probability for 2-jet events.

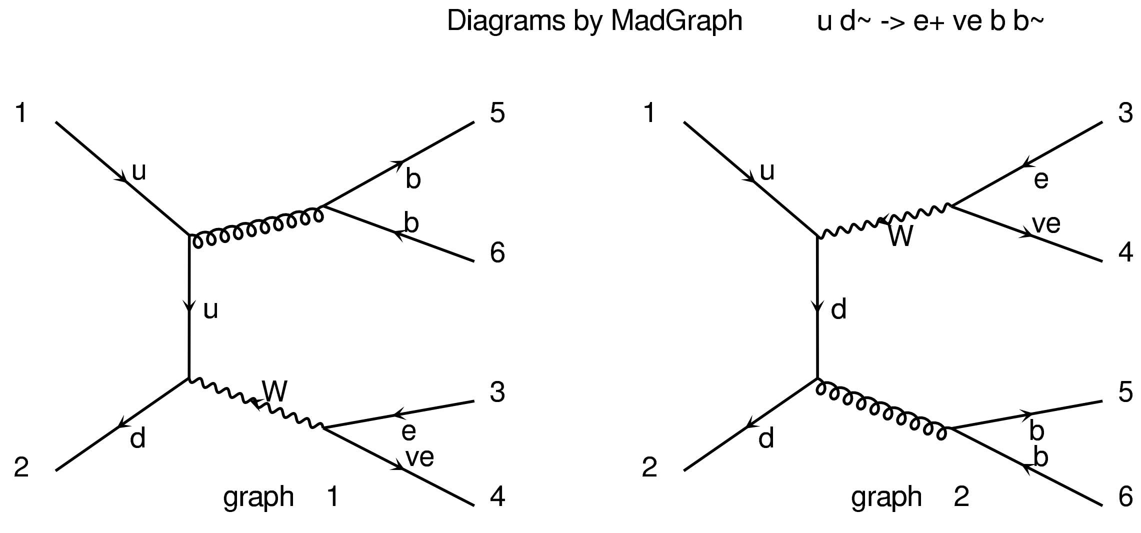

Figure B.3: Leading order Feynman diagram for $Wb\bar{b}$ production and decay used in the calculation of the $Wb\bar{b}$ event probability for 2-jet events.

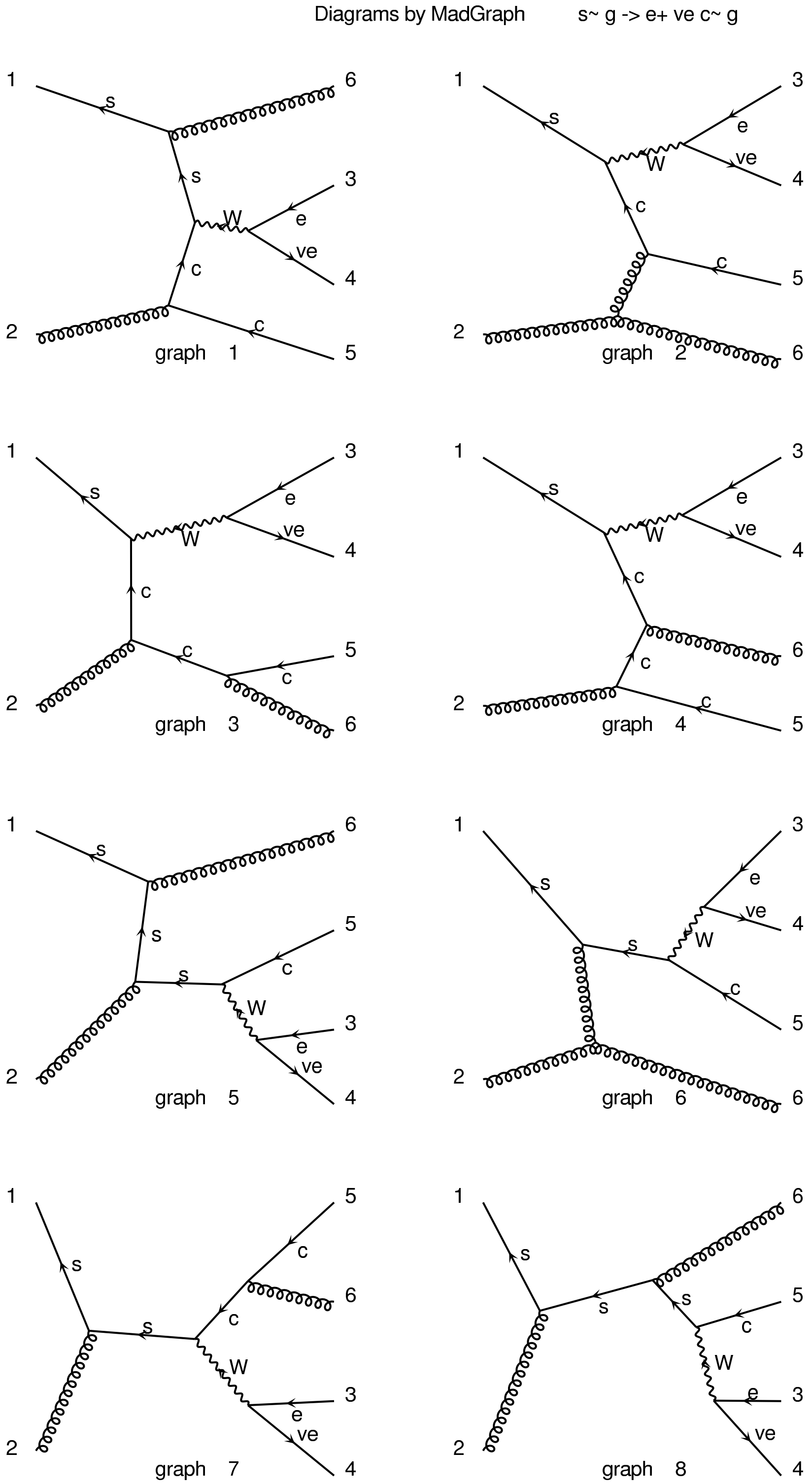

Figure B.4: Leading order Feynman diagrams for Wcj production and decay used in the calculation of the event probability density for 2-jet events.

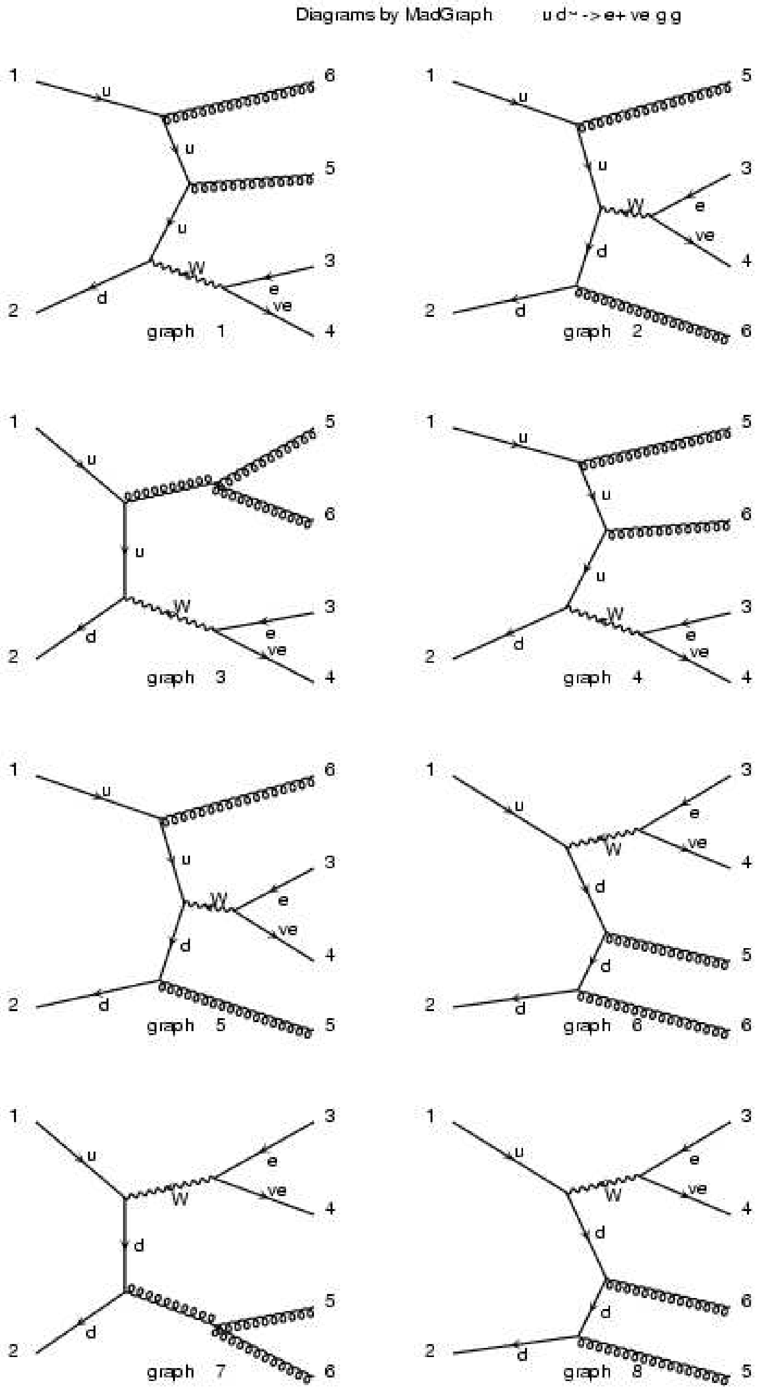

Figure B.5: Leading order Feynman diagrams for Wgg production and decay used in the calculation of the event probability density for 2-jet events.

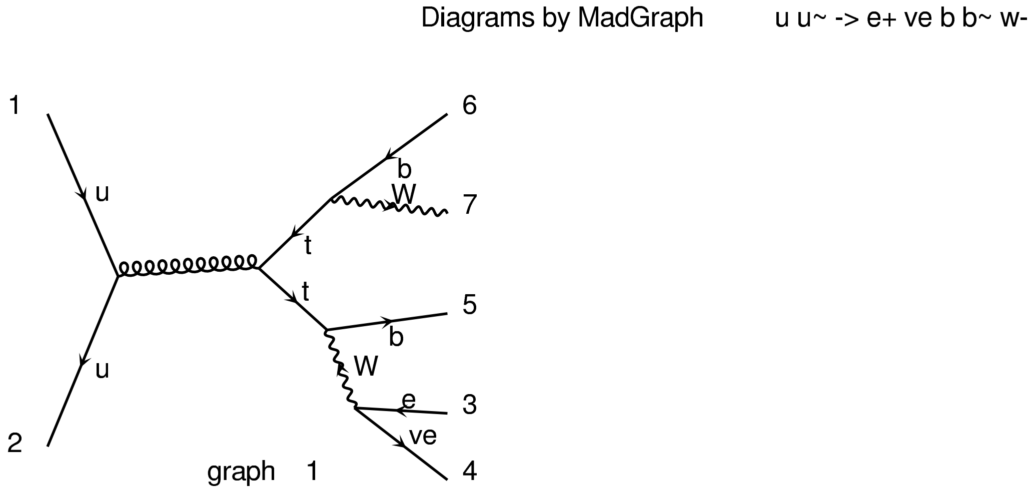

Figure B.6: Leading order Feynman diagrams for $t\bar{t}$ production and decay used in the calculation of the $t\bar{t}$ event probability for 2-jet events.

B.2 Three jets final state

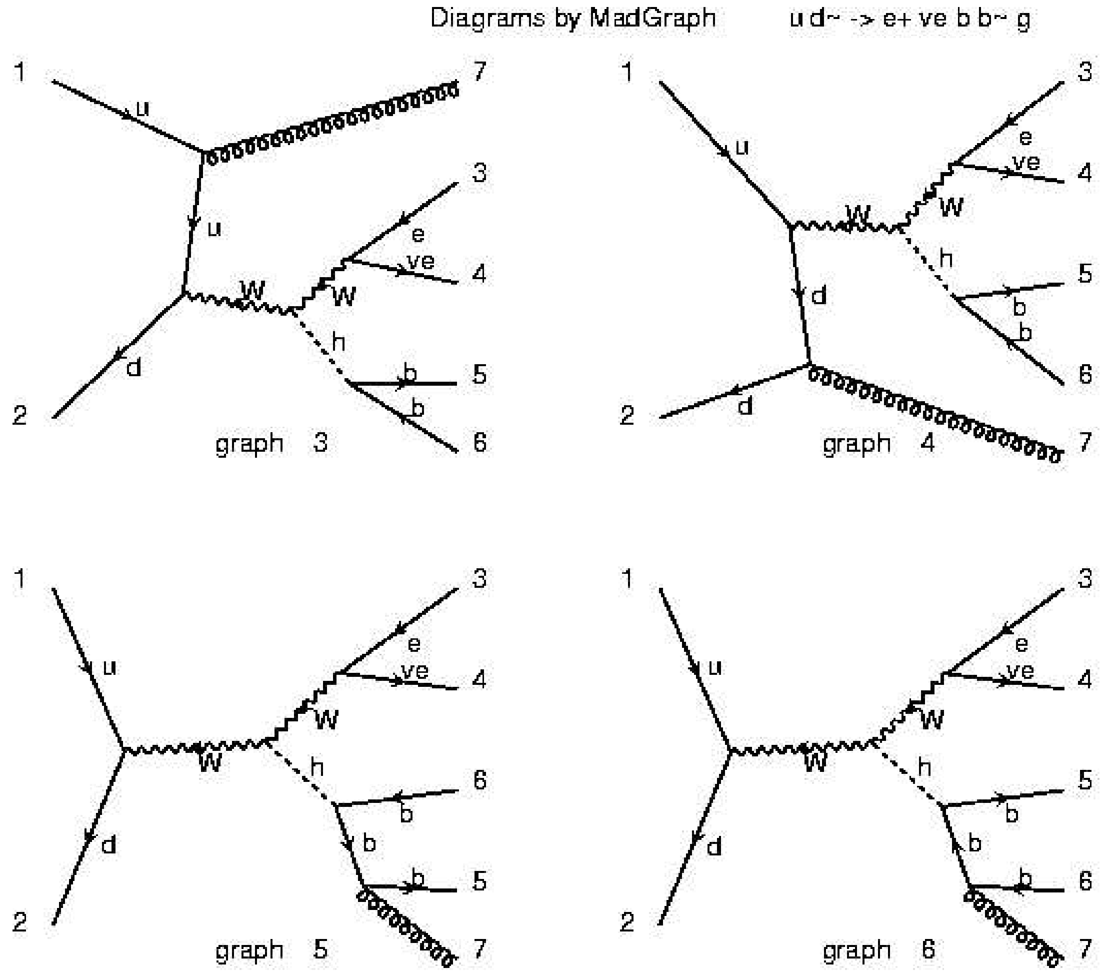

Figure B.7: Feynman diagram for Higgs production in association with a *W* boson in the 3-jets final state. Diagrams with a *ggh* coupling (not shown) have not been used in the calculation of matrix elements as they are heavily suppressed.

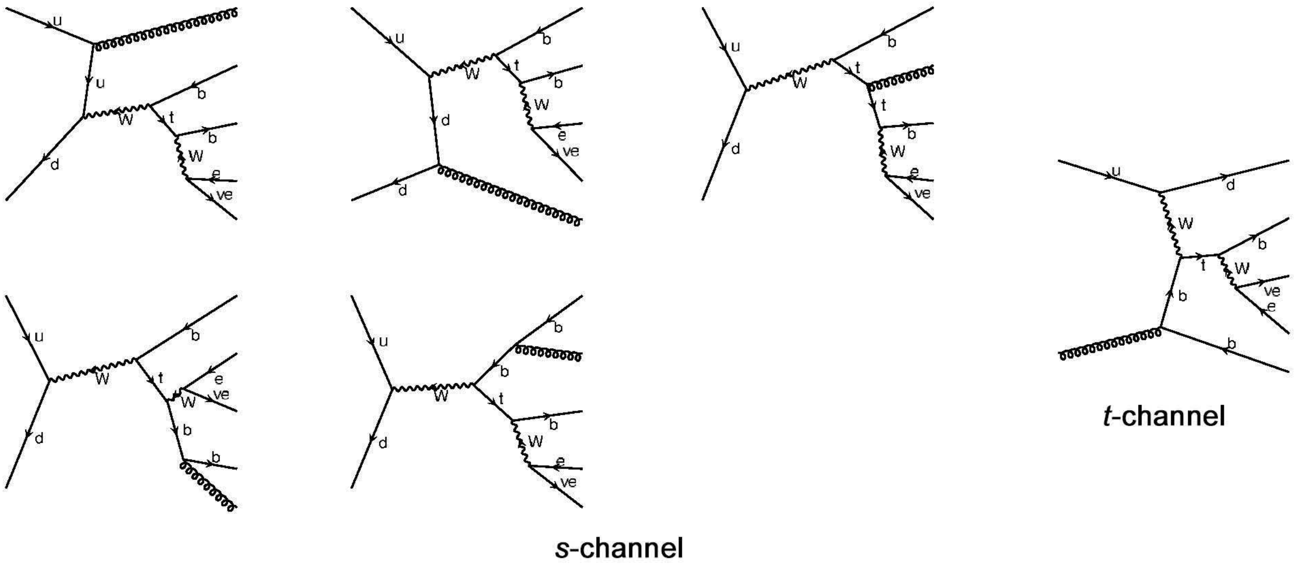

s-channel

t-channel

Figure B.8: Feynman diagram for s-channel (left) and t-channel (right) single top quark production and decay used in the calculation of the single top event probability for 3-jet events.

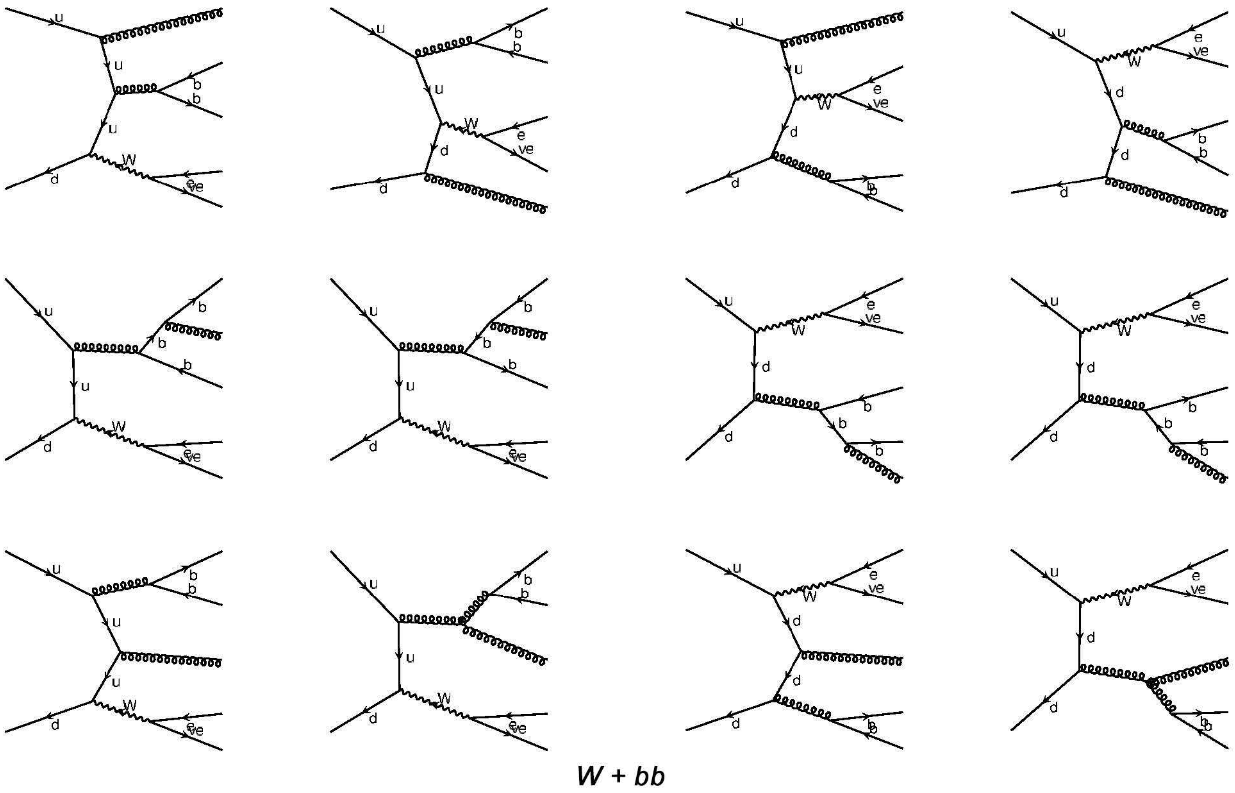

Figure B.9: Feynman diagram for $Wb\bar{b}$ production and decay used in the calculation of the $Wb\bar{b}$ event probability for 3-jet events. The Feynman diagram for $Wc\bar{c}$ is obtained by replacing of the b quarks by c quarks.

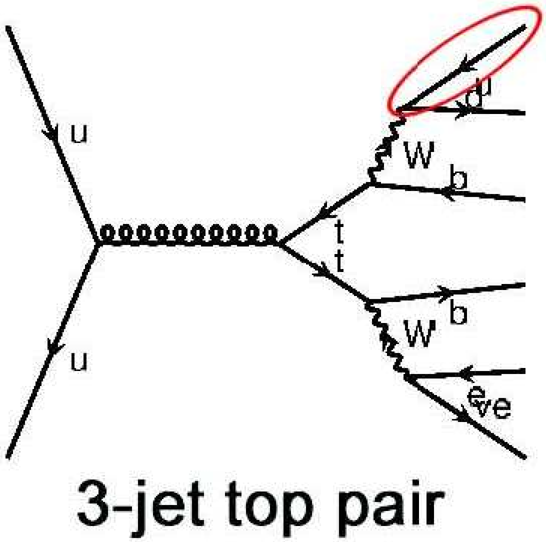

Figure B.10: Feynman diagrams for $t\bar{t}$ production and decay used in the calculation of the $t\bar{t}$ event probability for 3-jet events. One of the decay products of the hadronic W (circled) is assumed to be unobserved and an integral is taken over its momemta.

Appendix C

Neural Network Input Variables

In Figures C.1 to C.3, the distributions comparing data and Monte Carlo predictions for all the Neural Network input variables are shown in the signal regions, with at least one SecVtx jet, as well as in the untagged control regions.

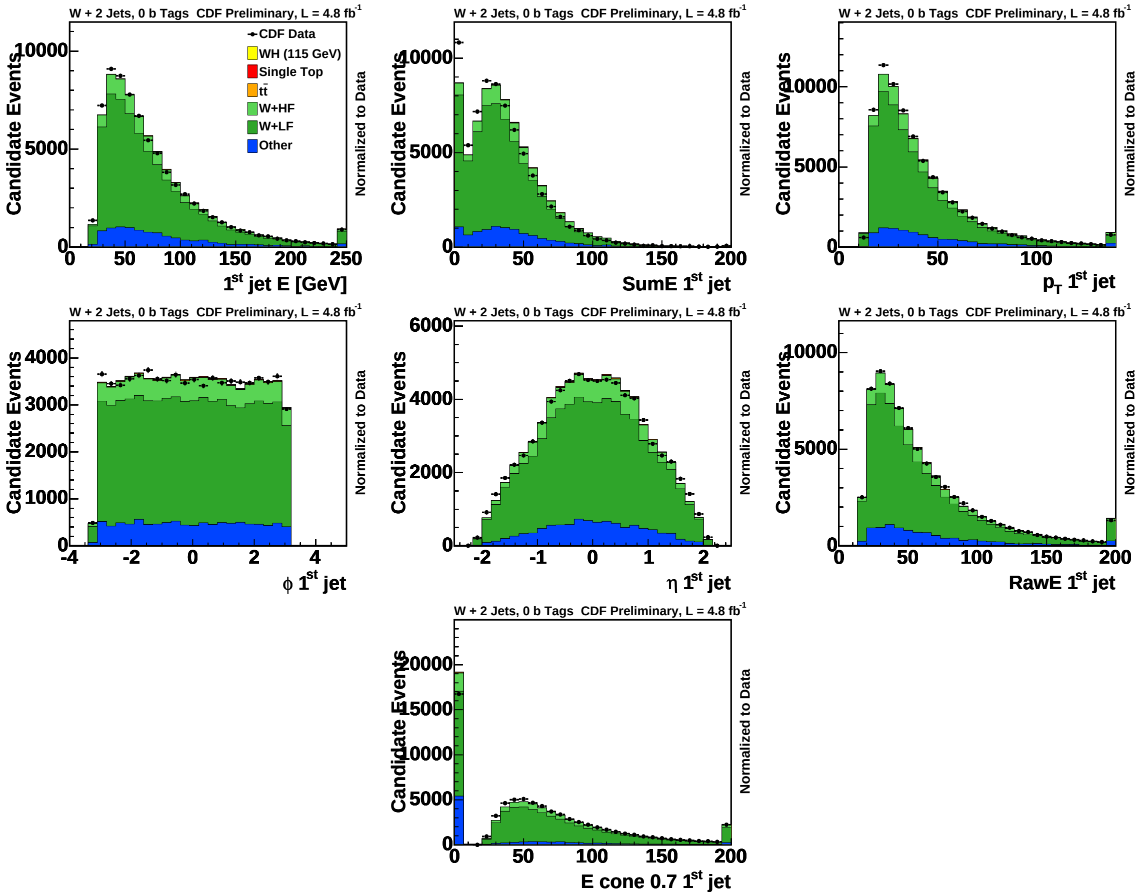

Figure C.1: E$_j$, SumE, p$_T$, ϕ, η, RawE$_j$, and Ejcone7 of the 1st leading jet distributions for 2-jet untag events.

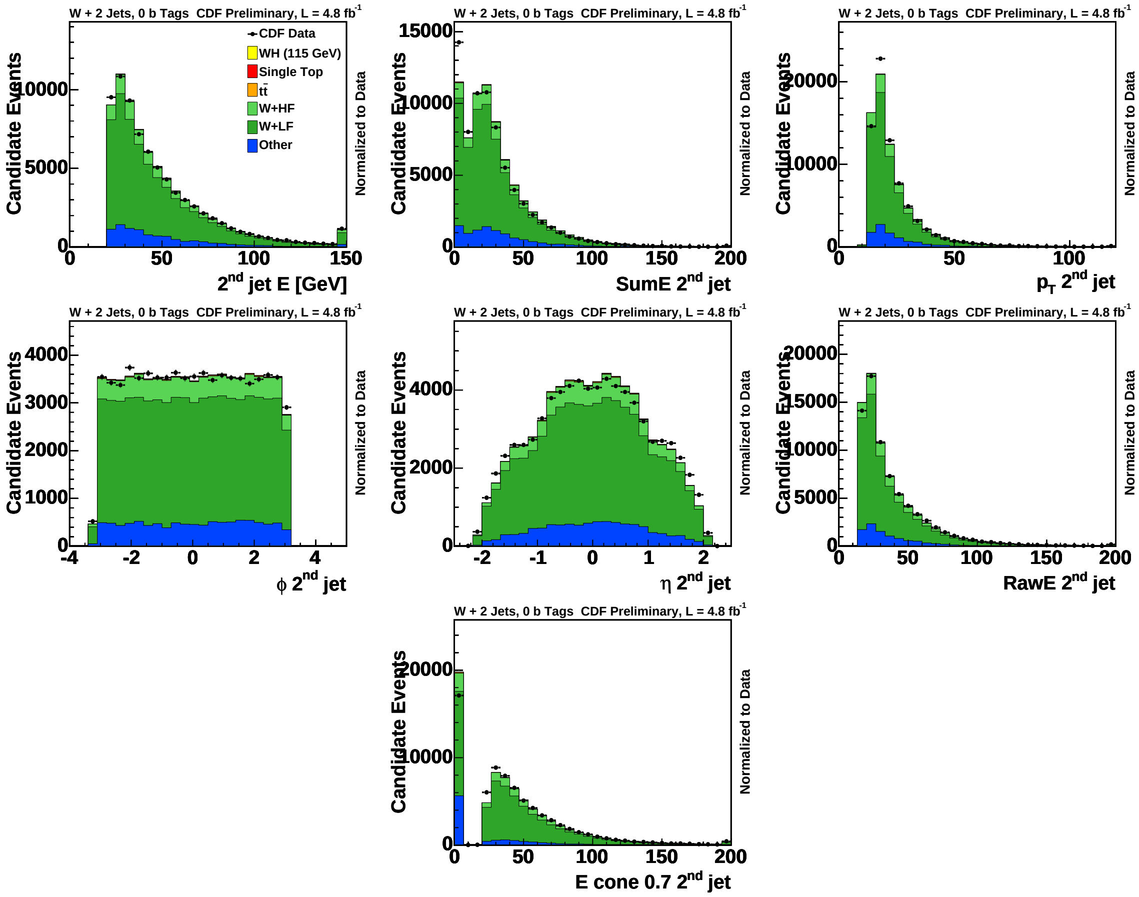

Figure C.2: E_j, SumE, p_T, ϕ, η, RawE_j, and Ejcone7 of the 2^{nd} leading jet distributions for 2-jet untag events.

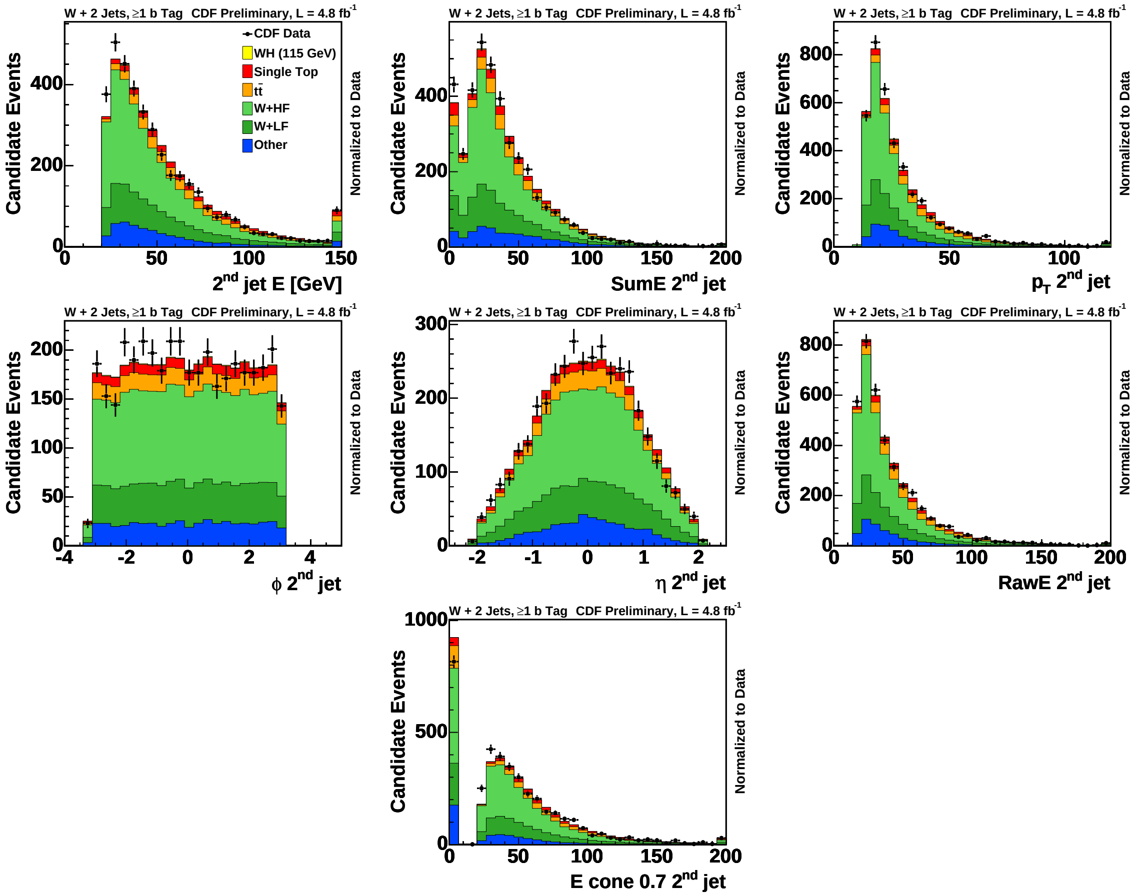

Figure C.3: E$_j$, SumE, p$_T$, ϕ, η, RawE$_j$, and Ejcone7 of the 2nd leading jet distributions for 2-jet tagged events.

Appendix D

Input Variables for Matrix Element Calculation

In Figures D.1 to D.8, the distributions comparing data and Monte Carlo predictions for all the input variables for the ME calculation are shown in the signal regions as well as in the untagged control regions.

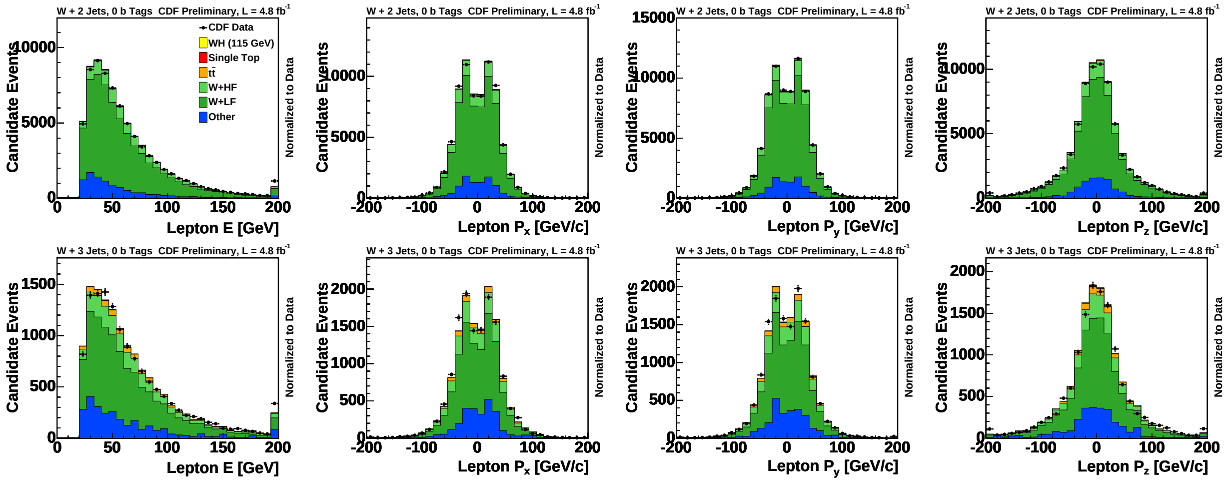

Figure D.1: Top (bottom): The four-vector of the lepton for 2-jet (3-jet) untag events.

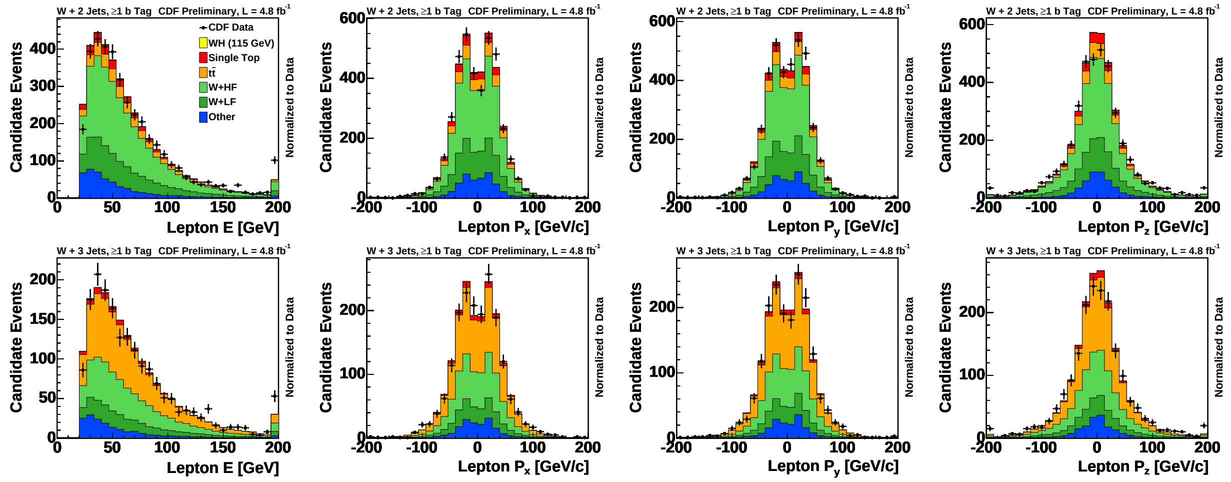

Figure D.2: Top (bottom): The four-vector of the lepton for 2-jet (3-jet) tagged events.

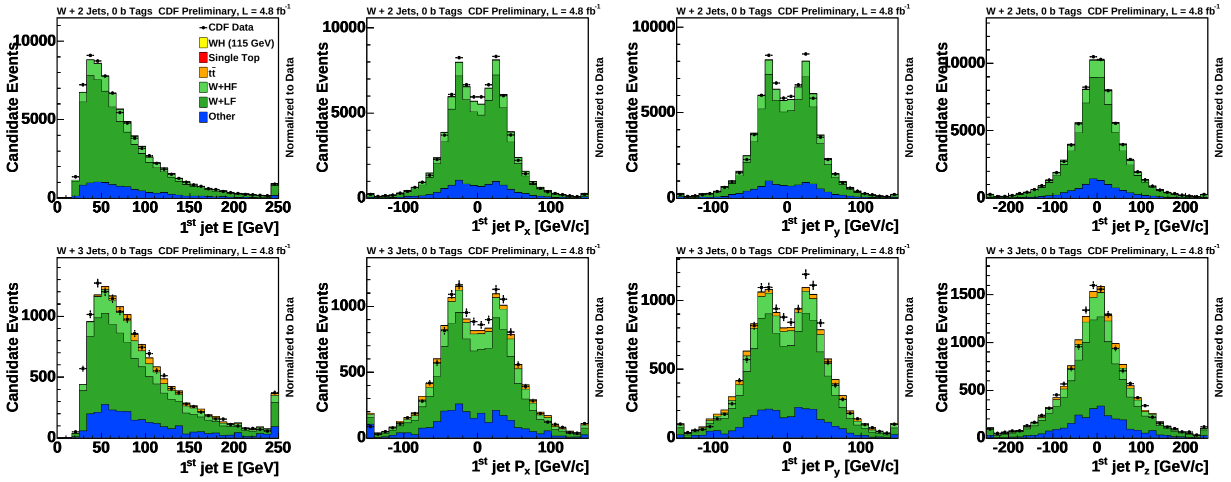

Figure D.3: Top (bottom): The four-vector of the 1^{st} leading jet for 2-jet (3-jet) untag events.

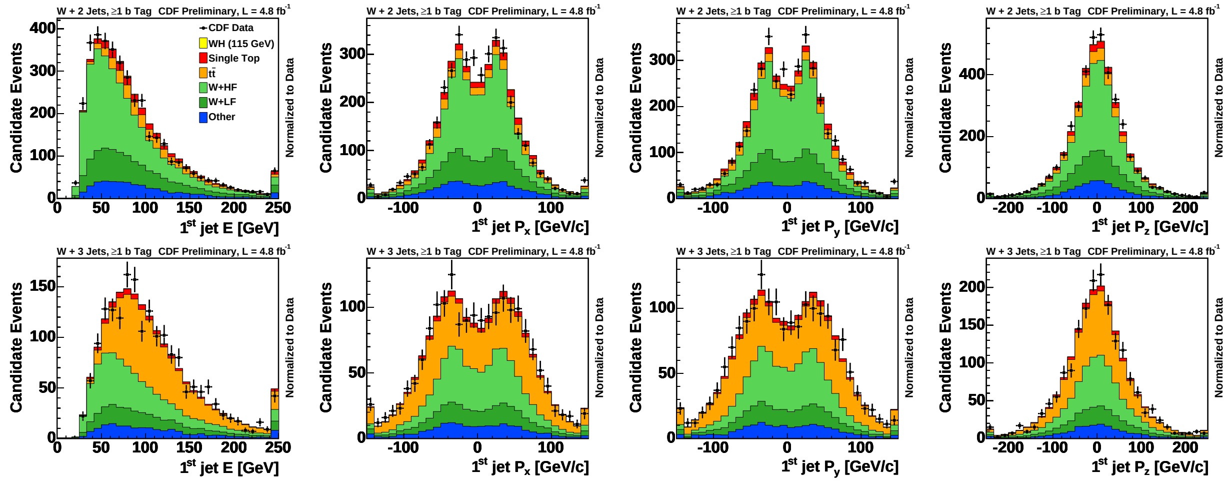

Figure D.4: Top (bottom): The four-vector of the 1^{st} leading jet for 2-jet (3-jet) tagged events.

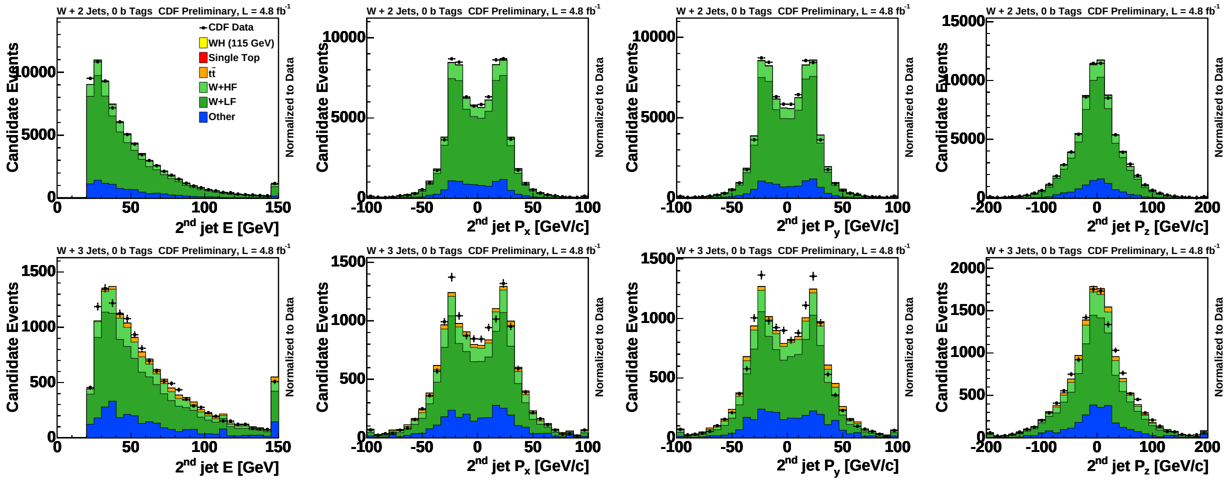

Figure D.5: Top (bottom): The four-vector of the 2^{nd} leading jet for 2-jet (3-jet) untag events.

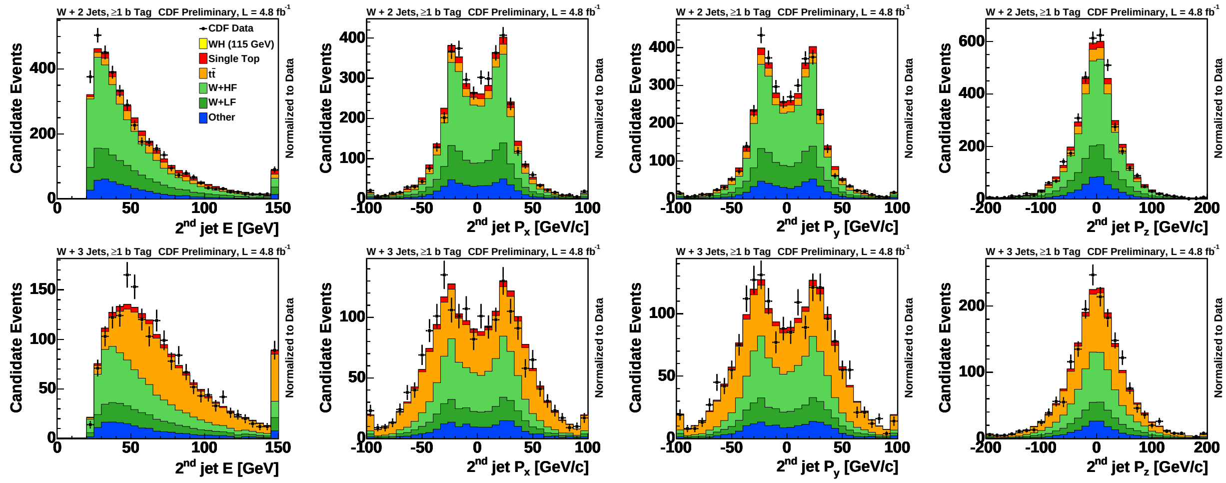

Figure D.6: Top (bottom): The four-vector of the 2^{nd} leading jet for 2-jet (3-jet) tagged events.

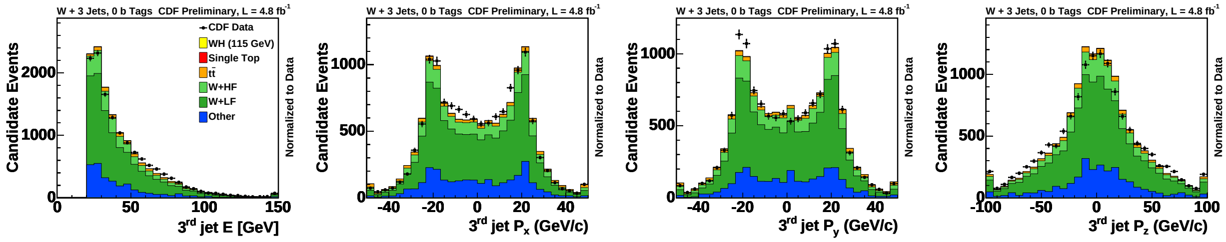

Figure D.7: The four-vector of the 3^{rd} leading jet for 3-jet untag events.

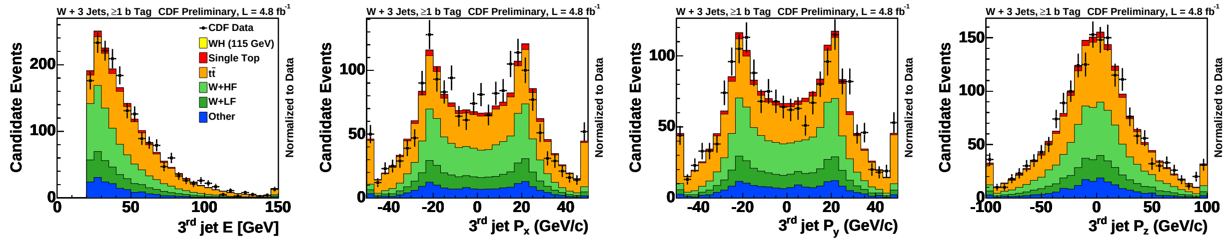

Figure D.8: The four-vector of the 3^{rd} leading jet for 3-jet tagged events.

Appendix E

Event Probability Distribution

Figures E.1 to E.8 show the event probability densities for all the background processed that have been calculated in this thesis.

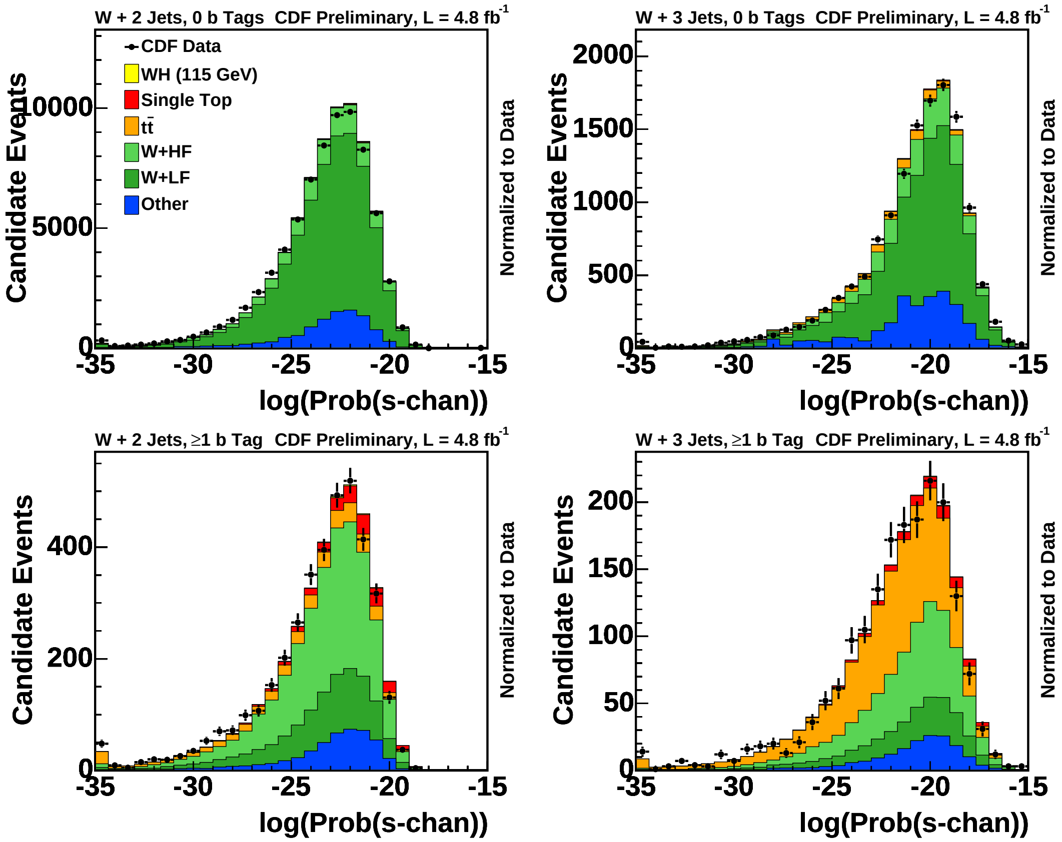

Figure E.1: Event Probability Densities for s-channel 2-jet pretag, 3-jet pretag, 2-jet tagged and 3-jet tagged events.

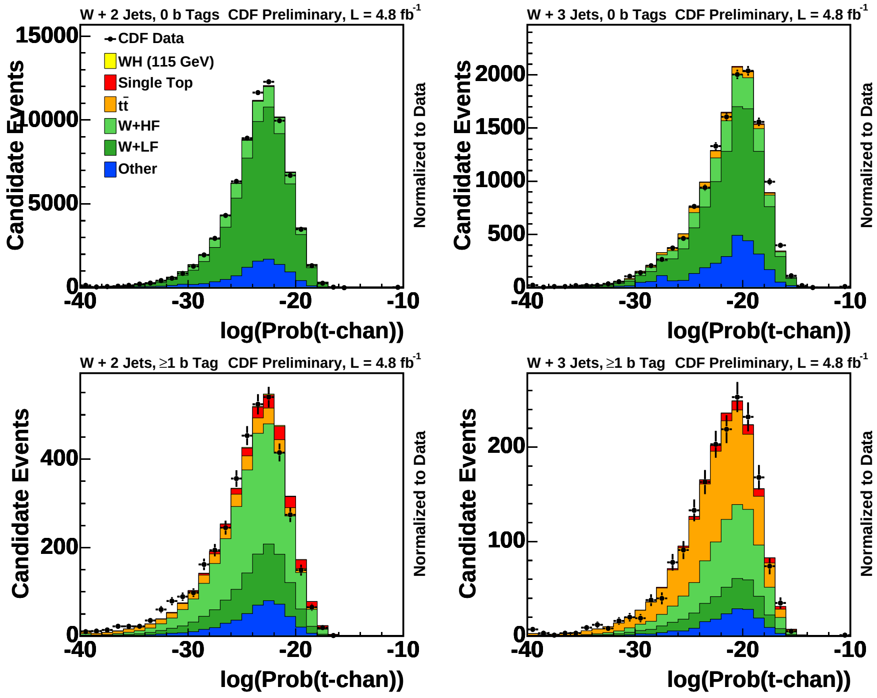

Figure E.2: Event Probability Densities for t-channel 2-jet pretag, 3-jet pretag, 2-jet tagged and 3-jet tagged events.

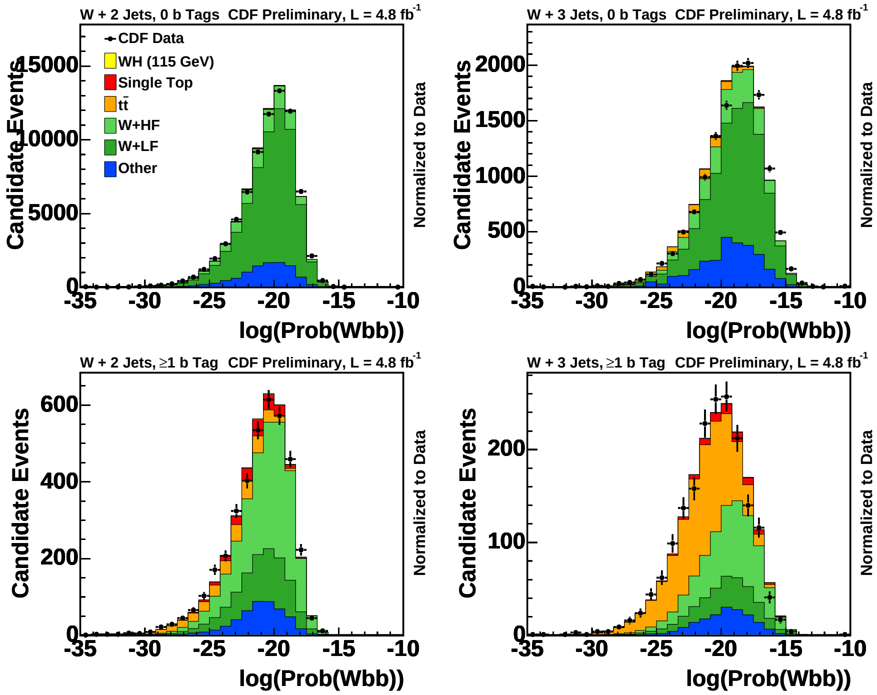

Figure E.3: Event Probability Densities for $Wb\bar{b}$ 2-jet pretag, 3-jet pretag, 2-jet tagged and 3-jet tagged events.

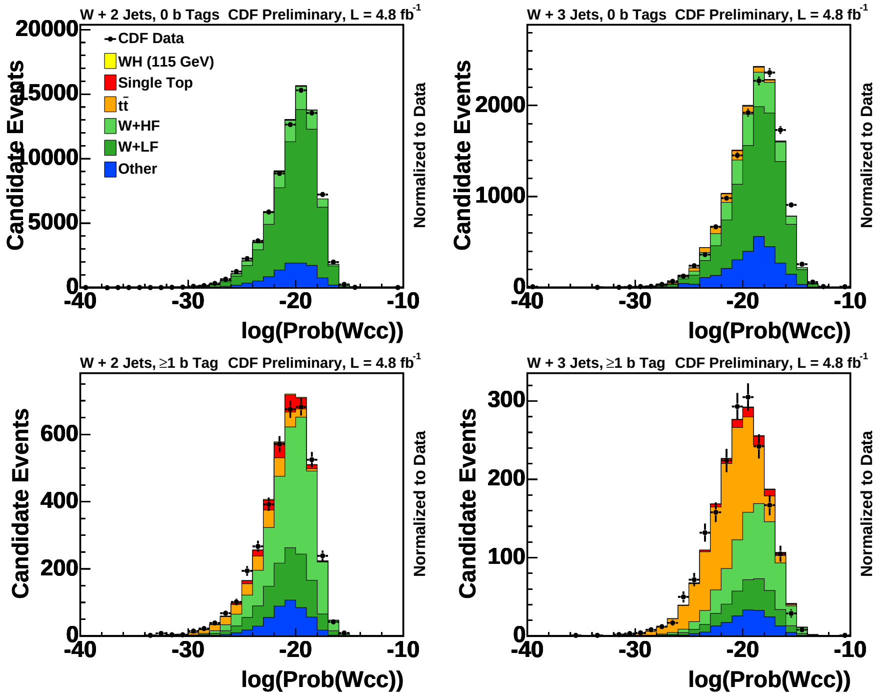

Figure E.4: Event Probability Densities for $Wc\bar{c}$ 2-jet pretag, 3-jet pretag, 2-jet tagged and 3-jet tagged events.

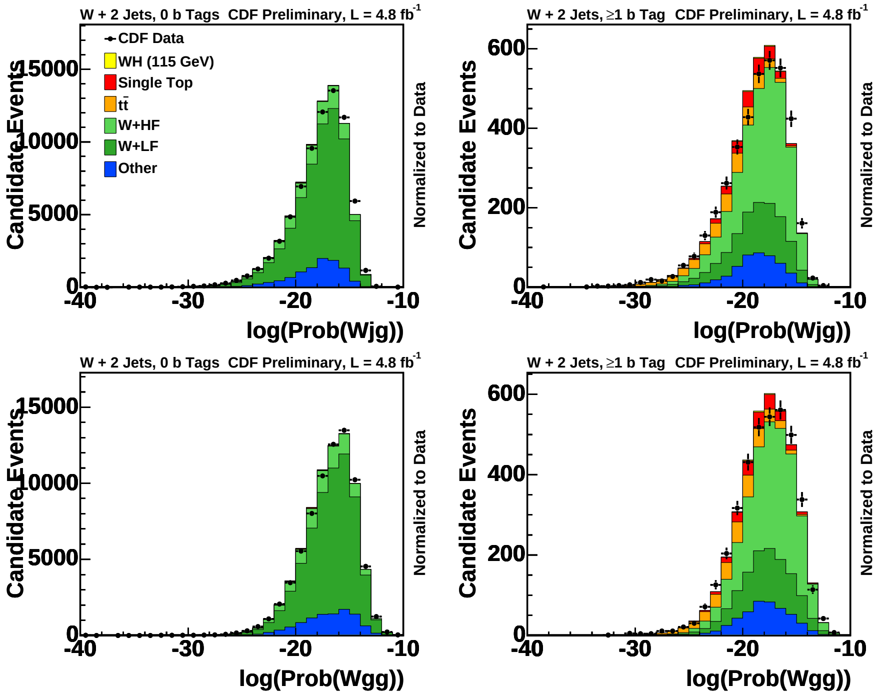

Figure E.5: Event Probability Densities for Wjg (left two plots) and Wgg (right two plots) 2-jet pretag, 3-jet pretag, 2-jet tagged and 3-jet tagged events.

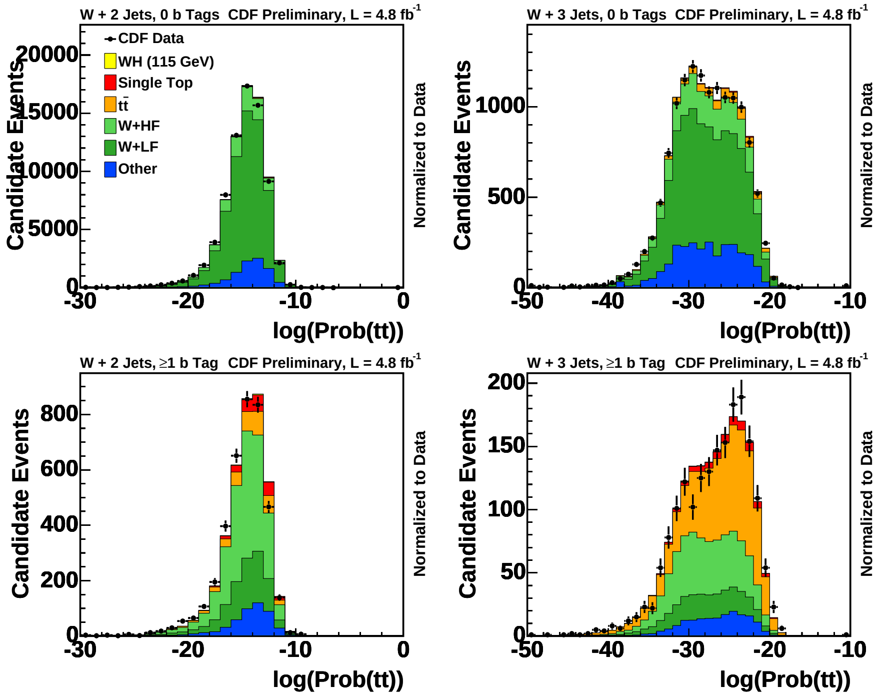

Figure E.6: Event Probability Densities for $t\bar{t}$ 2-jet pretag, 3-jet pretag, 2-jet tagged and 3-jet tagged events.

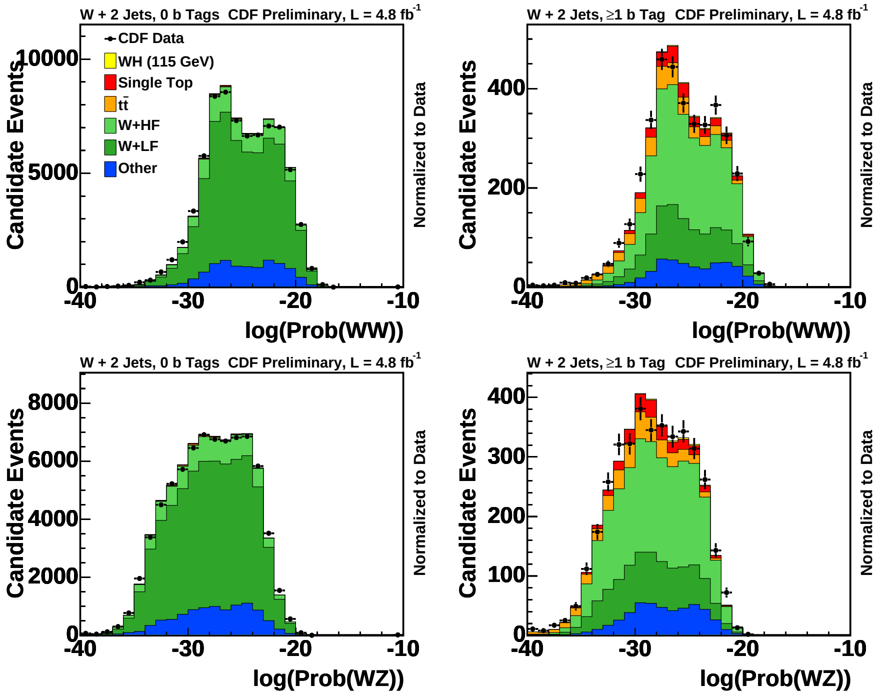

Figure E.7: Event Probability Densities for WW (left two plots) and WZ (right two plots) 2-jet pretag, and tagged events.

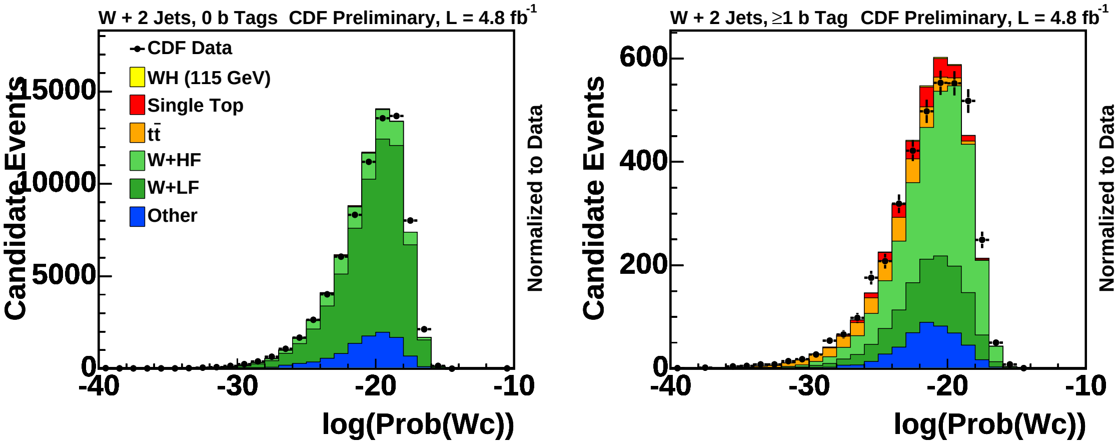

Figure E.8: Event Probability Densities for Wc 2-jet pretag, and tagged events.

Appendix F

Jet Energy Scale Shape Systematics

Variations of the Jet Energy Scale for 2 and 3 jet events for background events, $t\bar{t}$ and W+jets, are shown in Figure F.1 and Figure F.2, respectively.

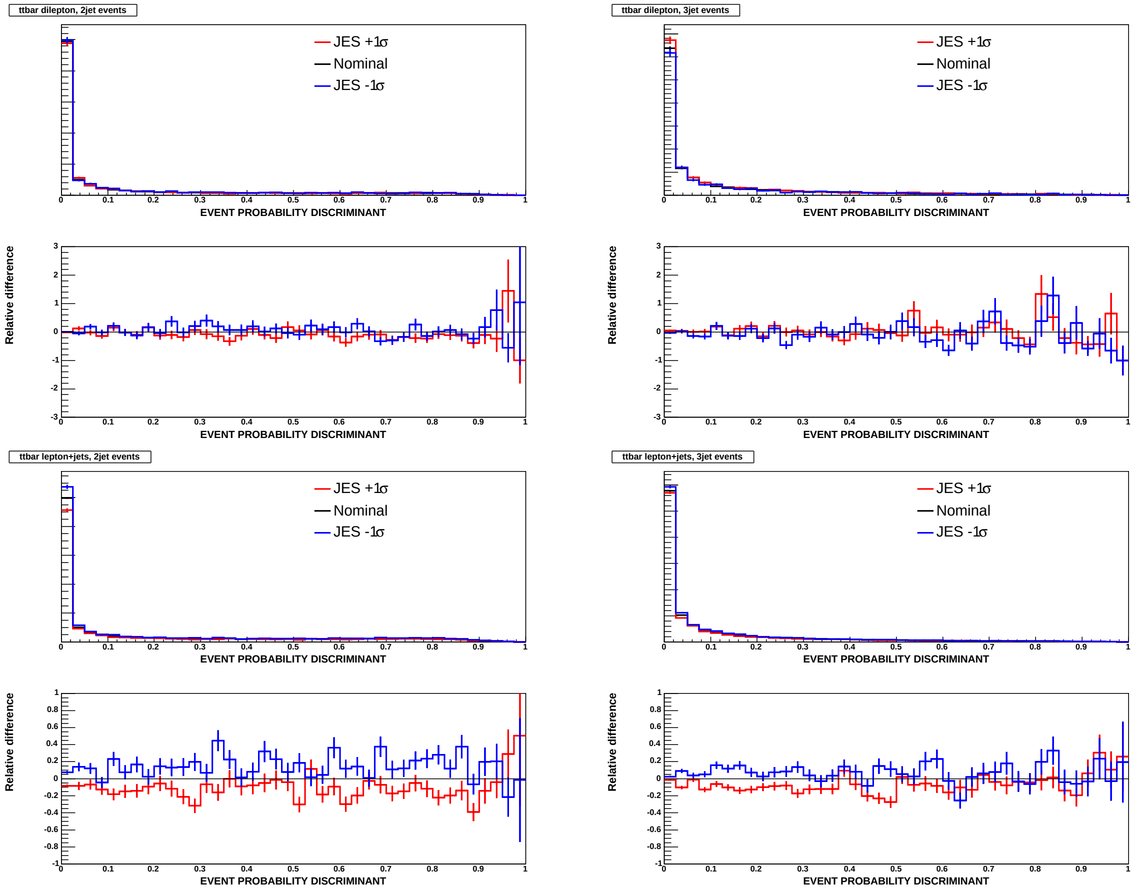

Figure F.1: $t\bar{t}$ dileptonic (top) and lepton+jets (bottom) Jet Energy Scale shape uncertainties for 2- (left) and 3-jet (right) events.

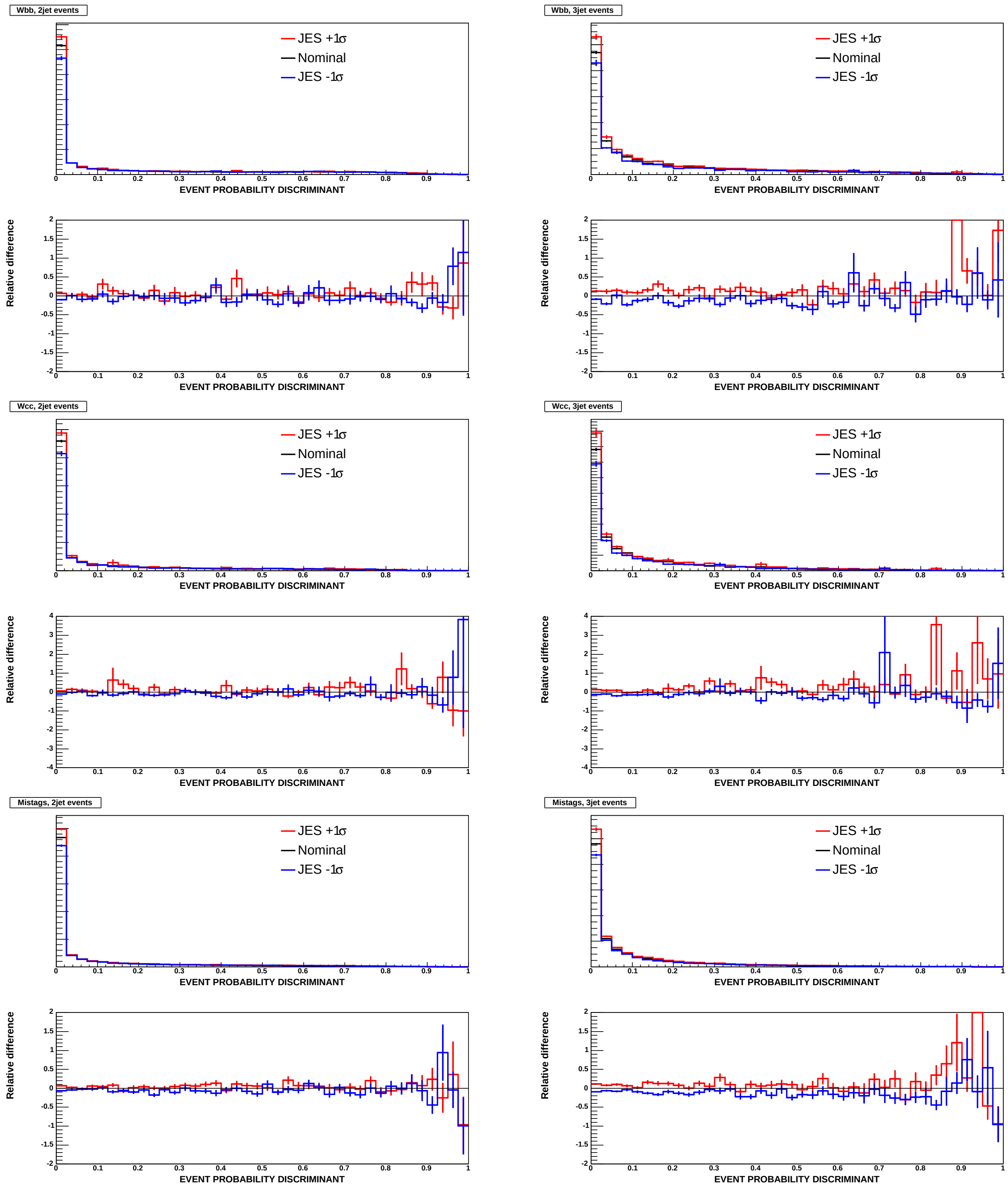

Figure F.2: W+jets Jet Energy Scale shape uncertainties: Wbb (top), Wcc (middle), and Mistags (bottom) for 2- (left) and 3-jet (right) events.

Bibliography

[1] ALEPH. The lep working group for higgs boson searches. *P.D.R*, 565:61, 2003.

[2] ALEPH. The lep working group for higgs boson searches. *P.D.R*, 47:547, 2006.

[3] *ATLAS TDR on Physics performance*, CERN-OPEN-2008-020, December 2008.

[4] CERN-LHCC-2006-001 CMS Collab. Cern-lhcc-2006-021. *CMS Note 2003/033*.

[5] E. Accomando et al. *Physics Reports*, 229:1–78, 1998.

[6] B. Autin et al. *(eds.), CERN 99-02*.

[7] C. Amsler et al. (Particle Data Group). *Phys. Lett. B*, 667:1, 2008.

[8] S. Fukuda et al. *Phys. Lett. B*, 539:179–187, 2002.

[9] Q. R. Ahmad et al. *Phys. Rev. Lett.*, 87:071301, 2001.

[10] Q. R. Ahmad et al. *Phys. Rev. Lett.*, 89:011301, 2002.

[11] S. L. Glashow. *Nucl. Phys. B*, 22:579–588, 1961.

[12] S. Weinberg. *Phys. Rev. Lett.*, 19:1264–1266, 1967.

[13] A. Salam. *Elementary particle theory: relativistic groups and analyticity. In Svartholm N, editor,* Nobel symposium No. 8 *page 367 Stockholm 1968. Almquist and Wiksell.*

[14] J. Goldstone. *Nuovo Cim.*, 19:154–164, 1961.

[15] J. Goldstone, A. Salam, and S. Weinberg. *Phys. Rev.*, 127:965–970, 1962.

[16] M. Kobayashi and K. Maskawa. *Prog. Theor. Phys.*, 49:652–657, 1973.

[17] J.M. Cornwall, D.N. Levin, and G. Tiktopoulos. *Phys. Rev. D*, 10:1145, 1974.

[18] B.W. Lee, C. Quigg, and H.B. Thacker. *Phys. Rev. D*, 16:1519, 1977.

[19] N. Cabibbo et al. *Nucl. Phys. B*, 158:295, 1979.

[20] For a compilation of the most accurate theoretical results for sm and mssm higgs cross sections at the tevatron and the lhc see:
`http://maltoni.home.cern.ch/maltoni/TeV4LHC/`.

[21] M. Carena and H. E. Haber. *Prog. in Part. Nucl. Phys.*, 50:152, 2003.

[22] K. Hagiwara et al. *Phys. Rev. D*, 66:010001–1, 2002.

[23] ALEPH, DELPHI, L3, and OPAL Collaborations. The lep working group for higgs boson searches. *Phys. Lett. B*, 565:61, 2003.

[24] S.L. Glashow, D.V. Nanopoulos, and A. Yildiz. *Phys. Rev. D*, 18:1724, 1978.

[25] T. Aaltonen et al. (CDF Collaboration). *Phys. Rev. Lett.*, 103:101802, 2009.

[26] V. M. Abazov et al. (D0 Collaboration). *Phys. Rev. Lett.*, 102:051803, 2009.

[27] http://www cdf.fnal.gov/physics/new/hdg//Results_files/results/whlnubbme_feb10/.

[28] V. M. Abazov et al. (D0 Collaboration). *Phys. Rev. Lett.*, 104:071801, 2010.

[29] T. Aaltonen et al. (CDF Collaboration). A search for the higgs boson using neural networks in events with missing energy and b-quark jets in $p\bar{p}$ collisions at $\sqrt{s} = 1.96$ tev. arXiv:0911.3935 [hep-ex].

[30] T. Aaltonen et al. (CDF Collaboration). *Phys. Rev. D*, 80:071101, 2009.

[31] V. M. Abazov et al. *Phys. Lett. B*, 655:209, 2007.

[32] Cristóbal Cuenca Almenar Ph.D. Thesis. *Fermilab-Thesis-2008-86*.

[33] G. Aubrecht *etal*. A teachers guide to the nuclear science wall chart. *Contemporary Physics Education Project*, page http://www.lbl.gov/abc/wallchart/teachersguide/pdf/Chap11.pdf, 2003.

[34] C. W. Schmidt. The fermilab 400-mev linac upgrade. *FERMILAB-CONF-93-111*, 1993.

[35] http://www boone.fnal.gov.

[36] J. Marriner. Stochastic cooling overview. *FERMILAB-CONF-03-158*, 2003.

[37] Fermilab Beams Division. Run ii handbook. *http://www-bd.fnal.gov/runII/index.html.*

[38] R. Blair *etal*. The cdf-ii detector: Technical design report. *FERMILAB-PUB-96/390-E*, 1996.

[39] D. Acosta *etal*. *Phys. Rev. D*, 71:032001, 2005.

[40] F. Abe *etal*. The cdf detector: an overview. *Nucl. Instrum. Methods A*, 271:387–403, 1988.

[41] C.S. Sill. Operational experience and performance of the cdf ii silicon detector. *Nucl. Instrum. Methods A*, 530:1–6, 2004.

[42] A. Sill *etal.* Cdf run ii silicon tracking projects. *Nucl. Instrum. Methods A*, 447:1–8, 2000.

[43] A. Affolder *etal.* Intermediate silicon layers detector for the cdf experiment. *Nucl. Instrum. Methods A*, 453:84–88, 2000.

[44] A. Affolder *et al.*(CDF Collaboration). *Nucl. Instrum. Methods A*, 526:249, 2004.

[45] http://penn01.fnal.gov/∼cot/.

[46] D. Acosta *etal.* A time-of-flight detector in cdf-ii. *Nucl. Instrum. Methods A*, 518:605–608, 2004.

[47] Enrique Palencia. Calibraciones del detector de tiempo de vuelo del experimento cdf en el tevatron. *Tesis de Licenciatura*, 2005.

[48] L. Balka *etal.* Cdf central electromagnetic calorimeter. *Nucl. Instrum. Methods A*, 267:272–279, 1988.

[49] S. Bertolucci *etal.* The cdf central and endwall hadron calorimeter. *Nucl. Instrum. Methods A*, 267:301–314, 1988.

[50] G. Ascoli *etal.* Cdf central muon detector. *Nucl. Instrum. Methods A*, 268:33, 1988.

[51] T. Dorigo *etal.* The muon system upgrade for the cdf ii experiment. *Nucl. Instrum. Methods A*, 461:560–562, 2001.

[52] D. Acosta *etal.* The cdf cherenkov luminosity monitor. *Nucl. Instrum. Methods A*, 461:540–544, 2001.

[53] D. Acosta *etal.* The performance of the cdf run ii luminosity monitor. *Nucl. Instrum. Methods A*, 494:57–62, 2002.

[54] J. Konigsberg S. Klimenko and T.M. Liss. Fermilab-fn-0741. 2003.

[55] W. Wagner *etal.* International europhysics conference on high-energy physics. *FERMILB-CONF-02269-E*, 12-18 Jul 2001.

[56] B. Angelos *etal.* International conference on computing in high-energy physics and nuclear physics. 7-11 Feb 2000.

[57] F. Abe et al. (CDF Collaboration). *Phys. Rev. D*, 45:1448, 1992.

[58] A. Bhatti et al. *Nucl. Instrum. Meth. A*, 566:375, 2006.

[59] D. E. Acosta et al. (CDF Collaboration). *Phys. Rev. D*, 71:052003, 2005.

[60] Enrique Palencia Cortezón Ph.D. Thesis. *University of Cantabria*, FERMILAB-THESIS-2006-50.

[61] S. Richter. Fermilab-thesis-2007-35.

[62] T. Aaltonen et al. (CDF Collaboration). Observation of electroweak single top-quark production. *Phys. Rev. Lett.*, 103:092002, 2009.

[63] R. Brun and F. Carminati. Cern programming library long writeup. *W5013*, 1993.

[64] T. Sjostrand *et al.*. *Comput. Phys. Commun.*, 135:238, 2001.

[65] H.L. Lai *et al.*(CTEQ Collaboration). *Eur. Phys. J*, C12:375, 2000.

[66] M. Mangano *et al.*. *J. High Energy Phys.*, 0307:001, 2003.

[67] J.A wall *etal*. Madgraph/madevent v4: The new web generation. *J. High Energy Phys.*, 0709:028, 2007.

[68] R. Veenhof. *Nucl. Instrum. Methods A*, 419:726, 1998.

[69] S. Peters G. Grindhammer, M. Rudowitz. *Nucl. Instrum. Methods A*, 290:469, 1990.

[70] M. Paulini E. Gerchtein. Econf (c0303241), tumt005 (2003), physics/0306031.

[71] J. M. Campbell and R. K. Ellis. Update on vector boson pair production at hadron colliders. *Phys. Rev. D*, 60:113006, 1999.

[72] D. Acosta et al. (CDF Collaboration). First measurements of inclusive w and z cross sections from run ii of the fermilab tevatron collider. *Phys. Rev. Lett.*, 94:091803, 2005.

[73] M. Cacciari et al. Updated predictions for the total production cross sections of top and of heavier quark pairs at the tevatron and at the lhc. *JHEP*, 0809:127, 2008.

[74] B.W. Harris et al. Fully differential single-top-quark cross section in next-to-leading order qcd. *Phys. Rev. D*, 66:054024, 2002.

[75] M. L. Mangano et al. *J. High Energy Phys.*, 07:001, 2003.

[76] D. Sherman (Ph. D. thesis). Measurement of the top quark pair production cross section with 1.12-fb(-1) of proton antiproton collisions at center of mass energy = 1.96-tev. *FERMILAB-THESIS-2007-82.*

[77] Measurement of the ttbar production cross section in ppbar collisions at sqrt(s)=1.96 TeV using lepton + jets events with secondary vertex b tagging. D. acosta et al. (cdf collaboration). *Phys. Rev. D*, 71:052003, 2005.

[78] T. Aaltonen et al. (CDF Collaboration). Measurement of the ww+wz production cross section using the lepton+jets final state at cdf ii. *Phys. Rev. Lett.*, 104:101801, 2010.

[79] T. Peiffer. Search for the Higgs Boson in the WH channel with the CDF II Experiment, FERMILAB Master Thesis, 2008-1.

[80] E. Murayama, I. Watanabe, and K. Hagiwara. Helicity amplitude subroutines for feynman diagram evaluations. *KEK Report*, 91:11, 1992.

[81] T. Stelzer and W. F. Long. Helas: Automatic generation of tree level helicity amplitudes. *Phys. Commun.*, 81:357–371, 1994.

[82] http://www.ra.cs.uni-tuebingen.de/snns/.

[83] Maria Florencia Canelli Ph.D. Thesis. *Rochester University*, FERMILAB-THESIS-2003-22.

[84] Martina Hurwitz. Measurement of the ww+wz production cross section in a semileptonic decay mode at cdf. *CDF/THESIS/EXOTIC/PUBLIC/10124*.

[85] A. Abulencia et al. (CDF Collaboration). Top quark mass measurement using the template method in the lepton+jets channel at cdf. *Phys. Rev. D*, 73:032003, 2006.

[86] L. Demortier. Bayesian treatments of systematic uncertainties, proceedings of advanced statistical techniques in particle physics, grey college, durham, 18 - 22 march 2002. *http://www.ippp.dur.ac.uk/Workshops/02/statistics/proceedings.shtml.*

[87] L. Read. *J.Phys. G.*, 28:2693, 2002.

[88] T. Junk. *Nucl. Instum. Meth.*, 434:435, 1999.

[89] The TEVNPH Working Group. *FERMILAB-CONF-09-557-E*, arXiv:0911.3930 [hep-ex].

[90] http://arxiv.org/abs/1003.4266.